Out-of-equilibrium body potential measurements on SOI substrates : implementation and applications for biochemical detection

Licinius Pompiliu Benea

Communauté UNIVERSITÉ Grenoble Alpes

THÈSE

Pour obtenir le grade de

DOCTEUR DE LA COMMUNAUTE UNIVERSITE GRENOBLE ALPES

Spécialité : **Nanoélectronique et Nanotechnologies (NENT)**

Arrêté ministériel : 25 mai 2016

Présentée par

Licinius BENEA

Thèse dirigée par **Irina IONICA,** et
codirigée par **Maryline BAWEDIN** et **Cécile DELACOUR**

préparée au sein du **Laboratoire IMEP-LaHC**
dans **l'École Doctorale EEATS**

Mesures de potentiel hors-équilibre sur substrats SOI : implémentation et applications pour la détection biochimique

Thèse soutenue publiquement le **08 Octobre 2019**,
devant le jury composé de :

M. Gérard GHIBAUDO
Directeur de recherche, IMEP-LaHC, Président
M. Francis CALMON
Professeur des Universités, INL, Rapporteur
Mme. Anne-Claire SALAÜN
Maître de Conférences, IETR, Rapporteur
Mme. Cristell MANEUX
Professeur des Universités, IMS, Examinateur
M. Frédéric ALLIBERT
Docteur, Ingénieur R&D, SOITEC, Examinateur
Mme. Irina IONICA
Maître de Conférences, IMEP-LaHC, Directrice de thèse
Mme. Maryline BAWEDIN
Maître de Conférences, IMEP-LaHC, Co-encadrante de thèse
Mme. Cécile DELACOUR
Chargé de recherche, Institut Néel, Co-encadrante de thèse

Acknowledgements

Firstly, I would like to express my sincere gratitude to my advisors Irina Ionica, Maryline Bawedin and Cécile Delacour for lending me an extremely interesting subject of research and for their support during my Ph.D, for their patience, motivation and shared knowledge. I also deeply thank Sorin Cristoloveanu who was always there to help me despite not being one of my official supervisors.

I would also like to thank the rest of my thesis committee: Gérard Ghibaudo, Francis Calmon, Anne-Claire Salaün, Cristell Maneux and Frédéric Allibert for their insightful comments, but also for their questions which encouraged me to perceive my research from various perspectives.

My sincere thanks also go to our collaborators from IMT Bucharest: Melania Banu, Monica Simion and Mihaela Kusko for their tremendous work and for their commitment to the project. Without their precious support and expertise it would not have been possible to conclude this research.

Many thanks are due to Xavier Mescot, Martine Gri and Aude Bouchard for all their valuable technical support and outstanding availability throughout my stay in the lab. Furthermore, I kindly thank for the help that I received from all the HR team members: Isabelle, Fabienne, Dalhila, Brigitte, Valérie and Annaïck.

I thank my fellow labmates Giuseppe Acri, Kyungwha Lee, Hyungjin Park, Miltiadis Alepidis, Dimitrios Damianos, Mukta Singh Parihar, Walid Aouimeur, Mohamad AWAD, Elodie Jordan, Namanu Panayanthatta, Thibauld Cazimajou for spending great moment in the lab and also during the conferences.

Last but not the least, I would like to thank my family for supporting me throughout the elaboration of this thesis and my life in general.

Abstract

In this thesis, we propose a new paradigm for biochemical detection based on the out-of-equilibrium body potential in silicon on insulator (SOI) substrates, used in the Ψ-MOSFET configuration. In this upside-down transistor typically used for unprocessed SOI wafer characterization, a channel is induced at the interface between the silicon film and the buried oxide by the back gate voltage applied on the bulk silicon. The current flow is then measured by two metallic pressure probes placed on the top silicon film. For thin films (<100nm), the channel is close to the surface of the SOI, allowing a straightforward influence of any deposited charges, on the conduction of the pseudo transistor. Instead of measuring a shift due to charges on the static I-V characteristics, we developed an innovative sensing method based on the out-of-equilibrium body potential, which appears due to the lack of carriers at the transition between the accumulation and inversion regimes. Charge injection through the metallic probes for channel formation is consequently critical for this effect. Surprisingly, the metal probes on the low-doped silicon film show experimentally an ohmic behaviour instead of Schottky, which we explained by the emergence of the metallic metastable high pressure phase of silicon by nanoindentation, due to the pressure applied by the pressure probes. Furthermore, we presented a simplified setup for the body potential measurements, which showed a great versatility and stability with regard to the pressure applied and the position of the probes. The experimental results were replicated through TCAD simulations, which ultimately showed that the influence of deposited charges on the silicon film can be measured using this method. Finally, the application of the body potential method for biosensing was realized by an incremental study starting from basic silicon functionalization methods to the detection of DNA molecules. The electric response was proportional to the DNA concentration and a limit of detection of 1μM was estimated from the experimental results. The proof of concept for this new reading method can be implemented to other field-effect devices (i.e. nanowires) and for other biochemical applications.

Keywords: Silicon-on-insulator (SOI), pseudo-MOSFET (Ψ-MOSFET), out-of-equilibrium body potential, biochemical sensors, DNA, nanoindentation.

Résumé

Dans cette thèse, nous proposons un nouveau paradigme pour la détection biochimique basé sur le potentiel hors équilibre dans des substrats de silicium sur isolant (SOI), utilisés dans la configuration Ψ-MOSFET. La configuration est typiquement utilisée pour la caractérisation des substrats SOI et est basée sur la structure intrinsèque du type transistor inversé du SOI, dans lequel un canal est induit à l'interface entre le film de silicium et l'oxyde enterré par la tension appliquée sur le substrat de silicium utilisé comme grille arrière. Le courant est mesuré par deux pointes métalliques à pression contrôlée posées sur le film de silicium. Le canal étant proche de la surface supérieure du SOI (<100nm), la conduction du pseudo-transistor est directement influencée par des charges déposées en surface. L'originalité de notre approche réside dans le fait qu'au lieu de mesurer le décalage dû à ces charges sur les caractéristiques statiques courant-tension, nous avons développé une nouvelle méthode basée sur le potentiel hors équilibre. Ce dernier apparait en raison du manque de porteurs nécessaires à la création du canal au moment de la transition entre les régimes d'accumulation et d'inversion. L'injection de charge à travers les pointes métalliques pour la formation de canaux est, par conséquent, essentielle pour obtenir cet effet. Contrairement à la théorie qui prédirait un contact Schottky, les pointes métalliques posées sur le film de silicium faiblement dopé montrent expérimentalement un comportement ohmique, que nous avons expliqué par l'apparition de la phase métallique métastable du silicium sous contrainte mécanique forte due à la nanoindentation provoquée par les pointes. Par la suite, nous avons mis en place une configuration simplifiée pour les mesures de potentiel, qui a montré une grande stabilité par rapport à la pression appliquée et la position des pointes. Les mesures ont été reproduites par des simulations TCAD, qui ont réussi également à montrer une influence des charges déposées sur le film de silicium sur le potentiel hors-équilibre. Enfin, l'application de la méthode du potentiel hors équilibre à la détection biochimique a été réalisée par une étude incrémentale allant de méthodes de fonctionnalisation de base sur silicium jusqu'à la détection d'ADN. La réponse électrique est proportionnelle à la concentration en ADN et une limite de détection de 1 μM a été estimée à partir des résultats expérimentaux. La preuve de concept de cette nouvelle méthode de lecture peut être appliquée à d'autres dispositifs à effet de champ (ex. : nanofils) et à d'autres applications biochimiques.

Mots-clés: silicium sur isolant (SOI), pseudo-MOSFET (Ψ-MOSFET), potentiel hors-équilibre, capteurs biochimiques, ADN, nanoindentation.

Table of Acronyms

Acronym	Nomination
AC	Alternative signal
APTES	((3-Aminopropyl)triethoxysilane)
Au-np	Gold nanoparticles
BOX	Buried oxide
CNT	Carbon nanotube
DC	Constant bias
DNA	Deoxyribonucleic Acid
EIS	Electrochemical impedance spectroscopy
FBE	Floating body effects
FD-SOI	Fully Depleted Silicon on Insulator
FIB-TEM	Focused Ion Beam Transmission electron microscopy
GOPS	(3-Glycidyloxypropyl)trimethoxysilane)
HF	Fluorhydric acid
ISFET	Ion sensitive field-effect transistors
ITRS	International Technology Roadmap for Semiconductors
IUPAC	International Union of Pure and Applied Chemistry
MCL	microcantilever
MD	Molecular dynamics
MOSFET	Metal-oxide-semiconductor field effect transistor
PCR	Polymerase chain reaction
pH	Power of hydrogen
QCM	Quartz crystal microbalance
RIE	Reactive ion etching
SiNW	Silicon nanowires
SOI	Silicon-on-insulator
SPR	Surface plasmon resonance
SSRM	Spreading resistance microscopy
TMAH	Tetramethylammonium hydroxide
WC	Tungsten carbide
Ψ-MOSFET	pseudo-MOSFET

Table of Symbols

Symbol	Unit in SI	Description
μ_0	m/Vs	Low field mobility
μ_{eff}	m/Vs	Effective mobility
c	mol/L	Concentration
C_{BOX}	F/m²	BOX capacitance
C_{Si}	F/m²	Silicon film capacitance
D_{it}	$cm^{-2}eV^{-1}$	Interface trap density
f_G		Geometrical factor in Ψ-MOSFET
I_D	A	Drain current
I_G	A	Gate current
R_{SD}	Ω	Access resistance
t_{BOX}	m	BOX thickness
t_{Si}	m	Silicon film thickness
V_B	V	Out-of-equilibrium body potential
V_D	V	Drain voltage
V_{FB}	V	Flat-band voltage
V_G	V	Gate voltage
V_T	V	Threshold voltage
θ_1	V^{-1}	First order attenuation factor
σ_{bl}		Standard deviation for reagent blank

Table of Contents

Chapter 1 : GENERAL INTRODUCTION AND CONTEXT

The first chapter provides the context and motivations of this thesis. After presenting the general context in the first part, an extended study which includes the state-of the art and theoretical considerations regarding the biosensor field is exposed. A particular attention is granted to the field-effect based sensors and the benefits of using silicon-on-insulator technology will be highlighted in order to render a specific orientation to our research. The main goals of the thesis are then presented.

Table of Contents

1.1. Context

The semiconductor industry was governed by Moore's law since the 1970s [1], which induced an exponential market growth due to transistor scaling. This enabled further investments in semiconductor technologies which would fuel further scaling. The decline in price of the electronic devices/circuits has been remarkable. In 1954, five years before the invention of the integrated circuits, the average selling price of a transistor was $5.52. In 2005, the price per bit of DRAM memory was one nanodollar [2].

The progress was anticipated by the International Technology Roadmap for Semiconductors (ITRS) [3], which was able to provide research guidance for the actors of the semiconductor ecosystem, increasing thus the resource efficiency of the very fast technological development of the semiconductor industry.

When the limitations of the miniaturization philosophy became obvious, two complementary directions were proposed. The one labelled "More Moore" aimed at continuing transistor down-scaling by incorporating new materials and by applying new transistor concepts.

The second trend was defined by a functional diversification of semiconductor-based devices. In view of the added functionality, this direction was labelled as "More than Moore". This functional diversification is in fact a complement of digital signal and data processing, which includes for example the system powering the product and the interaction of the electronic circuits with the "outside world" through an appropriate sensors and actuators. In the future, it is expected that the "More than Moore" component in the industry will increase. Thus, the expansion of the industry is no longer based only on device scaling, but on the many adjacent technological innovations and the added functionalities.

In this context, our research is aimed at contributing to the sensor field, more particularly biosensors, which are part of the "More than Moore" spectrum.

A biosensor can be simply defined as an analytical device that detects a biological response and converts it into an electrical signal. Since the discovery of the first glucose sensor by Clark and Lyons [4], biosensors attracted the attention of the scientific community and were developed under many forms and for various applications. A proof of it is the intensive scientific production in terms of publications, which continued to grow in the last decades (Figure I.1).

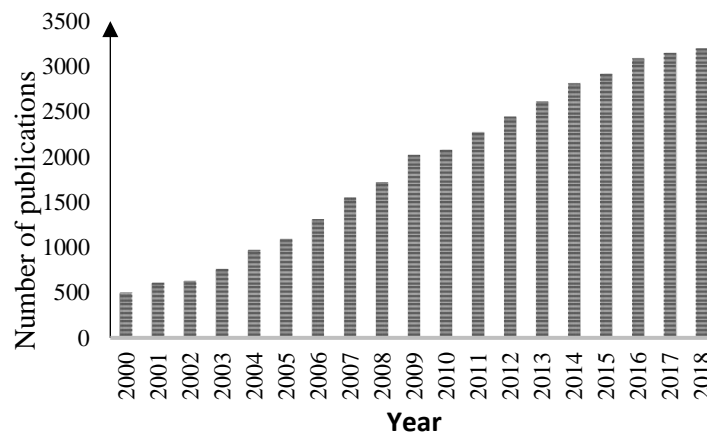*Figure I.1: Number of publications per year containing the term "biosensor" (Source: ISI Web of Knowledge).*

From an industrial point of view, the biosensor market was evaluated at 15.96 Billion USD in 2016 and is likely to reach 27.06 Billion USD by 2022, at an estimated growth rate of 8.84% [5]. The significant expansion is due to increasing demand in point of care testing caused by a rising prevalence

of chronic and lifestyle associated diseases, a growing geriatric population, the emergence of personalized medicine and non-invasive biosensors.

In order to be commercially successful, biosensors must meet some general criteria: sensitivity of medical interest, high specificity to the analyte of interest, shelf stability, high speed and convenience of use. Performance criteria and working principles will be described in more detail in the following sections.

1.2. Biosensor state of the art and theoretical considerations

A biosensor is an analytical device capable of providing quantitative or semi-quantitative information using a biological recognition system (biochemical receptor) which is in contact with an electrochemical transducer element [6]. Its continuous improvement necessitates interdisciplinary efforts of several fields: (bio)chemistry, electrochemistry, bioengineering, materials science, electrical engineering, microelectronics, software engineering and others [7].

Generally, the analytical system of a biosensor is composed of five elements (represented in Figure I.2):

- **The analyte** is the substance of interest that needs detection (e.g. glucose, proteins, etc.).
- **The biochemical receptor** is a molecule that specifically recognises the analyte. The process of generating the signal (light, heat, pH, charge or mass change etc.) during the interaction is named bio-recognition. Its main purpose is to provide the sensor with a high degree of selectivity. Some examples would be enzymes, cells, aptamers, DNA and antibodies.
- **The transducer** serves to transfer the signal from the output domain of the biochemical receptor (a bio-recognition event) into a measurable signal, mostly electrical.
- **The electronic system** is the part that processes the transduced signal and prepares it for display. The output signal is conditioned using amplification and conversion of the signal from analogue into digital by electronic circuitry.
- **The display** consists of a system (display or printer) that generates numerical results or graphs that can be interpreted by the user.

The improvement of the receptor and the transducer are key elements in the performance of the biosensor and are evaluated based in the criteria presented in the next section.
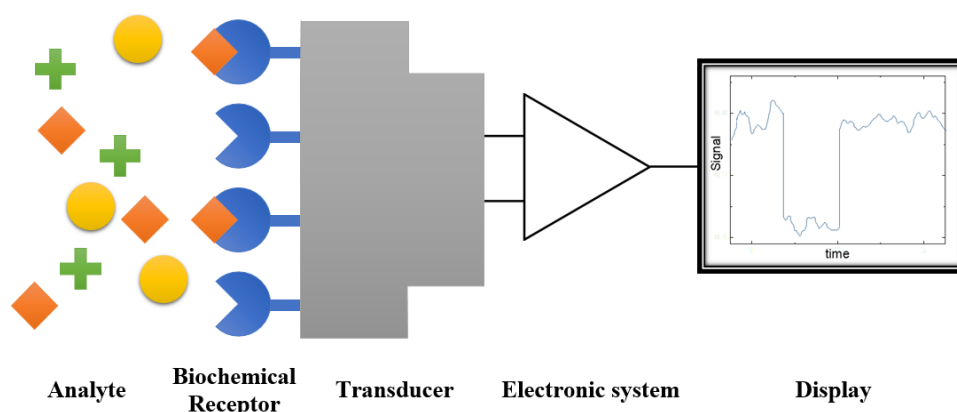

| Analyte | Biochemical Receptor | Transducer | Electronic system | Display |

Figure I.2: Schematic of biosensor components

1.2.1. Performance criteria

Rapid proliferation of biosensors and their diversity makes it of utmost importance to rigorously define the performance criteria. Although a sensor can only be genuinely evaluated for a specific application, it is still useful to establish standard protocols in accordance with standard IUPAC (International Union of Pure and Applied Chemistry) protocols and definitions [8]. They include four sets of parameters which will be subsequently described.

a. Calibration characteristics: sensitivity and limit of detection

The calibration of the device is realized by adding standard solutions of the analyte and by plotting steady state responses (R_{ss}) possibly corrected by a blank signal (R_{bl}) versus the concentration (c) or versus the logarithm of the normalized concentration ($\log {^c/_{c_0}}$, where c_0 is a reference concentration).

The biosensor calibration curve is traced therefore as $R_{ss} - R_{bl}$ versus c or $\log {^c/_{c_0}}$. The sensitivity and the linear concentration range can be directly obtained by plotting $\frac{R_{ss}-R_{bl}}{c}$ or $\frac{R_{ss}-R_{bl}}{\log{^c/_{c_0}}}$ versus $\log {^c/_{c_0}}$. The latter is more concise and gives the same weight to low and high concentrations. [6].

The limit of detection does not have a definition specific for biosensors. It represents the smallest measure that can be detected with a reasonable certainty for a given analytical procedure [9]. It is determined using the following formula:

$$S_{dl} = \overline{S_{bl}} + k \cdot \sigma_{bl} \tag{I.1}$$

where S_{dl} is the analyte signal at the detection limit, $\overline{S_{bl}}$ is the average signal for reagent blank, k is a numerical factor in accordance with the confidence level (i.e. 2σ, 4σ, 6σ level of accuracy) and σ_{bl} is the standard deviation for reagent blank.

b. Reproducibility, stability and lifetime

Reproducibility is the measure of the scatter or the drift in a series of results performed over a time frame [6]. In other words, it is the capability of a biosensor to have very similar responses for an identical experimental set-up. It is determined by the precision and accuracy of both the transducer and the electronic parts of a biosensor. Precision is the ability to generate similar results for every measurement of the same sample and accuracy represents the capability to provide a mean value close to the real one for multiple measurements of the same sample [7]. It is generally determined within the usable range of analyte concentration.

The operational stability of a biosensor response can vary depending on sensor geometry, method of preparation, biochemical receptor, transducer, response rate and operational conditions.

Biosensor lifetime represents the storage or operational time necessary for the sensitivity within the linear concentration range to decrease by a factor of 10 or 50%. The assessment method can be specific for each sensor and needs to be specified.

c. Selectivity and reliability

Selectivity refers to the discrimination shown by the bioreceptor when reacting to a specific analyte in a sample containing other compounds and/or contaminants. It depends on the choice of the biological receptor and the transducer and it is perhaps the most important characteristic of a sensor. It can be expressed, as in potentiometric or amperometric sensors, by calculating a selectivity coefficient ($k_{A/B}$) using the approaches described in the IUPAC methodology [10]. It represents a measure of the

sensitivity to the interfering ion B, as compared to that of the primary ion A. For the best selectivity, $k_{A/B}$ should be as high as possible.

An example of highly specific interaction is between antigen and antibody. The latter acts as bioreceptor and is immobilized at the surface of the transducer. The transducer is then exposed to a solution containing the antigen which is the only constituent interacting with the antibody. Other sensors with a good selectivity obtained by receptor-analyte interactions are oxygen, pH and enzymatic.

The reliability of a sensor is a result of both selectivity and reproducibility. It has to be determined under operating conditions. A reliable biosensor should have a response which is stable.in time and directly related to the analyte concentration and should not depend upon the influence of other interfering substances.

d. Steady-state and transient response times

Steady state response time is the time needed to reach 90% of the steady state response [11].
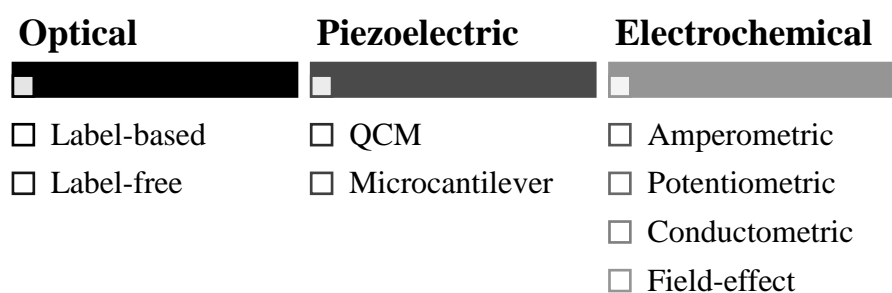
Transient response time is the time necessary for the first derivative of the output signal to reach its maximum value following the addition of analyte. Those parameters are essential for determining the experimental set-up in the static and transient measurements, respectively.

The general criteria mentioned in this section must be specified for each type of sensor. This allows the comparison between devices based on different working principles and various response parameters.

1.2.2. Biosensor principles and state of the art

The biosensor classification can be approached in two manners. It can be realized according to the biological recognition system or to the mode of signal transduction. In this section, we will concentrate on the latter, by describing the working principles of the main classes of biosensors and their applications.

There are four main classes: thermal, optical, piezoelectric and electrochemical. Each one includes multiple methods for transduction. In the following, the most widespread classes of biosensors will be reviewed: optical, piezoelectric and electrochemical (Figure I.3). A particular attention will be granted to the field-effect biosensors in order to have a more complete view of this type of biosensors which represents the topic of this thesis and will be described in a dedicated section.

Optical	**Piezoelectric**	**Electrochemical**
□ Label-based	□ QCM	□ Amperometric
□ Label-free	□ Microcantilever	□ Potentiometric
		□ Conductometric
		□ Field-effect

Figure I.3: Classes of biosensors and subsequent transduction methods.

Optical biosensors

Optical biosensors represent the most common type of biosensors. The research and development of this type of sensors has been directed mainly towards healthcare, environmental applications and the biotechnology industry. They were so far applied to various types of molecules: enzymes, antibodies, antigens, receptors, nucleic acids, whole cells and tissues [12].

There are also numerous photonic methods of transduction, but the general approach can be classified into label-free and label-based. While in the former the detected signal is simply produced by the interaction between the analyte and the transducer, in the latter involves the use of a fluorescent label attached to the molecule of interest, which generates the optical signal.

a. Label-free techniques

The label-free techniques are numerous (i.e. waveguide interferometry, ellipsometry, reflectometric interference spectroscopy, surface-enhanced Raman scattering). In the following, due to the attracted interest in the scientific community, we will only briefly describe the surface plasmon resonance based biosensors. SPR occurs on the surface of a conducting material (generally a metal) at the interface between two media (generally glass and liquid). When illuminated by a polarized light source at a specific angle, surface plasmons are generated, resulting in a reduction of the intensity of the reflected light. This angle is described as the resonance angle and is proportional to the mass on the surface. The measured output is indicated by a shift of reflectivity, angle of resonance or wavelength against time. SPR allows direct, label-free and real time changes of refractive index at the surface of the sensor, which is proportional to the analyte concentration (Figure I.4).
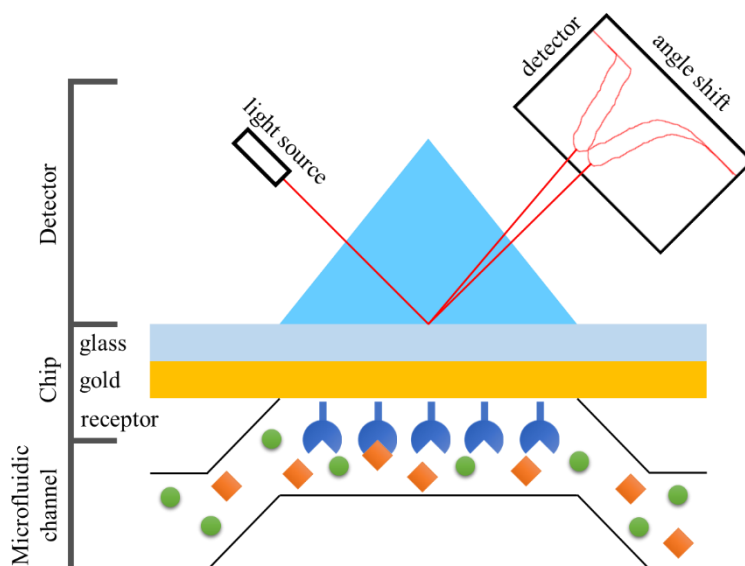

Figure I.4: Schematic of a surface plasmon resonance based biosensor.

SPR was first observed in 1902 and in 1983 was used for the first time to detect antibody adsorption of human γ-globulin (IgG) and antihuman γ-globulin [13]. Among its many applications, we will only cite DNA, which was detected at very low concentrations: 2.5 nM [14] or even 1.38 fM [15].

SPR can be realized in more complex ways. SPRi (SPR imaging) is a technique which combines the advantages in terms of sensitivity from the SPR and the spatial imaging of microarrays. This allows the study of multiple different interactions on an array of precisely patterned molecules. Also, localized SPR (LSPR) is realized by replacing the conductive layer by metallic nanoparticles (Au, Ag, etc.). Compared to classical SPR, LSPR is able to provide the same performance, while involving significantly lower surface densities of interacting molecules. This allows the reduction of the biosensor dimensions, which are generally expensive and bulky (e.g. Biacore™ [16]).

b. Label-based techniques

Biosensors based on fluorescence depend on the optical detection of a fluorescent dye which is initially attached to the analysed molecule. The dye is excited with a light source and reemits a

fluorescent signal at a higher wavelength which is acquired by a detector. These biosensors can be extremely sensitive as the limit of detection of DNA was proven to reach 10 aM [17]. However, the need of the previously attached dye makes this type of sensors unsuitable from a practical perspective.

Evanescent wave biosensors represent an interesting label-based technique. The recognition and binding occur within the boundaries of an evanescent wave which arises from the confined space of an optical waveguide or fibre (Figure I.5). The evanescent wave intensity decreases exponentially with the distance from the interface and can be found at a depth between 100nm and approximately the value of a wavelength. Since this is an entirely near-surface phenomenon, it helps minimizing background noise coming from the solution.

Waveguide-based biosensors were recently commercialized and are expected to produce an important impact in the healthcare fields. The assessment of more than 200 clinical samples coming from healthy and HIV, syphilis and hepatitic-C positive individuals demonstrated a great specificity [18].
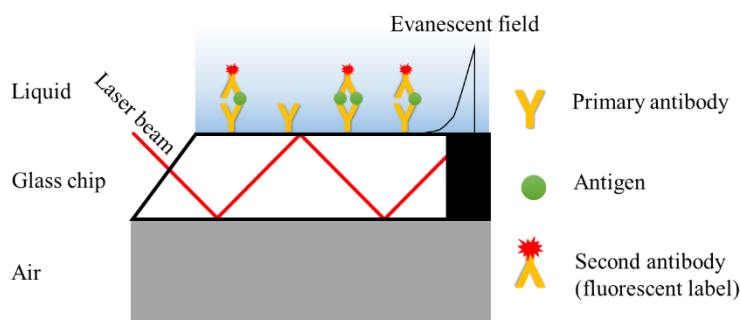

Figure I.5: Schematic of an evanescent wave biosensor.

Piezoelectric biosensors

Piezoelectricity is the ability of a material to produce a voltage when mechanically stressed. This phenomenon occurs in anisotropic crystals (without a centre of symmetry).

The piezoelectric biosensor is excited by an AC signal applied between two electrodes on the surface. This induces mechanical oscillations and the frequency of oscillations is measured. Analyte or any other mass attached to the surface of the crystal induces a change in the oscillation frequency [19], which is proportional to the added mass [20]. Also, a change in medium viscosity can influence the oscillations as well [21].

This class of sensors presents the advantage of detecting the interactions between the functionalized sensor and the analyte without the need of any specific reagents. However, a minimum sensitivity of the order of micrograms is necessary in order to have a measurable change in oscillation frequency. Also, some other factors such as fragility need to be taken into consideration [22].

Among the current techniques from this class of sensors, quartz crystal microbalance (QCM) is the most popular. They are widely used and also commercially available. Their structure consists in a thin plate of quartz with two gold electrodes on each side (Figure I.6a). Among many other molecules, they proved the ability to detect DNA at a concentration as low as 1pM [23].

An alternative device is the microcantilever (MCL). The absorption of analyte molecules on immobilized receptors on the cantilever result in a variation of the mass which translates into a deflection (in static mode) (Figure I.6b) or a modification of the resonance frequency (in dynamic mode) of the cantilever [24]. The bending can be measured in-situ using an optical beam in which each microcantilever is illuminated by a VCSEL (Vertical Cavity Surface Emitting Laser) [25]. They have been proven to detect DNA hybridization at a concentration as low as 1fM [26].
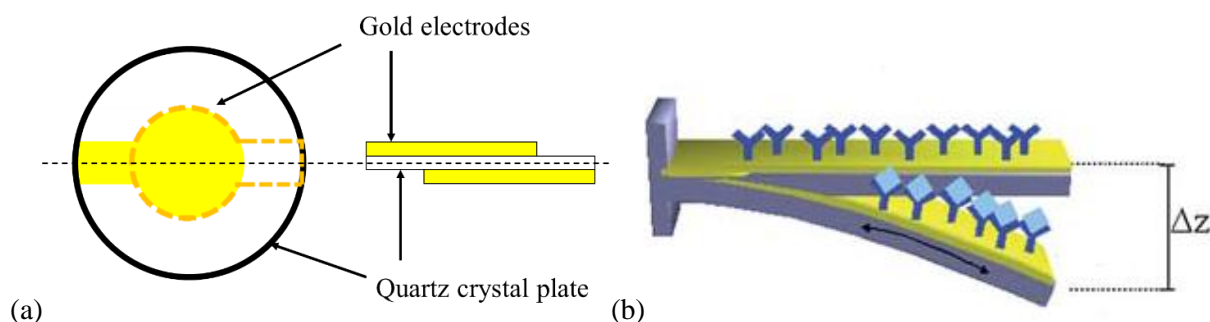
Figure I.6: Schematic of (a) a quartz crystal microbalance biosensor and (b) a microcantilever biosensor (reproduced from [24])

Electrochemical biosensors

The working principle of this class of biosensors is based on the reaction between immobilized biomolecules and target analyte that produces or consumes ions, which translates into a modification of the measurable electrical properties of the solution [27].

a. Amperometric

In this case, the transduction is based on the measurement of a current resulting from the electrochemical oxidation or reduction of an electroactive species. It is usually conducted by maintaining a constant potential at a Pt, Au or C based working electrode or array of electrodes with respect to a reference electrode. The measured current can be directly correlated to the concentration of the analyte [6].

The intrinsic simplicity plays a central role, making it capable of conceiving low-cost portable devices for applications ranging from disease diagnostics to environmental monitoring. They are the most widespread sort due to their application in glucose monitoring, which nowadays occupies 70% of the biosensor market [28].

b. Conductometric

The principle is based on measuring the impedance of the solution which is the ratio between the applied AC potential and the AC current that flows through it. Electrochemical impedance spectroscopy is the most common technique [28].

The frequencies used vary generally between 1 mHz and 100 kHz. The frequency domain response provides information about the physio-chemical changes appearing on an electrode where an analyte binds to a receptor. The information obtained comprises: charge transfer processes (from solution to electrode), solution resistance, diffusion transport of species, double layer capacitance formation [29].

c. Potentiometric

Their principle is based on a potential measurement between either an indicator and reference electrode or two reference electrodes separated by a permselective membrane, at almost 0 current flow. The potential difference is proportional to the logarithm of the ion activity or gas fugacity, as described by the Nernst-Donan equation [30].

Nearly all potentiometric sensors (i.e. glass electrodes, metal oxide based sensors, ion-selective electrodes) are commercially available. The most common devices are pH electrodes, but several other ions (F^-, I^-, CN^-, Na^+, K^+, Ca^{2+}, NH_4^+) or gas (CO_2, NH_3) selective electrodes are available [6].

d. Field-effect devices

They were initially considered as a category of potentiometric sensors, but are now separated into a fourth class of electrochemical sensors according to IUPAC [27]. Ion sensitive field-effect transistors (ISFETs) are essentially classical field-effect devices which have the gate insulator coupled with a biocatalytic or biocomplexing layer facing an electrolyte solution [6]. Consequently, the device is sensitive to the (bio-)chemical changes occurring at its sensitive surface, which appear as a change in the gate potential (Figure I.7a and Figure I.7b). A shift in the MOSFET drain current versus gate voltage characteristics is then observed (Figure I.7c). It can be measured either by a variation of current, generally in the subthreshold regime, or a variation of the threshold voltage. As this thesis addresses field-effect based biosensors, those type of devices will be described in more detail in the following section.
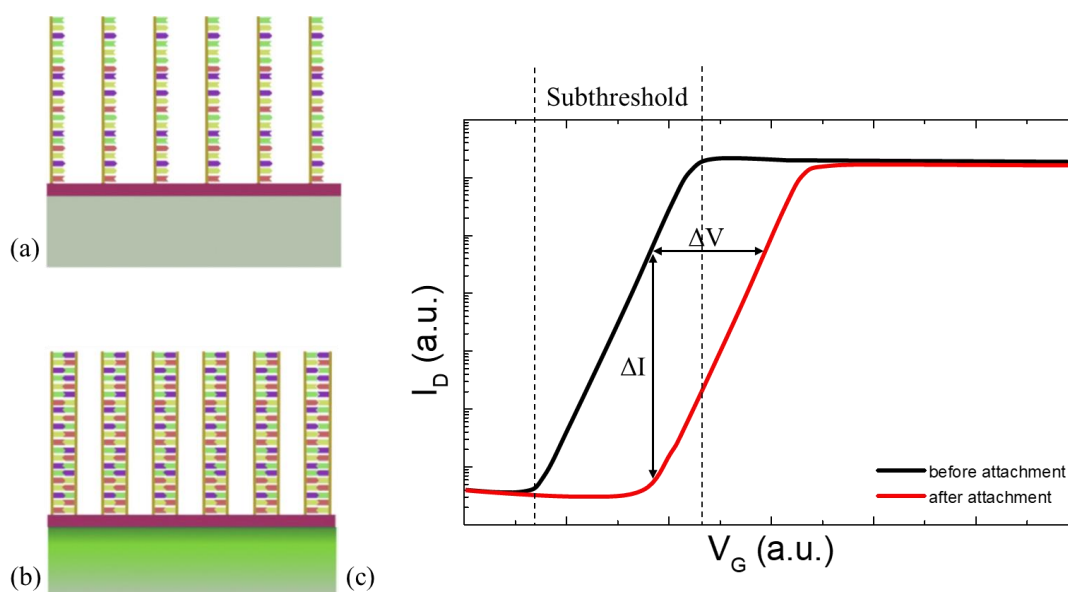

Figure I.7: Schematics of biomolecules attaching to the top surface of a silicon sensor (a) and (b) [31] and the consequent shift on a NMOS device (c).

1.3. Field-effect biosensors

At the beginning, field-effect sensors could be found under the form of traditional MOS (metal oxide semiconductor) transistors [32]. With the introduction of nanomaterials and scalable nanostructuring methods, nanometer-scale devices became of utmost importance in the development of novel sensors. They brought many advantages in terms of scalability, sensitivity and the possibility of multiplexed read-out capabilities, which are key points in the development of point-of-care systems [28].

Last decades of research were marked by the rise of two main nanodevices fabricated from different materials: carbon nanotubes (CNTs) and silicon nanowires (SiNW). Both are particularly interesting due to their high surface-to-volume ratios which confers them a great sensitivity. As a matter of fact, in the case of single walled CNTs, every atom is exposed to the environment, thus even small environmental changes can cause major changes to their electrical properties. Moreover, carbon atoms provide an excellent natural match for organic molecules. CNT found many applications such as the detection of antibody-antigen interactions, glucose sensing and DNA hybridization [33], showing a limit of detection which reaches fM level. For example, Maehashi et al. were able to determine a limit

of detection of DNA of 6.8 fM [34]. However, some drawbacks limit their application: the prevention of non-specific adsorption of biomolecules, the biodetection mechanism is not yet understood and the noise of the electrical signal needs to be reduced in order to obtain ultralow detection limits [35].

Nanowires are the other type of devices that attracted considerable attention from the scientific community of the bio-chemical sensing, thanks to their variety of applications. Some of the examples which indicate the large variety of applications are: insulin, streptavidin, influenza A virus, prostate specific antigen (PSA), dopamine, carbohydrate antigen- 15.3 (CA-15.3), cardiac troponin T (cTnT), creatine kinase, carcinoembryonic antigen (CEA), mucin-1, thyroid-stimulating hormone, troponin I, endoplasmic reticulum, RT-PCR product of dengue serotype 2, and microRNA [36].

a. Nanowire device performance

In terms of performance, nanowires are highly dependent on the device characteristics such as geometry, doping concentration, buffer screening (screening of the charges of the molecule of interest by other ions in the solution) or surface chemistry. In the following paragraph, only the characteristics related to the device will be addressed.

The width of the nanowire is strongly related to its sensitivity, which was proven to increase linearly between 800nm and 100nm and become even higher for 50nm [37]. Other works converged towards the same conclusion: a smaller width and height of the nanowire are equivalent to a higher surface-to-volume ratio, which translates into a higher sensitivity [38], [39]. Also, Kim et al. [40] argued that the sensitivity also increases with the length of the nanowire due to the higher channel resistance.

Moreover, the effect of NW doping showed that a low concentration is favourable because fewer carriers are available to screen the charges brought by DNA, having thus a larger depletion area induced by the charged molecules [39]. Additionally, in the same paper he advocated for the use of the subthreshold regime for an increase sensitivity, as the variation of the current increases exponentially with the quantity of added charges.

b. Nanowire biosensors: materials and applications

Many variants of the nanowire biosensors were so far presented in the literature. From a material point of view, besides silicon, many other materials were proposed for different applications. Zinc oxide (ZnO) NWs allowed the measurement of glucose in the concentration range of 0.1-100mM, matching the human physiological concentration [41], as well as uric acid [42]. Titanium dioxide (TiO_2) was used for example to detect rabbit immunoglobulin G [43]. Galium nitride NWs detected various proteins and biomolecules [44], [45] and indium oxide was applied to cancer biomarkers [46] or antibody mimic protein [47].

Silicon is however the most used material for field-effect biosensors. It is particularly interesting due to the fact that the transducers can be perfectly integrated with miniaturized electronics, while preserving their nanoscale dimensions. As such, silicon-based biosensors are, arguably, the most practical and scalable low cost diagnostic tools. On the other hand, the necessity to encapsulate part of the device, poor reproducibility and inconsistent attachment of biological receptors remain issues that need addressing [35].

The first SiNW biosensor was presented by Cui et al. [48]. The bottom-up fabricated devices (fabricated by growth) were able to be sensitive to pH variations and detect streptavidin at a remarkable 10 pM limit. After the first field-effect DNA sensor presented in 1997 by Souteyrand et al. [49], in 2004 Hahm and Lieber introduced the first SiNW DNA detector with a limit of detection of 10 fM using again a bottom-up approach [50].

The need for bottom-up hybrid fabrication resulted in severe integration issues that have inhibited widespread application. This approach (bottom-up) was chosen to the detriment of top-down (fabricated

by lithography and etching) because of the poor device performance induced by the fabrication process. In 2007 Stern et al. proposed an alternative top-down fabrication process by using ultrathin silicon on insulator wafers and an anisotropic wet-etch fabrication using tetramethylammonium hydroxide (TMAH). The Si(111) planes are etched 100 times faster than the other ones, which allowed the fabrication of SiNW with a high degree of conformity. Nuzaihan et al. later used an e-beam lithography fabrication method to produce a sensor that was capable of detecting DNA at 10 fM [51].

After a decade of development, the limit of DNA detection was further reduced to 50 aM [52] by carefully adjusting the fabrication characteristics of the NWs and the improvement of the measurement method. Some of the most remarkable results obtained for DNA detection are presented in Table I.1.

Table I.1: Summary of the SiNW biosensors chronological evolution for DNA detection and LOD.

Year	Reference	Device specification	LOD
2004	[50]	p-type SiNW (bottom-up), diameter 20nm, L≈2µm	10 fM
2004	[53]	n,p-type SiNW (top-down), W=50nm, L=20µm	12 pM
2006	[54]	n,p-type SiNW (top-down), W=20nm, L=30nm	10 pM
2008	[55]	n-type SiNW (top-down), W=50nm, T=60nm, L=100nm	10 fM
2010	[56]	p-type SiNW (top-down),W=50nm, H=80nm	1 pM
2011	[57]	p-type SiNW (top-down),W=40nm	200 pM
2011	[58]	p-type SiNW (top-down),W=20nm, L=6µm	1fM
2012	[59]	p-type SiNW (top-down), L=16µM	0.1fM
2013	[60]	p-type SiNW (top-down),W=60nm, H=200nm	1 nM
2013	[52]	p-type SiNW (top-down), W=20nm, L=6µm	50 aM
2013	[61]	p-type SiNW (top-down), L=3µm, W=200nm, T=40nm	0.1 fM
2013	[62]	p-type SiNW (top-down), W=70nm, L=2-5µm	1fM
2016	[51]	p-type SiNW (top-down),W=20nm, H=30nm	10 fM

Besides DNA, SiNW devices were used to detect other biological species such as dengue virus, streptavidin or prostate-specific antigen at a femtomolar level or for pH measurement (Table I.2).

Table I.2: SiNW biosensors for miscellaneous applications

Year	Reference	Device specification	Application	LOD or Sensitivity
2010	[63]	n-type SiNW (top-down), W=50nm, T=60nm, L=100nm	Dengue virus	10fM
2009	[64]	n-type SiNW (top-down), W=50nm, T=60nm, L=100nm	microRNA	1fM
2006	[65]	p-type SiNW (top-down),W=300nm, H=230nm, L=8µm	pH	60 mV/pH
2008	[66]	p-type SB-SiNW (top-down),W=50nm, H=100nm,L=µm	pH	49 mV/pH
2011	[67]	p-type Si-NW, W=50nm, H=40nm, L=10µm	pH	40 mV/pH
2012	[68]	p+n-type Si-NW (top-down) W=150 nm, H=80 nm, L=3µm	pH	162 mV/pH
2013	[69]	n-type DG-SiNW, W=110nm, T=30nm, L=100nm	pH	66 mV/pH
2007	[40]	n-type SiNW (top-down),W=67-141nm, H=40nm, L=2-20µm	PSA	30 aM
2005	[70]	n,p-type SiNW (bottom-up), diameter 20nm	PSA	2 fM
2001	[48]	p-type SiNW (bottom-up), diameter 20nm, L≈1µm	Streptavidin	10 pM
2007	[71]	n,p-type SiNW (top-down),W=50-150nm, H=40nm	Streptavidin	10 fM
2008	[38]	p-type Si-nanoribbons, W≈1µm, H=50-105nm, L≈2µm	Streptavidin	<pM
2010	[72]	p-type SiNW (bottom-up), diameter 30-60nm	Troponin-I	7nM

c. Industrial applications of nanowire biosensors

Despite the interest and progresses in research, corroborated by the intensive scientific production in terms of publications, the commercialization of nanowire biosensor technology did not follow the same accelerated trend. At an industrial level, NW technology is intended for diagnostic purposes, but for the moment there is no mainstream industrial application. For instance, the company QuantuMDx proposes point-of-care diagnostics tool with its Q-POC™ product (Figure I.8), which is still under development. It promises sample-to-result molecular diagnostic testing in less than 20 minutes. The main fields of application announced are the detection of Warfarin (anticoagulant medicine) sensitivity, human papilloma virus, tuberculosis and sexually transmitted infections.

Figure I.8: Q-POC™ diagnostic point-of-care unit by QuantuMDx

d. Commercially available DNA sequencers using field-effect biosensors

The method presented in the previous sections is only capable to detect a sequence known beforehand. Therefore, DNA sequencing using field-effect devices can be so far only realized effectively by using a more complex approach. This technology is based on polymerase chain reaction (PCR), a widely used method in biochemistry for replicating DNA chains. The chip used contains several millions of wells of ISFETs specifically designed to detect pH variations by having a Ta_2O_5 active layer on top of the gate. Before sequencing, the hybridized DNA is first denaturized (separation of strands) by a thermal treatment. Each fragment is then attached to an acrylamide bead. Millions of beads produced as a result cover the wells on the chip. The chip is flooded systematically with the four DNA nucleotides (cytosine (C), thymine (T), adenine (A), guanine (G)). Whenever a nucleotide is incorporated in the single strand of DNA, a H^+ ion is released which changes the pH of the solution which is measured by the ISFET (Figure I.9a) [73], [74].

This process occurs simultaneously in millions of wells (there are minimum 1.2 million wells per chip for the Ion Torrent technology). Each 15 seconds the process is repeated with a different nucleotide. In case there are two consecutive nucleotides of the same sort, the voltage variation doubles, so that the apparatus records the correct sequence of DNA. Errors arise from noise which comes from the incomplete nucleotide addition to all fragment extensions. These are particularly high for homopolymers (multiple identical bases). The measured error stands at 1% (1 of 100 bases) [75].

From an industrial point of view, this method (named Ion Torrent Technology) was introduced in 2010 by Jonathan Rothberg who developed its chip-based technology in the early 2000s and commercialized it in 2010 [76]. The company is now part of the Thermofisher Corp. The latter produces today the evolution of the previous apparatus under the name of Ion Proton System (Figure I.9b) which is part of a wider range of sequencers. Depending on analyte characteristics and the type of sequencer, it can determine a DNA sequence in as little as three hours.
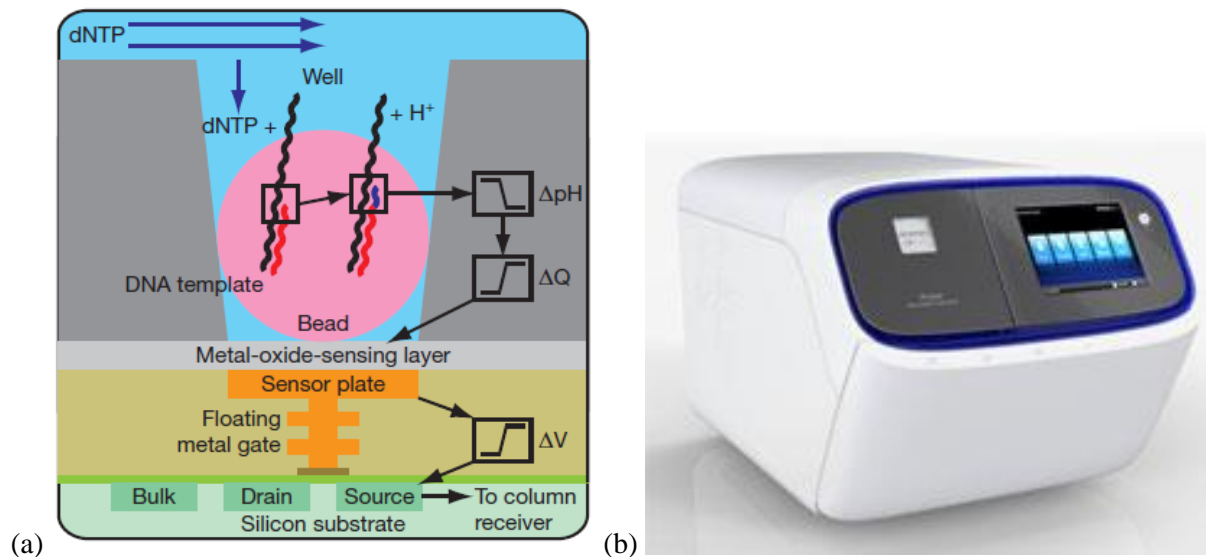
Figure I.9: Genome sequencing chip transducer well and detection schematics (a). Reproduced from [73]. Ion Proton System by ThermoFisher for Sequencing (b).

Illumina Inc. is another major contender in the sequencing market. Its first sequencer was introduced over a decade ago in 2007. The company developed its products along those years in order to become more performant and less costly (Figure I.10). A major breakthrough was achieved at the launch of the HiSeq X Series which delivered the long sought after milestone of the $1,000 human genome [77].

Figure I.10: Series of DNA sequencers produced by illumina (from left to right MiSeq 2011, MiSeqDx 2013, HiSeq X Series & NextSeq 500 2014, NovaSeq 2017). [77]

All in all, field-effect based sensors can be found so far on the market only for DNA sequencing. Despite their convenience in terms of size and speed of measurement, they still suffer from an error of measurement of at least 1% [75]. Important efforts are made to implement this technology for diagnostic purposes, but reliability and cost reduction issues due to the very complex system which involves the filtration, multiplication and then detection of molecules of interest refrained market insertion. However, the optimization of this type of devices would be a major breakthrough, allowing a proliferation of medical care worldwide.

e. <u>Silicon-on-insulator devices and their interest for sensing applications</u>

Most of the filed-effect biosensors presented in this state-of-the-art are fabricated from bulk silicon wafers. Some of the nanowire-based devices are realized starting from silicon-on-insulator (SOI) wafers using the top-down approaches. This is convenient due to the buried oxide which is used as an etch-stop layer and to the high quality top silicon film hosting the actual nanostructure. Nevertheless, they are not necessarily taking advantage of the specificity of SOI devices in terms of working principles. In this section, we will discuss how the sensing itself could benefit from the use of SOI.

Besides being one of the options to obtain high-performance devices in the microelectronics industry [78], SOI offers a wide panel of specific phenomena such as natural double gate configuration, coupling phenomena or floating body effects [79]. These particular phenomena can be exploited for sensing applications in order to improve the figures of merit of the sensor.

Double gate. The first element to consider in SOI transistors is their possibility to have two-gates. Indeed, beside the top gate of the FET, the substrate can act as a secondary gate, with the buried oxide (BOX) as gate dielectric (Figure I.11a). The characteristics of the conduction through the silicon film (body of the transistor) are thus the result of a combination of the two gate actions. Generally the BOX capacitance is lower, thus a change in potential at the front gate is equivalent to a larger change at the back gate, due to the ratio between the two capacitances. As observed from Figure I.11b for a 5nm thick silicon film transistor with a 1nm thick oxide for the front gate and a 10nm thick BOX, a change on the front gate is equivalent to a much larger variation of the back gate [80]. In this particular case, the authors calculated that a variation of 110mV on the front gate potential corresponds to a 1V change in the back gate. This means that if the front gate is used for detection and the back gate for reading, the influence of the charges added by the molecules attached at the top surface would create an amplified shift when reading with the back gate.

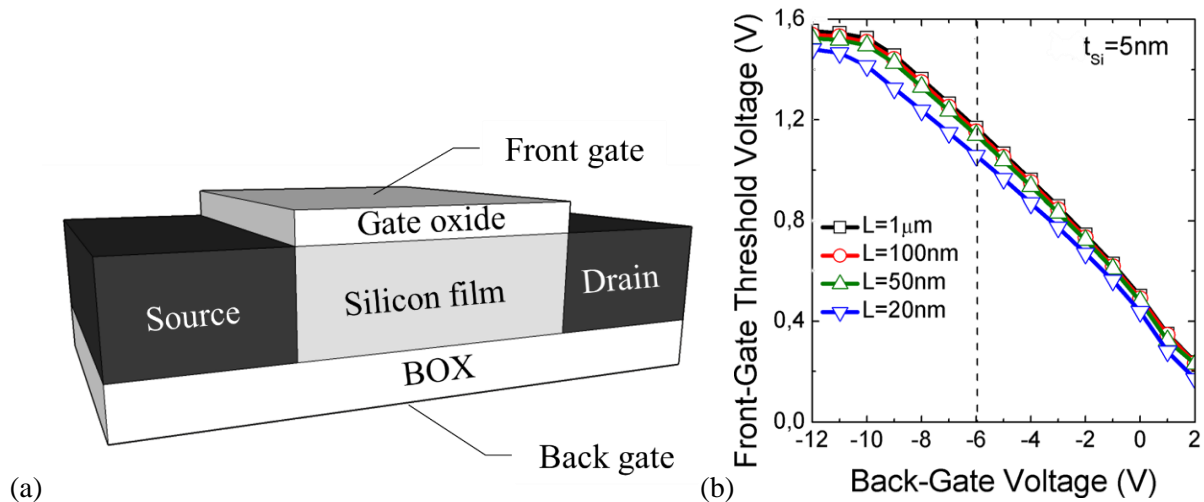(a)   (b)

Figure I.11: Schematics of a SOI-based transistor (a) and variation of the front gate threshold voltage depending on the back-gate voltage (b) reproduced from [80].

In practice, FD-SOI (Fully Depleted Silicon on Insulator) transistors with a back gate reading were already used for pH measurements [81], [82]. Lately, they showed a remarkable sensitivity which reached 12 times the physical Nernstian limit of 59mV/pH [83]. As mentioned previously, the variation of the potential on the front gate, which comes from the change in the pH, is equivalent to a much larger variation of the back gate, which confers this intrinsic amplification effect for SOI devices.

The double gate-configuration was used in Si nanodevices. For example, a comparison between front-gate and back-gate reading was realized in the case of silicon nanoribbons in [84]. The authors showed that for front-gate voltages of $V_{GF}=0V$ and $V_{GF}=2.2V$ the device can be switched on and off

independently of the voltage applied on the back gate. Although true from an electronic perspective, the equivalent potential variation induced by the attachment of charged molecules is generally less important. For example a pH variation of 10 would be equivalent to a maximum variation of 0.59V on the front gate. This is the reason why we consider that silicon on insulator devices are suitable for sensing applications if the biasing conditions are carefully chosen.

Floating-body effects and out-of-equilibrium body potential. While the double gate configuration was used for detection in SOI and other nanodevices supported by a buried oxide, no study took profit of out-of-equilibrium phenomena for sensing. Indeed, field-effect biosensors measure a difference of current or (threshold) voltage when detecting a certain desired species and for both cases, the device is considered at equilibrium. The key element for the out-of-equilibrium phenomena is that the body of the transistor has a very low doping concentration, while the source and the drain contacts are highly doped. In the case of an nMOSFET which has two highly doped source and drain regions, a fast transition from inversion (channel of electrons) to accumulation (channel of holes) may generate an out-of-equilibrium state. This is due to the difficulty of injecting majority carriers (holes) in the channel through the N-doped source and drain regions [85]. A body potential can be measured then using lateral contacts (Figure I.12). Note that the out-of-equilibrium body potential appears in the low conduction region of the transistor (where the film is depleted) and which is strongly influenced by the surrounding charges (the same way as the threshold of the transistor). Therefore, we could imagine a sensor based on these observations and this was the objective of this thesis.
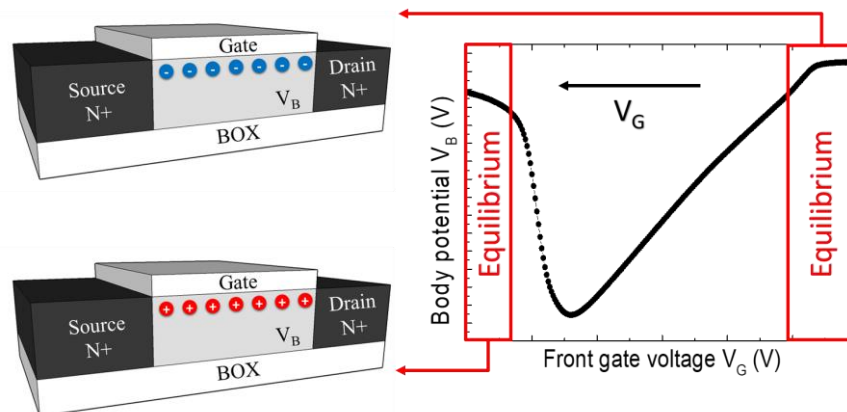

Figure I.12: Schematic of the out-of-equilibrium regime in nMOSFET transistors [85]

1.4. Objectives of this thesis

The main purpose of this thesis is to introduce a new reading paradigm based on the out-of-equilibrium body potential measurements in SOI. This technique can be advantageous due to the fact that it measures a potential instead of a low current in the subthreshold region, where the sensitivity of a field-effect biosensor is the greatest [39].

The goal of this thesis is to present a proof of concept for this new reading mechanism, without the need of any sophisticated fabrication steps, by using a simple SOI substrate. Therefore, this method was implemented in a 2D configuration, named Ψ-MOSFET (pseudo-MOSFET). This is essentially a electrical characterization technique of SOI wafers which uses the inherent upside-down MOSFET structure of a SOI wafer in which the buried oxide is used as a gate dielectric and two metallic probes placed on the top silicon film play the role of source and drain (Figure I.13).
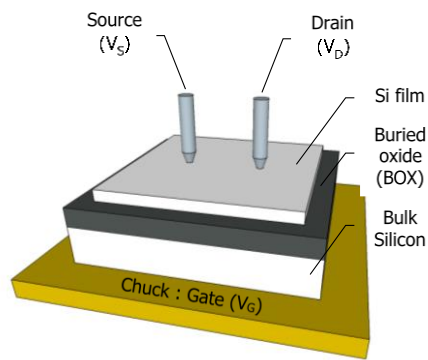
Figure I.13: Schematics of a Ψ-MOSFET structure.

Besides from the parameter extraction of the SOI, the Ψ-MOSFET was also used to detect chemical species deposited on the silicon film surface such as APTES ((3-Aminopropyl)triethoxysilane) and gold nanoparticles using the shifts in I_D - V_G characteristics [86]. This makes the Ψ-MOSFET an ideal candidate for our study.

This study on the detection using the out-of-equilibrium body potential with Ψ-MOSFET has three key-elements that will be addressed in different chapters:

- the contacts in the Ψ-MOSFET (Chapter 2), their nature and their ability to prevent/facilitate the arrival of carriers for the channel formation, knowing that this is a critical element for the out-of-equilibrium potential;
- the electrical set-up for body potential in the Ψ-MOSFET configuration (Chapter 3);
- sensing using the out-of-equilibrium body potential in Ψ-MOSFET configuration.

The contacts are of a great importance because the silicon film can be in an out-of-equilibrium state only if they do not provide steadily the necessary type of carriers. In the case of transistors, the source and the drain can only supply the type of carriers corresponding to their doping. The particularity of the Ψ-MOSFET is that the source and the drain are pressure-controlled metallic probes that can bring both electrons and holes in the silicon film. This well-known fact, even though exploited since its discovery, is not yet fully explained. Indeed, metal probes on low-doped silicon film should act as Schottky contacts but in practice they are ohmic. In chapter 2 we investigate the possibility to explain the ohmic behavior based on the effects of nanoindentation and silicon phase transformation into its metallic phase under high pressure conditions.

Chapter 3 is dedicated to the body potential measurements in the Ψ-MOSFET configuration. A description of the experimental results describing the body potential behaviour, characteristics and dependence on the measurement setup in the Ψ-MOSFET configuration is realized. The validation using simulation tools is illustrated at the end of the chapter.

In chapter 4, the proof of concept of the DNA sensor is presented. An incremental study is developed starting from well-known simple molecules, up to the detection of different concentrations of DNA using the out-of-equilibrium body potential measurements. This work was realized in collaboration with the National Institute for Research and Development in Microtechnologies from Bucharest, within a Campus France exchange project.

This thesis is meant to place the foundations for this new reading paradigm which uses the out-of-equilibrium body potential. The last chapter summarizes our results and addresses perspectives for future work.

Bibliography

[1] G. E. Moore, 'Cramming More Components Onto Integrated Circuits', *Solid State Technol.*, vol. 46, no. 7, pp. 51–58, Apr. 1965.

[2] W. Arden, M. Brillouët, P. Cogez, M. Graef, B. Huizing, and R. Mahnkopf, '"More-than-Moore" White Paper', p. 31, 2010.

[3] 'International Technology Roadmap for Semiconductors'. .

[4] L. C. Clark and C. Lyons, 'ELECTRODE SYSTEMS FOR CONTINUOUS MONITORING IN CARDIOVASCULAR SURGERY', *Ann. N. Y. Acad. Sci.*, vol. 102, no. 1, pp. 29–45, 1962.

[5] Persistence Market Research, 'Global Market Study on Biosensor', 2017.

[6] D. R. Thevenot, K. Toth, R. A. Durst, and G. S. Wilson, 'Electrochemical biosensors: recommended definitions and classification', p. 11, 2001.

[7] N. Bhalla, P. Jolly, N. Formisano, and P. Estrela, 'Introduction to biosensors', *Essays Biochem.*, vol. 60, no. 1, pp. 1–8, Jun. 2016.

[8] 'International Union of Pure and Applied Chemistry'. .

[9] A. D. McNaught and A. Wilkinson, *Compendium of Chemical Terminology*. Blackwell Science, 1997.

[10] Umezawa, Y, Umezawa, K, and Sato, H, 'Selectivity coefficients for ion-selective electrodes: recommended methods for reporting Ka/b values', *Pure Appl Chern*, vol. 67, no. 3, pp. 507–518, 1995.

[11] E. Lindner, K. Toth, and E. Pungor, 'Definition and determination of response time of ion selective electrodes', *Pure AppL Chem*, vol. 58, no. 3, pp. 469–479, 1986.

[12] P. Damborsky, J. vitel, and J. Katrlik, 'Optical biosensors', *Essays Biochem.*, vol. 60, no. 1, pp. 91–100, Jun. 2016.

[13] B. Liedberg, C. Nylander, and I. Lunström, 'Surface plasmon resonance for gas detection and biosensing', *Sens. Actuators*, vol. 4, pp. 299–304, Jan. 1983.

[14] I. Mannelli, M. Minunni, S. Tombelli, R. Wang, M. Michela Spiriti, and M. Mascini, 'Direct immobilisation of DNA probes for the development of affinity biosensors', *Bioelectrochemistry*, vol. 66, no. 1–2, pp. 129–138, Apr. 2005.

[15] X. Yao *et al.*, 'Sub-attomole oligonucleotide and p53 cDNA determinations via a high-resolution surface plasmon resonance combined with oligonucleotide-capped gold nanoparticle signal amplification', *Anal. Biochem.*, vol. 354, no. 2, pp. 220–228, Jul. 2006.

[16] 'Biacore surface plasmon resonance system'. .

[17] M. Bowden, L. Song, and D. R. Walt, 'Development of a Microfluidic Platform with an Optical Imaging Microarray Capable of Attomolar Target DNA Detection', *Anal. Chem.*, vol. 77, no. 17, pp. 5583–5588, Sep. 2005.

[18] M. J. Lochhead *et al.*, 'Rapid Multiplexed Immunoassay for Simultaneous Serodiagnosis of HIV-1 and Coinfections', *J. Clin. Microbiol.*, vol. 49, no. 10, pp. 3584–3590, Oct. 2011.

[19] M. Pohanka, 'The Piezoelectric Biosensors: Principles and Applications, a Review', *Int. J. Electrochem. Sci.*, pp. 496–506, Jan. 2017.

[20] Chunli Zhang, Nan Liu, Jiashi Yang, and Weiqiu Chen, 'Thickness-shear vibration of AT-cut quartz plates carrying finite-size particles with rotational degree of freedom and rotary inertia [Correspondence]', *IEEE Trans. Ultrason. Ferroelectr. Freq. Control*, vol. 58, no. 3, pp. 666–670, Mar. 2011.

[21] K. Keiji. Kanazawa and J. G. Gordon, 'Frequency of a quartz microbalance in contact with liquid', *Anal. Chem.*, vol. 57, no. 8, pp. 1770–1771, Jul. 1985.

[22] M. Pohanka, 'Overview of Piezoelectric Biosensors, Immunosensors and DNA Sensors and Their Applications', *Materials*, vol. 11, no. 3, p. 448, Mar. 2018.

[23] X. Mao, L. Yang, X.-L. Su, and Y. Li, 'A nanoparticle amplification based quartz crystal microbalance DNA sensor for detection of Escherichia coli O157:H7', *Biosens. Bioelectron.*, vol. 21, no. 7, pp. 1178–1185, Jan. 2006.

[24] M. Alvarez and L. M. Lechuga, 'Microcantilever-based platforms as biosensing tools', *The Analyst*, vol. 135, no. 5, p. 827, 2010.

[25] T. Miyatani and M. Fujihira, 'Calibration of surface stress measurements with atomic force microscopy', *J. Appl. Phys.*, vol. 81, no. 11, pp. 7099–7115, Jun. 1997.

[26] K. Rijal and R. Mutharasan, 'PEMC-based Method of Measuring DNA Hybridization at Femtomolar Concentration Directly in Human Serum and in the Presence of Copious Noncomplementary Strands', *Anal. Chem.*, vol. 79, no. 19, pp. 7392–7400, Oct. 2007.

[27] D. R. Thevenot, K. Toth, R. A. Durst, and G. S. Wilson, 'Electrochemical biosensors: recommended definitions and classification', *Pure Appl. Chem.*, vol. 71, no. 12, pp. 2333–2348, 1999.

[28] J. L. Hammond, N. Formisano, P. Estrela, S. Carrara, and J. Tkac, 'Electrochemical biosensors and nanobiosensors', *Essays Biochem.*, vol. 60, no. 1, pp. 69–80, Jun. 2016.

[29] F. Barsonkov and J. R. MacDonald, *'Impedance spectroscopy: theory, experiment and applications*, 2nd ed. Hoboken, New Jersey: Wiley Interscience, 2005.

[30] J. T. Stock *et al.*, 'Electrochemistry, past and present', 1989.

[31] M. Waleed Shinwari, M. Jamal Deen, and D. Landheer, 'Study of the electrolyte-insulator-semiconductor field-effect transistor (EISFET) with applications in biosensor design', *Microelectron. Reliab.*, vol. 47, no. 12, pp. 2025–2057, Dec. 2007.

[32] Piet Bergveld, 'Development of an Ion-Sensitive Solid-State Device for Neurophysiological Measurements', *IEEE Trans. Biomed. Eng.*, Jan. 1970.

[33] B. L. Allen, P. D. Kichambare, and A. Star, 'Carbon Nanotube Field-Effect-Transistor-Based Biosensors', *Adv. Mater.*, vol. 19, no. 11, pp. 1439–1451, Jun. 2007.

[34] K. Maehashi, K. Matsumoto, K. Kerman, Y. Takamura, and E. Tamyira, 'Ultrasensitive Detection of DNA Hybridization Using Carbon Nanotube Field-Effect Transistors', *Jpn. J. Appl. Phys.*, vol. 43, no. 12A, pp. L1558–L1560, 2004.

[35] W. Huang, A. K. Diallo, J. L. Dailey, K. Besar, and H. E. Katz, 'Electrochemical processes and mechanistic aspects of field-effect sensors for biomolecules', *J. Mater. Chem. C*, vol. 3, no. 25, pp. 6445–6470, 2015.

[36] R. Ahmad, T. Mahmoudi, M.-S. Ahn, and Y.-B. Hahn, 'Recent advances in nanowires-based field-effect transistors for biological sensor applications', *Biosens. Bioelectron.*, vol. 100, pp. 312–325, Feb. 2018.

[37] Z. Li, B. Rajendran, T. I. Kamins, X. Li, Y. Chen, and R. S. Williams, 'Silicon nanowires for sequence-specific DNA sensing: device fabrication and simulation', *Appl. Phys. A*, vol. 80, no. 6, pp. 1257–1263, Mar. 2005.

[38] N. Elfström, A. E. Karlström, and J. Linnros, 'Silicon Nanoribbons for Electrical Detection of Biomolecules', *Nano Lett.*, vol. 8, no. 3, pp. 945–949, Mar. 2008.

[39] X. P. A. Gao, G. Zheng, and C. M. Lieber, 'Subthreshold Regime has the Optimal Sensitivity for Nanowire FET Biosensors', *Nano Lett.*, vol. 10, no. 2, pp. 547–552, Feb. 2010.

[40] A. Kim *et al.*, 'Ultrasensitive, label-free, and real-time immunodetection using silicon field-effect transistors', *Appl. Phys. Lett.*, vol. 91, no. 10, p. 103901, Sep. 2007.

[41] A. Heller and B. Feldman, 'Electrochemical Glucose Sensors and Their Applications in Diabetes Management', *Chem. Rev.*, vol. 108, no. 7, pp. 2482–2505, Jul. 2008.

[42] F. Rees, M. Hui, and M. Doherty, 'Optimizing current treatment of gout', *Nat. Rev. Rheumatol.*, vol. 10, p. 271, Mar. 2014.

[43] Y.-M. Chu, C.-C. Lin, H.-C. Chang, C. Li, and C. Guo, 'TiO2 nanowire FET device: Encapsulation of biomolecules by electro polymerized pyrrole propylic acid', *Biosens. Bioelectron.*, vol. 26, no. 5, pp. 2334–2340, 2011.

[44] L. E. Bain, S. A. Jewett, A. H. Mukund, S. M. Bedair, T. M. Paskova, and A. Ivanisevic, 'Biomolecular Gradients via Semiconductor Gradients: Characterization of Amino Acid Adsorption to InxGa1–xN Surfaces', *ACS Appl. Mater. Interfaces*, vol. 5, no. 15, pp. 7236–7243, Aug. 2013.

[45] P. Sahoo, S. Suresh, S. Dhara, G. Saini, S. Rangarajan, and A. K. Tyagi, 'Direct label free ultrasensitive impedimetric DNA biosensor using dendrimer functionalized GaN nanowires', *Biosens. Bioelectron.*, vol. 44, pp. 164–170, 2013.

[46] H.-K. Chang *et al.*, 'Rapid, Label-Free, Electrical Whole Blood Bioassay Based on Nanobiosensor Systems', *ACS Nano*, vol. 5, no. 12, pp. 9883–9891, Dec. 2011.

[47] F. N. Ishikawa *et al.*, 'Label-Free, Electrical Detection of the SARS Virus N-Protein with Nanowire Biosensors Utilizing Antibody Mimics as Capture Probes', *ACS Nano*, vol. 3, no. 5, pp. 1219–1224, May 2009.

[48] Yi Cui, Qingqiao Wei, Hongkun Park, and Charles M. Lieber, 'Nanowire Nanosensors for Highly Sensitive and Selective Detection of Biological and Chemical Species', *Sci. Rep.*, vol. 293, no. 5533, pp. 1289–1292, Aug. 2001.

[49] E. Souteyrand *et al.*, 'Direct Detection of the Hybridization of Synthetic Homo-Oligomer DNA Sequences by Field Effect', *J. Phys. Chem. B*, vol. 101, no. 15, pp. 2980–2985, Apr. 1997.

[50] J. Hahm and C. M. Lieber, 'Direct Ultrasensitive Electrical Detection of DNA and DNA Sequence Variations Using Nanowire Nanosensors', *Nano Lett.*, vol. 4, no. 1, pp. 51–54, Jan. 2004.

[51] M. N. Nuzaihan *et al.*, 'Top-Down Nanofabrication and Characterization of 20 nm Silicon Nanowires for Biosensing Applications', *PLOS ONE*, vol. 11, no. 3, p. e0152318, Mar. 2016.

[52] A. Gao *et al.*, 'Signal-to-Noise Ratio Enhancement of Silicon Nanowires Biosensor with Rolling Circle Amplification', *Nano Lett.*, vol. 13, no. 9, pp. 4123–4130, Sep. 2013.

[53] Z. Li, Y. Chen, X. Li, T. I. Kamins, K. Nauka, and R. S. Williams, 'Sequence-Specific Label-Free DNA Sensors Based on Silicon Nanowires', *Nano Lett.*, vol. 4, no. 2, pp. 245–247, Feb. 2004.

[54] Y. L. Bunimovich, Y. S. Shin, W.-S. Yeo, M. Amori, G. Kwong, and J. R. Heath, 'Quantitative Real-Time Measurements of DNA Hybridization with Alkylated Nonoxidized Silicon Nanowires in Electrolyte Solution', *J. Am. Chem. Soc.*, vol. 128, no. 50, pp. 16323–16331, Dec. 2006.

[55] G.-J. Zhang *et al.*, 'Highly sensitive measurements of PNA-DNA hybridization using oxide-etched silicon nanowire biosensors', *Biosens. Bioelectron.*, vol. 23, no. 11, pp. 1701–1707, Jun. 2008.

[56] S.-W. Ryu *et al.*, 'Gold nanoparticle embedded silicon nanowire biosensor for applications of label-free DNA detection', *Biosens. Bioelectron.*, vol. 25, no. 9, pp. 2182–2185, May 2010.

[57] V. B. Pham *et al.*, 'Detection of DNA of genetically modified maize by a silicon nanowire field-effect transistor', *Adv. Nat. Sci. Nanosci. Nanotechnol.*, vol. 2, no. 2, p. 025010, May 2011.

[58] A. Gao *et al.*, 'Silicon-Nanowire-Based CMOS-Compatible Field-Effect Transistor Nanosensors for Ultrasensitive Electrical Detection of Nucleic Acids', *Nano Lett.*, vol. 11, no. 9, pp. 3974–3978, Sep. 2011.

[59] A. Gao *et al.*, 'Enhanced Sensing of Nucleic Acids with Silicon Nanowire Field Effect Transistor Biosensors', *Nano Lett.*, vol. 12, no. 10, pp. 5262–5268, Oct. 2012.

[60] P. Dai, A. Gao, N. Lu, T. Li, and Y. Wang, 'A Back-Gate Controlled Silicon Nanowire Sensor with Sensitivity Improvement for DNA and pH Detection', *Jpn. J. Appl. Phys.*, vol. 52, no. 12R, p. 121301, Dec. 2013.

[61] C.-J. Chu *et al.*, 'Improving Nanowire Sensing Capability by Electrical Field Alignment of Surface Probing Molecules', *Nano Lett.*, vol. 13, no. 6, pp. 2564–2569, Jun. 2013.

[62] G. Wenga, E. Jacques, A.-C. Salaün, R. Rogel, L. Pichon, and F. Geneste, 'Step-gate polysilicon nanowires field effect transistor compatible with CMOS technology for label-free DNA biosensor', *Biosens. Bioelectron.*, vol. 40, no. 1, pp. 141–146, Feb. 2013.

[63] G.-J. Zhang *et al.*, 'Silicon nanowire biosensor for highly sensitive and rapid detection of Dengue virus', *Sens. Actuators B Chem.*, vol. 146, no. 1, pp. 138–144, Apr. 2010.

[64] G.-J. Zhang, J. H. Chua, R.-E. Chee, A. Agarwal, and S. M. Wong, 'Label-free direct detection of MiRNAs with silicon nanowire biosensors', *Biosens. Bioelectron.*, vol. 24, no. 8, pp. 2504–2508, Apr. 2009.

[65] Y. Chen, X. Wang, S. Erramilli, P. Mohanty, and A. Kalinowski, 'Silicon-based nanoelectronic field-effect pH sensor with local gate control', *Appl. Phys. Lett.*, vol. 89, no. 22, p. 223512, Nov. 2006.

[66] Sung Keun Yoo, Sung Yang, and Jong-Hyun Lee, 'Hydrogen Ion Sensing Using Schottky Contacted Silicon Nanowire FETs', *IEEE Trans. Nanotechnol.*, vol. 7, no. 6, pp. 745–748, Nov. 2008.

[67] S. Kim *et al.*, 'Silicon nanowire ion sensitive field effect transistor with integrated Ag/AgCl electrode: pH sensing and noise characteristics', *The Analyst*, vol. 136, no. 23, p. 5012, 2011.

[68] J. Lee *et al.*, 'Complementary Silicon Nanowire Hydrogen Ion Sensor With High Sensitivity and Voltage Output', *IEEE Electron Device Lett.*, vol. 33, no. 12, pp. 1768–1770, Dec. 2012.

[69] J.-H. Ahn *et al.*, 'A pH sensor with a double-gate silicon nanowire field-effect transistor', *Appl. Phys. Lett.*, vol. 102, no. 8, p. 083701, Feb. 2013.

[70] G. Zheng, F. Patolsky, Y. Cui, W. U. Wang, and C. M. Lieber, 'Multiplexed electrical detection of cancer markers with nanowire sensor arrays', *Nat. Biotechnol.*, vol. 23, no. 10, pp. 1294–1301, Oct. 2005.

[71] E. Stern *et al.*, 'Label-free immunodetection with CMOS-compatible semiconducting nanowires', *Nature*, vol. 445, no. 7127, pp. 519–522, Feb. 2007.

[72] J. Lin *et al.*, 'A portable impedance biosensor instrument for rapid detection of avian influenza virus', in *Sensors, 2010 IEEE*, 2010, pp. 1558–1563.

[73] J. M. Rothberg *et al.*, 'An integrated semiconductor device enabling non-optical genome sequencing', *Nature*, vol. 475, no. 7356, pp. 348–352, Jul. 2011.

[74] J. H. Leamon, K. L. Lohman, J. Rothberg, and M. P. Weiner, 'Methods of amplifying and sequencing nucleic acids', 8158359, 17-Apr-2012.

[75] S. J. Salipante *et al.*, 'Performance Comparison of Illumina and Ion Torrent Next-Generation Sequencing Platforms for 16S rRNA-Based Bacterial Community Profiling', *Appl. Environ. Microbiol.*, vol. 80, no. 24, pp. 7583–7591, Dec. 2014.

[76] A. Porterfield, 'All in the Chip: Ion Torrent Sequencers', *bitesizebio.com*, 09-Jul-2016.

[77] illumina Inc., 'Explore a decade of sequencing'. .

[78] C. Sorin and S. Li, *Electrical characterization of silicon-on-insulator materials and devices*. Kluwer Academic Publishers, 1995.

[79] S. Cristoloveanu, M. Bawedin, and I. Ionica, 'A review of electrical characterization techniques for ultrathin FDSOI materials and devices', *Solid-State Electron.*, vol. 117, pp. 10–36, Mar. 2016.

[80] C. Navarro, M. Bawedin, F. Andrieu, B. Sagnes, F. Martinez, and S. Cristoloveanu, 'Supercoupling effect in short-channel ultrathin fully depleted silicon-on-insulator transistors', *J. Appl. Phys.*, vol. 118, no. 18, p. 184504, Nov. 2015.

[81] H.-J. Jang and W.-J. Cho, 'Performance Enhancement of Capacitive-Coupling Dual-gate Ion-Sensitive Field-Effect Transistor in Ultra-Thin-Body', *Sci. Rep.*, vol. 4, Jun. 2014.

[82] Y.-J. Huang *et al.*, 'High performance dual-gate ISFET with non-ideal effect reduction schemes in a SOI-CMOS bioelectrical SoC', in *2015 IEEE International Electron Devices Meeting (IEDM)*, Washington, DC, USA, 2015, pp. 29.2.1-29.2.4.

[83] G. T. Ayele *et al.*, 'Ultrahigh-Sensitive and CMOS Compatible ISFET Developed in BEOL of Industrial UTBB FDSOI', *Symp. VLSI Technol. Dig. Tech. Pap.*, p. 2, 2018.

[84] E. Accastelli, G. Cappi, J. Buckley, T. Ernst, and C. Guiducci, 'Comparison between front- and back-gating of Silicon Nanoribbons in real-time sensing experiments', in *2013 13th IEEE International Conference on Nanotechnology (IEEE-NANO 2013)*, Beijing, China, 2013, pp. 517–520.

[85] M. Bawedin, S. Cristoloveanu, D. Flandre, and F. Udrea, 'Dynamic body potential variation in FD SOI MOSFETs operated in deep non-equilibrium regime: Model and applications', *Solid-State Electron.*, vol. 54, no. 2, pp. 104–114, Feb. 2010.

[86] I. Ionica, A. E. H. Diab, and S. Cristoloveanu, 'Gold nanoparticles detection using intrinsic SOI-based sensor', in *Nanotechnology (IEEE-NANO), 2011 11th IEEE Conference on*, 2011, pp. 38–43.

Chapter 2 : Ψ-MOSFET Configuration and Contacts

One of the key elements of the out-of-equilibrium body potential measurements in the Ψ-MOSFET configuration is the contact between the metallic probes and the thin silicon film of the SOI. Theoretically, the contact should behave as Schottky, but electrical measurements reveal that they are ohmic. This fact, known ever since the discovery of the Ψ-MOSFET, was not yet fully and clearly explained. In this chapter, we explore an alternative interpretation based on the formation of a metallic crystallographic form of silicon due to nanoindentation under the pressure applied by the probes on the silicon film.

Table of Contents

2.1. Ψ-MOSFET for silicon on insulator characterization

As presented in the introduction, sensors based on silicon on insulator have multiple advantages related to their double gate structure. Those advantages can be exploited even in the bare SOI substrates used in the Ψ-MOSFET configuration, which does not need a full device fabrication. In the followings, we will present the Ψ-MOSFET, as used for SOI characterization.

The SOI is a multilayer stack which is composed of a thin top silicon film acting as an active layer for devices, a buried oxide (BOX) used to isolate the active layer from the substrate and a low-doped silicon substrate used as a mechanical support of the structure (Figure II.1) [1].
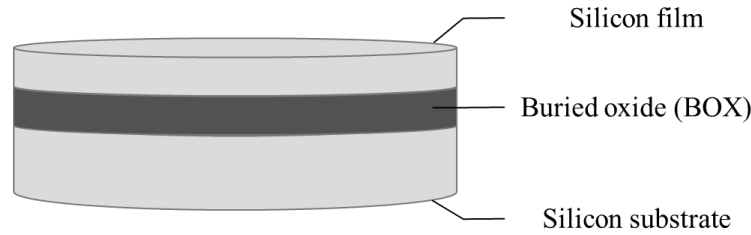
Figure II.1: Structure of a SOI substrate

The Ψ-MOSFET characterization method was introduced in 1992 [2]. The silicon substrate of the SOI wafer can be used as a gate and biased using the chuck. The BOX is employed as gate dielectric. The gate voltage (V_G) induces a channel at the interface between the top silicon film and the BOX. Two probes with controlled pressure are directly placed on the silicon film and act as source and drain of the pseudo-transistor (Figure II.2a). This is the Ψ-MOSFET configuration used for the characterization of SOI for more than 25 years.

Due to the low doping concentration of the film (i.e. p-type 10^{15}cm^{-3}), the conduction can be ensured by holes or electrons depending on the polarity of V_G. Thus, there are two distinct V_G values that set the boundaries of the working regimes: the threshold voltage (V_T) marks the beginning of the inversion and the flat-band voltage (V_{FB}) the one for the accumulation. We can identify thus three different regimes:

- For $V_G < V_{FB} < 0V$, the conduction channel is made up of holes (accumulation regime - Figure II.2b);
- For $V_{FB} < V_G < V_T$, the energy bands in the film are bent down and the silicon film is depleted (depletion regime);
- For $V_G > V_T > 0V$, the conduction between source and drain is realized by electrons (inversion regime - Figure II.2c).

Consequently, depending on the V_G polarity, the drain current versus gate voltage characterization gives access to both electron and hole electrical transport properties. This technique was also used for noise [3] and capacitance measurements [4].

This technique, besides its simplicity, has also its drawbacks resulting mainly from two aspects:

(1) the source/drain metallic probe-silicon film contacts. When the metallic probes are placed, they penetrate the silicon film leaving a crater of some tens of nanometres deep, damaging the silicon film [5];

(2) the channel of the Ψ-MOSFET is not well defined geometrically, therefore the parameter extraction (such as the mobility) needs preliminary calibration.
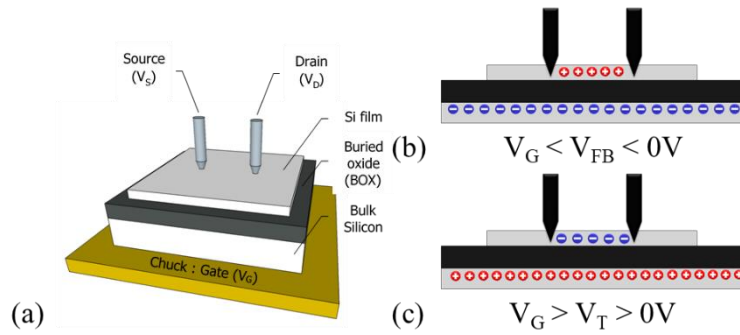
Figure II.2: Schematics of the Ψ-MOSFET configuration (a) and representation of the conduction channel in accumulation (b) and in inversion (c).

In order to overcome the issues related to the contacts, two other variants were proposed. In 1997, the mercury contacts in a corbino configuration were used as source and drain (Figure II.3b) [6]. This was unpractical due to the need of hydrofluoric acid cleaning before measurement in order to remove the oxide on top of the SOI. The measurement is also time dependant as the silicon dioxide native layer regenerates within hours when silicon is exposed to the atmosphere.

The other proposed technique is to deposit metal contacts that would take over the role of the metallic probes, leaving the silicon film undamaged (Figure II.3c) [7]. Additionally, the channel dimensions are well defined in this case, but the method is unpractical due to the additional fabrication steps and the Schottky contacts.
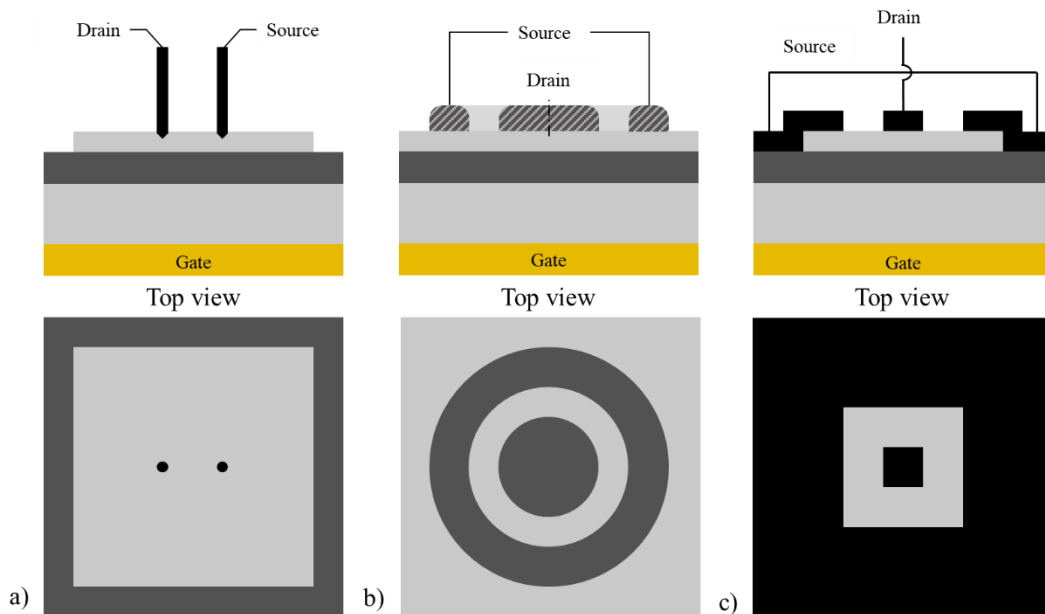
Figure II.3: Different characterization configurations of SOI wafers: Ψ-MOSFET (a), HgFET (b), and deposited source and drain contacts (c).

All methods considered, the Ψ-MOSFET with pressure probes remains the most suitable due to its simplicity and its capability of determining the essential parameters provided that a preliminary calibration was realized. It is for its simplicity that we used the Ψ-MOSFET as a mean for the proof of concept of our detection method, in this thesis. In the following sections, we will describe the working principles and the parameter extraction methods specific for the Ψ-MOSFET, which will be used in the following chapters for detection.

In order to avoid parasitic leakage currents that may occur at some places on the SOI wafer, islands of silicon film are isolated using photolithography and reactive ion etching (RIE). Different dimensions were used (3x3 mm², 5x5 mm², 8x8 mm²), but most of the studies are realized on 5x5 mm² dies.

After patterning, the structure is composed by silicon film islands having a low p-type doping concentration of 10^{15} cm^{-3} and separated by the tranches of exposed BOX (Figure II.4).
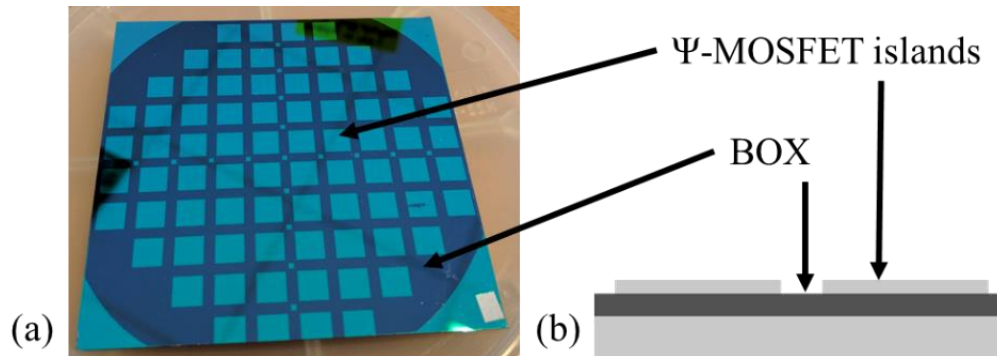

Figure II.4: Image of our SOI wafer prepared for Ψ-MOSFET configuration (a) and cross-section of the same structure (b)

Measurement setup

The measurements on the Ψ-MOSFET configuration are realized using a Jandel® four-probe station (Figure II.5). The probes on our setup are distanced by 1mm and have a pressure control system which can be set between 0g and 100g. The probes have a tip radius between 40µm and 100µm and are fabricated from tungsten carbide (WC). They are a key element of this configuration as the contact characteristics are entirely dependent on them. Moreover, vacuum was used in order to stabilize the SOI on the chuck and improve the back-gate contact. All the electrical measurements presented in this thesis were performed using an HP4155 analyser.

Time parameters

In order to correctly apply the MOSFET models, stable electrical measurements need to be obtained. Therefore, the measurement time parameters need to be in accordance with the dynamic characteristics of the sample. They are very important in order to reduce transient effects and noise. There are three main specifications that need to be carefully configured [8]:

- Integration time represents the interval over which the desired parameters are measured under the same biasing conditions. It varies from "short" to "long" and it is a compromise between a noisier, but more rapid measurement and a more stable, but slower one.
- Hold time is the interval under which the device is put on the initial bias conditions before starting the measurement. It must be long enough so that the structure is at equilibrium at the beginning of the measurement.
- Delay time is the time between two consecutive measurement points. A compromise value is necessary to reduce transient effects without having a too long measurement.

Back contact is an important characteristic as the gate voltage is applied directly through the chuck onto the silicon substrate. By using the vacuum system, a better contact patch is ensured, avoiding thus parasitic effects. They are particularly observable in the case of capacitance measurements [4].
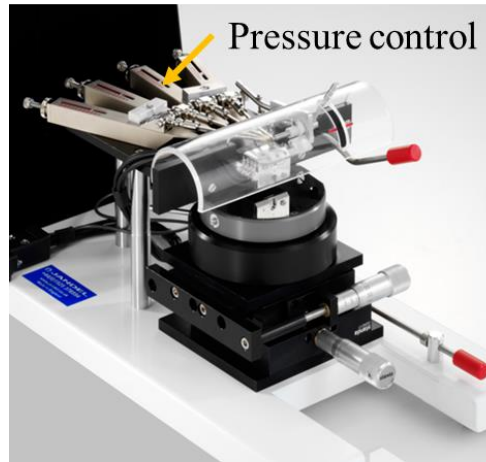
Figure II.5: Jandel 4-probe station image. Adapted from www.jandel.co.uk.

I_D-V_D and ohmic behaviour

Figure II.6 shows the drain current (I_D) vs. drain voltage characteristics (V_D) for the accumulation (V_G = -6.4V) and the inversion (V_G = 7V) regimes. The choice of this particular gate voltage values granted the same voltage overdrive for electrons (V_G-V_T) and for holes ($|V_G$-$V_{FB}|$), which induced the same charge concentration in the channel of electrons and holes. The contacts show an ohmic behaviour in both cases. In the measurements presented in this work, V_D was set to 100mV, staying clearly in the linear regime for which the parameter extraction models (described in the next section) were conceived.
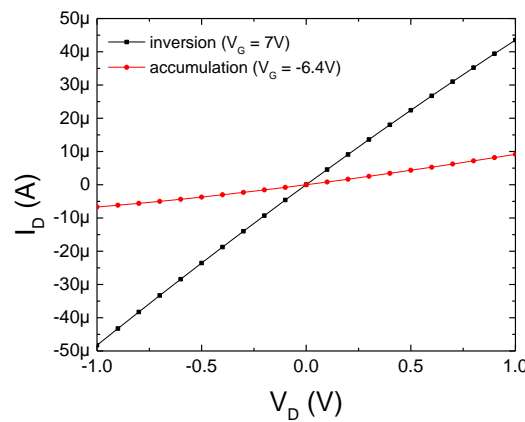
Figure II.6: Drain current vs. drain bias in inversion (V_G = 7V) and accumulation (V_G = -6.4V). V_T=1.8V, V_{FB}=-1.2V. Values chosen so that the overdrive of the gate voltage is the same for electrons and holes: V_G - V_T = $|V_G$ - $V_{FB}|$ = 5.2V. Pressure 100g. . t_{Si} = 88nm, t_{BOX} = 145nm.

I_D-V_G and parameter extraction

Figure II.7 traces typical drain current (I_D) versus gate voltage (V_G) curves for low V_D. Due to the fact that the probes used as source and drain contacts are metallic, we can observe that the drain current has both a PMOS and a NMOS behaviour in the accumulation and in the inversion regimes. This is very advantageous because parameters for both types of carriers can be obtained simultaneously. The transconductance ($g_m = dI_D/dV_G$) represented also in Figure II.7 highlights the hybrid PMOS and NMOS behaviour of the Ψ-MOSFET configuration.
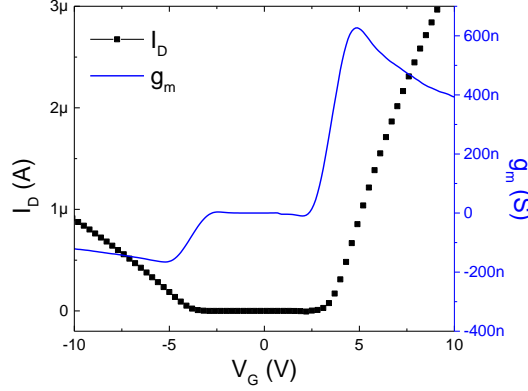
Figure II.7: Typical drain current (left) and transconductance (right) vs. gate voltage. . t_{Si} = 88nm, t_{BOX}=145nm.

The structure is in fact an upside-down MOSFET structure, so the parameter extraction is realized using similar models as in the case of the traditional MOSFET transistors. They can be implemented to extract carrier mobility and interface trap density [2], [9]–[11]. In essence, the drain current in the linear regime (low V_D) can be modelled by:

$$I_D = f_g C_{BOX} \mu_{eff} (V_G - V_{T/FB}) V_D \tag{II.1}$$

where C_{BOX} is the capacitance of the BOX, μ_{eff} is the effective mobility, $V_{T/FB}$ is the threshold or the flat band voltage respectively and f_g represents the geometrical factor which replaces the W/L (width over length ratio) term from MOSFETs and generally has a value of 0.75 determined by comparing I_D-V_G characteristics of the Ψ-MOSFET with the I_{14}-V_G characteristics of the four probe measurements [2].

The effective mobility takes into account the first order attenuation factor θ_1 which includes the series resistance [12]:

$$\mu_{eff} = \frac{\mu_0}{1 + \theta_1 (V_G - V_{T/FB})} \tag{II.2}$$

where μ_0 is the low field mobility.

For the extraction of the threshold/flat-band voltages and the low field mobility, the Y function method is generally employed in order to avoid contact resistance effects [13]. It is defined in equation (II.3):

$$Y = \frac{I_D}{\sqrt{g_m}} = \sqrt{f_g \mu_0 C_{BOX} V_D} (V_G - V_{T/FB}) \tag{II.3}$$

The low field mobility can be extracted from the slope and the threshold/flat-band voltages are the intersection of the linear regression curves in inversion and accumulation with the Y = 0 ordinate (Figure II.8a). The attenuation factor is extracted based on the following function [13]:

$$\theta(V_G) = \frac{\dfrac{I_D}{g_m (V_G - V_{T/FB})} - 1}{(V_G - V_{T/FB})} \tag{II.4}$$

This $\theta(V_G)$ function has constant values in the inversion and accumulation regimes (Figure II.8b). The plateaus are the first order attenuation factor (θ_1) from which the access resistance can be estimated using [13]:

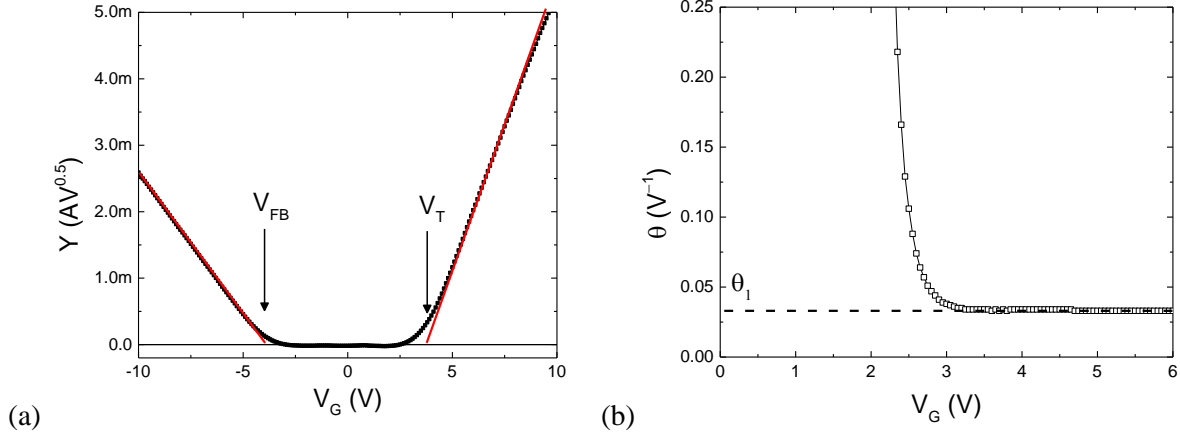$$R_{SD} \approx \frac{\theta_1}{f_g \mu_0 C_{BOX}} \tag{II.5}$$

Figure II.8: Typical Y function (a) and the mobility attenuation factor (b) versus gate voltage. $t_{Si} = 88nm, t_{BOX} = 145nm$.

As for the MOSFET transistors, interface trap density (D_{it}) can be obtained from the subthreshold swing [14]:

$$S_S = 2.3 \frac{kT}{q} \cdot \left(1 + \frac{C_{Si} + q \cdot D_{it}}{C_{BOX}}\right) \qquad (II.6)$$

where C_{Si} is the silicon film capacitance. It is important to mention that in the case of SOI, there are two interfaces at the top and at the bottom of the silicon film. They can both contribute to the extracted D_{it} because of the coupling between them. In the case of thick silicon films, the coupling is low and the D_{it} is mainly obtained from the bottom interface. For thin silicon layers (<20 nm) where a stronger coupling effect occurs, the obtained value of D_{it} has contributions from both interfaces (Figure II.9).
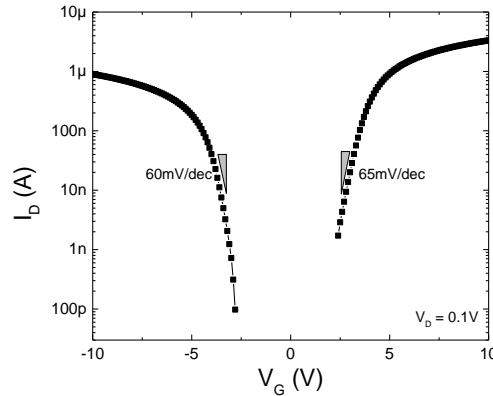

Figure II.9: Typical drain current (logarithmic scale) vs. gate voltage. $t_{Si} = 88nm, t_{BOX} = 145nm$.

Probe-related effects

Probe position is important in the Ψ-MOSFET configuration because it affects the lateral distribution of the electrical field lines in the film and, consequently, the current. The drain current is reduced as the probes are placed closer to the borders as a consequence of the edge effects. Note that this also affects the geometrical factor f_g (Figure II.10a) [8].

The extracted parameters can be thus modified. For example in [8], the low-field mobility was calculated using the corresponding Y-functions from measurements (Figure II.10b). The corresponding calculated low field mobility (μ_0) using f_g=0.75 is reported in Table II.1. The μ_0 appears to be reduced by a maximum of 10% when the probes are placed close to the borders. As the low field mobility cannot change in a homogenous material, this was attributed to the change in the geometrical factor. This

proved that for parameter extraction, the probes should be placed in the centre of the structure, where the variation of f_g is negligible.
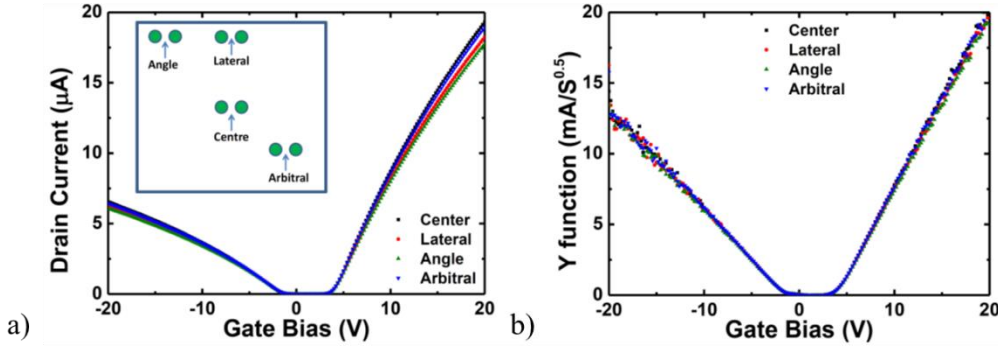

Figure II.10: Drain current (a) and Y-function (b) vs. gate bias for different placements of the probes. 8x8 mm² sample of non-passivated SOI with t_{Si} = 88nm, t_{BOX} = 145nm. Reproduced from [4].

Table II.1: Low field mobility calculated for both electrons and holes. 8x8 mm² sample of non-passivated SOI with t_{Si} = 88nm, t_{BOX} = 145nm. Reproduced from [4].

Position	μ_e (cm²/Vs)	μ_h (cm²/Vs)
Centre	458	150
Lateral	442	149
Angle	431	143
Arbitrary	460	152

Probe pressure is also important in Ψ-MOSFET, affecting directly the access resistance of the source and drain contacts. The drain current is known to increase with the applied pressure (Figure II.11a) [4]. The dependence on contact resistance is clearly attenuated in the Y-function (Figure II.11b), where we can observe that the threshold and flat-band voltages do not change. Also, the slopes in the inversion and accumulation regimes are very similar. Knowing the invariance of the Y-function with contact resistance, this means that the modifications of current with pressure in Figure II.11a are related to the access resistance (Figure II.12a). Moreover, the probes placed on the silicon film create craters by destroying a part of the film [5]. As expected, their size (diameter and depth) increases when the pressure is higher (Figure II.12b).
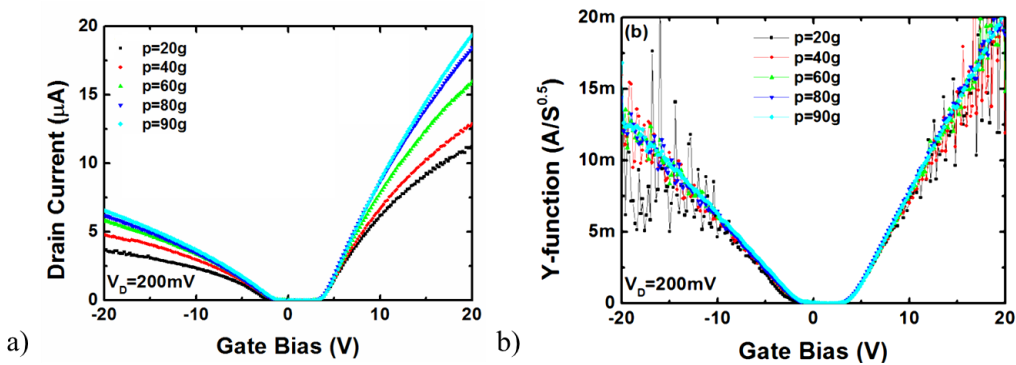

Figure II.11: Drain current (a) and Y-function (b) vs. gate bias for different probe pressures. 8x8 mm² sample of non-passivated SOI with t_{Si} = 88nm, t_{BOX} = 145nm. Reproduced from [4].
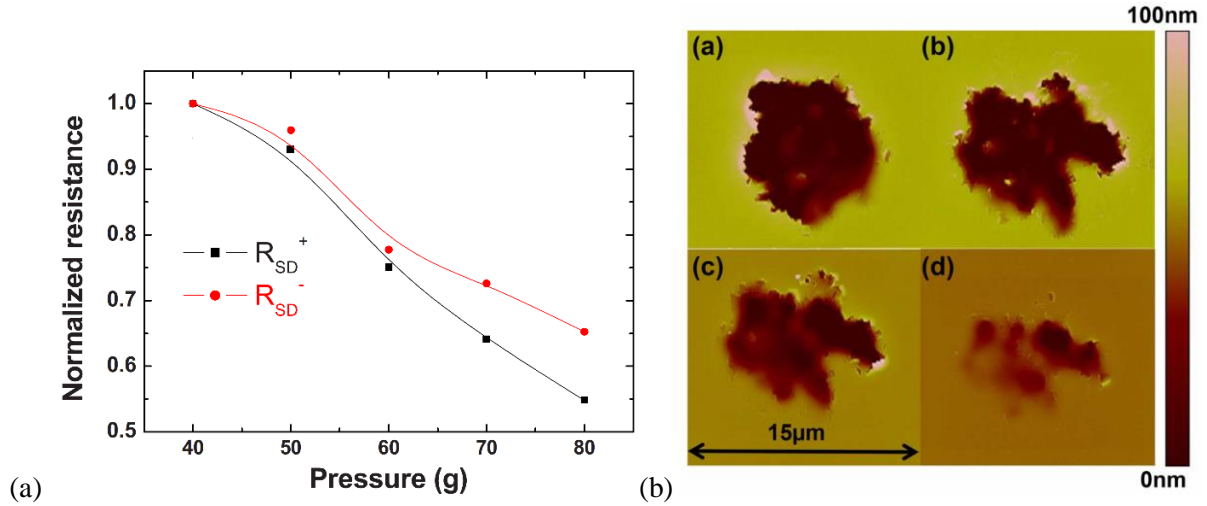
Figure II.12: Normalized access resistance in accumulation (circles) and inversion (squares) (a). Topography of different craters after probe positioning for pressures of 90g (probe 1-a) and 90g, 70g, 50g (probe 2 – b,c,d). t_{Si} = 200nm, t_{BOX} = 400nm (b). Reproduced from [5].

The existence of the craters on the film after probe removal was considered as a confirmation that crystallographic defects were responsible for the ohmic behaviour [8]. Noise measurements in Ψ-MOSFET confirmed a high noise source coming from the region close to the probes [15]. Nevertheless, a complete explanation of the ohmic behaviour has never been provided. The craters observed in Figure II.12b may suggest that an interpretation based on an allotropic transformation due to nanoindentation could explain the physics of the ohmic contacts in Ψ-MOSFET.

2.2. Nanoindentation – state-of-the-art

In this thesis we explore, for the first time, a different hypothesis for the ohmic behaviour, namely the phase transformation of silicon under nanoindentation, already documented in the literature. This section presents a state-of-the art of nanoindentation effects on silicon describing its effects from an electrical measurement perspective.

The silicon crystal can be found in many allotropic forms [16]. The most general form, which is used in applications, is the Si-I which has a face-centred cubic structure. One way to modify its structure is to apply a compressive strain on the structure. Starting from a pressure of 11.3-12.5 GPa, Si-I undergoes an allotropic transformation into Si-II, which has a tetragonal β-Sn crystallographic structure and, more importantly, a metallic behaviour [17]. This transformation is also associated with a 22% increase in density. Upon pressure release, Si-II transforms into other allotropic forms of silicon depending on the unloading conditions. The structure of the remnant phase depends on the rate at which the pressure is released and contains a rhombohedral (r8) Si-XII, a body-centered cubic (bc8) Si-III phases as well as silicon in amorphous form [18]. All the above-mentioned structures are represented in Figure II.13.
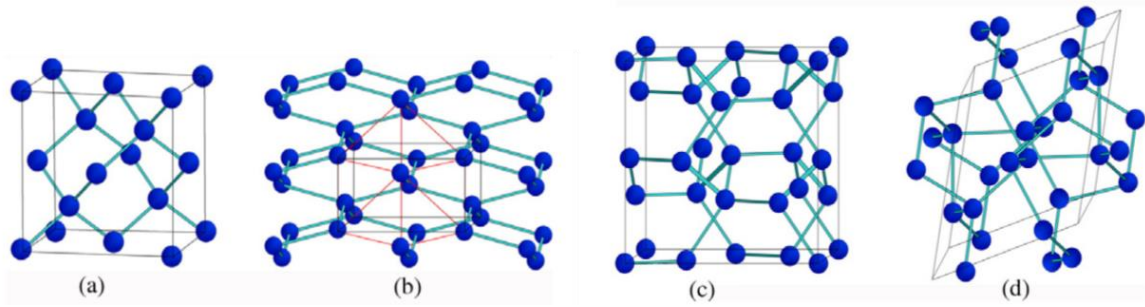
Figure II.13: Different allotropic form of silicon present during and after nanoindentation. Si-I, cubic face-centred, diamond type (a), Si-II, tetragonal, β tin structure type (b), Si-III, cubic centred, BC8 type (c), Si-XII, rhombohedral, R8 type (d). Reproduced from [19].

The electric behaviour of the metallic form of silicon (Si-II) was highlighted through electrical measurements. Gridneva et al. realized the first in-situ electrical measurements which described the resistance drop between metal contacts deposited on crystalline silicon during indentation with a probe placed between them [20]. This was attributed to the formation of the Si-II phase which connected the two metallic contacts, resulting in an increased current. Furthermore, Clarke et al. showed that the indentation on only one contact is enough to induce a change in the resistance [16].

Pharr et al. realized a very comprehensive work which investigated the resistance change between two deposited contacts with an indentation occurring in different places [21]. This is particularly interesting, as it describes the flow of current for different zones where the phase transformation takes place. The studied structure was composed of two Au-Cr contacts deposited on top of a silicon or germanium wafer at a certain distance that would allow the placement of a Berkovich indenter (three-sided pyramid) between them (Figure II.14a). The resistance was measured constantly between the pads polarized positively and negatively. Note that the two metal-semiconductor structures at contacts were in forward and reverse biasing conditions respectively (Figure II.14b).
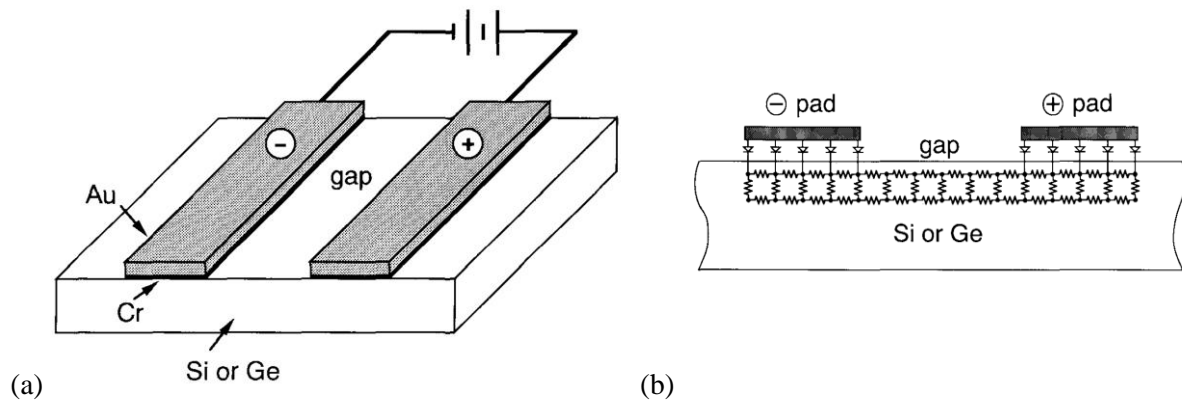

Figure II.14: Schematic of two metal contacts deposited on a silicon/germanium wafer. A voltage is applied between the two contacts (a). The indenter is added on different positions on or in between contacts. Schematic of the equivalent electrical circuit of this configuration (b). Reproduced from [21].

In the first experiment, the distance between the contacts was larger than the indenter size, so that when the indenter was placed between them, there will be no transformation under the contact area. It was observed that when the indenter was placed between the contacts, there was no change in the measured resistance (Figure II.15a). Moreover, when the indentation was realized on the contacts, an important drop in resistance was observed for the negative pad (Figure II.15b), which was under a reverse bias condition, while only a small decrease was measured for the positive pad (Figure II.15c -

forward bias). This proves that the indentation effects change the behaviour of the contact at the metal-semiconductor junction, which changes from rectifying to ohmic.
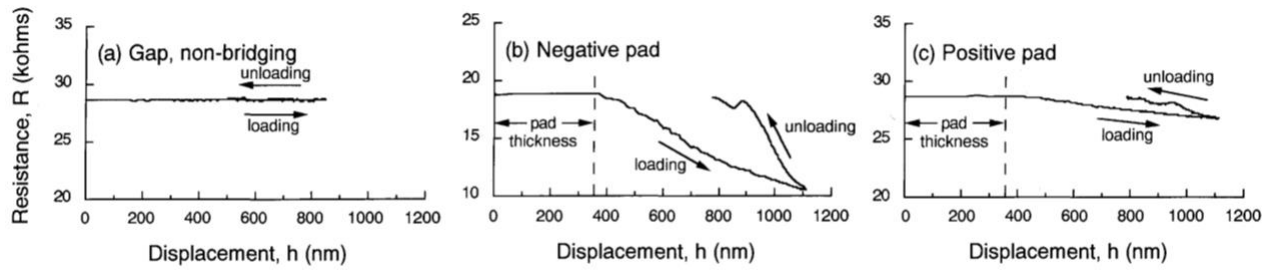

Figure II.15: Measured resistance versus displacement for different positions of the indenter: in the gap between the two contacts (a), on the negative (reverse bias) contact (b) and on the positive (forward bias) contact (c). Reproduced from [21].

Furthermore, in another experiment, the distance between contacts was reduced so that the indenter would fit exactly between them. It was noticed that when the indentation occurs above the negative contact, the drop in resistance occurs at a much lower displacement than when the indenter is placed between the contacts (Figure II.16). In the first case, the transformation occurs immediately under the contact, while in the other it starts in the middle, moving towards the contacts. When the phase change area arrives under the negative contact, a sudden drop in resistance is measured. This proves again that the metal-semiconductor contact behaviour is changed only when the phase transformation occurs at the metal-semiconductor interface.
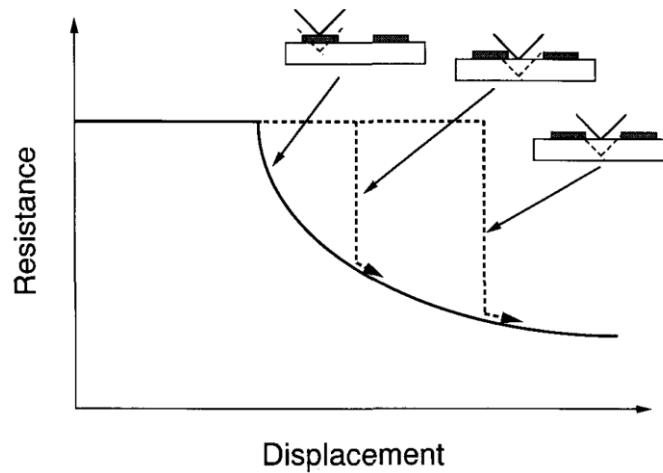

Figure II.16: Resistance versus displacement for different positions of the indenter between the contacts. Reproduced from [21].

More recently, Bradby et al. developed an in-situ electrical characterization method that is sensitive to the Si-I to Si-II phase transformation [18]. The structure uses (100) oriented silicon samples with a 7µm thick epilayer of high resistivity silicon (5 $\Omega \cdot$cm) on a substrate with low resistivity (6·10^{-3} $\Omega \cdot$cm). Aluminium contacts were deposited on the top and bottom of the samples. A Schottky contact is then formed between the upper metal contact and the epilayer which acts as a barrier to the current flow in reverse bias (Figure II.17). The setup was used to study the variation in current for different loading conditions (applied force and indenter shape).
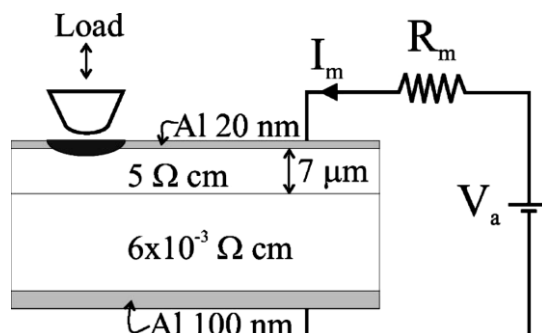
Figure II.17: Schematic of experimental setup composed of two metal layers used as contacts, silicon bulk layer containing a p-doped epilayer. Berkovich indenter. Reproduced from [18].

A comparison between a spherical (with a radius of approximately 4.2 µm) and a Berkovich (three-sided pyramid) indenters was realized. Figure II.18 presents the variations of current with time (proportional to the load) during a loading-unloading cycle. Spherical indentation shows an increase in current only after a load of approximately 22mN, while, in the case of the Berkovich indenter, the change occur directly after the beginning of loading. This is due to the distribution of the compressive stress induced by the indenters which stems from the indenter footprint. While the pointed Berkovich indenter starts with a very small area (very high stress), the spherical indenter needs a much higher load to apply the same stress due to the higher contact patch, which induced a lower compression stress. In view of this, it is clear that the current dramatically increases starting from a threshold load which is determined by the silicon phase transformation. Nonetheless, during unloading, both indenters induce a similar current decrease to the preindentation level.
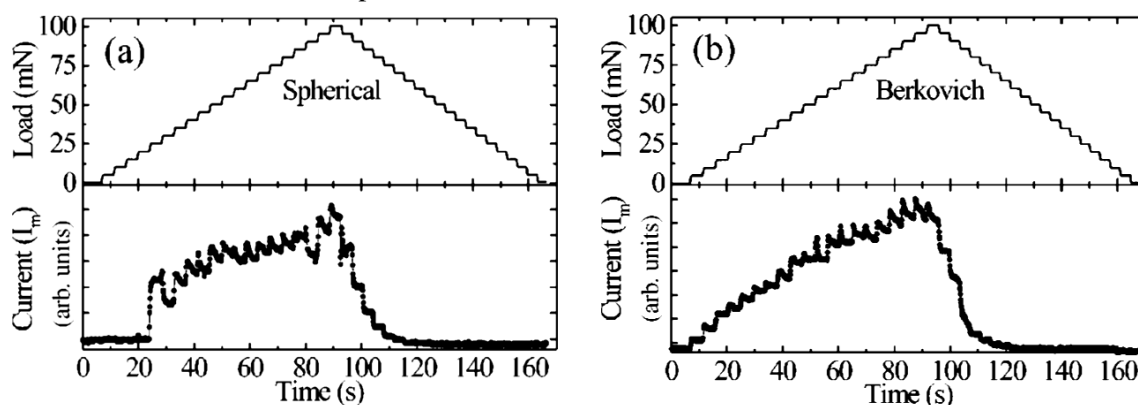

Figure II.18: Current versus time (proportional to the load) for spherical and Berkovich (three-sided pyramid). Reproduced from [18].

Based on this evidence, the following model was presented in order to explain the electrical and mechanical behaviour. During the loading phase, Si-II is formed under the indenter (Figure II.19a). With further loading, the diameter of the transformed region becomes higher than the contacts with the indenter, letting the ductile Si-II flow out of the region under the indenter (Figure II.19b). In the extruded material, the pressure immediately decreases and the Si-II transforms rapidly into other low pressure forms (i.e. amorphous silicon) (Figure II.19c). As soon as the unloading begins, the Si-II transforms into a less dense phase of silicon. If the unloading rate is high, Si-II can be entirely transformed into amorphous silicon. However, if the unloading rate is low enough, Si-II may transform into the thermodynamically preferred non-metallic Si-III and Si-XII (Figure II.19d and Figure II.19e).
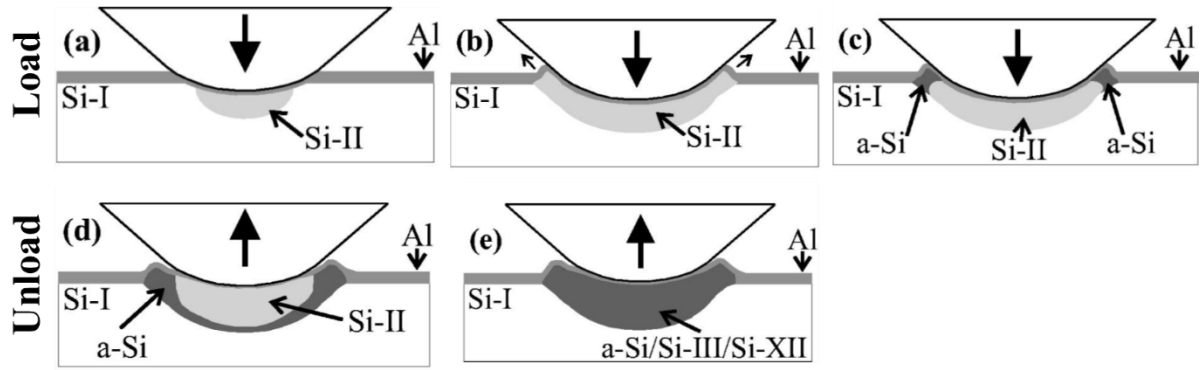
Figure II.19: Interpretation of nanoindentation results as a matter of silicon crystallographic phase transformation during a loading-unloading cycle. Adapted from [18].

Molecular dynamics (MD) simulations supported the theoretical predictions of the anisotropic behaviour of structural phase transition in silicon [19]. When nanoindentation is performed onto an (100) crystallographic orientation, in the region along the centreline, the Si-II (in red) was observed under the indented region (Figure II.20). Besides this, fivefold (bct5 type silicon) and metastable fourfold coordination atoms were determined. Similar results were found by Mylvaganam et al. [22].
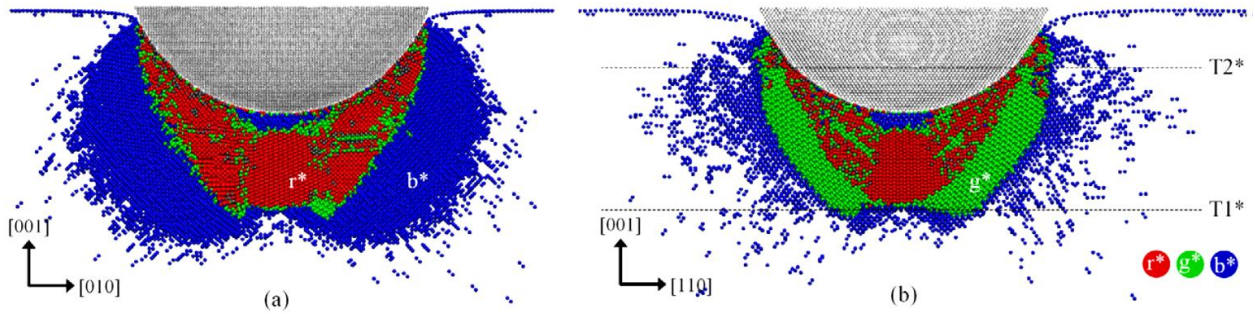

Figure II.20: Cross-section view of the transformed region produced by nanoindentation on (100) oriented silicon surface. Silicon atoms in a diamond cubic structure (Si-I) are not represented, red atoms represent sixfold coordinated Si-II atoms and green and blue are fivefold (bct5) and metastable fourfold coordination atoms. Reproduced from [19].

The same author realized a study matching simulation and experimental results by comparing MD simulations to in-situ scanning spreading resistance microscopy (SSRM) [22]. The latter uses a diamond AFM probe which is placed on a lowly dopes n-type (100) silicon sample, having a resistivity of 42 Ω·cm. Figure II.21 compares the residual indentation depth with respect to the indentation force for both MD simulation and SSRM realized in a N_2 atmosphere. The results are in excellent agreement and prove that both are correlated in terms of mechanical characteristics.
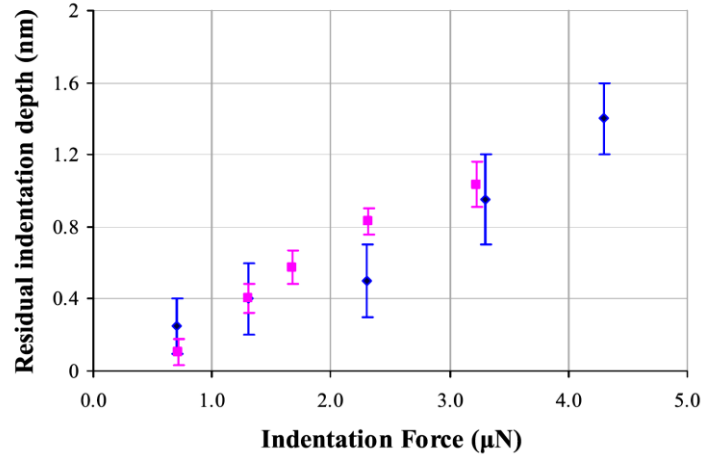
Figure II.21: Residual indentation depth versus indentation force for experimental SSRM (blue diamonds) and MD simulation (pink squares). Reproduced from [22].

In order to perform the in-situ electrical measurements, a DC bias was applied between the back contact of the sample and the diamond tip. The resulting current was measured between the two using an amplifier. The resistance measured is composed of the following elements: (1) tip resistance, (2) tip-silicon contact resistance, (3) phase transformed material and (4) resistance of the rest of the silicon sample. Components (1), (2) and (4) remain unchanged when the tip starts to touch the sample. Therefore, only the resistance of the transformed phase changes. It can be correlated with the simulation results knowing that the resistance R is proportional to the length divided by the cross-sectional area A (R ~ l/A). l/A was determined from MD simulations and compared to the experimentally measured resistance (using SSRM) for various indentation forces (Figure II.22). A significant drop can be observed in both cases at approximately 1.3µN, confirming the emergence of the Si-II phase during nanoindentation loading.
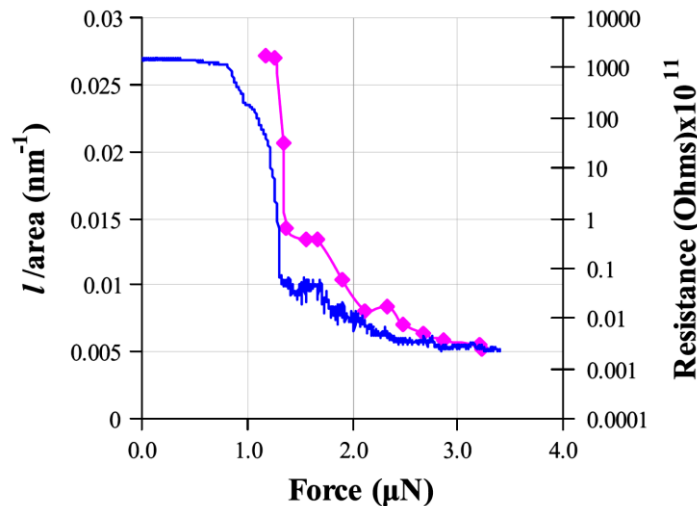

Figure II.22: Length over area ratio determined from MD simulations (pink ◆) and electrical resistance obtained from SSRM (blue line) versus indentation force. Reproduced from [22].

In conclusion, it has been proven experimentally and theoretically that a high pressure applied on a metal-silicon interface can transform the nature of the contact from rectifying (Schottky) to ohmic. This change was attributed to the high pressure phase of silicon (Si-II), which has a metallic behaviour. Nevertheless, this explanation was never used before to support the ohmic contact behaviour obtained with metallic pressure probes on the low-doped silicon film in the Ψ-MOSFET.

2.3. Nanoindentation and Ψ-MOSFET

In this section, we will describe the experimental results that indicate a phase transformation of silicon under the pressure of the metallic probes during Ψ-MOSFET characterization. Unlike the studies from the literature which had calibrated load systems, we simply manually adjusted the pressure by using the pressure control system provided by the Jandel 4-probe station. Additionally, probe blunting over time can also account for a slight change in contacts. Therefore, the results presented here have a qualitative purpose and are not calibrated for specific loads as in the litterature. Note however that in the Ψ-MOSFET, there is a conduction channel of either electrons or holes according to the gate voltage. Therefore, V_G is a supplementary parameter that will be considered. Our study involved two types of samples with different silicon film thicknesses (88nm and 12nm). The BOX was 145nm thick in both cases.

Thick film (88nm) behaviour

Drain current versus drain voltage characteristics (Figure II.23) show an ohmic behaviour in the area close to the origin, which ranges from -1V to +1V approximately.
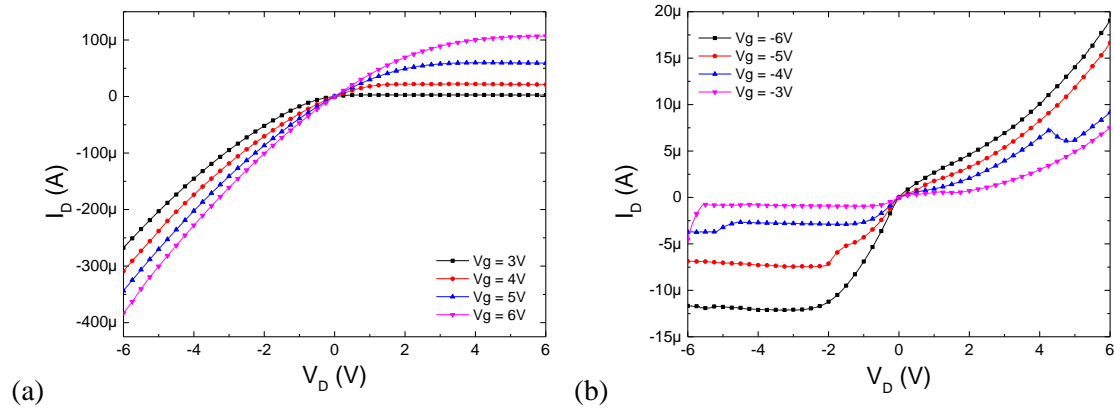

Figure II.23: Drain current versus drain voltage characteristics in inversion (a) and accumulation (b) conditions. Pressure 100g. $t_{Si} = 88nm$, $t_{BOX} = 145nm$.

In order to obtain the current versus load curves in the Ψ-MOSFET configuration, the gate voltage was fixed to values corresponding to strong inversion or accumulation. The drain current was measured using the HP4155 analyser in sampling mode, by making an average over a 40 seconds sampling interval (Figure II.24).
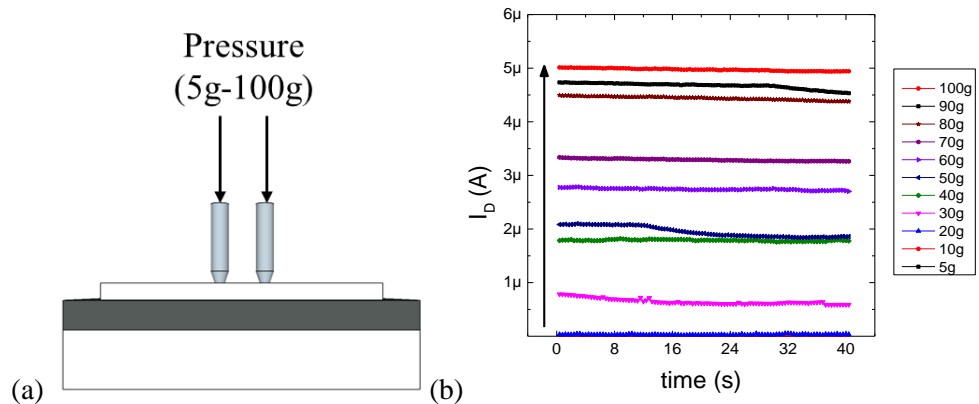

Figure II.24: Schematic of the Ψ-MOSFET configuration with pressure applied on both probes (a). Drain current versus time (for 40 seconds) for different pressures applied on the probes (b). $t_{Si} = 88nm$, $t_{BOX} = 145nm$.

In the case of a thick SOI film (88nm), the drain current increases with the pressure applied on the probes (Figure II.25a). The growth rate diminishes as the pressure increases. Figure II.25b presents a curve measured for bulk silicon. The variation of the current is represented on the left axis during a load-unload cycle (right axis) [23]. Comparing the two, we can observe that the shape of the curves is similar suggesting that the same transformation occurs in our SOI substrate.
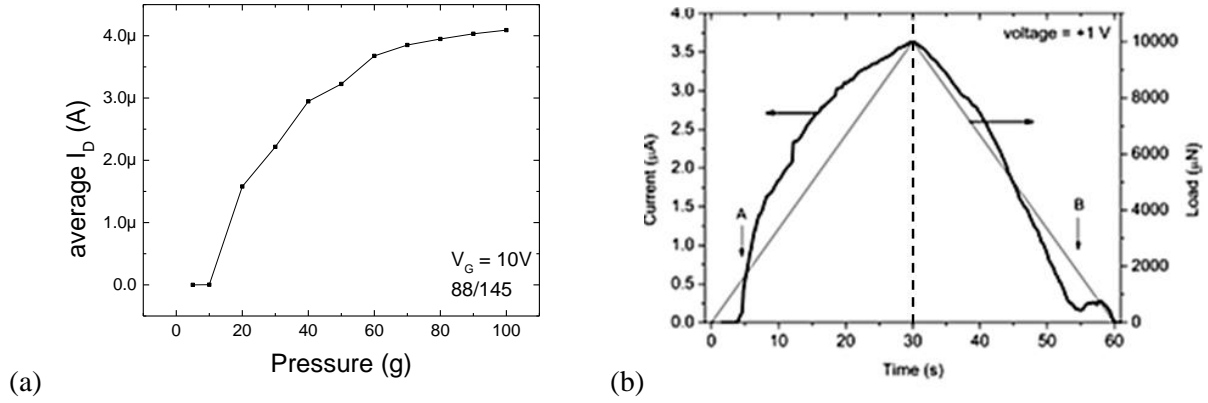

(a)   (b)

Figure II.25: Drain current versus pressure in inversion condition (V_G=10V) for the Ψ-MOSFET configuration. t_{Si} = 88nm, t_{BOX} = 145nm (a). Current versus time (proportional to the load) in a bulk experimental setup using a Berkovich (three-sided pyramid) indenter. Reproduced from [24].

Indeed, for an 88nm thick silicon film, the drain current versus drain voltage characteristics display an ohmic behaviour for pressures above 10g on the probe station pressure control system (*Figure II.26*), proving that in this range there is no modification of the nature of the contact.
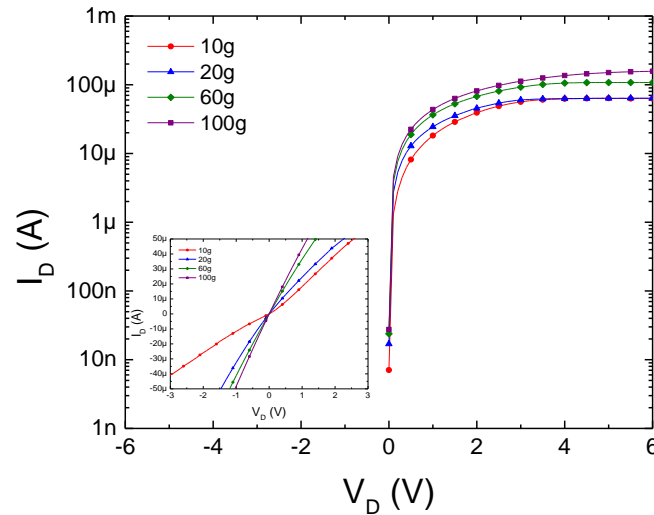

Figure II.26: Drain current versus drain voltage (linear scale in the inset) for different probe pressures in accumulation conditions (V_G = -6V, V_D = 0.1V). t_{Si} = 88nm, t_{BOX} = 145nm.

The drain current dependence with the pressure applied on the probes was studied as well for different polarization conditions. As such, the device was biased in both accumulation and inversion regimes. For each pressure applied on the probes, the gate bias was chosen in order to have the same overdrive, which means that the difference (V_G-V_T) or (V_G-V_{FB}) is equal in inversion and accumulation. This indicates the same amount of charges in the accumulation/inversion regimes. The absolute value of drain current does not vary with the sign of the drain bias (Figure II.27). This shows that the drain

current does not depend on the drain probe polarization sign in the linear regime close to 0V (symmetrical response regardless the sign of V_D). Additionally, in accumulation, the drain current is lower than in inversion as expected from the drain current versus gate voltage characteristics. The contact is ohmic starting from a pressure of 10g, raising the question on the crystallographic modifications induced by the probes.
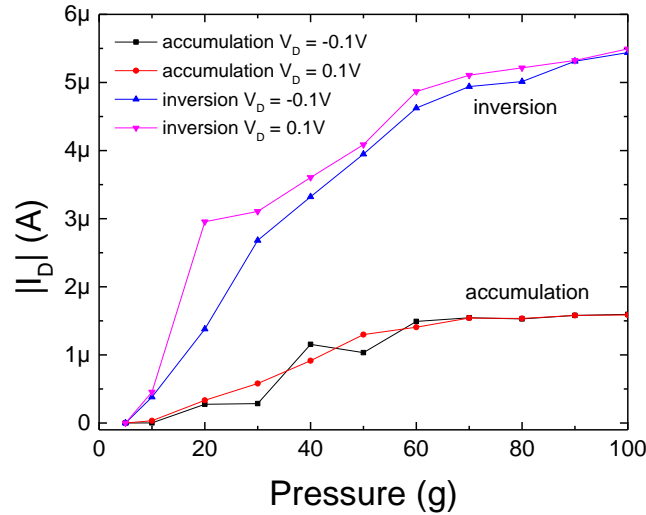

Figure II.27: Absolute value of the drain current for positive and negative drain bias in the linear regime for accumulation and inversion regimes (V_G = -5V and V_G = 6V respectively). t_{Si} = 88nm, t_{BOX} = 145nm.

FIB-TEM images (realized at the LTM laboratory by T. Cerba) reveal, besides a crater left by the extruded material, no change in microstructure of the silicon film (Figure II.28). Indeed, the other allotropic forms of silicon (Si-III, Si-XII), which typically appear following indentation in bulk silicon [19], are not present.
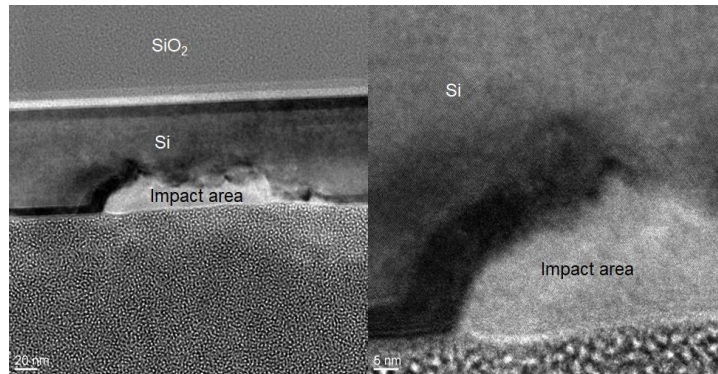
Figure II.28: FIB-TEM image of the SOI wafer and the crater left after the probe loaded at 90g (left) and zoom on the impact area (right). t_{Si} = 88nm, t_{BOX} = 145nm.

Images of the craters left by the probes indicated that there is an important quantity of extruded material after indentation. If the extruded material plays a particular role in the contact behaviour, the measurement of a second load-unload cycle would offer different current values. Consequently, we measured the drain current for consecutive cycles in both inversion (Figure II.29a) and accumulation (Figure II.29b). In the inversion regime, the drain current has the same characteristics for the two

consecutive cycles showing an "elastic" behaviour. However, the shape of the drain current versus pressure curve is slightly different in the accumulation regime. The distinction is made during unload (while decreasing the pressure), where for pressures inferior to 20g, the drain current is lower than upon loading. This dissymmetry between the load/unload phases for different polarization conditions was also presented in [21], [23]. This suggests that the Si-II phase has an important effect on the conduction of holes.
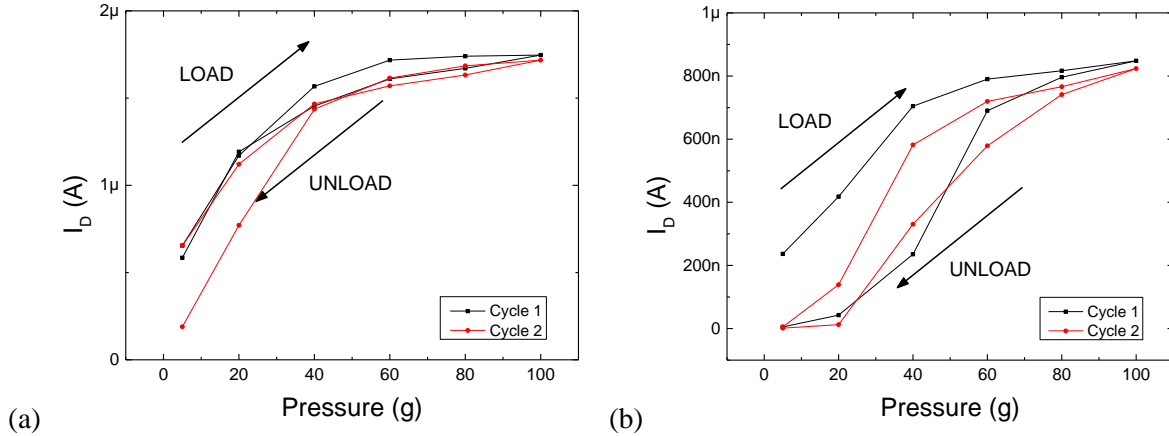

(a)

(b)

Figure II.29: Drain current versus probe pressure. t_{Si} = 88nm, t_{BOX} = 145nm. Measurements performed in inversion (a) (V_G = 6V, V_D = 0.1V, V_T = 2.1V) and accumulation (b) (V_G = -5V, V_D = 0.1V, V_{FB} = -1.1V).

Thin film (12nm) behaviour

As for the thick film, drain current versus drain voltage characteristics (Figure II.30) show an ohmic behaviour in the area close to the origin. However, the range is narrower (±200mV), but increases with the overdrive from the threshold (V_G - V_T) and flat-band ($|V_G$ - $V_{FB}|$) voltages. Additionally, a saturation level is achieved in this case when the metal-semiconductor structure is directly biased. This limitation is caused by the thinner film which restricts current flow.

(a)

(b)
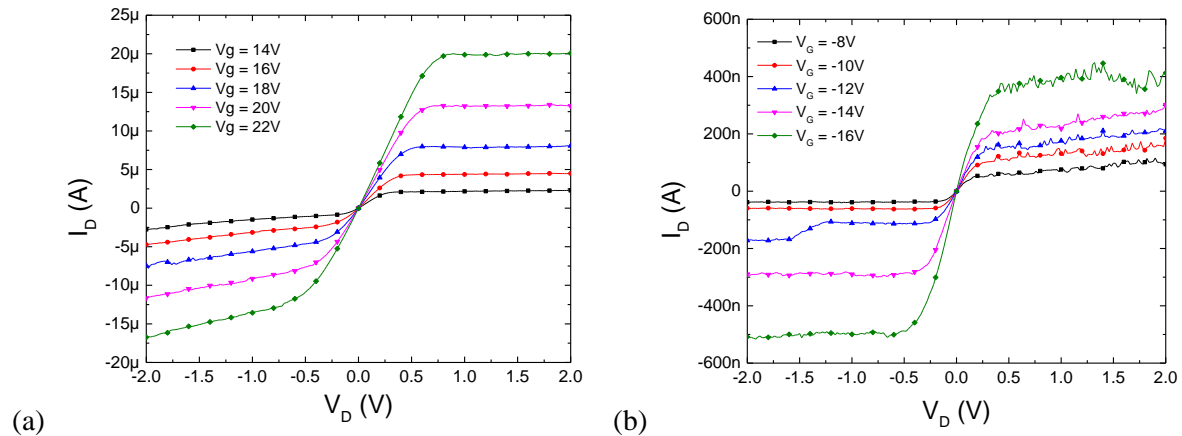
Figure II.30: Drain current versus drain voltage characteristics in inversion (a) and accumulation (b) conditions. Pressure 100g. t_{Si} = 12nm, t_{BOX} = 145nm.

The drain current dependence with the pressure applied on the probes was studied as well for this type of substrate. In the strong inversion regime, the drain current starts to increase only after a threshold pressure of 20g for V_G=20V (Figure II.31). Surprisingly, this suggests that the formation of Si-II phase appears for higher pressures in thin SOI silicon film. The mechanism might be related to the proximity of the Si-SiO$_2$ interface to the top surface. As investigated in [25] for a 12 nm thick silicon film and a

25nm BOX, the oxide breakdown due to probe penetration occurs from as little as 15g. This means that for this thickness, the probe reaches the oxide for very low pressures, which does not allow the formation of Si-II under the probe. Therefore, we can assume that the high-pressure phase of silicon appears as a consequence of the lateral propagation of the compressive stress.
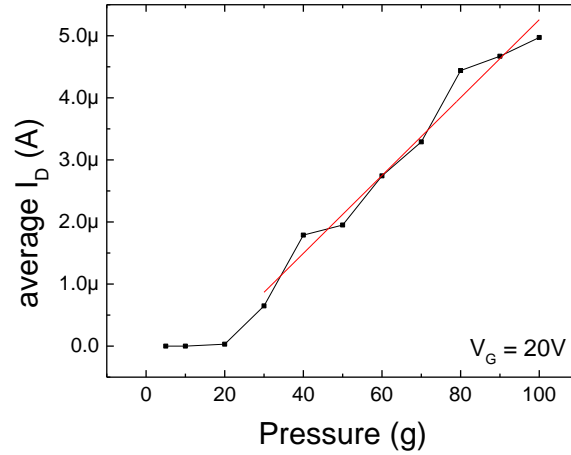

Figure II.31: Drain current versus pressure in inversion condition (V_G=20V) for the Ψ-MOSFET configuration. t_{Si} = 12nm, t_{BOX} = 145nm.

The pressure dependence of the current was studied as well for a complete load-unload cycle realized in both inversion (Figure II.32a) and accumulation (Figure II.32b). The electrical measurements show an increase of the drain current that begins only from a threshold pressure of around 50g for electrons and 70g for holes. Similarly with the thicker silicon film, the load-unload curve follows the same path. The higher pressures needed in this case (compared to Figure II.31) are due to the values chosen for the gate voltage which are closer to the threshold and the flat band voltages, which means that there are less carriers in the silicon film to ensure the conduction.
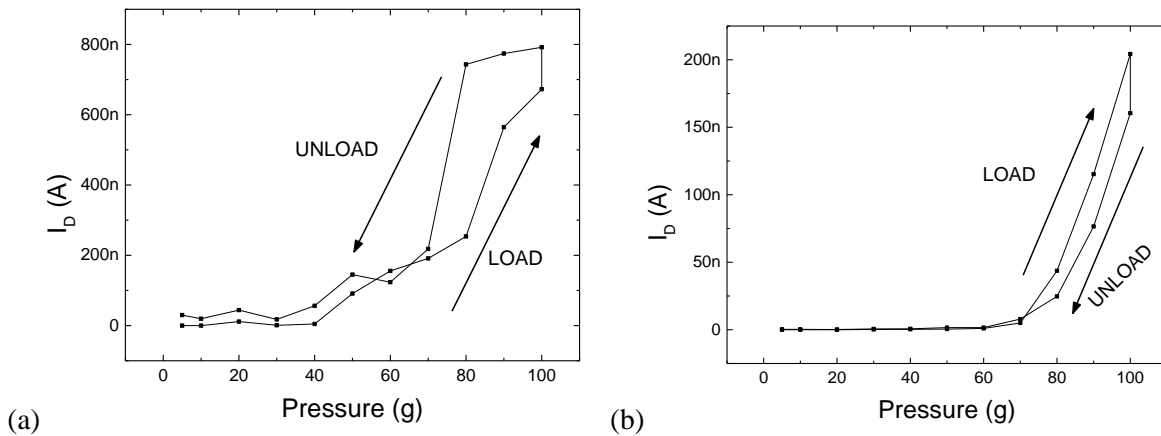
Figure II.32: Drain current versus probe pressure. Measurements performed in inversion (V_G= 16V, V_D = 0.1V, V_T = 11.2V) and in accumulation (V_G= -12V, V_D = 0.1V, V_{FB} = -7.1V). t_{Si} = 12nm, t_{BOX} = 145nm.

The I_D-V_D characteristics traced in the accumulation regime further emphasize the change in behaviour observed at the threshold pressure of 70g. Between 20g and 40g, the shape of the drain current in a thin silicon film completely modifies in the logarithmic scale (Figure II.33a). This might be due to the penetration of the probe through the native oxide layer. Furthermore in Figure II.33b we can observe

a different behaviour of the contact between 60g and 80g, which transforms from Schottky to ohmic. This further confirms the results presented in Figure II.32. This transformation does not occur in the case of a thick film which was ohmic right from the beginning (Figure II.26).

(a) (b)

Figure II.33: Drain current versus drain voltage for different probe pressures in accumulation conditions ($V_G = -12V$, $V_D = 0.1V$) in linear (a) and logarithmic (b) scales. $t_{Si} = 12nm$, $t_{BOX} = 145nm$.

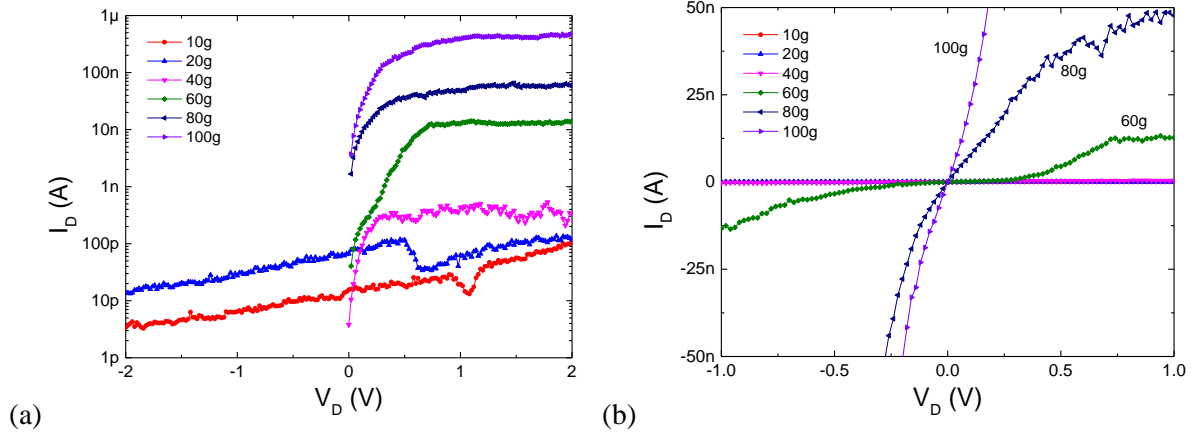The FIB-TEM images (Figure II.28) showed that for the 88nm thick silicon film, the depth of the craters was approximately 35nm, three times higher than the 12nm silicon film used in this experiment. The AFM image of a crater showing the mark of the probe loaded at 100g of pressure (the maximum value that can be applied during the electrical measurements), indicates as expected a maximum depth of 15nm (Figure II.34), which means that the tip of the probe reaches the BOX. It follows that the Si-II phase transformation can only take place laterally.
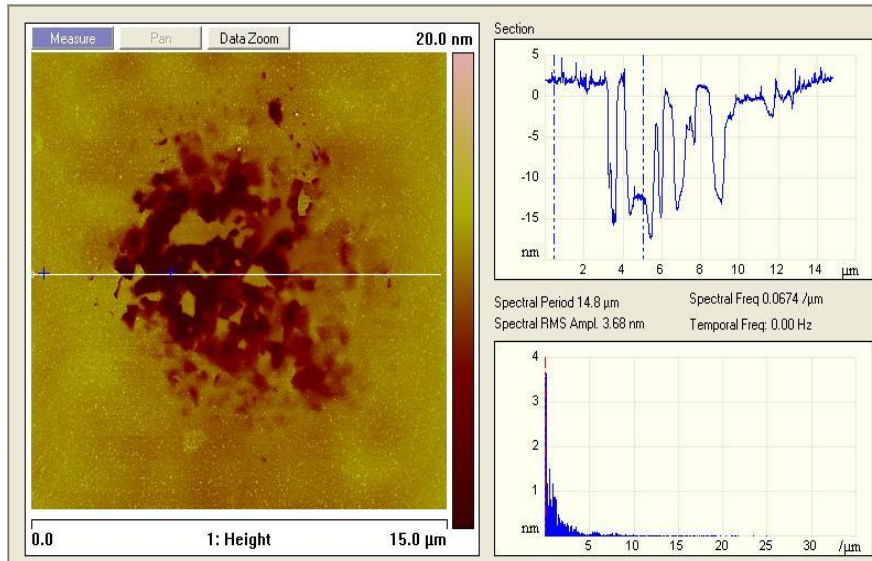
Figure II.34: AFM image (left) and section depth (right) of the crater left by the probe loaded at 100g (right). $t_{Si} = 12nm$, $t_{BOX} = 145nm$.

Moreover, as described in the literature for a spherical indenter, simulation show that the critical compression stress is reached at a certain distance from the indenter. For instance, for an indenter radius of 10nm, molecular dynamic simulations show that the Si-II atoms appear at a depth of around 4nm (Figure II.35) [22]. We therefore assume that for the 40µm in radius indenter which was employed the area where the critical compression stress occurs, in order for the phase change to take place, should be lower than the silicon film-BOX interface.
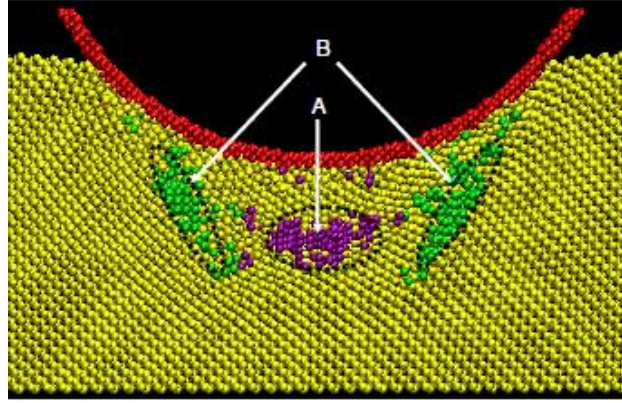
Figure II.35: Cross-sectional view of molecular dynamic simulations for a 10nm in radius spherical indenter. Atoms in region A are Si-II and in region B other six-coordinated silicon atoms. Reproduced from [22].

All evidence considered, we conclude that for a thick silicon film, the allotropic transformation appears to occur under the probe/indenter (Figure II.36a), beginning from the smallest pressure applied in the range allowed by the Jandel station (10g). Furthermore, the current-load curve is similar to the ones found in the literature, which further proves this transformation takes place.

However, in the case of a thin (12nm) silicon film, the drastic current increase takes only after a certain threshold pressure. This can be explained by the penetration of the indenter inside the silicon film, which reaches the BOX from the smallest pressures. Therefore, we assume that Si-II can only form laterally, when the pressure applied on the probes is high enough so that the lateral propagation of the compressive stress occurs (Figure II.36b).

(a) (b)
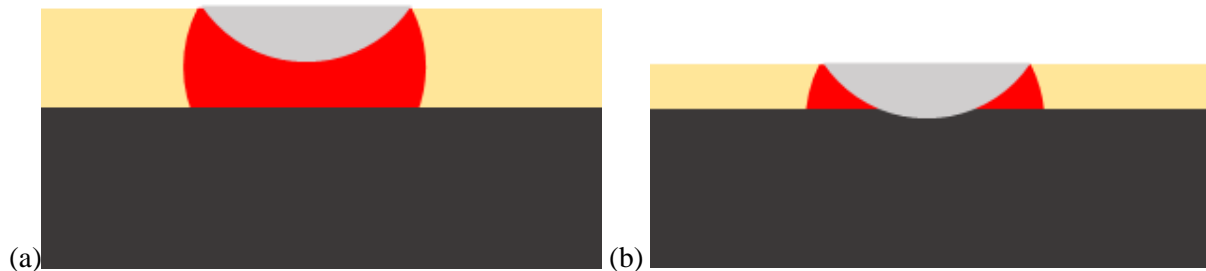
Figure II.36: Schematic of a cross-sectional view describing the formation of the Si-II phase in the Ψ-MOSFET configuration.

From our experimental results, the thinner film needs a higher pressure in order to achieve the same level of current. This is in opposition to the idea that the pressure needs to be high enough to reach the conduction channel, which would imply the opposite (i.e. higher pressure for thicker films).

Moreover, the current-load characteristics showed an elastic behaviour upon repeated load-unload cycles. This fact opposes the idea that crystallographic defects are responsible for the ohmic behaviour of contact in the Ψ-MOSFET contacts, as they would be already created upon the first loading phase and would not revert upon unloading. All this indicates that silicon phase transformation during probe indentation is a plausible explanation for the ohmic behaviour of the Ψ-MOSFET contacts.

2.4. Conclusion

This chapter begins by presenting the working principles, the characteristics and the extraction of the parameters in the Ψ-MOSFET configuration. Those parameter extraction methods (e.g. V_T, V_{FB}) will be used in chapter 4 for detection.

Due to the observed craters in the silicon film, we proposed a new hypothesis based on nanoindentation induced silicon phase change. Research realized so far proved that this allotropic form changed the electrical behaviour of the metal-semiconductor contact from Schottky (rectifying) to ohmic. Our experimental results proved that there is indeed a threshold load starting from which a dramatic change in current can be observed. Also, a superposition of the current – load curves during repeated loading-unloading cycles proved that crystallographic defects are not the reason why the contacts present an ohmic behaviour. The overall electrical characteristics curves are in agreement with the silicon phase change induced by nanoindentation, which transforms the contacts from Schottky to ohmic. The ohmic contacts will be of high importance for the body potential measurements in the next chapter.

Bibliography

[1] C. Sorin and S. Li, *Electrical characterization of silicon-on-insulator materials and devices*. Kluwer Academic Publishers, 1995.

[2] S. Williams, S. Cristoloveanu, and G. Campisi, 'Point contact pseudo-metal/oxide/semiconductor transistor in as-grown silicon on insulator wafers', *Mater. Sci. Eng. B*, vol. 12, no. 1–2, pp. 191–194, 1992.

[3] A. El Hajj Diab *et al.*, 'Low-frequency noise in SOI pseudo-MOSFET with pressure probes', *Microelectron. Eng.*, vol. 88, no. 7, pp. 1283–1285, Jul. 2011.

[4] L. Pirro, I. Ionica, G. Ghibaudo, and S. Cristoloveanu, 'Split-CV for pseudo-MOSFET characterization: Experimental setups and associated parameter extraction methods', in *2014 International Conference on Microelectronic Test Structures (ICMTS)*, Udine, Italy, 2014, pp. 14–19.

[5] I. Ionica, I. Savin, W. Van Den Daele, T. Nguyen, X. Mescot, and S. Cristoloveanu, 'Characterization of silicon-on-insulator films with pseudo-metal-oxide-semiconductor field-effect transistor: Correlation between contact pressure, crater morphology, and series resistance', *Appl. Phys. Lett.*, vol. 94, no. 1, p. 012111, Jan. 2009.

[6] H. J. Hovel, 'The HgFET: a new characterization tool for SOI silicon film properties', in *IEEE International SOI Conference Proceedings*, Fish Camp, CA, USA, USA, 1997, pp. 180–181.

[7] K. Park, P. Nayak, S. Cristoloveanu, and D. K. Schroder, 'Pseudo-MOSFET Substrate Effects of Drain Current Hysteresis and Transient Behavior', *IEEE Trans. Electron Devices*, vol. 56, no. 6, pp. 1269–1276, Jun. 2009.

[8] D. Munteanu, S. Cristoloveanu, and E. Guichard, 'Numerical simulation of the pseudo-MOSFET characterization technique', *Solid-State Electron.*, vol. 43, no. 3, pp. 547–554, 1999.

[9] S. Cristoloveanu, M. Bawedin, and I. Ionica, 'A review of electrical characterization techniques for ultrathin FDSOI materials and devices', *Solid-State Electron.*, vol. 117, pp. 10–36, Mar. 2016.

[10] S. Cristoloveanu, D. Munteanu, and M. S. Liu, 'A review of the pseudo-MOS transistor in SOI wafers: operation, parameter extraction, and applications', *IEEE Trans. Electron Devices*, vol. 47, no. 5, pp. 1018–1027, 2000.

[11] G. Hamaide, F. Allibert, H. Hovel, and S. Cristoloveanu, 'Impact of free-surface passivation on silicon on insulator buried interface properties by pseudotransistor characterization', *J. Appl. Phys.*, vol. 101, no. 11, p. 114513, Jun. 2007.

[12] D. K. Schroder, *Semiconductor material and device characterization*. John Wiley & Sons, 2006.

[13] G. Ghibaudo, 'New method for the extraction of MOSFET parameters', *Electron. Lett.*, vol. 24, no. 9, p. 543, 1988.

[14] S. M. Sze and K. N. Kwok, *Physics of Semiconductor Devices*, 3rd ed. Hoboken, New Jersey: John Wiley & Sons, 2007.

[15] L. Pirro, I. Ionica, S. Cristoloveanu, and G. Ghibaudo, 'Low-frequency noise in bare SOI wafers: Experiments and model', *Solid-State Electron.*, vol. 125, pp. 167–174, Nov. 2016.

[16] D. R. Clarke, M. C. Kroll, P. D. Kirchner, R. F. Cook, and B. J. Hockey, 'Amorphization and Conductivity of Silicon and Germanium Induced by Indentation', *Phys. Rev. Lett.*, vol. 60, no. 21, pp. 2156–2159, May 1988.

[17] J. Z. Hu, L. D. Merkle, C. S. Menoni, and I. L. Spain, 'Crystal data for high-pressure phases of silicon', *Phys. Rev. B*, vol. 34, no. 7, p. 4679, 1986.

[18] J. E. Bradby, J. S. Williams, and M. V. Swain, '*In situ* electrical characterization of phase transformations in Si during indentation', *Phys. Rev. B*, vol. 67, no. 8, Feb. 2003.

[19] D. E. Kim and S. I. Oh, 'Atomistic simulation of structural phase transformations in monocrystalline silicon induced by nanoindentation', *Nanotechnology*, vol. 17, no. 9, pp. 2259–2265, May 2006.

[20] I. V. Gridneva, Yu. V. Milman, and V. I. Trefilov, 'Phase transition in diamond-structure crystals during hardness measurements', *Phys. Status Solidi A*, vol. 14, no. 1, pp. 177–182, Nov. 1972.

[21] G. M. Pharr *et al.*, 'Electrical resistance of metallic contacts on silicon and germanium during indentation', *J. Mater. Res.*, vol. 7, no. 04, pp. 961–972, Apr. 1992.

[22] K. Mylvaganam, L. C. Zhang, P. Eyben, J. Mody, and W. Vandervorst, 'Evolution of metastable phases in silicon during nanoindentation: mechanism analysis and experimental verification', *Nanotechnology*, vol. 20, no. 30, p. 305705, Jul. 2009.

[23] S. Ruffell, J. E. Bradby, N. Fujisawa, and J. S. Williams, 'Identification of nanoindentation-induced phase changes in silicon by *in situ* electrical characterization', *J. Appl. Phys.*, vol. 101, no. 8, p. 083531, Apr. 2007.

[24] S. Ruffell, J. E. Bradby, J. S. Williams, and O. L. Warren, 'An in situ electrical measurement technique via a conducting diamond tip for nanoindentation in silicon', *J. Mater. Res.*, vol. 22, no. 03, pp. 578–586, Mar. 2007.

[25] W. Van Den Daele, C. Malaquin, N. Baumel, O. Kononchuk, and S. Cristoloveanu, 'Adaptation of the pseudo-metal–oxide–semiconductor field effect transistor technique to ultrathin silicon–on–insulator wafers characterization: Improved set-up, measurement procedure, parameter extraction, and modeling', *J. Appl. Phys.*, vol. 114, no. 16, p. 164502, Oct. 2013.

Chapter 3 : BODY POTENTIAL IN THE Ψ-MOSFET CONFIGURATION

The raise of an out-of-equilibrium body potential is one of the signatures of floating body effects in the silicon on insulator devices. It can be seen as a parasitic effect or exploited for applications. In this chapter, we will explain the appearance of the out-of-equilibrium body potential in the Ψ-MOSFET configuration. In the first part, we will describe the significance and the characteristics of this type of measurement and propose a simplified experimental setup which will be used for the sensing measurements in the next chapter. Finally, the body potential experimental results will be reproduced by TCAD simulation. The proof of concept of charge detection using the body potential will be also validated with simulations by adding surface charges on top of the SOI.

Table of Contents

3.1. Out-of-equilibrium body potential – state of the art

Silicon on insulator technology implemented to the CMOS applications increased device performance. Among the advantages, we can mention: an excellent lateral and vertical isolation of devices from substrate, faster device operation due to the reduction of parasitic capacitances, lower power consumption and direct control of each transistor through the back-gate bias [1], [2].

However, the complete isolation of the body of the transistor from the substrate gave rise to floating body effects (FBEs) which are the major parasitic effects in SOI-based MOSFETs. This originates from an accumulation of carriers in the silicon body of the transistor, which cannot be removed fast enough as a repercussion of the isolated device structure [3].

There are numerous consequences of FBEs: the kink-effect (appearance of a kink in I_D-V_G characteristics in saturation mode ($V_D > V_G$-V_{TH}) , negative conductance and transconductance, hysteresis and instabilities, single transistor latch (the transistor cannot be turned off by reducing the gate voltage), bipolar transistor action and premature breakdown [4].

One of the signatures of the out-of-equilibrium regime is the appearance of a body potential variation in the body of the transistor, due to the lack or excess of carriers during a gate voltage sweep between different working regimes. For example, in the case of an nMOSFET a fast transition from inversion (channel of electrons) to accumulation (channel of holes) generates an out-of-equilibrium state due to the lack of a source of holes, which translated into a negative body potential (Figure III.1).
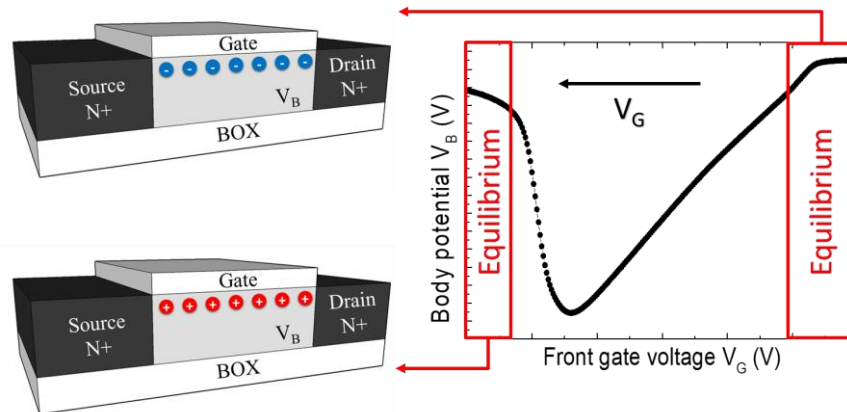

Figure III.1: Schematic of the out-of-equilibrium regime in nMOSFET transistors [5].

The main aspect of the body potential is represented by its out-of-equilibrium nature. This was illustrated in the case of SOI-based transistors by changing the sweeping speed of the gate voltage. In Figure III.2a the measured body potential is represented with respect to the front gate bias [5]. We can observe that the measured potential is higher for faster sweeps. In view of using this type of measurement as a reading method for a sensor, this would favour a fast detection.

The out-of-equilibrium body potential appears in the low conduction region of the transistor and is consequently influenced by surrounding charges. A demonstration of this characteristic was evidenced through simulation [5]. The proposed model for describing the body potential was used for different front gate flat-band voltages (V_{FBB} = -1.1V, -0.8V and +0.2V). Figure III.2b illustrates the variation of the body hole quasi-Fermi (Ψ_P) and front-surface (Φ_{S1}) potentials with respect to the front gate bias for the three different cases. The two parameters represent the hallmark of the body potential. It can be observed that the curves shift corresponding to the imposed flat-band voltage. This scenario is very similar to the addition of charged molecules on top of the device, so the effect should be adapted for sensing..
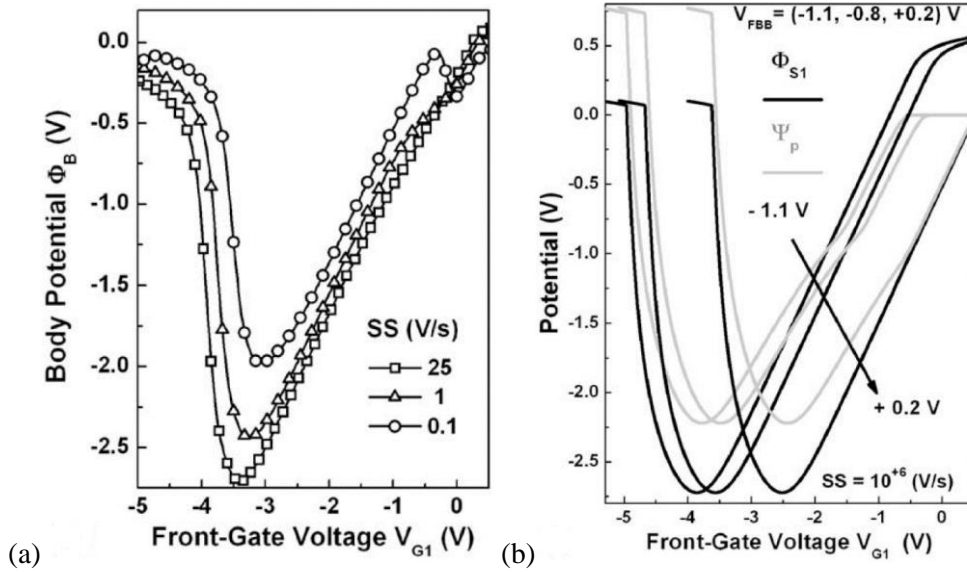
Figure III.2: Measured body potential versus front gate voltage for three difference scan speeds (a). Simulated body hole quasi-Fermi (Ψ_P) and front-surface (Φ_{S1}) potentials for different front gate flat-band voltages. Both reproduced from .[5]

Although FBEs are generally considered as parasitic effects, detrimental to the performance of the transistor, they prove to be beneficial in the case of 1T-DRAM (single-transistor Dynamic Random Access Memory). Their working principle is based on the charge stored in the floating body. The "1" state of the structure is defined when the majority carriers are in excess in the body of the transistor resulting in an increased drain current. The "0" state is reached by removing those charges which leads to a low drain current [6].

Among all 1T-DRAM flavours, three promising structures based on this effect can be listed. First, the MSDRAM (metastable dip (MSD) effect-based Random Access Memory) is a typical SOI transistor which has a film thick enough to prevent the supercoupling effect (Figure III.3a) [7]. The A2RAM is also based on a thick SOI transistor, but the source and drain are shorted by a doped layer called "bridge" (Figure III.3b) [8]. Finally, the Z²-FET is a p-i-n diode partially covered by the front gate under which the charge is stored (Figure III.3c) [9]. Simulations realized in the 28nm node FD-SOI technology showed that MSDRAM does not have sufficient performance for 1T-DRAM applications and that the Z²-FET outperforms the A2RAM in terms of read current margin and retention time, but it has a larger footprint due to its partially covered gate structure [10].
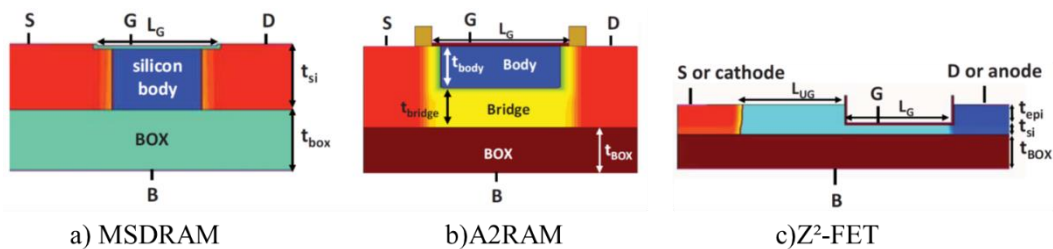
Figure III.3: Structure of MSDRAM (a), A2RAM (b), Z²FET (c). Reproduced from [10].

The applications of the body potential can be expanded in order to encompass charge sensing, as V_B is sensitive to the charge state on the top surface. Additionally, we can expect fast detection, since it is an out-of-equilibrium phenomenon, for which a greater response is obtained for faster scan speeds. In this chapter, we will implement the out-of-equilibrium body potential measurements in the Ψ-MOSFET configuration. This method will be used for detection in chapter 4.

3.2. Body potential measurements in Ψ-MOSFET configuration

The conditions to obtain an out-of-equilibrium potential in SOI devices are: (1) a buried oxide layer to inhibit carrier flow from/into the substrate, (2) a gate voltage transition that would drive the film from strong accumulation to strong inversion or vice-versa and (3) source and drain that cannot provide one type of carriers (or at least not instantaneously). This results in a deep depletion out-of-equilibrium region at the transition values of the gate voltage. All those conditions are also present in the Ψ-MOSFET configuration and in the following section the main characteristics of this type of measurement will be presented.

a. Measuring the body potential in the Ψ-MOSFET configuration

In FD-SOI transistors, the body potential measurements are realized using body contacts [2]. Those are replaced by a third probe in the case of the Ψ-MOSFET which is interposed between the source and the drain. The three probes are separated by 1mm each (Figure III.4).
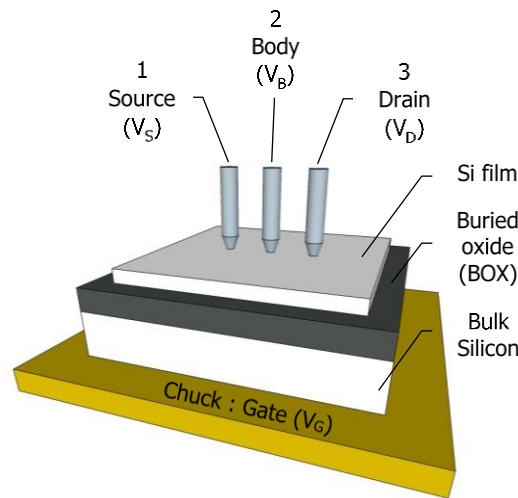

Figure III.4: Experimental setup for body-potential measurements in the Ψ-MOSFET configuration.

All the measurements presented in this thesis were realized on a HP4155 analyser. For potential measurements, two possibilities are available: a Voltage Monitor Unit (VMU) or a Source/Monitor Unit (SMU) used in a current source mode by imposing a zero current condition. Both configurations were used to measure the same sample, with the aim of determining the most appropriate one. In the absence of a leakage current through the measurement system, the sum of all the currents through the device should be equal to 0, so that $I_G = -(I_D+I_S)$ for both experimental setups. Figure III.5 traces the gate current (I_G) and the opposite of the sum of the drain and source currents $-(I_D+I_S)$. For SMUs, we can observe that the two terms are equal (Figure III.5a). In the case of the VMU (Figure III.5b), a leakage current of 0.8nA was observed. This is consistent with the ~1nA leakage current announced by the HP4155 manual for VMU measurements [11]. Since an appropriate voltage measurement must be achieved, we chose SMUs for V_B measurements as they insure lower leakage current through the voltage measurement system.

It can be also observed for V_G greater than 2V that the $-(I_D + I_S)$ curve using an SMU for V_B measurement presents an important noise and that it is not correlated to the I_G curve. We suppose that it is related to the fact that I_D and I_S are at least 3 orders of magnitude higher than I_G, so, the difference in calibration range (and in precision) shows this behaviour in this region.
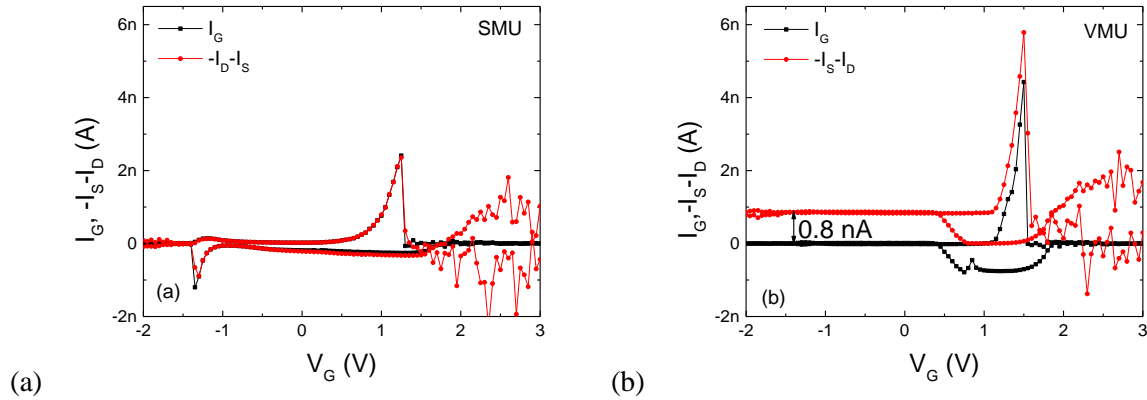
(a)

(b)

Figure III.5: Gate current and the opposite of the sum of drain and source currents vs. gate bias. Body potential measured with SMU (a) or VMU (b). A leakage current of 0.8nA is observed for VMU measurements. 3 probe measurement, V_D=0.1V, V_G step 50mV, P=100g. t_{Si}=88nm, t_{BOX} = 145nm.

As required by the HP4155 manual for high impedance DUTs, this measurement setup was further validated by comparing the potential obtained under a zero current condition (I=0A) and a very small (I=1pA) current imposed through the SMU used to measure V_B. The values obtained for the body potential were perfectly matched, which allowed us to conclude that the correct method to measure the body potential is to use a SMU in a zero current condition (Figure III.6). Additionally, the input impedance is $\geq 10^{15}\Omega$ for the SMU and $\geq 1G\Omega$ for the VMU, which confirms that the SMU are more appropriate for V_B measurements.
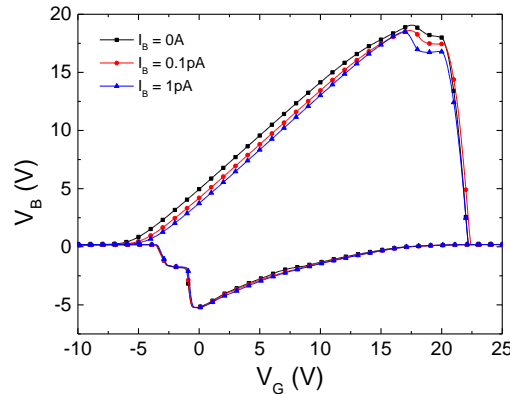
Figure III.6: Body potential versus gate voltage traced for different current conditions applied to the body potential measuring probe. V_D=0.1V, V_G step 100mV, P=100g. t_{Si} = 12nm, t_{BOX} = 145nm.

b. Relationship between and significance of the measured parameters

Using the method described in the previous section, we realized the measurement of the three main parameters namely the drain current (I_D), the body potential (V_B) and the gate current (I_G). The drain current indicates the charge state of the silicon film (inversion, accumulation or depletion), the body potential is the desired parameter and the gate current shows the displacement current allowing the formation of the inversion/accumulation channels. Figure III.7 presents those three main parameters for different sweeping directions of the gate bias – from accumulation to inversion (Forward) and from inversion to accumulation (Reverse). The body potential probe stands halfway between the source and the drain. According to the voltage divider bridge principle, in the accumulation and in the inversion regimes, the value of V_B is equal to approximately half of V_D.

The body potential variation takes place in the depletion region, where the drain current is negligible and where the transition from a channel of holes to a channel of electrons (or the opposite) is imposed by the V_G variation. When the gate bias is scanned from accumulation to inversion (Figure III.7a), the body potential increases linearly, following V_G, and then sharply decreases when the inversion channel begins to form.

An equivalent response can be observed when the gate is scanned from inversion to accumulation (Figure III.7b). However, due to the fact that the sweeping direction is opposite compared to the previous case, the body potential has negative values. The polarity change observed for the I_G peak is associated to the different signs of the carriers involved in these two cases. Note additionally that the I_D values in this region are negative (empty black squares) or positive (filled black squares) depending on the sweeping direction.

Figure III.7: Drain current, body potential and gate current vs. gate voltage sweep from accumulation to inversion (a) and from inversion to accumulation (b). All curves were measured simultaneously. 3 probe measurement, $V_D=0.1V$, step 100mV, P=100g. t_{Si} = 88nm, t_{BOX} = 145nm.

The drain current, body potential and gate current characteristics were also plotted for a 12nm thick silicon film (Figure III.8). As observed in chapter 2, the flat-band and the threshold voltages have larger values (in absolute value) for thinner silicon films. This means that the depletion regime is more spread. Hence, as the slope of the body potential is fairly affected by the film thickness, the body potential can reach higher values as it sweeps through a larger V_G range.
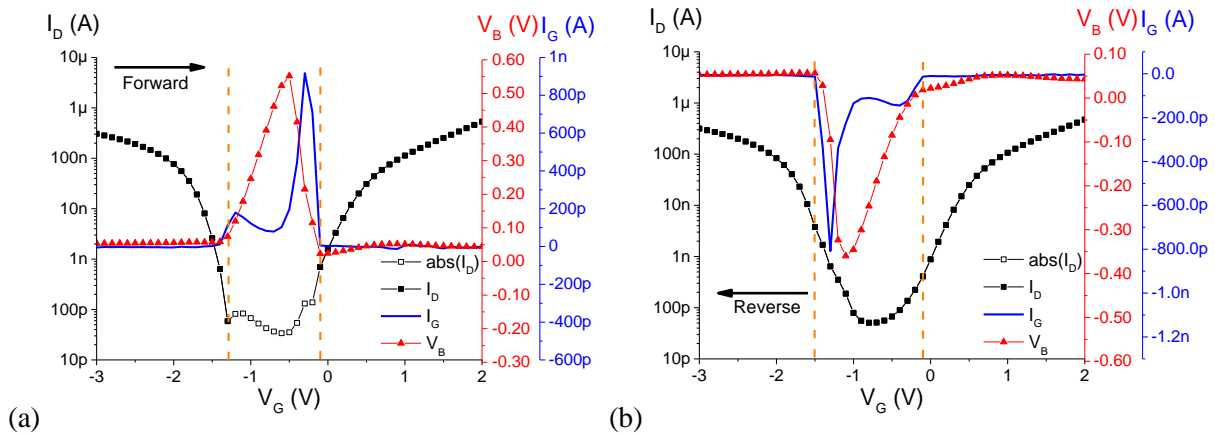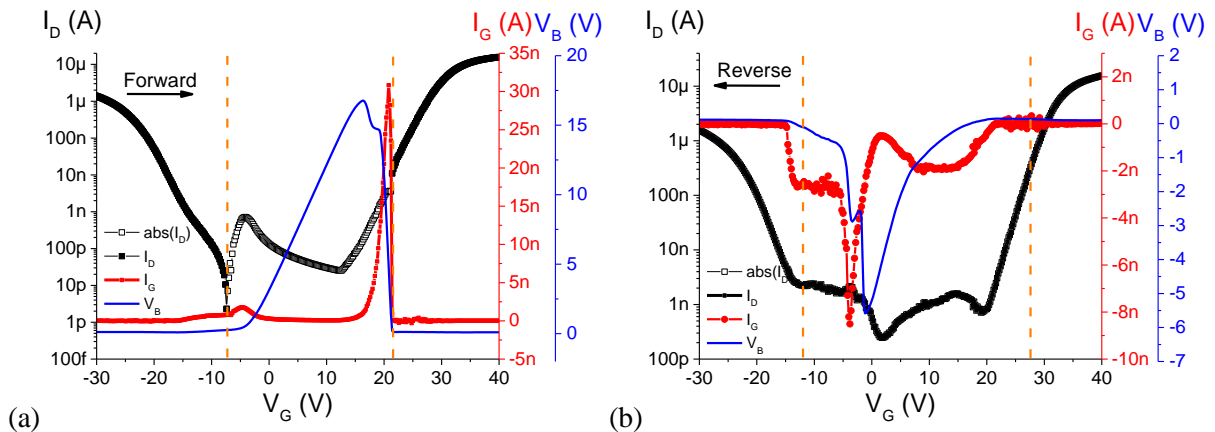

Figure III.8: Drain current, body potential and gate current vs. gate voltage sweep from accumulation to inversion. (a) and from inversion to accumulation (b). All curves were measured simultaneously. 3 probe measurement, $V_D=0.1V$, V_G step 100mV, P=100g. t_{Si} = 12nm, t_{BOX} = 145nm.

Significant variations of V_B are associated with corresponding variations of I_G. This particular behaviour appears when switching from accumulation to inversion and vice versa. An evidence that the I_G peak is related to the variations of V_B is provided by the derivative of V_B with respect to V_G (Figure III.9a and b). The dV_B/dV_G curve follows the same trend as I_G regarding the peak. The direct relationship between the out-of-equilibrium body potential and the formation of the accumulation/inversion layer is thus confirmed. These terms are related via a capacitance coefficient (C in equation (III.1)), as in [5]:

$$\frac{I_G}{C} = \frac{\Delta(V_G - V_B)}{\Delta t} \Leftrightarrow \frac{\Delta V_B}{\Delta V_G} = 1 - \frac{I_G}{C} \cdot \frac{\Delta t}{\Delta V_G} \qquad \text{(III.1)}$$

(a)   (b)
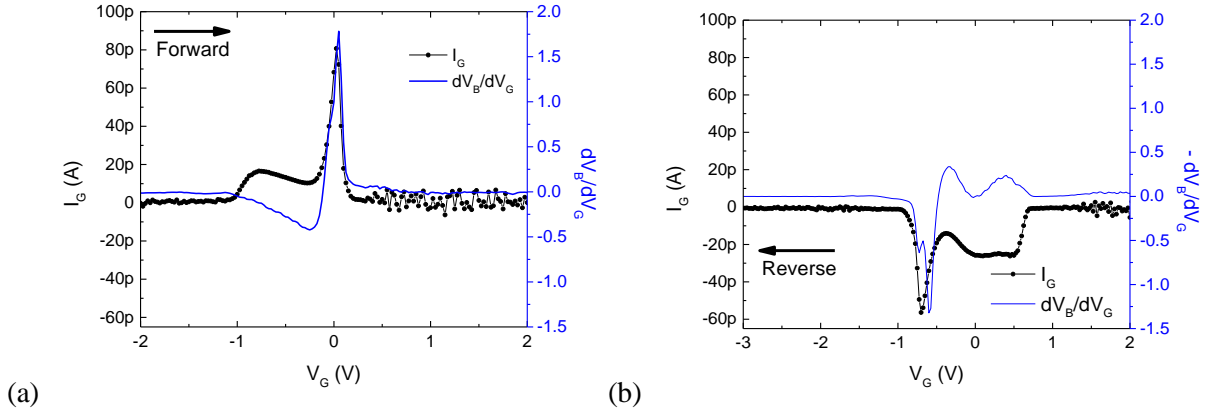
Figure III.9: Gate current and dV_B/dV_G vs. gate voltage sweep from accumulation to inversion (a) and from inversion to accumulation (b). The two peaks correspond in both cases, which probes the direct connection between V_B and I_G. 3 probe measurement, V_D=0.1V, step 25mV, P=100g. t_{Si} = 88nm, t_{BOX}=145nm.

The out-of-equilibrium body potential is the consequence of the time needed to evacuate the excess of carriers out of the body in the SOI-based devices. Besides the direct relationship with I_G, equation (III.1) shows that V_B is also time dependant, in other words it depends on the variation speed of the V_G sweep. In Figure III.10a and Figure III.10b, the transient behaviour of V_B (V_G) and I_G (V_G) are experienced with different measurement steps. In this way, the ratio between the measurement times is thus approximately inversely proportional to the ratio between the steps. It can be observed that faster sweeps (i.e. with a longer measurement step) induce higher peaks of V_B as well as I_G. This reflects the time dependant characteristics of the body potential and highlights its out-of-equilibrium trait.

(a)   (b)

Figure III.10: Body potential vs. gate voltage (a) and gate current vs. gate voltage (b) for different measurement steps. Faster sweeps (higher measurement step) induce higher values of both V_B and I_G. 3 probe measurement, V_D=0.1V, P=100g. t_{Si} = 88nm, t_{BOX} = 145nm.

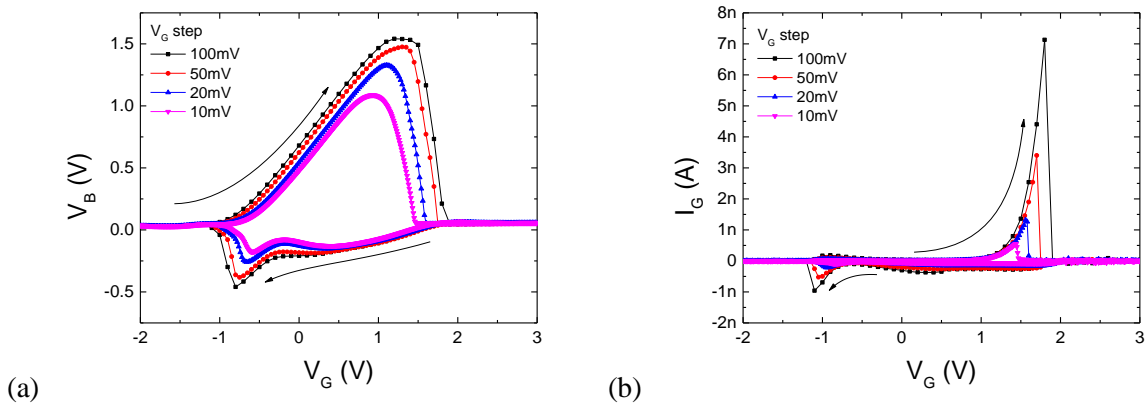The I_G peak occurs just before the onset of the electron channel (forward sweeping direction) or the hole channel (reverse sweeping direction) as evidenced in Figure III.7 by the I_D current. Consequently, I_G in this region is probably a displacement current responsible for the charge/discharge of the BOX capacitance. In order to verify this statement, the total charge needed for equilibrium should always be the same regardless of the V_G scanning dynamic. The injected charge (Q_G) can be calculated by integrating I_G over time:

$$Q_G = \int I_G \cdot dt \qquad \text{(III.2)}$$

As the time is a parameter that is not directly available for these measurements, the gate bias had to be introduced in the calculation:

$$Q_G = \int (I_G \cdot dV_G) \cdot \left(\frac{dt}{dV_G}\right) = \left(\int I_G \cdot dV_G\right) \cdot \left(\frac{dt}{dV_G}\right) = (area\ under\ curve) \cdot \left(\frac{1}{step\ size}\right) \qquad \text{(III.3)}$$

The $\frac{dt}{dV_G}$ term is inversely proportional with the measurement V_G step, which is constant for a given experiment. I_G can then be integrated over V_G in the 0V to 2V interval. The total charge injected needed to charge the BOX capacitance when switching from accumulation to inversion should always be the same independently of the scanning speed (Q_G must be the same for all the curves in Figure III.10b). The approximate measurement time is calculated using the $\frac{dt}{dV_G}$ term (inversely proportional to the measurement step) and is presented in Table III.1 as a ratio with respect to the 10mV curve (e.g. the measurement time of the 100mV step curve is a tenth of the measurement time of the 10mV curve). Column 3 presents the integral $\int I_G \cdot dV_G$ over the [0V; 2V] interval. This quantity was also normalized with respect to the 10mV curve in column 4. This amount of charges (Q_G), as a ratio with respect to a reference, was then calculated as the product between the relative measurement time with respect to the 10mV curve (column 2) and the relative value of the integral, also with respect to the 10mV curve (column 4). The obtained values are consistently close to 1 (column 5), with the exception of the 100mV case, which can be explained by its low resolution (greater distance between measuring points). This confirms that the I_G current peak corresponds to a displacement current. It is worth noting that this displacement current is probably limited by the charge at the silicon film-BOX interface and not by the bulk substrate. This is mainly due to a lower value of the substrate resistance (approximately 3Ω for a 5x5mm² die, a 575µm thick silicon mechanical substrate and a silicon resistivity of 13.6 Ω·cm) compared to the series resistance between the probes and the silicon film (in the order of 10^4Ω in the inversion regime and 10^5Ω in the accumulation regime as extracted from I_D-V_D measurements - Figure II.6 in chapter 2).

Table III.1: Values following the integration of I_G over V_G for different measurement steps, using experimental data from

Figure III.10b.

Measurement step	Approximate measurement time ratio (/10mV)	Integration (A·V) [0V;2V]	Integration ratio (/10mV) [0V;2V]	Q_G (a.u.) [0V;2V]
10mV	1	$1.38*10^{-10}$	1	1.00
20mV	0.5	$2.86*10^{-10}$	2.07	1.04
50mV	0.2	$6.99*10^{-10}$	5.07	1.01
100mV	0.1	$17.4*10^{-10}$	12.6	1.26

As previously mentioned, in the out-of-equilibrium region, the body potential follows the behaviour of the gate bias, and this regardless of the starting point of the measurement (Figure III.11 a to d). When starting the measurement in the depletion region, without a hold time (time imposed for the settlement of the initial equilibrium conditions of the measurement), the body potential directly follows the gate bias (Figure III.11 a and c). The return to equilibrium (when V_B drops), is not modified significantly, which is confirmed by the unchanged I_G peak (Figure III.11 b and d).
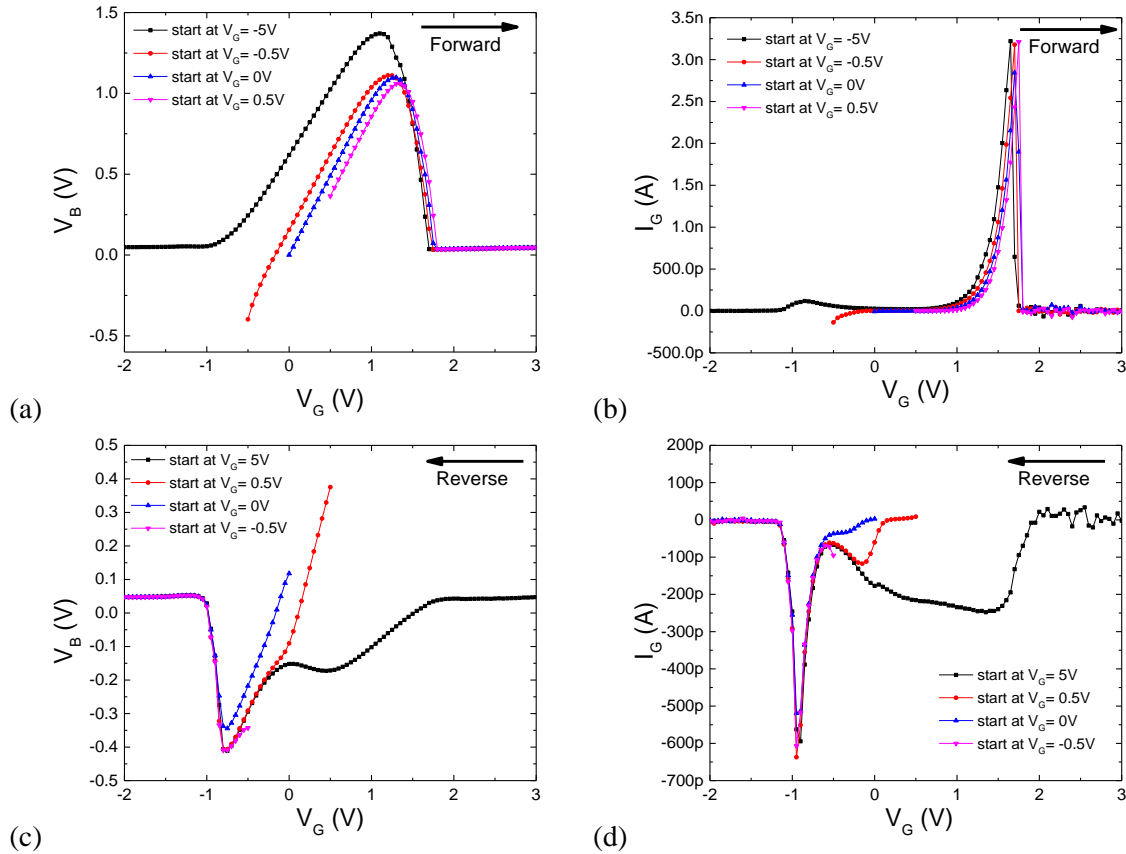
Figure III.11: Body potential vs. gate voltage (a) and (c) and gate current vs. gate voltage (b) and (d) for different starting points and for different sweeping directions. The body potential follows the gate bias in the depletion region. 3 probe measurement, $V_D=0.1V$, V_G step 50mV, P=100g, hold time = 0s. $t_{Si} = 88nm$, $t_{BOX} = 145nm$.

c. Influence of the measurements setup on the body potential

The **drain probe usefulness** is obvious for I_D measurement, but is its presence mandatory for measuring the body potential only? To answer this question, the body potential (Figure III.12a) and the gate current (Figure III.12b) are plotted against the gate voltage for three different setups: with three probes and V_D equal to 0.1V or 0V or with two probes only (no drain probe). It can be noticed that the absence of the drain probe only results in a slight increase of the body potential (as well as the gate current peak). Indeed, the drain probe, when connected and biased, helps the evacuation/injection of carriers in the film (during the accumulation or the inversion regime).

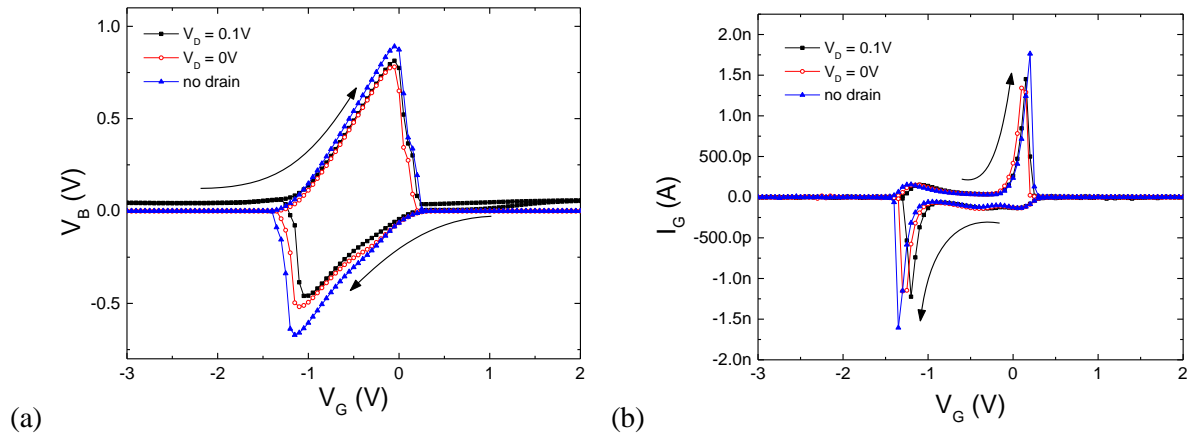(a)   (b)

Figure III.12: Body potential vs. gate voltage (a) and gate current vs. gate voltage (b) for different drain configurations. 3 probe versus 2 probe measurement. Step 50mV, P=100g. t_{Si} = 88nm, t_{BOX} = 145nm.

In the Ψ-MOSFET characterization, it is known that the I_D measurements are affected by the **distance between the probes** [12]. The influence of the probe distance on V_B was also investigated. As illustrated in Figure III.13a, V_B has a slightly lower value (approximately 0.1V, corresponding to 11% of the maximum value), when the distance between the two probes diminished. Due to the fact that the reference probe is grounded, a small potential drop around the source probe can be expected due to the equipotential lines around the grounded source probe. The same response can be observed for the I_G peak, as the two are related.

(a)   (b)
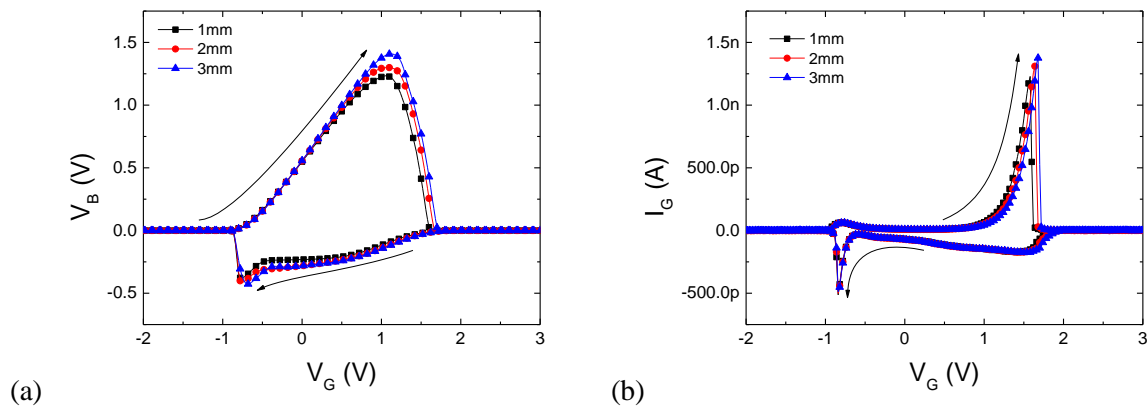
Figure III.13: Body potential vs. gate voltage characteristics (a) and gate current vs. gate voltage characteristics (b). Both are slightly higher for a shorter distance between the probes. 2 probe measurement, step 50mV, P=100g. t_{Si} = 88nm, t_{BOX} = 145nm.

The effect of the **position of the probes** was also investigated. In the case of a drain current measurement, it directly impacts the intensity of the current due to a change of the geometrical factor (see Figure III.10 in chapter 2) [13]. The body potential measurement probe and the reference probe were placed in different positions of the Ψ-MOSFET island area: in the centre, on the edge and in the corner (Figure III.14a). The measurements show no change in either V_B or I_G characteristics (Figure III.14b).

(a)   (b)
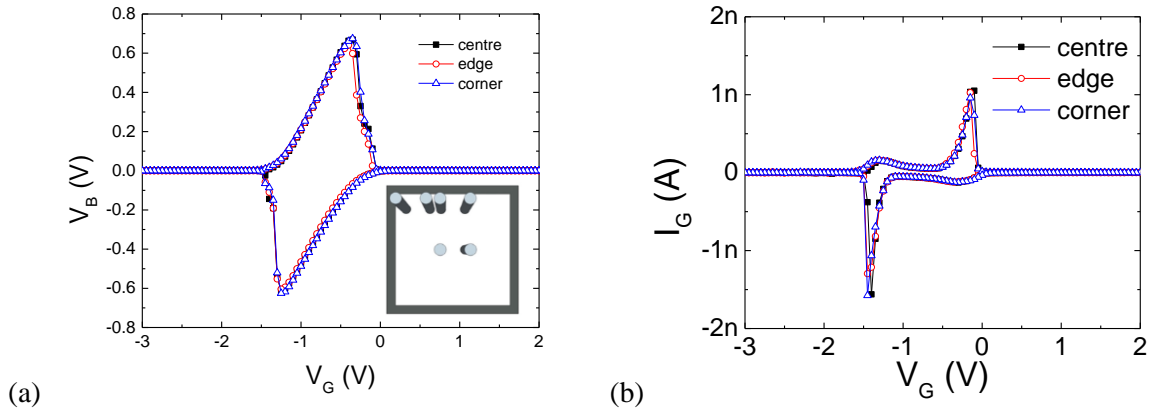
Figure III.14: body potential vs. gate voltage characteristics for different positions on the SOI surface with probe position in the insert (a), and gate current vs. gate voltage characteristics for different positions on the SOI surface (b). 2 probe measurement, step 50mV, P=100g. $t_{Si} = 88nm$, $t_{BOX} = 145nm$.

Those characteristics are very advantageous in view of the biochemical sensing applications, because it simplifies the electrical setup with two probes only and it allows the free positioning of the probes. This would enable the positioning of the molecules to be detected in the center of the device, while the measurement can be carried out with the probes placed on the edges of the Ψ-MOSFET (Figure III.15).
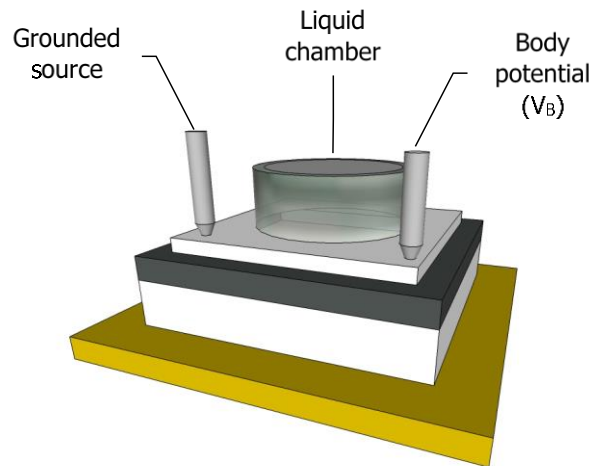

Figure III.15: Schematic of the possible setup for biochemical sensing with a liquid chamber in the centre of the SOI die.

In the Ψ-MOSEFT configuration, the drain current is known to be highly dependent on the **pressure of the probes** [14]. It is the stability of the V_B sensing with respect to the applied pressure on the probes which will be subsequently validated. Figure III.16 presents the results for different pressures applied to the body potential measuring probe while the reference probe is maintained at 100g (Figure III.16 a and b) or to the reference electrode while the body potential probe is maintained at 100g (Figure III.16 c and d). In all instances, the values of V_B as well as I_G are very similar and a small variation of less than 100mV can be observed only in the region where V_B reaches equilibrium (approximately half of V_D). This proves that the body potential measurements are not influenced by the pressure applied on the probes.

All of the results in this section lead to the conclusion that the body potential measurements in the "Ψ-MOSEFT 2 probe configuration" provide a highly reliable sensing method due to its invariability with respect to the position, the distance and the pressure applied on the probes. The ultimate goal of the out-of-equilibrium body potential measurements is their implementation in the biochemical sensing field. Experimental characteristics showed a great versatility of the measurements, allowing us to obtain the same results independently of the position or the pressure applied on the probes.
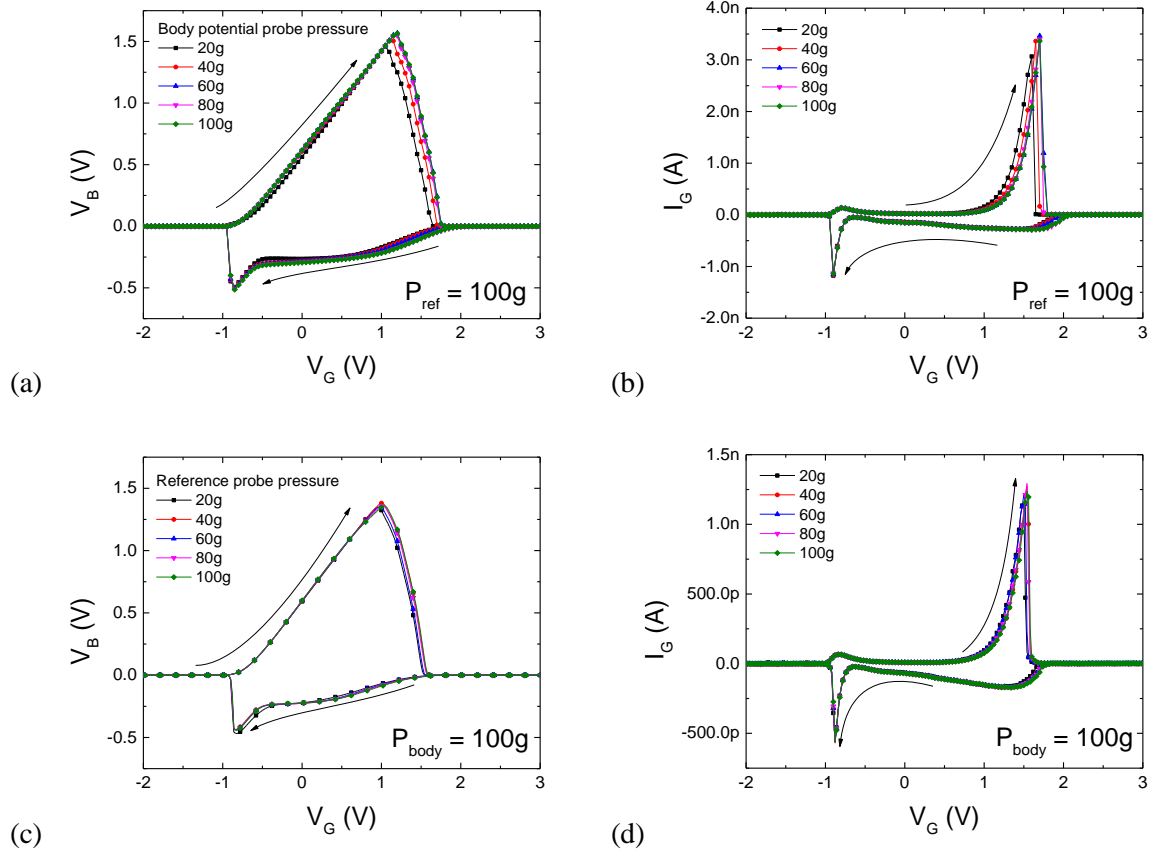
Figure III.16: The influence of the pressure on the body potential probe (a) and (b), on the reference probe (c) and (d). The differences observed are negligible. 2 probe measurement, step 50mV. t_{Si} = 88nm, t_{BOX} = 145nm.

3.3. Simulation of the body potential in Ψ-MOSFET

In order to study the feasibility of the body potential method for biosensing applications, we reproduced the behaviour of the Ψ-MOSFET through simulations. In the first part of this section, we will establish a contact structure capable of replicating the dual conduction of the Ψ-MOSFET (i.e. with electrons and holes). The second part will present the appearance of the out-of-equilibrium body potential and the influence of charges added at the top surface.

a. Simulation of contact behaviour

As already mentioned, out-of-equilibrium body potential in the Ψ-MOSFET configuration is highly dependent on contact behaviour. Therefore, in order to simulate the out-of-equilibrium state, we will try to reproduce the electrical behaviour of the metal probe-silicon layer contacts in static conditions.

The implementation of the Ψ-MOSFET configuration in a TCAD environment has two main issues:

(1) Metal on lowly doped silicon contacts presents a Schottky behaviour in simulation, which is not in accordance with the experimental data;

(2) Creating a structure for which the contacts would allow the injection of both electrons and holes in the silicon film.

Our study began with a simple structure which would allow us to get an insight on how the conduction of a metal-silicon interface can be modified in order to allow the conduction of both types of carriers. We chose a 1µm long by 100nm thick 2D silicon section, doped with boron at a concentration of 10^{15} cm^{-3} (Figure III.17). Two metal contacts were added on each side. One of them was grounded and the other was swept from -5V to 5V.

Figure III.17: Structure used to study metal-semiconductor contacts.

Multiple conditions and conduction mechanisms were activated at the interface between metal and semiconductor with the goal of finding one which would show a significant increase in the current. This would indicate a behavioural change which could allow a conduction using both types of carriers (electrons and holes).

First, even though the structure was built from two metallic contacts on silicon, the Schottky behaviour must be declared. The ohmic contact has a linear behaviour at the origin, then saturates due to the high field saturation condition (Figure III.18). On the other hand, the Schottky contact only increases from a certain threshold voltage.

The influence of the following conduction mechanisms was studied in order to determine one which substantially modifies the amount of current flow through the structure:

- Thermionic – thermally induced flow of charges over a potential/energy barrier;
- Band to band tunnelling (Band2band) – conduction between the valence band and the conduction band of two separate regions;
- Shockley-Read-Hall Recombination – exchange of carriers between the conduction band and the valence band through deep defect levels in the band gap;
- Barrier lowering – accounts for image force, tunnelling and dipole effects at a metal-semiconductor interface;
- A combination of the above mentioned mechanisms.

Those mechanisms were activated one by one or collectively, but, unfortunately, none had an influence on the applied current (Figure III.18) Therefore any metallic contact boundary conditions allowed to provide viable assumption about what would be at the origin of a metal-semiconductor contact that would provide a conduction realized by holes, the measured current being exclusively composed of electrons. However, in the Ψ-MOSFET, the back gate affects the carrier density in the silicon film, which might also influence the contact behaviour. In the following part we will directly simulate the Ψ-MOSFET structure.
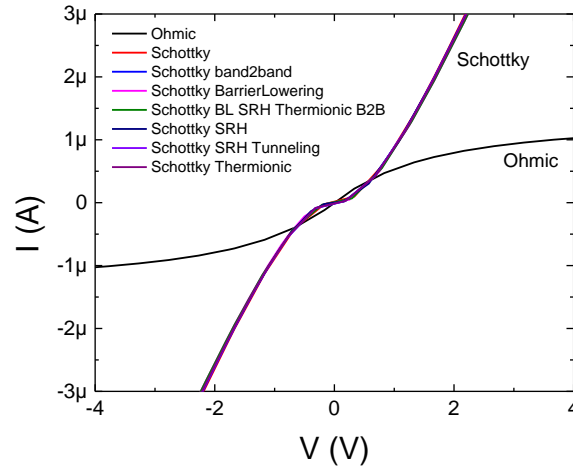
Figure III.18: Current versus potential characteristics for metal-silicon contacts structure.

b. Simulation of I_D - V_G characteristics in Ψ-MOSFET

The Ψ-MOSFET structure was replicated using an 88nm thick silicon layer on top of a 145nm silicon dioxide buried oxide (Figure III.19). The length was scaled down by a factor of 100 (to 10µm) in order to have a dense mesh and faster calculations. Two metal contacts were added on the left- and right-hand sides of the structure in order to replicate the metallic probes, the source being grounded and the drain at 0.1V in order to replicate the experimental setup. The gate contact was directly applied to the BOX layer, neglecting the small potential drop in the silicon bulk layer [15].
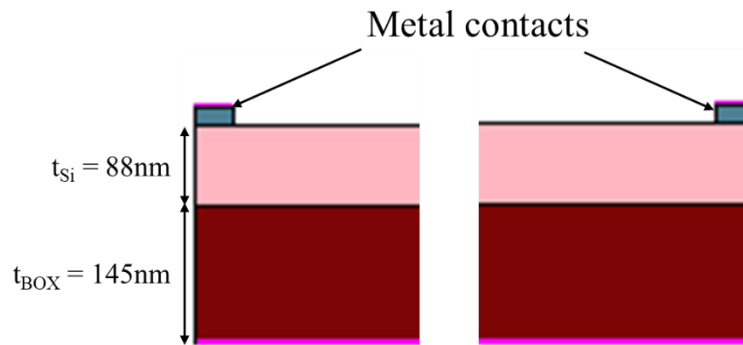
Figure III.19: Simulated structure of the Ψ-MOSFET configuration. Length scaled down to 10µm.

The following conduction mechanisms were activated in order to investigate their influence on the conduction:

- Band to band tunnelling – conduction between the valence band and the conduction band of two separate regions;
- Nonlocal Barrier tunnelling – barrier tunnelling with a nonlocal mesh;
- Thermionic – thermally induced flow of charges over a potential/energy barrier;
- Trap assisted tunnelling - defects give rise to tunnelling processes.

As represented in Figure III.20, none of those mechanisms had any influence on the electrical behaviour of the Ψ-MOSFET. An important drain current was only obtained in inversion, but no current in present in the accumulation regime (V_G<0V).
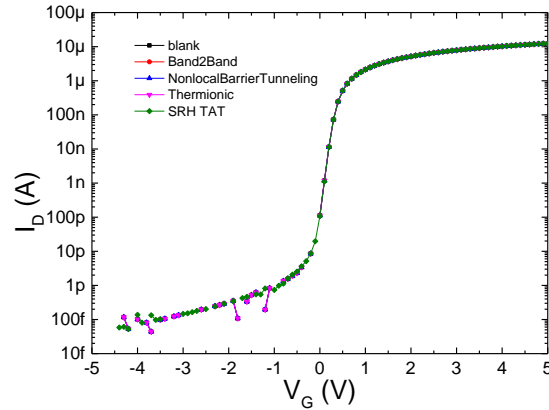
Figure III.20: Drain current versus gate voltage characteristics in the simulated Ψ-MOSFET configuration, with different conduction mechanisms activated.

As our attempts did not provide any good results, we concentrated on the intrinsic properties of the metallic contacts by adjusting the work function. Furthermore, in order to emulate the real experimental setup, the metallic regions were placed inside the silicon film (Figure III.21a).

Indeed, in this configuration, the conduction can be switched between holes and electrons by changing the work function of the metal contacts (Figure III.21b). As observed from the band diagrams (Figure III.21c and Figure III.21d), the current between source and drain contacts is issued from a drift diffusion mechanism as other mechanisms did not allow charge transfer. Due to the adjustment of the work function, the energy bands at contact interfaces are favourable to electron (Wf = 4.25 eV) or to hole (Wf = 5eV) conduction. Those values are able to cover the two ways of conduction, knowing that the silicon doped at 10^{15} cm^{-3} has a work function of 4.73 eV.
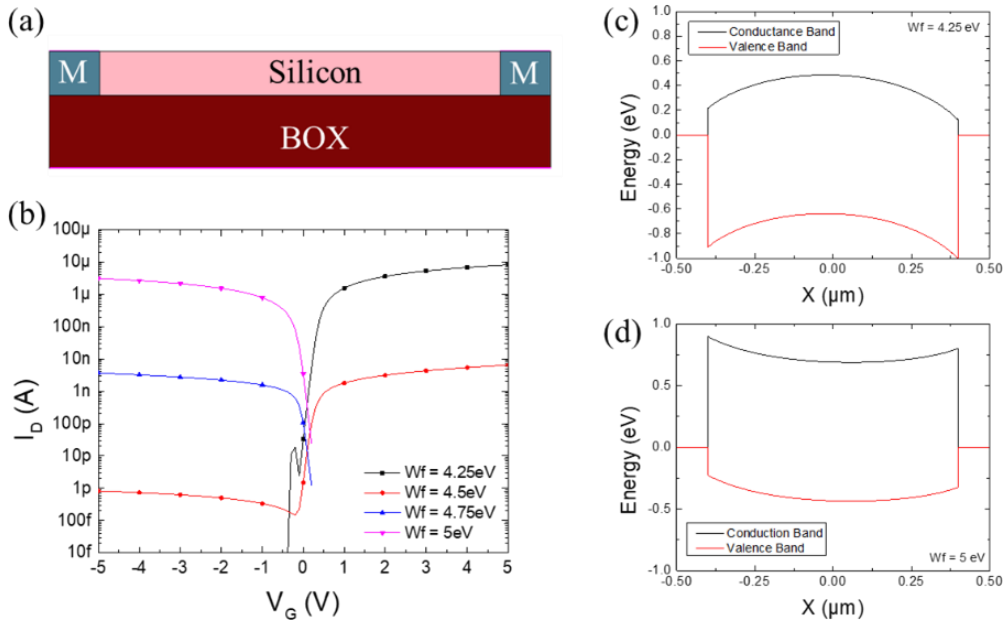
Figure III.21: Schematic of simulated Ψ-MOSFET structure with metal contacts inside the silicon film (a). Drain current versus gate voltage for different metal contact workfunctions (b). Band diagram for contact workfunctions of 4.25eV (c) and 5eV (d).

The work function adjustment allows the simulation for both types of channels, but in different structures. In order to put together the 2 behaviours in only one structure, we proposed a new configuration with two different metallic zones as contacts. A metal-like material named

GatePolySilicon in the simulation software was added below the main contact (Figure III.22a). This is generally used on top of the transistor gate and has metallic properties. In order to recreate the behaviour of Si-II, all the parameters were kept by default with the exception of the work function. In the two tested configurations, GatePolySilicon was parametrized so that it had both a greater (5.5eV) and a lower (4eV) work function which was equally distanced from the one of the silicon film (4.73eV – for a doping concentration of 10^{15}cm^{-3}). This structure allows having a conduction realized by either electrons or holes in the silicon film, although the simulated current on the contacts is exclusively made of electrons (Figure III.22b).

(a)   (b)
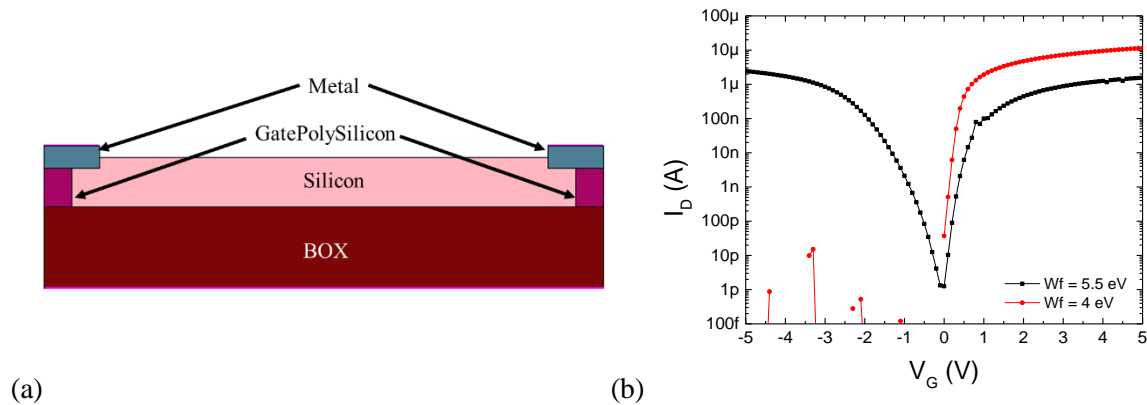
Figure III.22: Simulated structure of the Ψ-MOSFET with two metal-like areas under the probes (a). Drain current versus gate voltage electrical characteristics for different work functions of the metal-like area (b).

c.   Body potential simulation

In order to simulate the body potential measurements, we used the simplified two probe setup described in the previous section. One contact was therefore grounded and for the other, we imposed a zero current condition. The simulated body potential is equal to zero for the whole range of gate potential (Figure III.23). Due to the fact that in metals the concentration of carriers is much higher than in silicon, the metallic contacts proposed in the previous section would not be able to measure the body potential.
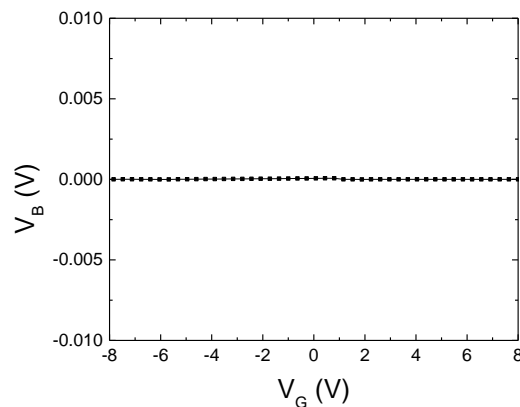
Figure III.23: Body potential versus gate bias for metal contacts.

The two metallic regions were therefore replaced by an N$^+$ and a P$^+$ doped regions (at a concentration of 10^{20} cm^{-3}) which would allow electron and hole conduction respectively. Their lengths are 50nm for the P$^+$ region and 100nm for the N$^+$ region (Figure III.24).
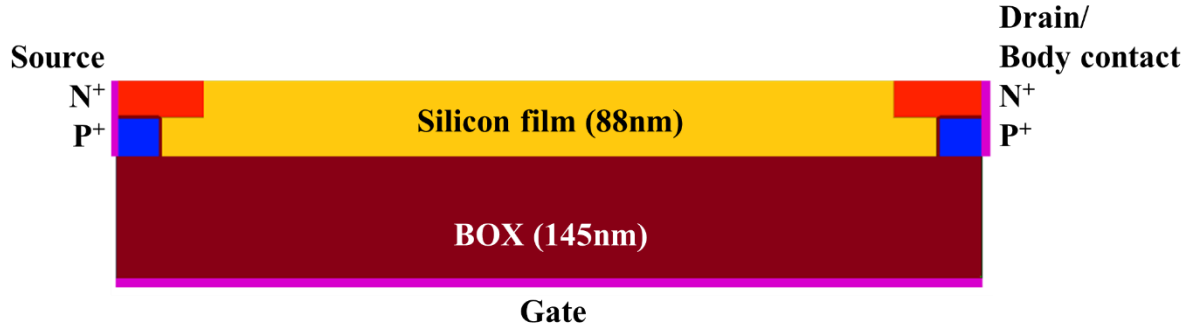
Figure III.24: Simulated structure used to replicate body potential measurements in the Ψ-MOSFET configuration. Composed of two layers corresponding to the buried oxide and the silicon film. Contacts are made up of two N⁺ and P⁺ doped regions.

The drain current and gate potential were simulated under the same conditions as for the experimental measurements. One of the contacts would be used as a grounded source and the other used as either a drain contact onto which a $V_D = 0.1V$ condition was imposed or a body potential contact onto which a zero current condition was imposed. The gate bias was swept between -8V and +8V, replicating exactly the experimental setup.

Due to the structure of the contacts which recovers electrons and holes on different places inside the silicon film, the drain current curves are comparable, but not similar to the experimental ones (Figure III.25a). For the same reason, the body potential curves are also similar, but have different amplitudes depending on the sweeping direction (Figure III.25b).

(a)

(b)
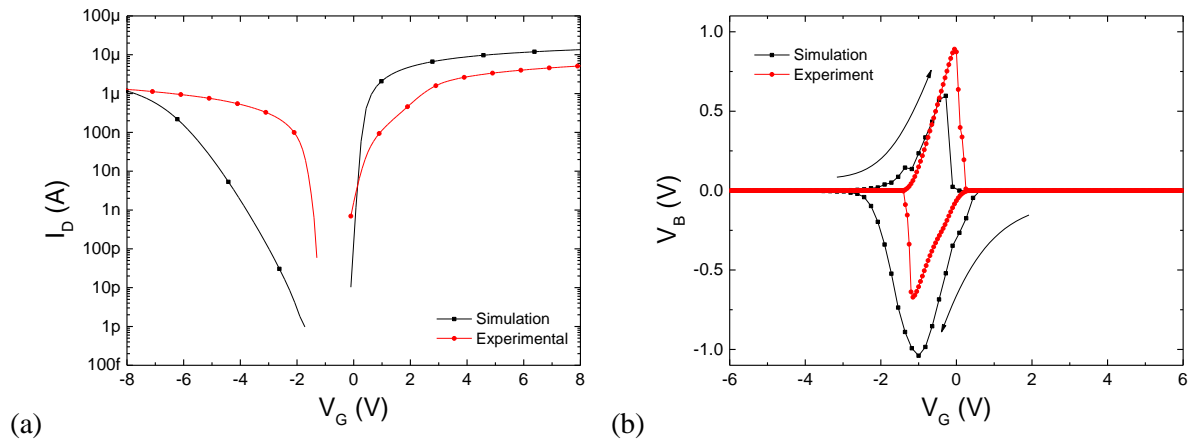
Figure III.25: Simulated drain current (a) and body potential (b) versus gate bias.

d.   Influence of charges added on the top surface

Using this structure, we tried to reproduce the response of the structure functionalized with charged molecules of different polarities and concentrations. In this sense, the structure presented in Figure III.24 was modified by adding a 3nm thick silicon dioxide layer in order to replicate the native/passivation oxide on top of the silicon film and a layer of charges imposed directly by a contact on top of the oxide (Figure III.26).
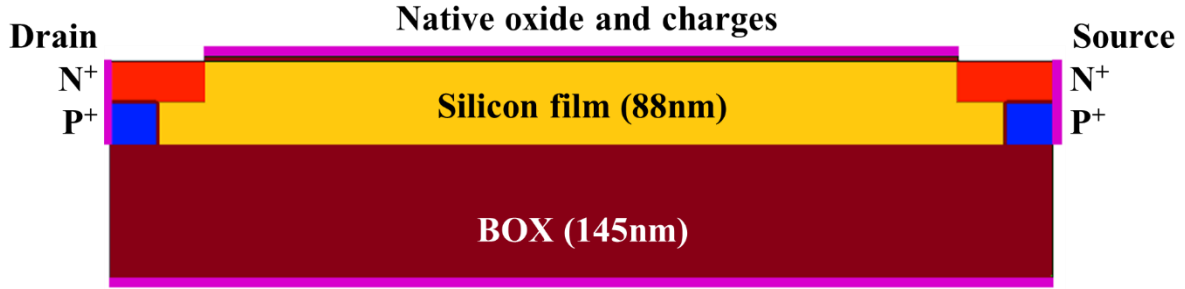
Figure III.26: Simulated structure used to replicate body potential measurements in the Ψ-MOSFET configuration for different charges added on top of the silicon film.

Using the same methodology as before, we traced the simulated drain current and body potential versus the gate voltage curves. The former shows a negative shift as the added charge increases from negative to positive (Figure III.27a). The shift is significantly lower in the accumulation than in inversion due to the structure of the contacts which recover the hole current directly from the silicon film – BOX interface and the electrons closer to the top oxide layer.

In the case of the body potential, it can be observed a negative shift for the positive added charges and a positive shift for the negative added charges (Figure III.27b) as expected from the classical MOSFET models [1]. Due to the fact that the shifts in drain current are lower in the accumulation region, the parts of the curves in accumulation in inversion are getting closer. The body potential peak is lower as the charge becomes more positive. The sensitivity obtained is approximately $400mV/10^{-16}C$, determined by measuring the distance between the maximum values of V_B. This allows us to conclude that the body potential measurement is a reliable sensing method which can be used to detect charged molecules added on top of the device.

(a) (b)
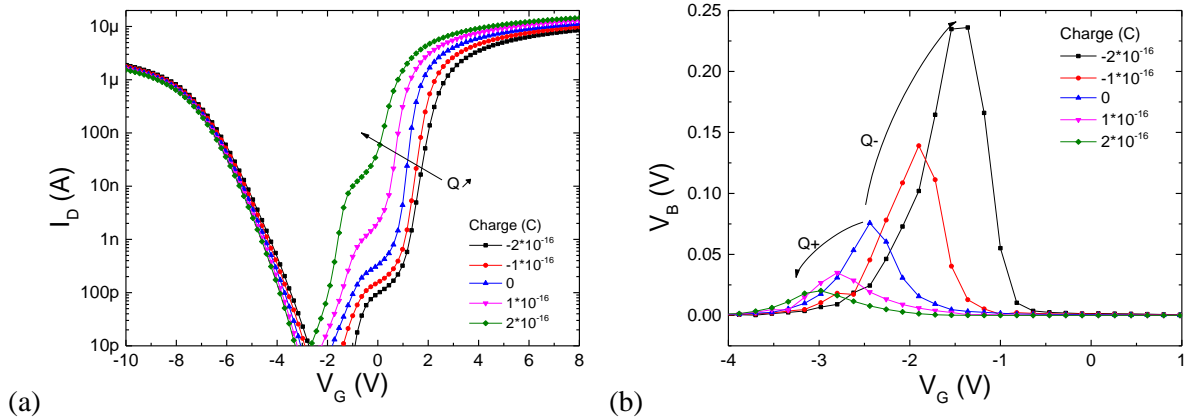
Figure III.27: Simulated drain current (a) and body potential (b) versus gate bias for different charge states added on top of the silicon film.

Conclusion

This chapter assesses the out-of-equilibrium body potential measurements applied to the Ψ-MOSFET configuration as a mean for sensor reading paradigm. This structure is very convenient for the following reasons: (1) it allows the deposition of charged molecules directly on the top surface, avoiding the metallic contact layers present in the case of a transistor, (2) it has a high detection surface (5x5 mm²) and (3) it can be fabricated using only two fabrication steps.

In the first part, the correspondence between and the significance of the main parameters was determined. It was proven that in the depletion region, where I_D is negligible, V_B is directly related to

V_G and with the state of the inversion/accumulation channel as described by the displacement current represented through the gate current peak. The out-of-equilibrium nature of the body potential was also exposed through measurements with different gate voltage sweeping speeds.

Subsequently, a simplified version using only two probes was established and its advantages in terms of stability with respect to the position, the distance and the applied pressure on the probes were illustrated.

The measured experimental behaviour was then replicated fairly accurately through simulation. The simulation of the Ψ-MOSFET contacts was realized by mimicking the silicon phase change region under the probe using a metal-like material. This structure is based on a plausible explanation that allows both electron and hole conduction.

For body potential simulations, the contact structure was modified by using two highly doped N and P regions instead of metals. At the end, the proof of concept was realized through simulations which proved the sensitivity of this type of measurement to the added charges on the top surface.

Bibliography

[1]   C. Sorin and S. Li, *Electrical characterization of silicon-on-insulator materials and devices*. Kluwer Academic Publishers, 1995.

[2]   J.-P. Colinge, *Silicon-on-Insulator Technology: Materials to VLSI*. Boston, MA: Springer US, 1997.

[3]   B. Vandana, 'Study of Floating Body Effect in SOI Technology', *Int. J. Mod. Eng. Reseatch*, vol. 3, no. 3, pp. 1817–1824, Jun. 2013.

[4]   S. C. Lin and J. B. Kuo, 'Temperature-dependent kink effect model for partially-depleted SOI NMOS devices', *IEEE Trans. Electron Devices*, vol. 46, no. 1, pp. 254–258, Jan. 1999.

[5]   M. Bawedin, S. Cristoloveanu, D. Flandre, and F. Udrea, 'Dynamic body potential variation in FD SOI MOSFETs operated in deep non-equilibrium regime: Model and applications', *Solid-State Electron.*, vol. 54, no. 2, pp. 104–114, Feb. 2010.

[6]   Hsing-Jen Wann and Chenming Hu, 'A capacitorless DRAM cell on SOI substrate', in *Proceedings of IEEE International Electron Devices Meeting*, Washington, DC, USA, 1993, pp. 635–638.

[7]   M. Bawedin, S. Cristoloveanu, and D. Flandre, 'A Capacitorless 1T-DRAM on SOI Based on Dynamic Coupling and Double-Gate Operation', *IEEE Electron Device Lett.*, vol. 29, no. 7, pp. 795–798, Jul. 2008.

[8]   N. Rodriguez, C. Navarro, F. Gamiz, F. Andrieu, O. Faynot, and S. Cristoloveanu, 'Experimental Demonstration of Capacitorless A2RAM Cells on Silicon-on-Insulator', *IEEE Electron Device Lett.*, vol. 33, no. 12, pp. 1717–1719, Dec. 2012.

[9]   J. Wan, C. Le Royer, A. Zaslavsky, and S. Cristoloveanu, 'A Compact Capacitor-Less High-Speed DRAM Using Field Effect-Controlled Charge Regeneration', *IEEE Electron Device Lett.*, vol. 33, no. 2, pp. 179–181, Feb. 2012.

[10] J. Lacord *et al.*, 'MSDRAM, A2RAM and Z ^{2} -FET performance benchmark for 1T-DRAM applications', in *2018 International Conference on Simulation of Semiconductor Processes and Devices (SISPAD)*, Austin, TX, 2018, pp. 198–201.

[11] Hewlett-Packard Company, 'Semiconductor Parameter Analyzer User's Dictionary Reference'. 1995.

[12] K. Komiya, N. Bresson, S. Sato, S. Cristoloveanu, and Y. Omura, 'Detailed Investigation of Geometrical Factor for Pseudo-MOS Transistor Technique', *IEEE Trans. Electron Devices*, vol. 52, no. 3, pp. 406–412, Mar. 2005.

[13] L. Pirro, I. Ionica, G. Ghibaudo, and S. Cristoloveanu, 'Split-CV for pseudo-MOSFET characterization: Experimental setups and associated parameter extraction methods', in *2014 International Conference on Microelectronic Test Structures (ICMTS)*, Udine, Italy, 2014, pp. 14–19.

[14] I. Ionica, I. Savin, W. Van Den Daele, T. Nguyen, X. Mescot, and S. Cristoloveanu, 'Characterization of silicon-on-insulator films with pseudo-metal-oxide-semiconductor field-effect transistor: Correlation between contact pressure, crater morphology, and series resistance', *Appl. Phys. Lett.*, vol. 94, no. 1, p. 012111, Jan. 2009.

[15] M. Daanoune, A. Kaminski-Cachopo, D. Blanc-Pelissier, and Y. Sayad, 'Extraction of Bulk Lifetime and Surface Recombination Velocity on Thin Layer by Photoluminescence', in *Proceedings of the 28th European Photovoltaic Solar Energy Conference and Exhibition, (EU PVSEC 2013)*, Paris, France, 2013, pp. 2638–2640.

Chapter 4 :

DNA DETECTION USING THE OUT-OF-EQUILIBRIUM BODY POTENTIAL IN THE PSEUDO-MOSFET CONFIGURATION

In this chapter the out-of-equilibrium body potential measured in the Ψ-MOSFET configuration is investigated for detecting DNA molecules. The Ψ-MOSFET electrical parameters are known to be impacted by the state of the top interface and/or surface of the silicon film, especially for thin films. Starting from this observation, it is possible to extend the use of the Ψ-MOSFET to detect electrically charged molecules intentionally deposited on top. In the first part, we review the already existing models and applications. In the second part, we describe our novel method and its applications for DNA detection. Many parameters were investigated to optimize the detection efficiency, such as the silicon film and the buried oxide thicknesses, the functionalization steps and in particular the protocol for DNA attachment.

Table of contents

4.1. Influence of the silicon top surface on the Ψ-MOSFET

In the Ψ-MOSFET, the silicon film covered by native or passivated oxide can be exposed to the influence of the charges added at the top surface by functionalization. The structure of SOI wafers contains three interfaces: (1) the top (free) surface, (2) the interface between the silicon film and the buried oxide and (3) the interface between the buried oxide and the silicon substrate (Figure IV.1). All these interfaces contain a certain density of dangling bonds and thus of traps which modify the electrical properties of the wafer and in particular of the active silicon film.
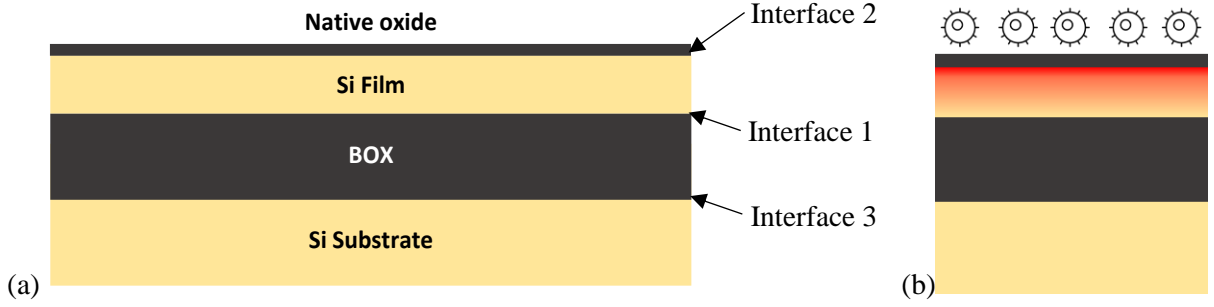
Figure IV.1: Structure of a silicon on insulator wafer and interfaces (a) and schematic of the influence of added charges (charged molecules) on carrier distribution of the active silicon layer (b).

As in classical MOSFETs [1], any charge close to the conduction channel, at the silicon film – BOX interface, shifts the threshold and the flat-band voltages of the pseudo transistor (Figure IV.1b). A particularity of the Ψ-MOSFET is that the charge can be either on the BOX side or at the top surface of the silicon film (interface 1 and 3, respectively). If the film is too thick, the top surface will have no influence. Nevertheless, in the case of the thin silicon film (fully depleted) wafers, the interaction with the top surface can be significant. These effects are reported in the models of the threshold and flat-band voltages briefly described in the followings for the Ψ-MOSFET.

Brief Background. The first models dedicated to thick (larger than 100nm) silicon films [2] did not take into account the state of the top surface. The threshold and the flat-band voltages were calculated using:

$$V_T - V_{FB} \approx 2\Phi_F + \frac{qN_A}{C_{BOX}}t_{Si} + \frac{qN_A}{C_{BOX}} \times 2\Phi_F \qquad \text{(IV.1)}$$

$$V_{FB} \approx \Phi_{ms} - \frac{Q_{BOX}}{C_{BOX}} \qquad \text{(IV.2)}$$

where: Φ_F is the Fermi level in the silicon measured from the midgap level, N_A the doping concentration of the silicon film, C_{BOX} the capacitance of the buried oxide, t_{Si} the thickness of the silicon film, Φ_{MS} the work-function difference between the film and the substrate at equilibrium and Q_{BOX} the fixed charge inside the buried oxide.

The impact of surface states on the electrical characteristics of the Ψ-MOSFET configuration was first observed by comparing passivated (low density of interface states - D_{it}) vs. non-passivated (high D_{it}) wafers for films under 88nm [3]. It was observed that reducing the thickness of the Si film (1) increases the absolute value of the threshold voltage (V_T) and the flat-band voltage (V_{FB}) and (2) the reduction of the two parameters, which is the effect of the passivation ($\Delta V_{FB,T}$ before and after passivation) (Figure IV.2).
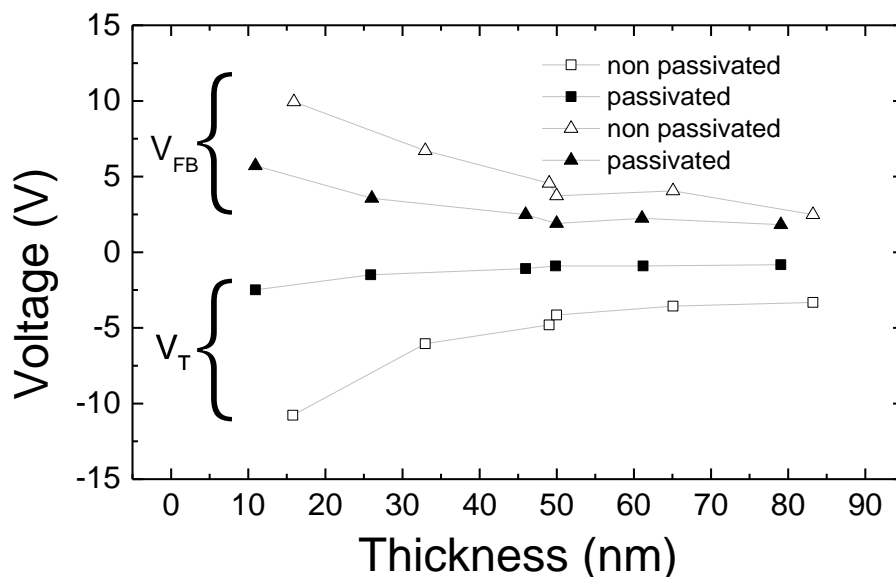
Figure IV.2: Experimental evidence of the impact of the interfaces on the conduction channel. Threshold and flat-band voltages for different silicon film thicknesses. The absolute value of V_T and V_{FB} increases for thinner films and for higher trap density (from non-passivated Si-film).Open symbols for non-passivated films and solid symbols for passivated films. Reproduced from [3]

This behaviour originates from the preparation of the top silicon film and it is not an indication of any degradation of the intrinsic SOI material. The influence of the top surface on the electrical characteristics originates from two mechanisms: (1) the influence of the surface state on the silicon-buried oxide interface by electrostatic coupling and (2) the majority charge carriers (i.e. holes) that flow partly through the bulk of the silicon film due to the higher extension of the accumulation layer [4].

N. Rodriguez et al. investigated the effect of passivation on several films thickness (from 16, 80 and 200 nm), by calculating the mobile charge density as function of the (back) gate voltage V_G, all other parameters being kept constant [5]. The passivated wafer was considered to have the density of states at the interface 1 and 2 equal to $D_{it1} = D_{it2} = 2x10^{11}$ cm^{-2}eV^{-1} and the non-passivated wafer $D_{it1} = 2x10^{11}$ cm^{-2}eV^{-1} and $D_{it2} = 2x10^{13}$ cm^{-2}eV^{-1}. As in Figure IV.3, there is no impact of the top surface on the electrical characteristics for thick Si-film (200 nm). However, when reducing the silicon film thickness (80 nm), the threshold voltage increases, and the impact of the passivation (ΔV_T) cannot be neglected, i.e. the channel-to-surface coupling becomes visible. In the case of ultrathin (16 nm) silicon film, the threshold voltage increases by 2V for a passivated surface and up to 12V for a non-passivated surface. This reflects the sensitivity of thin films to the state of the top surface [6] for which the coupling effect between interfaces is more important.
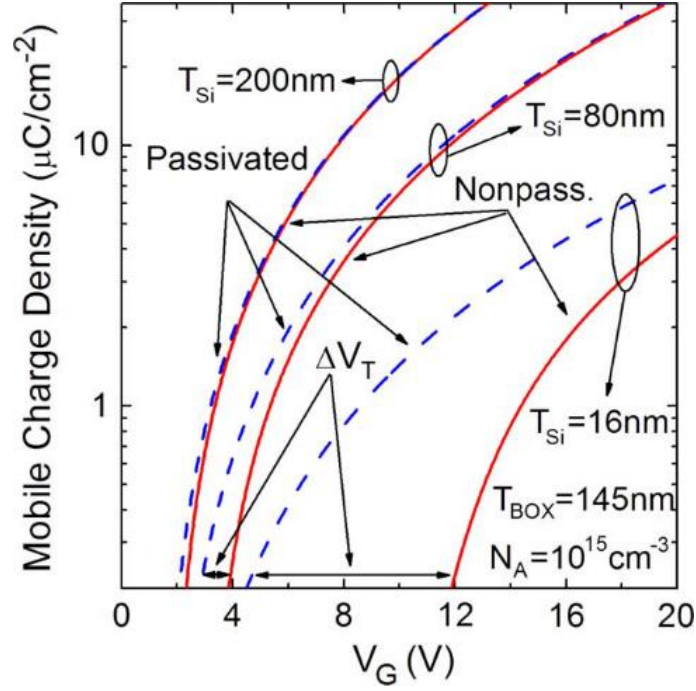
Figure IV.3: Simulated effect of silicon film thickness and interface traps on V_T and V_{FB}. Simulated inversion charge density vs. gate voltage for 16, 80, and 200 nm thick silicon films and for passivated (dash line) and non-passivated (red lines) surfaces. V_T increases when the thickness is smaller, in particular for non-passivated samples. BOX thickness 145 nm. Reproduced [6]

Later models included the coupling effect between the two interfaces of the silicon film and took into consideration the film thickness and the interface states on both sides of the silicon film [3]. The threshold and the flat-band voltages are therefore calculated using:

$$V_T = V_{FB} + \frac{2\Phi_F}{C_{BOX}}\left(C_{BOX} + C_{it1} + \frac{C_{Si}C_{it2}}{C_{Si} + C_{it2}}\right) + \frac{qN_At_{Si}}{2C_{BOX}} \times \left(1 + \frac{C_{Si}}{C_{Si} + C_{it2}}\right) \quad \text{(IV.3)}$$

$$V_{FB} = \Phi_{ms} - \frac{Q_{BOX}}{C_{BOX}} + \frac{2\Psi_1}{C_{BOX}}\left(C_{BOX} + C_{it1} + \frac{C_{Si}C_{it2}}{C_{Si} + C_{it2}}\right) \quad \text{(IV.4)}$$

where: $C_{it1} = q \cdot D_{it1}$, $C_{it2} = q \cdot D_{it2}$ the capacitances corresponding to the traps on interfaces 1 and 2, C_{Si} the silicon film capacitance and Ψ_1 the surface potential at the silicon film/BOX interface (interface 2 from Figure IV.1a).

Due to the uncertainty of several parameters (D_{it1}, D_{it2}, Φ_F and Ψ_1) which need to be fitted, the quantitative comparison with experimental results was difficult. Nonetheless, the trends of the flat-band voltage and the threshold voltage match well with the experimental data. Note again, that for thinner films, the sensitivity to the top surface is well higher, increasing sharply (also shown in

Figure IV.*4*).
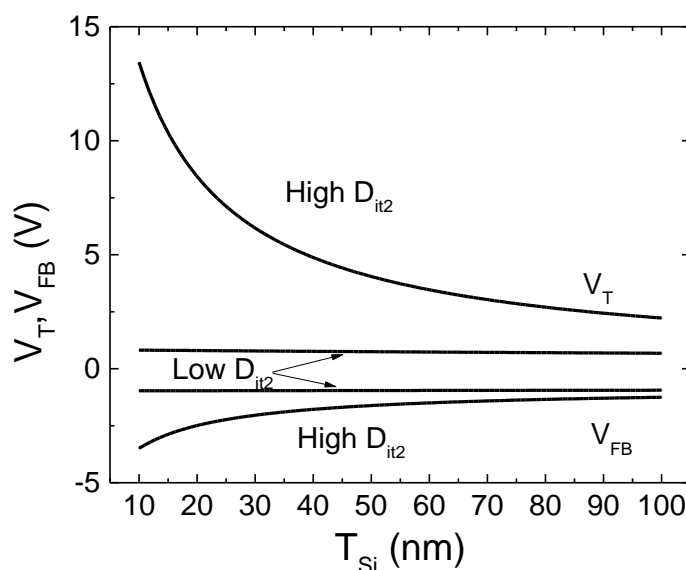
Figure IV.4: Influence of the film thickness and interface traps on V_T and V_{FB}. Threshold and flat band voltage for different film thicknesses and for high and low densities of interface states at the top interface 2 [3].

The later models (in addition of accounting for the state of the top silicon surface) tried to fit the results with the experimental data. As such, by considering different hypothesis for passivated (low D_{it}) and non-passivated (high D_{it}) silicon films, other formulations were proposed [6]. Those models are presented in more detail in Appendix 1. Nevertheless, the influence of the top silicon surface state goes along the same lines and remains enhanced for thin films.

4.2. Ψ-MOSFET for sensing: state of the art

As reported in the previous section, the top free surface traps can have a strong impact on the electrical characteristics of the Ψ-MOSFET. As a consequence, the pseudo-transistor can detect charged molecules intentionally added to the top surface. This makes it a good candidate for sensing applications and some variants have already been conceived. For instance, chemical sensors detecting APTES ((3-Aminopropyl)triethoxysilane), gold nanoparticles [7], [8] and molecules with electron-donating capabilities [9] as well as radiation sensors [10] showed interesting results.

One of the first sensing applications of the Ψ-MOSFET was the detection of proton irradiation [10]. This introduces positively charged traps in the buried oxide and amphoterically charged traps (can act as donors or acceptors) at the film-BOX interface which can be positively (donor-like) or negatively (acceptor-like) charged.

Figure IV.5 presents the I_D - V_G characteristics for different doses of irradiation. As the dose increases, the curves shift more towards negative V_G, which is consistent with the charge (polarity and quantity) of the injected protons.
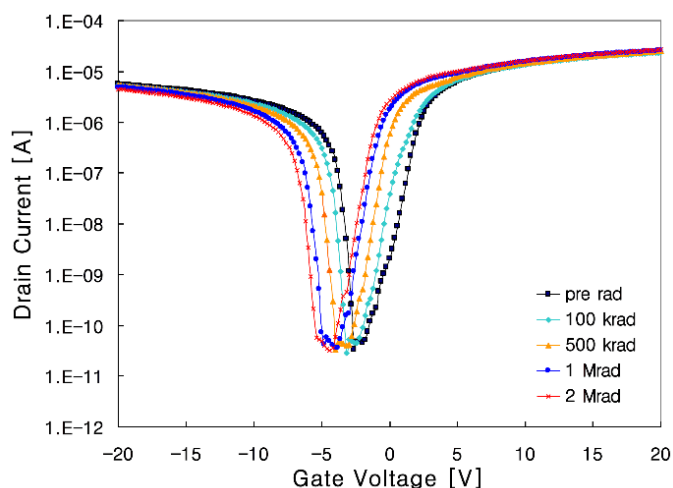
Figure IV.5: Effect of proton radiation on the Ψ-MOSFET. Drain current vs. gate voltage characteristics for different doses of proton radiation after irradiation and subsequent annealing. SOI wafer, with silicon film and BOX thicknesses of 65nm and 145nm respectively. Reproduced from [10].

The first attempt to modulate the electrical properties of the top surface of a Ψ-MOSFET was realized by grafting a dedicated monolayer of molecules on top of the H-passivated silicon surface [9]. The electrically controlled molecules (strong π-electron donors and acceptors) were covalently attached. Four types of molecules were tested (Figure IV.6a): compounds 3 and 4 induce a positive dipole (reference taken so that the negative pole points away from the surface), while 1 and 2 induce a negative dipole. In particular, the functional groups of compound 1 (-N(CH$_3$)$_2$) and 2 (-NH$_2$) make the molecules act as donors, compound 3 has a (-NO$_2$) functional group, being an acceptor, and compound 4 has a polymolybdate cluster, which makes it a strong acceptor.

The relative electron donor ability of the each compound correlates with the measured shift of the threshold voltage ΔV_T (Figure IV.6b), although the reason why compound 3 exhibits an apparent negative dipole is unclear (contrarily to the theory).

(a)   (b)
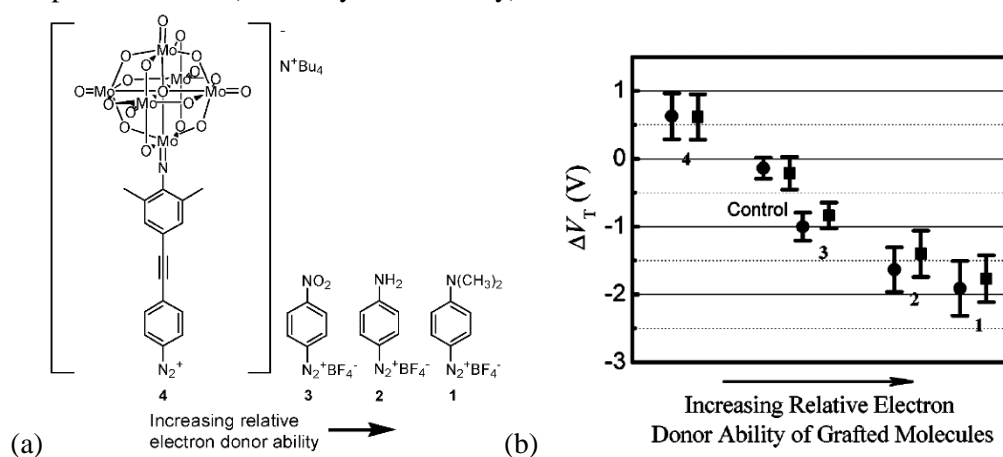
Figure IV.6: Molecular structures of the grafted molecules on top of the silicon film. Structure 1 is the most electron-rich system due to the dimethylamino substituent, 2 is slightly lower in its electron donation capability, followed by 3, and 4 which contains an extremely electropositive radical (polymolybdate) (a). Threshold voltage variation (ΔV$_T$) extracted from forward (■) and backward (●) scans, after grafting the several molecular monolayers (1-4), and compared with bare (control) samples. Data shown here are the average value for 14 devices. The vertical bars indicate standard deviations for each condition(b) [9].

The Ψ-MOSFETs were also used to detect other chemical species such as APTES, and gold nanoparticles. The first is generally employed on the silicon-based sensors in order to functionalize the surface, and in particular for DNA (deoxyribonucleic acid) detection [11]. The first attempt was realized by [7], by measuring the effect of APTES and gold nanoparticles on thin SOI wafers (30 nm thick silicon film and 145nm BOX thickness).

The APTES attachment creates an amino-terminated top surface which is positively charged [12]. Following the surface treatment with gold nanoparticles, which had an average diameter of 50nm, a negative charge is added to the surface of the device [13]. This protocol allows to measure on the same sample the effect of positive and negative charges on the transport properties, all other parameters being constant (defects within the film, charges at the buried interfaces etc). As expected, the electrical characterization shows a negative shift of the I_D - V_G curves for APTES (positive charges), and a positive shift for gold nanoparticles (negative charges), as shown within Figure IV.7a and 7b, respectively [7]. This behaviour is predicted by the basic MOSFET theory [1] considering the type of charges added.
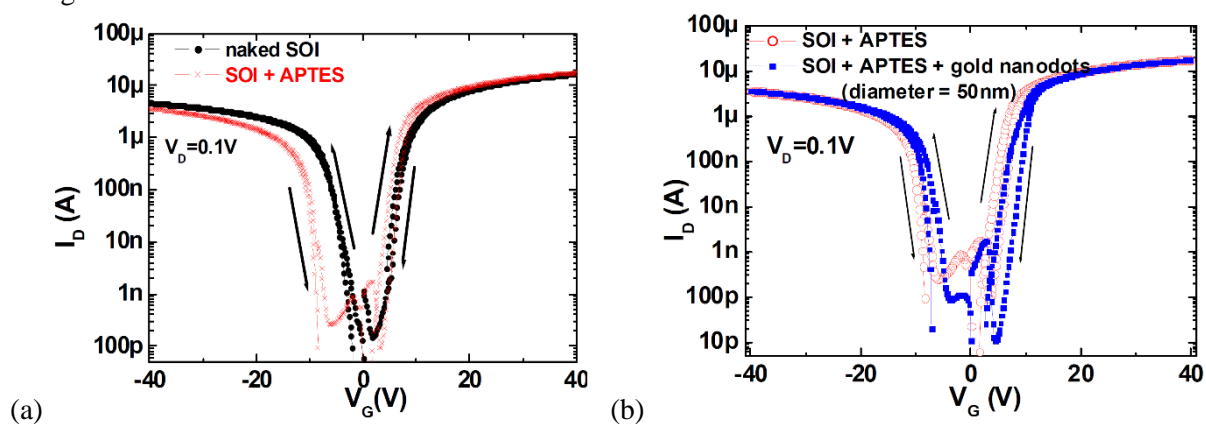
Figure IV.7: APTES and Au-np functionalization results on Ψ-MOSFET. Drain current vs. gate voltage characteristics for a film thickness of 30nm and a BOX of 145nm after APTES (a) and gold nanoparticle (b) functionalization. Reproduced from [7].

The threshold and flat-band voltages were extracted for samples for various nanoparticle densities (Figure IV.8). A correlation was shown between the variation of those parameters and the quantity of expected charges attached to the top surface. This proves that the parameters of the pseudo-transistor increase significantly for higher quantities of charge at the top silicon surface, as expected from the theory.
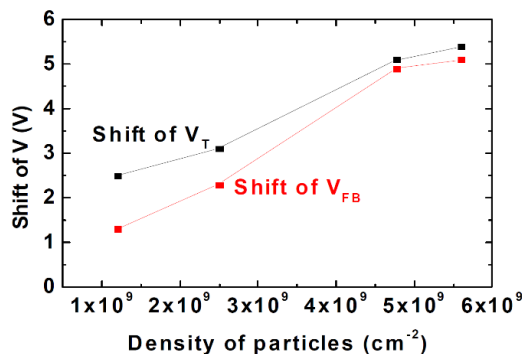
Figure IV.8: V_T and V_{FB} shifts for different density of particles. V_T and V_{FB} were extracted from static I_D-V_G curves, while the nanoparticle density was evaluated from atomic force microscopy images. Reproduced from [7].

More recently, Fernandez et al. (2015) [8] proposed a model in order to quantify the deposited charge from the value of the threshold voltage. It begins by solving the Gauss' law at the top and bottom interfaces of the silicon film, while assuming: (1) the traps to be uniformly distributed in terms of energy, (2) a linear drop of the electrostatic potential across the BOX and (3) that the potential inside the silicon film can be approximated by a linear law for non-passivated films. Thus, the following formula was found for the threshold voltage:

$$V_T = \Phi_{FB} + \Psi_1 \left(1 + \frac{C_{it1}}{C_{BOX}} + \frac{C_{Si} C_{it2}}{C_{BOX}(C_{Si} + C_{it2})} \right) + Q_{SUP} \cdot \frac{C_{Si}}{C_{BOX}(C_{Si} + C_{it2})} \qquad \text{(IV.5)}$$

where: Q_{SUP} is the supplementary charge added at the top surface of the silicon film.

Thus, the added charge at the top surface can be calculated from the variation of the threshold voltage between APTES functionalization as:

$$\Delta Q_{SUP} = \Delta V_T \frac{C_{BOX}(C_{Si} + C_{it2})}{C_{Si}} \qquad \text{(IV.6)}$$

The experimental part was carried out on 15 cells having a 12nm thick silicon film and a 145nm thick BOX. The APTES shifted the I_D -V_G characteristics towards more negative values of V_G (Figure IV.9a). The threshold and flat-band voltages (noted here V_{TH-E} and V_{TH-H}) were extracted for all the samples as presented in Figure IV.9b.

(a)   (b)
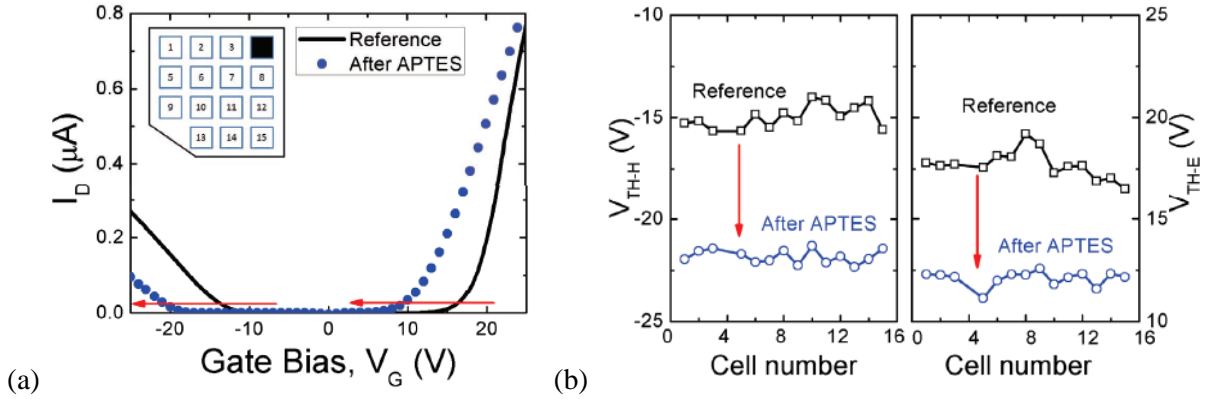
Figure IV.9: Drain current vs. gate voltage before and after APTES functionalization. In the inset the schematic of the sample containing mesas of isolated SOI cells (a). Threshold (noted here V_{TH-E}) and flat-band (noted here V_{TH-H}) voltages extracted from the 15 devices which had a 12nm thick silicon film and a 145nm thick BOX [8].

The total added charge Q_{SUP} was calculated by averaging the shifts in ΔV_T and ΔV_{FB} obtained experimentally. The obtained charge was $3.32 \cdot 10^6$ C/cm² for a hole channel (extracted from V_{FB}) and $3.76 \cdot 10^6$ C/cm² for an electron channel (extracted from V_T) which validates the model for the use of APTES.

All together, these pioneering studied have shown the ability to use thin film SOI as a transducer. Ψ-MOSFET in this configuration can indeed translate a variation of the quantity of charges added at the top surface (e.g. charged molecules) or in the BOX (e.g. protons) into a shift of the electrical characteristics. In the next part, we further explore the pseudo-transistor for DNA detection and in particular the out-of-equilibrium method described in chapter 3 as a measurement method.

4.3. Body potential measurements in Ψ-MOSFET for detection

As shown in the previous section, the detection capabilities of the Ψ-MOSFET were always evaluated from the I_D-V_G characteristics. This method requires the measure of a very low current if the measurement is realized in the subthreshold regime or the use of a high gate voltage in the linear regime (V_G higher than the threshold voltage). This principle is valid for other devices used as sensors such as nanowires.

During this thesis, we employed the out-of-equilibrium body potential measurements in Ψ-MOSFET for sensing charges deposited on the surface of the thin SOI film. As described in Chapter 3, this new method is expected to have several advantages: (1) the measurement of a voltage instead of a low current, (2) the invariability of the measurements with respect to the position and the pressure applied on the probes and especially (3) the low gate voltage needed for the measurement point (close to 0V).

In order to validate the proof of concept, we firstly applied our method for detection, beginning with well-known molecules and particles, namely APTES ((3-Aminopropyl)triethoxysilane) and gold nanoparticles. The motivation for this was twofold: first, the influence of those molecules was already known for the traditional I_D-V_G characteristics and secondly, the molecules present opposite charges, which would prove the response in V_B can differentiate the sign of the charges.

Secondly, we tested our out-of-equilibrium body potential technique for the detection of DNA molecules. Briefly, two types of processes were used for DNA deposition, which were based on APTES and GOPS (((3-Glycidyloxypropyl)trimethoxysilane)) molecules. APTES was first employed in order to attach DNA to the top (Si-film) surface of the samples by a very well documented and experimentally developed method [14]. Subsequently, APTES was then replaced with GOPS in order to reduce the number of functionalization steps and to eliminate the toxicity of the glutaraldehyde which is used in the APTES protocol. At first, the GOPS was deposited in liquid form with a method similar to the one used for APTES. For the last series of measurements, GOPS was deposited in vapour phase in order to ensure a better quality deposited layer and multiple concentrations of DNA were used in order to discriminate the influence of the DNA molecules from the one of the buffer (blank) solution. Figure IV.10 presents a summary of the step-by-step method followed during this thesis to show the DNA sensing with VB in the pseudo-MOSFET configuration
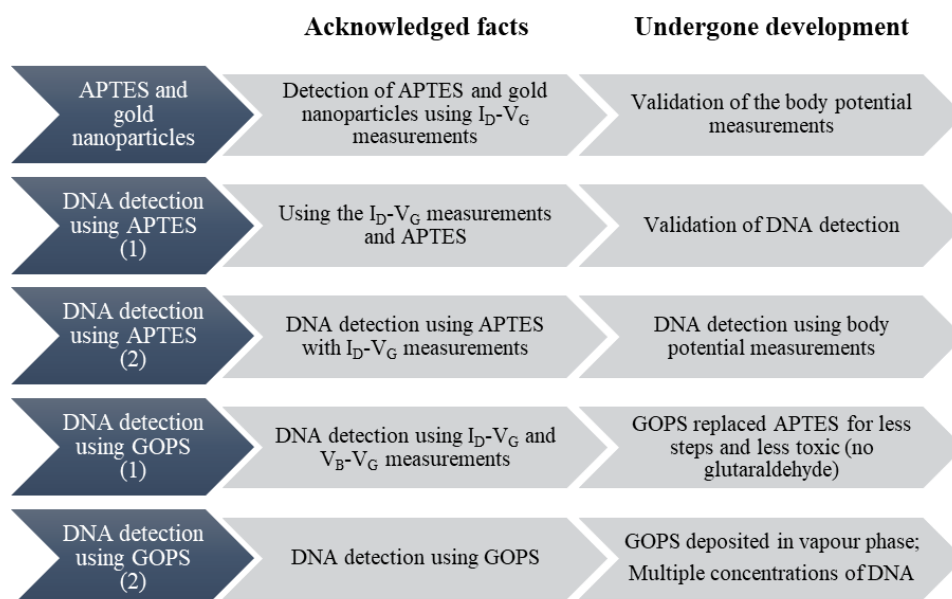

Figure IV.10: Steps of the method: from gold nanoparticles to DNA detection.

4.3.1. Proof of concept: APTES and gold nanoparticle detection

Sample fabrication

The suitability of body potential measurements for sensing applications was first assessed by using chemical treatments and samples that were already used in the conventional Ψ-MOSFET configuration (as described previous in part 4.2).

In particular, the samples used were based on SOI wafers having an 88nm thick silicon film and a 145nm thick BOX. Note that the samples used had a passivated silicon film which have a good quality silicon dioxide layer grown by thermal oxidation (few nanometers thick).

The measurements were realized after APTES deposition and gold nanoparticles (Au-np) attachment to the surface (process similar to [7]).

The functionalization steps are briefly described within Figure IV.11. Before the first step, the samples were cleaned with deionized water and ethanol, then immersed for 30 minutes into a diluted solution of APTES (APTES (99% v/v) to ethanol volume ratio of 1:5 – 5mL and 25mL, respectively). The samples were then rinsed with ethanol and deionized water, dried under nitrogen N_2 stream and then annealed at 120°C for 30 minutes on a hotplate (in ambient atmosphere).

Then the gold nanoparticles (Au-np) attachment was realized by covering the sample (Ψ-MOSFET device) with a solution containing Au-nps of 20 nm diameter (753610 from Sigma-Aldrich) stabilized suspension in 0.1 mM PBS (Phosphate-buffered saline) solution for 20 minutes (in ambient atmosphere). Afterwards, the samples were rinsed with deionized water and then dried with a nitrogen blower. In both cases, the chemical treatment modifies the top surface charge (positive after APTES and negative after Au-np deposition).
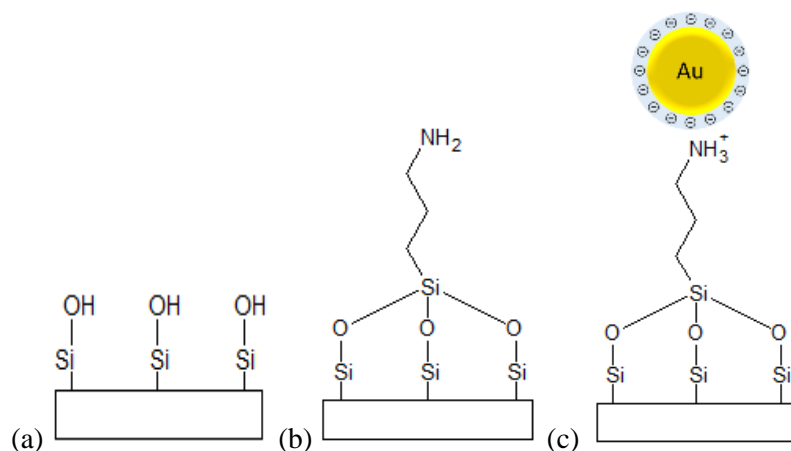
Figure IV.11: Schematics of the APTES and Au-np functionalization processes of the SOI samples. (a) Bare silicon film coated with native oxide, (b) covered with APTES monolayer, and (c) after adding the gold nanoparticles.

Electrical characterization results

We have assessed the impact of the functionalization by measuring the transfer I_D-V_G curves in the three configurations: bare SOI (black curve), after APTES (red curve) and after gold nanoparticle (blue curve) depositions (Figure IV.12). The I_D-V_G curves in logarithmic and linear scale (inset) (Figure IV.12 a), present a shift towards negative values after APTES deposition and toward positive values after gold nanoparticles deposition, as expected, according to the sign of the charges added on the surface.

Despite the higher silicon film thickness - being almost 4 times thicker than in previous reports [7] - the relative shift of the threshold voltage is still significant, around 1V for both APTES and Au-nps.

Those first results highlight a significant impact of the functionalization steps on the transport properties of the Ψ-MOSFET.

We have then measured the body potential as a function of the gate voltage V_B-V_G (Figure IV.12 b). The characteristics show the same behaviour, i.e. a shift of the body potential V_B toward negative and positive values for APTES and Au-nps deposition respectively.
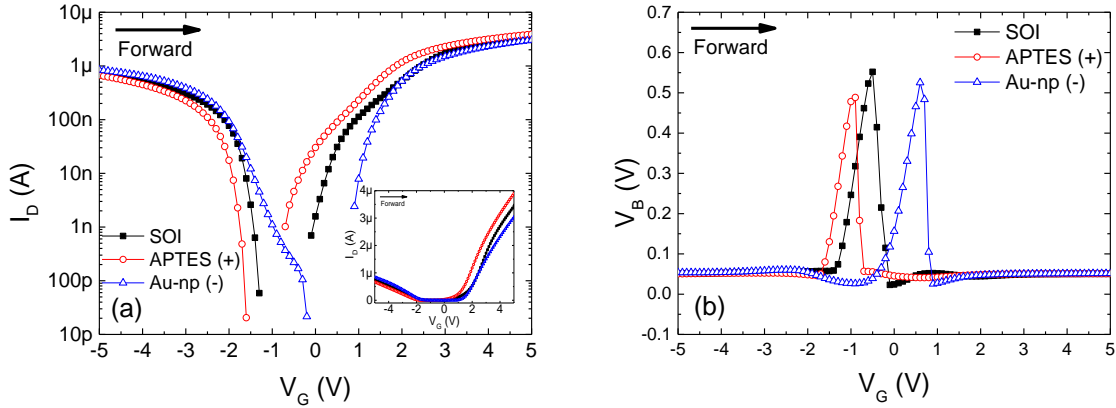
Figure IV.12: Drain current (a) and body potential (b) vs. gate voltage for several surface treatments of the SOI sample (88 nm Si, 145 nm BOX): Bare (black curves), APTES-coated (red curves) and Au-nps-coated (blue curves) samples. The shifts are well correlated with the expected charge added at the surface. 3 probe measurement, V_D=0.1V, step 100mV, pressure 100g.

In order to benchmark the two methods (Figure IV.12a and b), we compared the impact of the functionalization on the shifts of the (1) threshold and flat-band voltages, and (2) on the body potential.

Regarding the conventional detection method (Figure IV.12a), the values of V_T and V_{FB} were extracted after each functionalization step using the Y function [15], as described in Chapter 2. Briefly, the ΔV_T and ΔV_{FB} shifts are extracted from the I_D-V_G characteristics as the difference between the values obtained before and after each step. An example of I_D-V_G and Y-V_G curves is shown in Figure IV.13. The extracted values are reported Table IV.1 and will be used later for the benchmark.
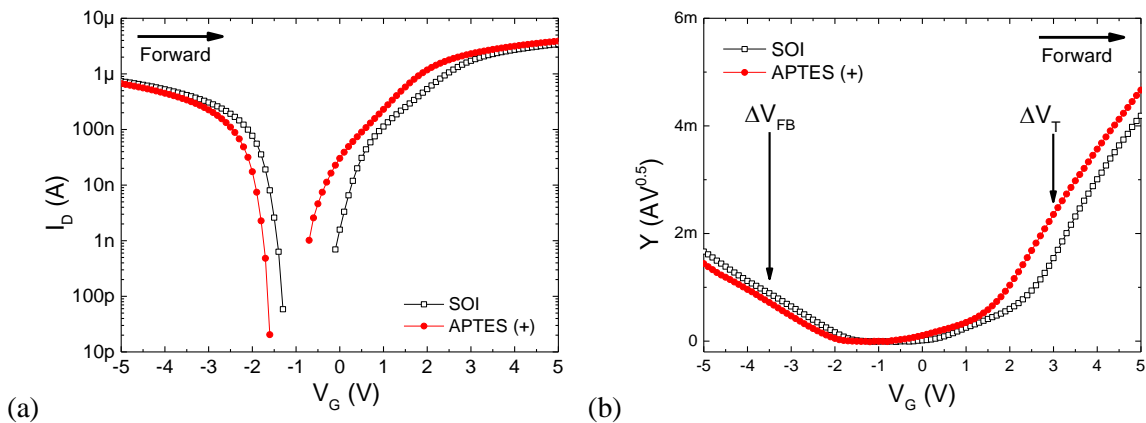
Figure IV.13: Example of parameter extraction from the I_D-V_G characteristics for the APTES. (a) I_D-V_G curves obtained from Figure IV.12a, before (black curve) and after APTES functionalization (red curve). (b) Y function calculated from Figure IV.13a. Arrows indicate the values of V_G at $\Delta V_{T, FB}$ extraction.

For the body potential measurement, we first need to determine a stable point that can be used to measure the shift in the body-potential after functionalization. One can observe V_B-V_G characteristics for different sweeping speeds. This was realized by modifying the delay time (time between two measurement points), the integration time and the measurement step. As it can be observed from Figure IV.14a, the only stable point is the one who marks the border between the accumulation and the out-of-equilibrium regimes in the case of a forward sweeping direction (from accumulation to inversion). The shifts will be measured using this point as represented in Figure IV.14b.

(a)   (b)
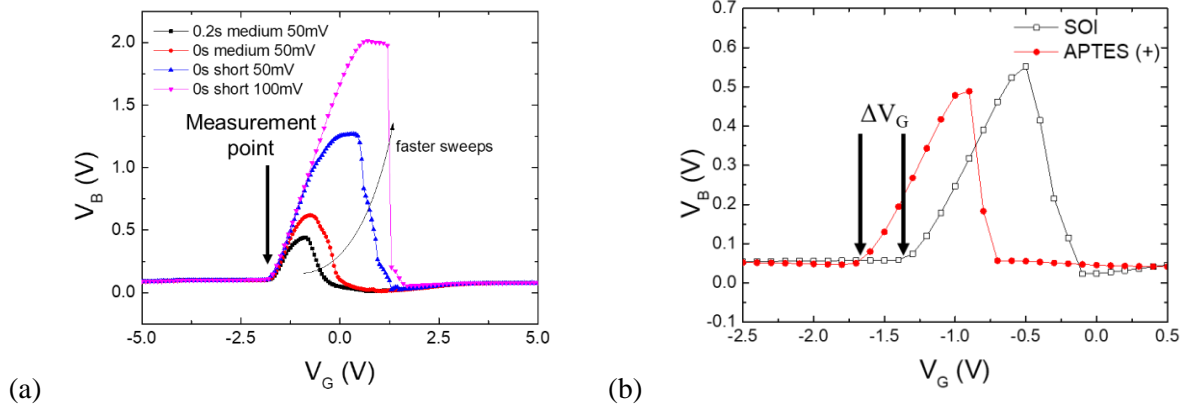
Figure IV.14: Method for shift evaluation from the V_B-V_G characteristics for the detection. (a) V_B-V_G characteristics for different sweeping speeds. Measurements obtained by varying the delay time (time between two measurement points), the integration time and the step. (b) Example of the body potential shift extraction after APTES treatment. V_D=0.1V

The shifts of V_T, V_{FB} and V_B after APTES and Au-np functionalization are presented in Table IV.1. All shifts are consistent, in terms of expected polarity and amplitude regarding previous results (Figure IV.7, [7]). The shift of the body potential exhibits similar amplitude changes, and can thus be used to monitor the surface charge state. The observed shifts induced by functionalization are greater than typical parameter fluctuations in Ψ-MOSFET. For example, the measurement variations (errors) observed for the same die are estimated at about 150mV (originating from contact variation) or for different dies on the same SOI wafer they are of 300mV (originating also from eventual silicon film and contact variations) Those estimations were done with measurements obtained from 9 different devices which had identical structures as the ones used in this section (more details in Appendix 1).

Table IV.1: Main parameters extracted from I_D-V_G and V_B-V_G curves before and after functionalization with APTES and Au-np.

Functionalization	V_T (V)	ΔV_T (V)	V_{FB} (V)	ΔV_{FB} (V)	ΔV_B (V)
Bare SOI	0.5		- 1.0		
APTES (+)	0.1	- 0.4	- 1.6	- 0.6	- 0.4
Au-np (-)	0.9	+ 0.8	- 0.5	+ 1.1	+ 1.3

We conclude that the out-of-equilibrium body potential reacts in a similar way as the traditional current measurement method to the charges added on top of the silicon film. The shift of V_B (V_G) curve associated to the charges on top, being at least equal to the ΔV_T, ΔV_{FB} shift in current configuration. The method discriminates between charges of opposite polarities and its response can be evaluated at weaker gate polarizations compared to drain current measurements.

4.3.2. DNA detection

After the proof of concept of the out-of-equilibrium body potential method as a mean of charge detection presented in the previous section, we extended our study towards a more pragmatic application: DNA detection. In order to realize this type of sensor, the probe DNA (or ssDNA – single stranded DNA) needs to be attached at the surface of the device. The detection is realized when the hybridization between the probe and target DNA (complementary single strands – marked as dsDNA – double stranded DNA) adds negative charges on top of the sample, which must be detected by the transducer.

Two different processes were used in order to attach the probe DNA to the surface of the Ψ-MOSFET. They use two different molecules that covalently attach to the silicon oxide top surface: APTES ((3-Aminopropyl)triethoxysilane) and GOPS ((3-Glycidyloxypropyl)trimethoxysilane). We started with the APTES since it had already been used to attach gold nanoparticles and its impact on Si-film properties was already known. However, the GOPS presents among its advantages the possibility to directly attach the DNA to the device surface without any other cross-linker because the epoxy group of the GOPS can react to the amino group present at the end of the DNA probe [16]. Furthermore, it eliminated the use of glutaraldehyde (necessary in the APTES process), which exhibits a high degree of toxicity [17]. A schematic of the top surface modifications is presented in Figure IV.15. Both processes were developed at the Institute for Micronanotechnology in Bucharest during a bilateral Campus France project.
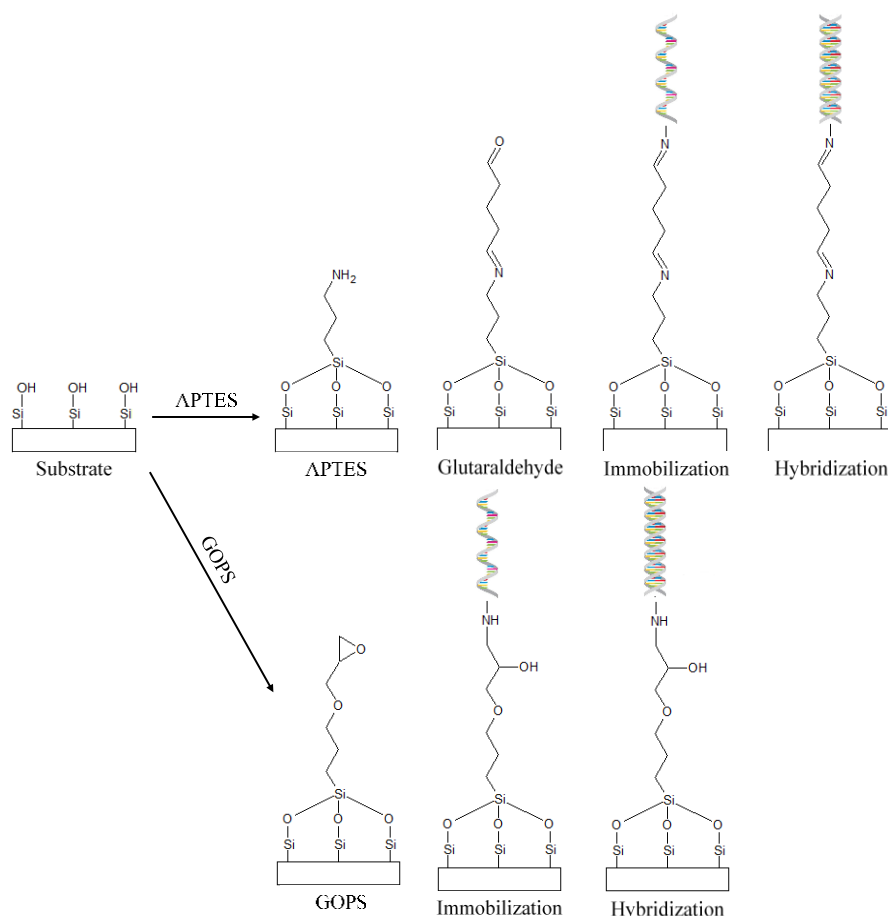
Figure IV.15: Top surface functionalization steps for APTES and GOPS methods of DNA attachment.

DNA detection using APTES

Functionalization process using APTES

First, the 5x5mm² cells were cleaned for 10 min in Piranha solution (H_2SO_4:H_2O_2 3:1 v/v) in order to remove all organic compounds (cleaning) and generate hydroxyl groups (activation) on the top oxide surface (Figure IV.16) [18], [19]. Samples were then cleaned in deionized (DI) water, ethanol and dried under a nitrogen stream.
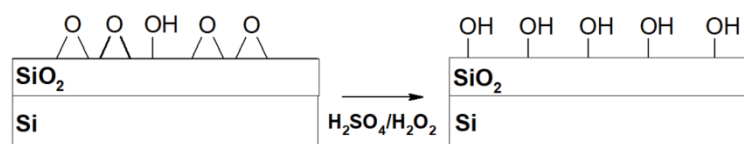
Figure IV.16: Schematic view of hydroxyl groups (OH-) generated by Piranha treatment of the top silicon oxide surface.

The solution-phase silanization was achieved by immersing the SOI samples for 2 h in 2.5% hydrolysed APTES. The latter is obtained by mixing water with ethanol in 1:19 (v/v) ratio [20]. At the end of the silanization process, the cells were rinsed with ethanol, deionized water and then dried under N_2 stream and thermally annealed for 30 min at 110℃ in an oven. The APTES-modified SOI substrates were further exposed to 5% glutaraldehyde (GAD, Sigma-Aldrich G7776) for 4 h, in order to have aldehyde active moieties (Figure IV.17). The process was adapted from [14].
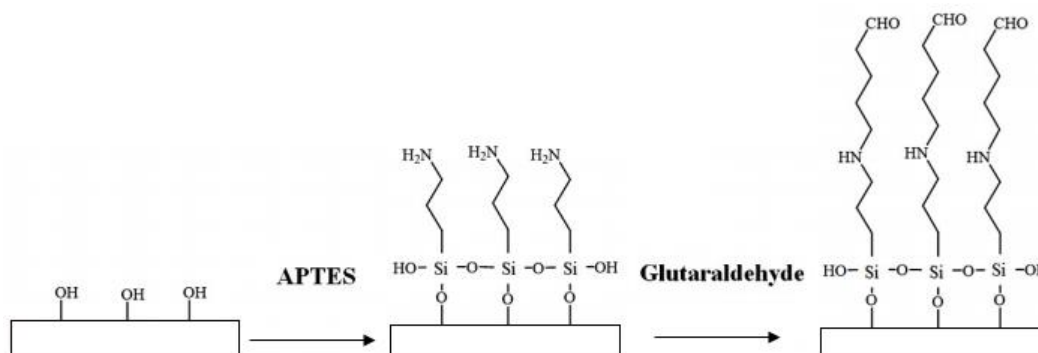
Figure IV.17: Schematics of APTES and glutaraldehyde attachment to the surface prior to DNA deposition. Adapted from N. Majoul (2015) [18]

For the immobilization step, 15µL of probe DNA solution (200mM, acquired from Biomers.net) were diluted in 45µL buffer solution (Na_2HPO_4 at pH 8.5), arriving at a final DNA concentration of 50µM. Then, 10 µL of the DNA/Na_2HPO_4 mix is added on the cells, which are then incubated at 25 ℃ for the overnight reaction in a humid chamber. This takes place in a Petri dish with a humid tissue on the lid, to ensure the solution does not dry. The rinsing is realized three times successively in each of the following solutions:

1. Washing buffer I (2x SSC and 0.1% w/v SDS (Sodium dodecyl sulphate) – Sigma-Aldrich S6639)
    o 2x SSC (saline sodium citrate): NaCl (300 mM), Trisodium citrate (30 mM).
2. Washing buffer II (1x SSC- - Sigma-Aldrich L6026)
    o 1x SSC (saline sodium citrate): NaCl (150 mM), Trisodium citrate (15 mM).
3. Deionized water (DIW).

Before the hybridization step, the optional blocking step can be realized in order to avoid unspecific attachment of the target DNA to the APTES-GAD complex present on top of the devices. This is realized by immersing the SOI samples in a blocking solution (30 min, 42 ℃, 250 rpm). The composition of the blocking buffer solution is: 5x SSC, 0.1% SDS and 1 % BSA (Sigma-Aldrich S6639, L6026, 10735078001).

The hybridization is obtained by using 1.5 µL of target DNA (acquired from Biomers.net) diluted in 28.5 µL hybridization buffer (2x Denhardt's solution [21] – Sigma-Aldrich H7140) to reach a final concentration of 10 µM target DNA. The concentration of the target DNA is considerably less than the one of the probe DNA. In order to have the maximum attachment of the target DNA, probe DNA should be deposited in excess in order to maximise the number of available hybridization sites. The obtained mix (30µL) is preheated to 60-62˚C and 5 µL is added on each structure. The structures are then kept 4h, at 42˚C in a humid chamber (Petri dish with humid tissue inside the lid) to prevent sample evaporation. Rinsing was performed made in the same way as previously described for the immobilization step.

Denhardt's solution is a blocking agent routinely used to reduce non-specific binding of detection reagents to the Northern and Southern Blot membranes.

Composition:

- 0.04% Ficoll 400
- 0.04% Polyvinylpyrrolidone (PVP)
- 0.04% Bovine Serum Albumin (Sigma, Fraction V)

The immobilization and hybridization involved the use of nucleotide sequences corresponding to the L2 gene fragment from HPV 16 (human papillomavirus type 16), acquired from Biomers [22] (detailed in Table IV.2).

Table IV.2: Probe and target DNA sequences

HPV 16 specific probe	5'-*NH₂-C6*-TGGGAGGCCTTGTTCCCAATGGA-3'
Control probe (noncomplementary sequence)	5'-*NH₂-C6*-CTAGGAATTGCGGGAGGAAAATGGG-*Cy3*-3'
Complementary sequence (target DNA)	5'-TCCATTGGGAACAAGGCCTCCCA-3'

Fluorescent dye attached on DNA probes The Cy3-labelled noncomplementary sequence was employed to certify by microarray scanning (GeneTAC UC4, Genomic Solutions, USA) the presence of DNA probes, attached onto the surface. As shown in Figure IV.18, the high fluorescent intensity above the MOSFETs indicates an efficient functionalization and oligonucleotide attachment protocols.
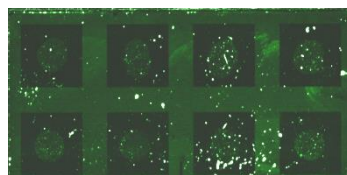
Figure IV.18: Immobilization results on an SOI substrate functionalized with APTES and GAD.

Electrical response of the APTES method of functionalization

For each functionalization step, samples containing six devices were used in order to measure the influence of every chemical treatment on the electrical characteristics. The samples were characterised two times. The first characterization was carried out before the samples were sent for functionalization. Then, each sample underwent a certain number of steps. For example for the ssDNA sample (with probe

DNA), the following molecules were attached to the top surface: APTES, glutaraldehyde and probe DNA, while the control sample only underwent the cleaning step. After six samples were prepared for each functionalization step (Figure IV.19), they were characterized a second time. Note that, while initially having six devices for each functionalization step, for some of them, the BOX was leaking after some specific treatment, therefore the corresponding data will not be represented in the electrical measurements. The number of devices still functional for the samples representing the corresponding functionalization step was: Control (3/6), APTES (2/6), GAD (5/6), ssDNA (6/6), dsDNA (2/6). The sequence of steps and characterization is represented in Figure IV.19.

		Cleaning	APTES	GAD	Immobilization	Hybridization (blocking included)	
Initial characterization	Control Samples	✓	✗	✗	✗	✗	**Final characterization**
	APTES Samples	✓	✓	✗	✗	✗	
	GAD Samples	✓	✓	✓	✗	✗	
	ssDNA Samples	✓	✓	✓	✓	✗	
	dsDNA Sample	✓	✓	✓	✓	✓	

Figure IV.19: Description of the process steps and measurement points procedure. Starting from SOI wafer (Silicon film 70nm, BOX 145 nm), we monitor the impact of each chemical treatment (described in the text), from the cleaning to hybridization processes. Six samples tested for each step.

Before the electrical measurements of the functionalized samples, we measured the I_D-V_G characteristics for 19 bare SOI samples in order to have reference curves. Based on these measurements we also determine the reproducibility of the results in terms of threshold and flat-band voltages. The evaluated results for both parameters (the average and standard deviation) are presented in Table IV.3. We estimated the variation between the 19 devices at V_T=4.1±0.2V for the threshold voltage and V_{FB}= -1.7±0.3V for the flat-band voltage.

Table IV.3: Average and standard deviation of the threshold voltage and flat-band voltage obtained for 19 devices. t_{Si}=70nm, t_{BOX}=145nm, V_D=0.1V, forward scan direction (negative to positive V_G).

	V_T (V)	V_{FB} (V)
Average	4.1	-1.7
Standard Deviation	(0.2)	(0.3)

The results for the variation of the threshold and flat-band voltages induced by each functionalization step for all the measured devices are presented in Figure IV.20a and Figure IV.20b. The average values are represented as orange dots.

The effect of the charges added by the APTES is not as presumed. This functionalization step is expected to leave a positively charged surface, and thus a negative shift of the threshold and flat-band voltages as measured previously on similar samples (Table IV.1) [23]. The negative V_{FB} shift is in agreement with the positive charge, but the threshold voltage shift toward positive values is not as expected.

As presented in the first part of this chapter, there are two different contributions that can shift the characteristics of the Ψ-MOSFET: (1) fixed charges could induce an equal shift in V_T and V_{FB} [8], while interface states makes the two move in opposite directions (Figure IV.2) [3]. Taking in consideration the obtained mean value of the threshold voltage and flat-band voltage, the average shift of the curves is -0.2V which is consistent with the attachment of positive charges (brought by APTES) on the surface. In addition, the threshold and flat-band voltages are spread by around 0.9V suggesting an increase of interface states that could result from a degradation of the film during the cleaning procedure.

After the glutaraldehyde attachment, the V_T and V_{FB} are both shifted toward negative values, with almost the same amplitude (mean values $-0.8 \pm 0.3V$). This suggests that this step equates to a uniform positive charge added at the top surface.

The variation of the threshold voltage induced by the immobilization and hybridization steps induce similar positive shifts of +0.3 V (obtained from the mean values). This corresponds to the negative charge of the DNA sugar phosphate backbone [24]. The same trend is observed in the case of the flat-band voltage, which slightly increases (Figure IV.20b). The shifts induced by immobilization and hybridization are however significantly lower: +0.1 V for both steps (also obtained from the mean values). It is important to notice that while the tendency of the shift is clear, the variation is greater than the standard deviation ($\pm 0.2V$ compared to 0.3V of shift) in the case of the threshold voltage, but lower for the flat-band voltage ($\pm 0.3V$ compared to 0.1V of shift).

Considering one intrinsic negative charge per base, for the 23 base-long strand used and the use of 5µL of 10µM/L concentration of target DNA, we obtain a total available charge of $1.1 \cdot 10^{-4}$ C. By estimating the diameter of the drop to 4mm, the maximum charge per unit of area deposited on the samples would be $2.2 \cdot 10^{-4}$ C/cm². In comparison, by using the model proposed by [8] for a 0.3V shift in the threshold voltage, applied to a wafer having a 70nm silicon film, 145nm BOX and a D_{it2} estimated at 10^{11} cm^{-2}, the calculated added charge would be of $8.3 \cdot 10^{-9}$ C/cm². The five orders of magnitude of difference might be due to the attachment efficiency and to the orientation of the DNA molecules, which are not horizontally distributed as needed for an ideal detection of their intrinsic total charge.

(a)   (b)
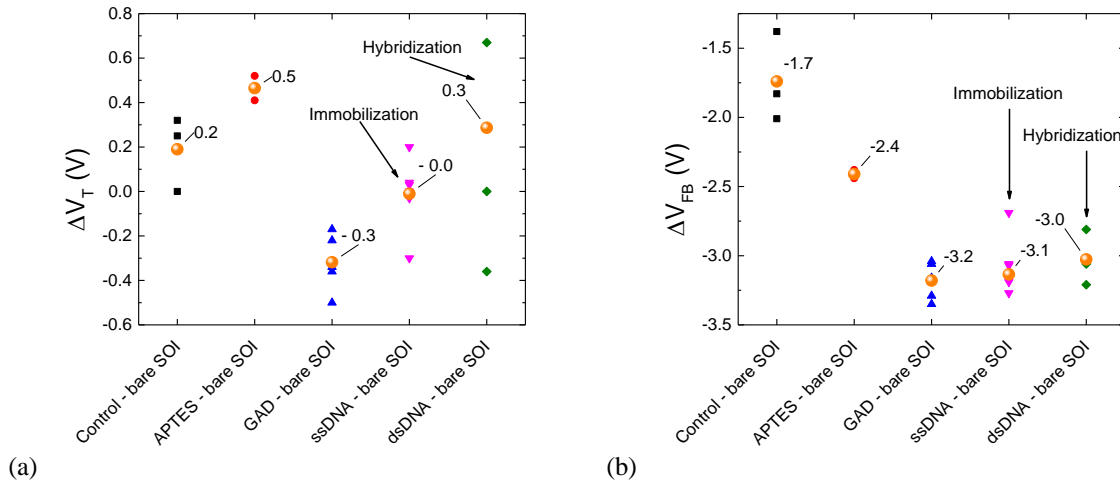
Figure IV.20: Variation of the V_T (a) and V_{FB} (b) for different functionalization steps. Each dot represents one sample. Mean values (average of all sample tested in each condition) represented in orange dots. t_{Si}=70nm and t_{BOX}=145nm.

We conclude that the mean shifts for the I_D-V_G characteristics are consistent with the expected charge added at the top surface in the case of glutaraldehyde, immobilization and hybridization steps, although large fluctuations are observed over the tested samples.

Unexpectedly, APTES shows opposite shifts for V_T and V_{FB}. The mean value of the two parameters (V_T and V_{FB}) presents an average shift of -0.2V, which is consistent with the charge of the molecule. A spread of +0.9V between the two parameters suggests an increase in the D_{it} concentration which might be due to the Piranha treatment.

Furthermore, the shifts of the flat-band voltage are considerably lower compared to the threshold voltage (for immobilization and hybridization steps only) and we suspected the blocking step to be at the origin of it. For this reason, the influence of the blocking solution (functionalization step before hybridization) will be evaluated next.

Influence of the blocking solution

Another set of measurements was realized using the same process, but additional measurements were performed between immobilization and hybridization to monitor the impact of the blocking buffer solution. This step is essential to avoid unspecific attachment of the target DNA, but has been shown to decrease significantly the response of the sensors (as shown in the previous section).

Similarly, SOI samples were immersed in blocking solution for 30 min, at 42ºC under stirring (250rpm) between the immobilization and the hybridization steps. The composition of the buffer is the following: 5x SSC (saline sodium citrate: NaCl (150 mM), Trisodium citrate (15 mM)), 0.1% SDS (sodium dodecyl sulphate) and 1 % BSA (bovine serum albumin).

For this measurements, APTES induces a negative shift for both the threshold and flat-band voltages ΔV_T = -0.5 ± 0.2V and ΔV_{FB} = -2 ± 0.3V, as expected from its charge (Figure IV.21). Glutaraldehyde induces also a negative shift (lower than previously obtained) of -0.2V (V_T) and -0.3V (V_{FB}) respectively, instead of -0.8V during the first set of measurements.

For the immobilization a shift of 0.7V in the threshold voltage and 0.6V in the flat-band voltage is observed, which is again in accordance to the sign of the charge added at the top surface. The binding efficiency slightly improves from the previously obtained results. However, the blocking and the hybridization step induce non-significant voltage variation which suggests that hybridization process was obstructed. This effect most probably comes from the blocking buffer.

(a) (b)
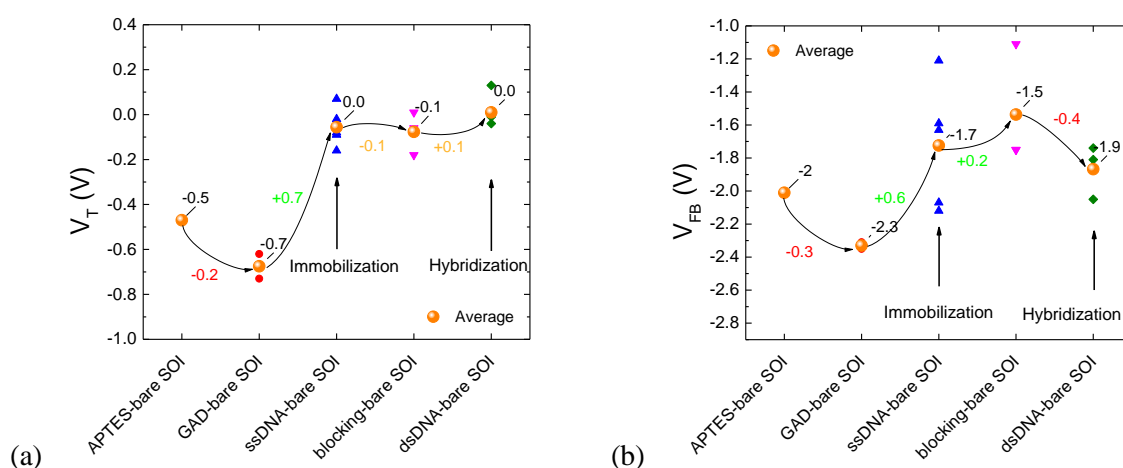
Figure IV.21: Threshold voltage (a) and the flat-band voltage (b) for different functionalization steps. Mean values represented in orange dots. t_{Si}=70nm and t_{BOX}=145nm.

For this set of samples, we also implemented the body potential measurements. As explained in Figure IV.14, we extracted V_B at the transition between the equilibrium and the out-of-equilibrium. For this method, the shifts induced by APTES, glutaraldehyde attachment and DNA immobilization are very similar to the ones extracted from the threshold and the flat-band voltages (Figure IV.22).

The blocking step induces a negative shift of -0.5V while the hybridization a positive shift of +0.7V which incidentally is similar to the shift induced by DNA immobilization. Compared to the drain current measurements, this difference can be explained by the different behaviour induced by a molecule deposited at the top surface. In a recent study on silica binding protein (SBP) and an antigen of avian influenza (AIa), the authors investigate the dual influence of the species involved, which manifest a dielectric and a charge effect simultaneously [25]. Similarly to a gate capacitance dielectric layer, deposited molecules have a charge which is specifically distributed along their length and a dielectric component which stems from their intrinsic permittivity which is greater than the one of vacuum. As such, the linear and the depletion regime show a different behaviour depending on the dominant characteristic in the respective regime. It was determined that in the subthreshold regime (which would correspond to the depletion regime of the Ψ-MOSFET) the charge effect is dominant, while the dielectric effect is dominant in the linear regime.
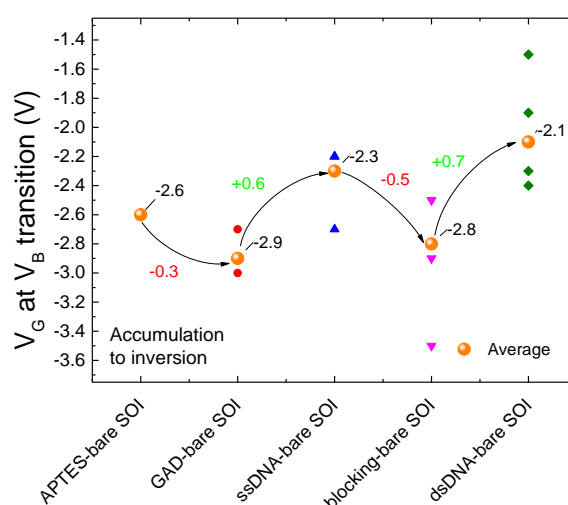
Figure IV.22: Variation of body potential for different functionalization steps. Mean values represented in orange dots. $t_{Si}=70nm$ and $t_{BOX}=145nm$. $V_D = 0.1V$.

We can conclude that the body-potential method is validated for DNA detection, the results being consistent with the traditional drain current measurements. Moreover, the electrical response in V_B was stronger for the hybridization step. However, the blocking step had a strong impact the surface charge and could render DNA detection more difficult, thus it was no longer used in the following studies.

DNA detection using GOPS

In the followings, the functionalization protocol was changed in order (1) to reduce the number of process steps and (2) to eliminate the glutaraldehyde which presented toxicity concerns [17]. Moreover, the electrical characterization was realized on the same device after every functionalization step. At first, GOPS (3-Glycidyloxypropyl)trimethoxysilane) was deposited onto the samples (silicon oxide) surface in liquid form with a protocol similar to APTES, but for the last series of measurements, the process was realized in vapour form in order to avoid the water molecules reaction with the epoxy rings, which leads to their opening and inactivation [26] as represented in Figure IV.23.
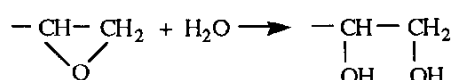
Figure IV.23: Epoxy group reaction with water.

Description of the functionalization process using GOPS

The devices were first cleaned using a Piranha solution (H_2SO_4:H_2O_2 3:1 v/v) for one minute in order to generate hydroxyl groups at the top surface [18], [19]. Then the devices were rinsed in deionized water for 5 minutes and then dried under a N_2 stream.

For a deposition in liquid phase, a 2.5% solution of GOPS was realized using the following substances: 1mL deionized water, 18.5mL ethanol and 0.5mL GOPS. This solution was subjected to hydrolysis for 2 hours under magnetic stirring (as in the APTES process). The GOPS was attached to the top surface of the devices by submersion in the hydrolysed GOPS solution for 2 hours, under stirring at 250 rpm at 25°C (Figure IV.25). At the end of the silanization process, the samples were rinsed 3 times with ethanol, deionized water and then dried under a N_2 stream. The silanized samples were cured at 110 ºC, for 30 min in a stove.

For the deposition in vapour phase, pure GOPS, 1-2 mL (Sigma-Aldrich 440167) were put in a Falcon cap situated in a Petri dish, in the middle (Figure IV.24). The other Falcon caps are used as support for the SOI samples. The silanization was realized by heating the Petri dish on a hotplate at 85°C for 3h30. At the end of silanization process, each sample was rinsed alternatively three times with ethanol, deionised water and dried in N_2 stream. The silanized samples were cured at 110 ºC, for 30 min in a stove. The process was adapted from [27].
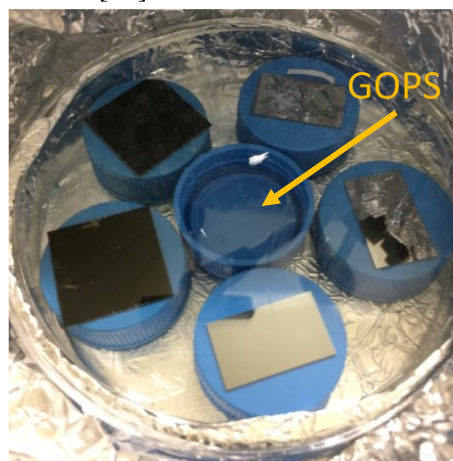
Figure IV.24: Petri dish setup used for vapour phase GOPS deposition.
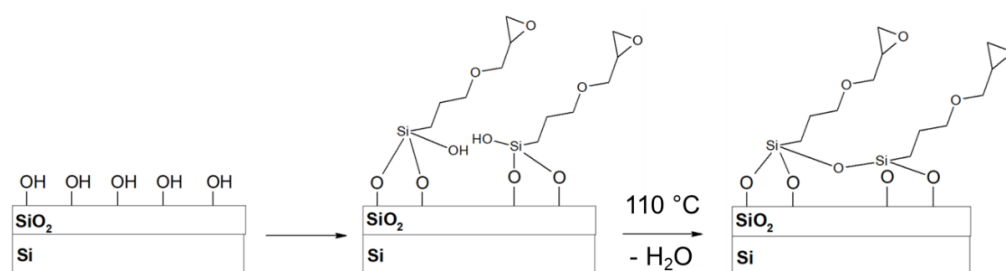
Figure IV.25: Schematic of the silanization process by using GOPS attachment to the top surface. First, the GOPS molecules are attached to the surface. Then, the samples are cured at 110⁰C for dehydration.

For the immobilization step (Figure IV.26), 15µL of probe DNA solution (200mM, acquired from Biomers.net) were diluted in 45µL buffer solution (Na_2HPO_4 at pH 8.5), arriving at a final DNA concentration of 50µM. 10 µL of the DNA/Na_2HPO_4 mix added on each structure, the structures being incubated at 60ºC for the overnight reaction (approximately 12h) in a humid chamber. This takes place

in a Petri dish with a humid tissue on the lid, to ensure the solution does not dry overnight. The rinsing is realized three times successively (5 min, 42 ℃, 250 rpm) in each of the following solutions:

1. Washing Buffer I (2x SSC/0.1% w/v SDS)
   o 2x SSC (saline sodium citrate): NaCl (300 mM), Trisodium citrate (30 mM).
2. Washing buffer II (1x SSC)
   o 1x SSC (saline sodium citrate): NaCl (150 mM), Trisodium citrate (15 mM).
3. Deionized water.
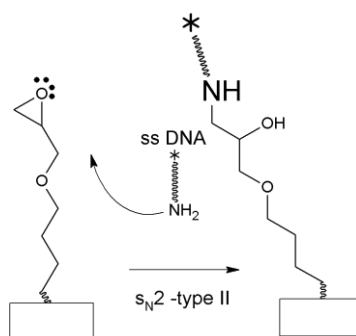
Figure IV.26: Immobilization reaction using GOPS.

The hybridization is obtained by using 1.5 µL of unlabelled target DNA (complementary strand) diluted in 28.5 µL hybridization buffer (2x Denhardt's solution) to reach a final concentration of 10 µM DNA. The obtained mix is preheated to 60-62˚C; 5 µL will be added on each structure. As previously said, the concentration of the target DNA is considerably less than the one of the probe DNA. In order to have the maximum attachment of the target DNA, probe DNA should be deposited in excess in order to maximise the number of available hybridization sites. The structures are kept 4h, at 42˚C in a humid chamber (Petri dish with humid tissue inside the lid) to prevent sample evaporation. Rinsing was performed in the same way as for the immobilization step (see previous paragraph). The sequences used here are the same as in the APTES process (see previous paragraph), but without the fluorescent dye attached at the end of the complementary DNA sequence.

For this process, the electrical characterization of the devices was realized after each functionalization step. This ensured a better understanding on the influence of each characterization step on the electrical characteristics. The sequence of steps and characterization is represented in Figure IV.27.
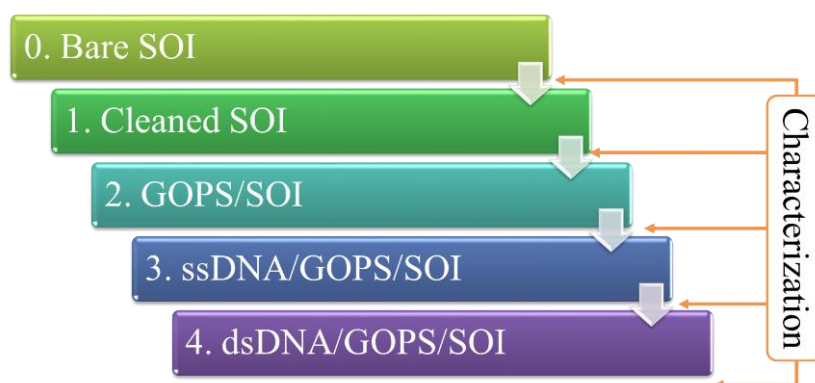
Figure IV.27: Process flow and characterization points during the DNA depositions using GOPS.

Electrical response to the GOPS functionalization

GOPS deposited in liquid phase

A first series of measurements was realized on two types of wafers: a thin film/BOX having a 30nm thick silicon film and a 15nm thick BOX and a thick silicon film/BOX having a 70nm thick film and a 145nm thick BOX.

Unfortunately, during this series, many of the devices were suffering from a leakage current through the BOX, especially after the Piranha cleaning treatment. The procedure was performed for the first time in the clean room of the laboratory under the same conditions as performed at IMT Bucharest. As it was the first trial with this method of functionalization, the robustness was an important problem for this series of measurements (Table IV.4). Only two devices of each kind could be measured for the hybridization step.

Table IV.4: Device reliability for the first series of GOPS treatment

| Thin film/BOX (30 nm / 15 nm) no. 4					Thin film/BOX (30 nm / 15 nm) no. 3					
Devices	Bare	Cleaned	GOPS	ssDNA	dsDNA	**Devices**	Bare	Cleaned	GOPS	ssDNA	dsDNA
SOC3.4.1	OK	leakage				SOC3.3.1	OK	leakage			
SOC3.4.2	OK	OK	OK	OK	OK	SOC3.3.4	OK	leakage			
SOC3.4.3	OK	OK	OK	OK	OK	SOC3.3.5	OK	OK	OK	OK	leakage
SOC3.4.4	OK	leakage				**Thick film/BOX (70 nm / 145 nm) no. 6**					
SOC3.4.5	OK	OK	OK	leakage		W2.6.1	OK	leakage			
						W2.6.2	OK	OK	OK	OK	OK
						W2.6.3	OK	OK	OK	OK	leakage
						W2.6.5	OK	OK	OK	OK	OK

The I_D-V_G and V_B-V_G characteristics for the thick film/BOX are presented in Figure IV.28a and Figure IV.28b respectively. For immobilization and hybridization steps they visually show a negative shift in the characteristics.

Threshold voltage determination shows insignificant shifts of approximately $\Delta V_T = +0.1V$ for immobilization and $\Delta V_T = -0.2V$ for hybridization. Regarding the flat-band voltage, the shifts are more important: $\Delta V_{FB} = -2.1V$ for immobilization and $\Delta V_{FB} = -0.5V$ for hybridization.

This difference regarding the amplitude of the shift for the threshold and flat-band voltage could be explained by the thick silicon film and the P-type doping. The extension of the accumulation layer is higher and thus closer to the top surface than the inversion channel which is formed in the close proximity of the interface between the silicon film and the BOX [4]. Consequently the holes side might be more sensitive to the surface.

The V_B-V_G (Figure IV.28b) curves show the same behaviour as the current characteristics, by being shifted towards the negative values of V_G. The amplitude of the V_B shifts are reported in Table IV.5, for each step (GOPS deposition, immobilization and hybridization). The values were obtained by extracting the gate bias for which the body potential reaches the out-of-equilibrium regime in a forward sweeping bias (V_G from negative to positive) as detailed previously (Figure IV.14). The average shift is of $\Delta V_{B0} = -3V$ for immobilization and $\Delta V_{B0} = -0.6V$ for hybridization (obtained from the two samples). It can be noticed that the values are very close between the two tested devices. More interestingly, the amplitude of the measured shifts is higher in the case of the body potential, confirming that this method is at least as sensitive as the traditional drain current method. This is in agreement with

our previous results (Table IV.1 and Figure IV.12). Those results demonstrate that thick film devices are stable while having a good sensitivity.

Figure IV.28: I_D-V_G (a) and V_B-V_G (b) curves for different functionalization steps. Symbols used: ■ for device 2 and □ for device 5. The immobilization as well as hybridization induce a negative shift of the curves. $t_{Si}=70nm$ and $t_{BOX}=145nm$.

Table IV.5: Parameter extraction (threshold voltage, flat-band voltage and body potential) results for the thick film/BOX samples ($t_{Si}=70nm$ and $t_{BOX}=145nm$.).

	Device 2			Device 5		
	GOPS	ssDNA	dsDNA	GOPS	ssDNA	dsDNA
V_T (V)	3.4	3.5	3.3	3.3	3.4	3.2
ΔV_T (V) for step		0.2	-0.2		0.1	-0.2
V_{FB} (V)	-2.5	-4.6	-5.0	-2.1	-4.2	-4.8
ΔV_{FB} (V) for step		-2.1	-0.5		-2.1	-0.6
V_{B0} (FW) (V)	-0.3	-3.4	-3.9	-0.1	-3.1	-3.8
ΔV_{B0} (FW) (V) for step		-3.1	-0.5		-3	-0.7

However, compared to previous results (for the APTES method), after the immobilization and hybridization, a positive charge was detected as indicated by the negative shifts of the electrical characteristics. This behaviour is unusual, as it is known that the DNA molecule is negatively charged under physiological conditions [28].

This might be explained in two ways. First, the target DNA used in the GOPS functionalization did not have a fluorescent dye (Cy3 - Figure IV.29) attached compared to APTES. The dye attaches to the 5' end of the oligonucleotide via a phosphate group [29]. The basic cyanine structure has a +1 overall positive charge coming from positively charged nitrogen atom as described in [30].
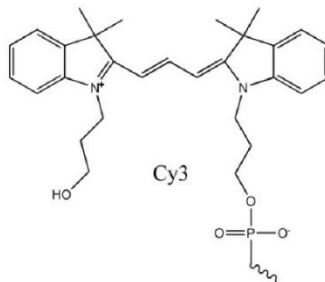
Figure IV.29: Chemical structure of the Cyanine 3 (Cy3) fluorescent dye attached to the 5' end of the target DNA strand. Reproduced from [29].

Secondly, we can also assume that during the immobilization and hybridization steps we have possibly induced charge inversion in DNA molecule. This is a counterintuitive phenomenon in which the DNA molecule – a polyanion – attracts opposite charges in excess of its own nominal charge, so that its charge changes its sign [31]–[34].

For both cases, positive charges might have also come from the immobilization and hybridization solutions employed, which were rich in Na^+ that shielded the overall negative charge of DNA molecules. It is possible that, after the washing steps, the Na^+ ions remained attached mostly to the O1P atoms in the pentose phosphate backbone [35].

We have also investigated the behaviour of a thin silicon film (t_{Si}=30nm and t_{BOX}=15nm), as it should increase the sensitivity by having the deposited charges at the top surface closer to the accumulation/inversion channel.

In the case of the thin film/BOX wafer, the I_D-V_G and V_B-V_G characteristics (Figure IV.30a and Figure IV.30b) show a negligible shift of less than 0.2V for both immobilization and hybridization (values reported in Table IV.6). The variation for both functionalization steps is very small and is similar to the measurement error in the case of the Ψ-MOSFET configuration (Appendix 2). Moreover, the difference in variability between the two tested devices can go up to 0.3V (threshold voltage for immobilization). The results can be thus considered inconclusive.

The theoretical increase in sensitivity which could be attributed to the thinner film (charges added at the top surface are closer to the inversion/accumulation channel at the film-BOX interface), might be counterbalanced by the thinner BOX (15nm versus 145nm). The ratio between the top surface oxide capacitance and the BOX capacitance is lower, which means that a smaller shift of the gate bias is needed for the exact same charge added at the top surface.
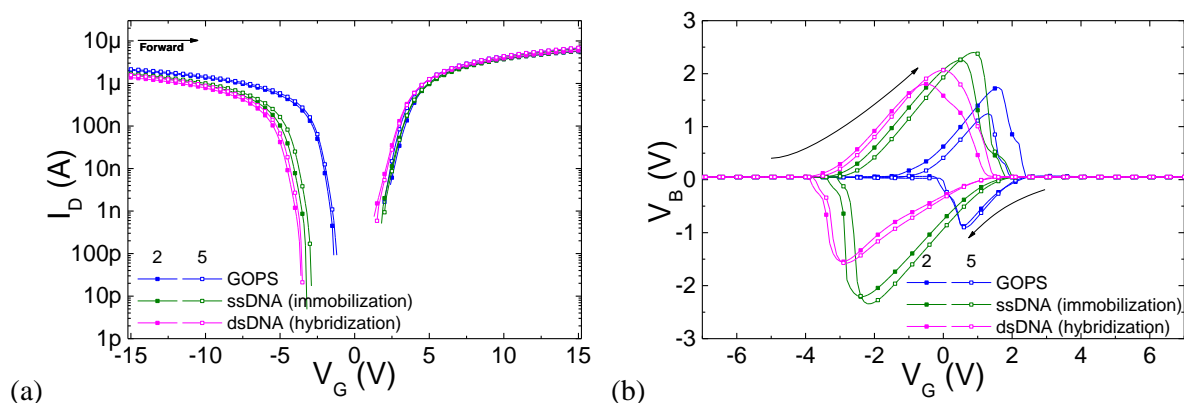

(a) (b)
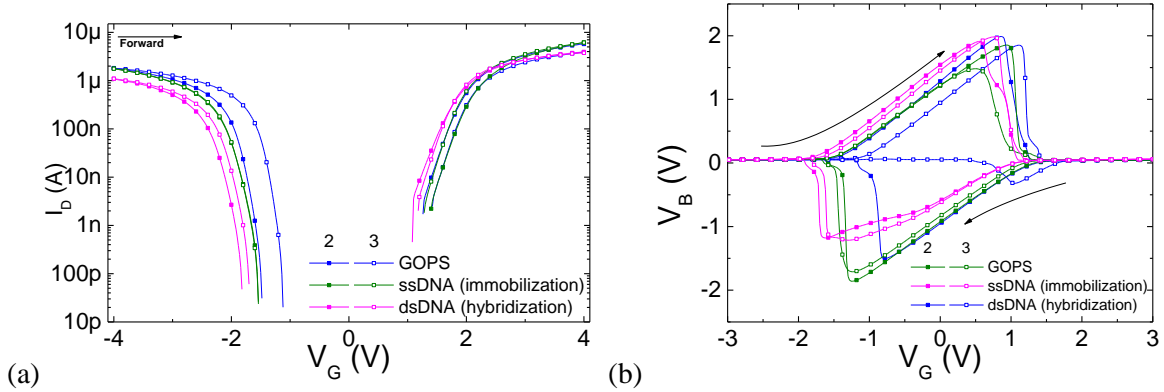
Figure IV.30: I_D-V_G (a) and V_B-V_G (b) curves after different functionalization steps. Symbols used: ■ for device 2 and □ for device 3. The immobilization as well as hybridization induce a negative shift of the curves. t_{Si}=30nm and t_{BOX}=15nm.

Table IV.6: Parameter extraction (threshold voltage, flat-band voltage) results for the thin film/BOX samples.

	Device 2			Device 5		
	GOPS	ssDNA	dsDNA	GOPS	ssDNA	dsDNA
V_T (V)	1.9	2.1	1.9	2	1.9	1.8
ΔV_T (V)		0.2	-0.2		-0.1	-0.1
V_{FB} (V)	-1.9	-2.1	-2.3	-1.7	-2.1	-2.2
ΔV_{FB} (V)		-0.2	-0.2		-0.4	-0.1

We infer that the thick silicon film/BOX devices have a more coherent behaviour and that a thinner silicon film although more advantageous theoretically in terms of sensitivity, also increases the

variability between the devices. In order to have a good sensor, a thicker BOX is preferred and the right compromise should be find for the silicon film thickness.

GOPS deposited in vapour phase: samples with different DNA concentrations

A new series of measurements was made after modifying the GOPS deposition method. The process was realized in vapour form in order to avoid the reaction of water molecules with the epoxy rings, that leads to their opening and inactivation [26] which obstructs probe DNA attachment. Moreover, four different concentrations of DNA were used in the hybridization step in order to discriminate the electric response of the DNA molecule from the one of the buffer solution and to evaluate if the calibration of the electrical response is possible.

Considering previous results, the devices were fabricated from a thick silicon film and BOX wafer (88nm/145nm respectively) which should ensure a better reproducibility of the results (as observed in the preliminary results for GOPS deposited in liquid phase). From the initial 15 devices, only four of them had gate leakage problems after GOPS deposition. They were replaced by other 5 devices for the immobilization and hybridization steps. Thus, for the last step, the 16 available devices were divided into 4 different groups of 4 which were functionalized with different concentrations of target DNA: hybridization buffer (0µM), 0.01µM, 0.1µM and 1µM. After the hybridization step, the following number of devices were still functional for the different concentrations used: buffer (3/4), 0.01µM (2/4), 0.1µM (4/4), 1µM (1/4). Despite the relatively low number of devices, a statistical study was carried out in order to estimate the figures of merit as described in chapter 1. The results are presented under the form of box plots in order to better visualize the variability. The sour areas represent the four quarters where the experimental data is distributed.

The variations in the threshold and flat-band voltages (Figure IV.31) show consistent results for the first step: GOPS shifts the curves towards positive V_G. The immobilization step induces a negative shift of ΔV_T=- 1.8V for the threshold voltage and ΔV_{FB}=-1.9V for the flat-band voltage. This is again in contradiction with the negative charge of the DNA. The buffer solution shifts V_{FB} towards positive values. This demonstrates that the buffer influence is important and emphasizes the necessity to distinguish its influence from the DNA molecule. For hybridization, the shift is also negative, being consistent with the immobilization step. Its amplitude increases with the concentration of the DNA. Although the reason why DNA induces a negative shift is not clearly established, the Ψ-MOSFET response is clearly proportional to the target DNA concentration.
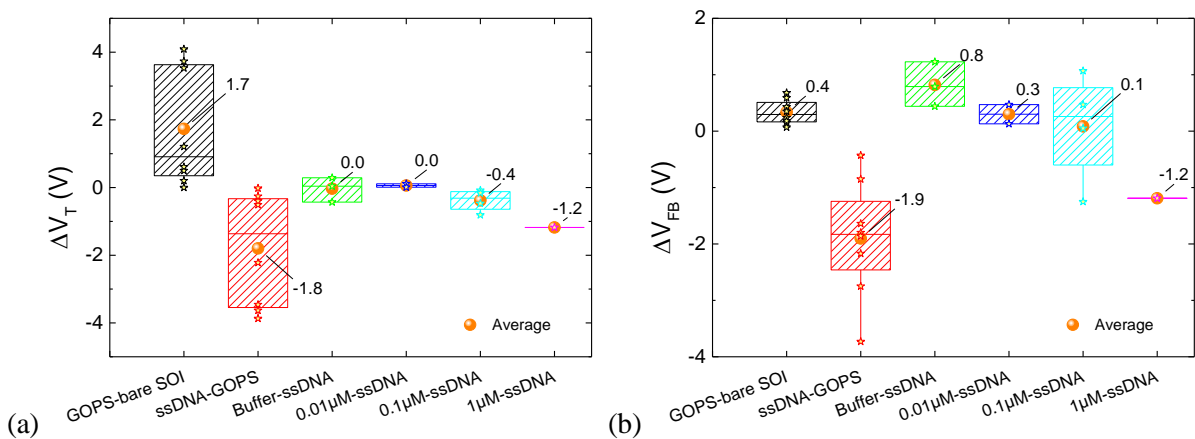

Figure IV.31: Relative variations of V_T (a) and V_{FB} (b) for different functionalization steps. Extracted values from each device are indicated by ✦ symbols. Parameter extraction results for the thick film/BOX measurements. t_{Si}=88nm and t_{BOX}=145nm.

The relative V_B measurements for each device were represented in Figure IV.32 for a forward sweeping direction (gate voltage from negative to positive). The shifts are consistent with the current measurements (Figure IV.31), the ΔV_{B0} shift induced by GOPS deposition being positive, while for immobilization it is negative. For hybridization, measurements show a clear negative trend, which increases with the DNA concentration, proving again that this type of measurements are exclusively sensitive to the DNA molecule and not only to the buffer solution.
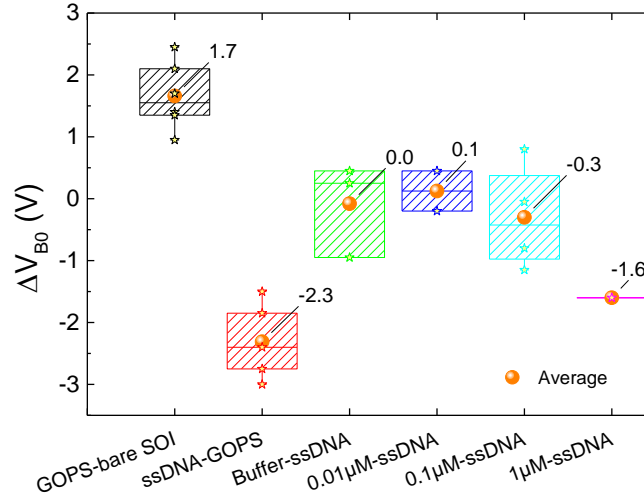
Figure IV.32: Relative variations of body potential in forward sweep for different functionalization steps. Extracted values from each device are indicated by ★ symbols. Parameter extraction results for the thick film/BOX measurements. t_{Si}=88nm and t_{BOX}=145nm.

The calibration curve $\frac{\Delta V_{T/FB/B0\,(c\%)} - \Delta V_{T/FB/B0\,(buffer)}}{\log(c/c_0)}$ $vs.\log(c/c_0)$ (Figure IV.33 - cf. Chapter 1) was traced in order to determine the sensitivity of the device for the hybridization step. The average values of ΔV_T, ΔV_{FB} and ΔV_{B0} were used for the three concentrations of DNA (from 0.01μM to 1μM). It can be observed an exponential variation of the sensitivity with the concentration, the maximum sensitivity corresponding to the 1μM concentration. The calculated estimations are of 0.38, 0.67 and 0.50 V/decade of concentration of target DNA for ΔV_T, ΔV_{FB} and ΔV_{B0} respectively.
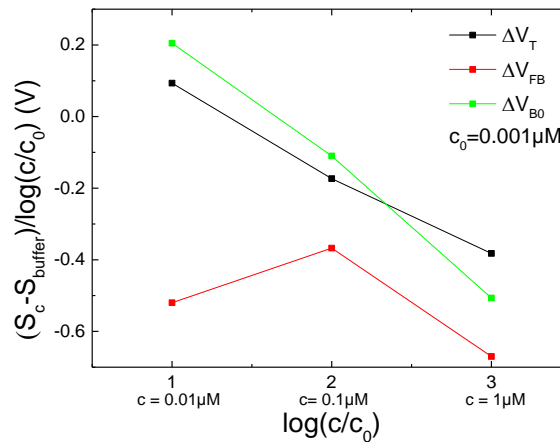
Figure IV.33: Calibration curve for the three extracted parameters (ΔV_T, ΔV_{FB} and ΔV_{B0}). The reference concentration (c_0) was set to 0.001μM for a good representation of the results. t_{Si}=88nm and t_{BOX}=145nm.

The limit of detection can be calculated using the formula presented in Chapter 1:

$$S_{dl} = \overline{S_{bl}} + k \cdot \sigma_{bl} \qquad (IV.7)$$

Where S_{dl} is the analyte signal at the detection limit, $\overline{S_{bl}}$ is the average signal for reagent blank, k is a numerical factor in accordance with the confidence level and σ_{bl} is the standard deviation for reagent blank. In our case, the signal is represented by ΔV_T, ΔV_{FB} and ΔV_{B0} and the reagent blank is the hybridization buffer solution.

It is important to mention that the measurement uncertainty (present in the standard deviation) of the determined parameters (ΔV_T, ΔV_{FB} and ΔV_{B0}) comes from three sources: the variability between the devices (approximately 300mV – cf. Appendix 2), measurement variability on the same device (100mV– cf. Appendix 2) and the variability of the chemical treatment. The limit of detection is determined using the standard deviation of the chemical treatment. By presenting the results under the form of a relative variation between two functionalization steps for each device, the variability between the devices is not integrated in the results. Also, the measurement variability between the devices is very low compared to the others and can thus be neglected. We can thus estimate the standard deviation of the reagent blank by calculating it directly from the values of ΔV_T, ΔV_{FB} and ΔV_{B0} obtained for the buffer solution. Moreover, as the number of devices for this particular step is low (only 3), the formula for the sample standard deviation was used $\left(\sigma = \sqrt{\frac{\Sigma(x-\bar{x})^2}{n-1}} \right)$ so that the result would be as close as possible to the one obtained from a larger number of devices. The sample standard deviation for the three parameters is presented in Table IV.7.

Table IV.7: Sample standard deviation for reagent blank (buffer solution).

	ΔV_T	ΔV_{FB}	ΔV_{B0}
σ_{bl} (V)	0.36	0.39	0.76

The limit of detection was determined by establishing the level of the signal (for ΔV_T, ΔV_{FB} and ΔV_{B0}) for which the amplitude is higher than the standard deviation of the reagent blank (buffer solution). The factor of confidence was set to k=1. In Figure IV.34 the extracted values of ΔV_T, ΔV_{FB} and ΔV_{B0} are presented with an offset so that the mean value of the buffer solution is 0. It can be observed that in all cases, only the 1µM concentration exceeds the calculated level of minimum detection and can thus be considered the limit of detection for our device.

(a)

(b)

(c)
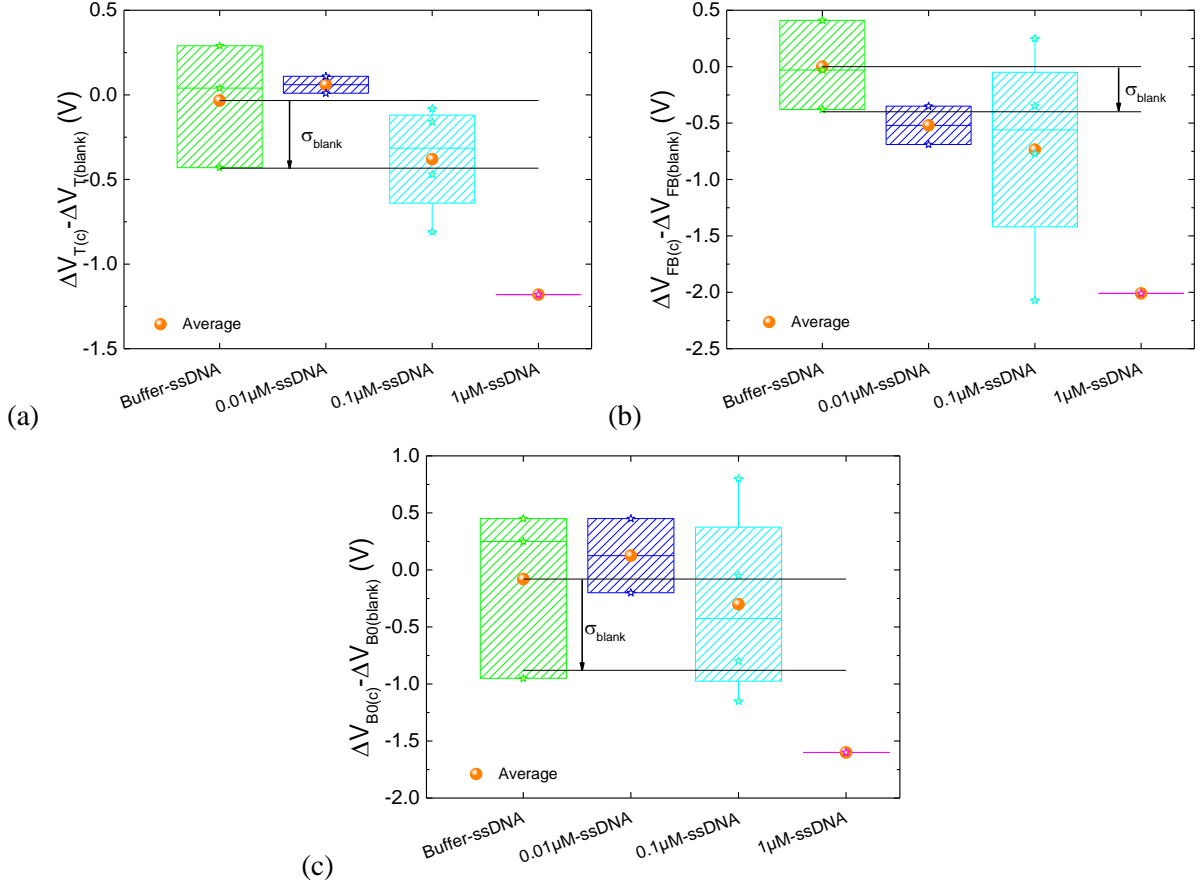
Figure IV.34: Determination of the limit of detection for the three parameters ΔV_T (a), ΔV_{FB} (b) and ΔV_{B0} (c). t_{Si}=88nm and t_{BOX}=145nm.

4.4. Conclusion and figures of merit of the body potential method

All results considered, the Ψ-MOSFET was able to clearly detect a concentration of 1µM of DNA (for ΔV_T, ΔV_{FB} and ΔV_{B0}). This is very high compared to the nanowire counterparts, which can reach 1fM [36]–[41]. This is mainly determined by the very large surface of our device.

The supplementary charge per surface unit added by a certain molecule can be estimated:

$$\frac{Q_{SUP}}{S} = \frac{n \cdot c_{molecule} \cdot V}{S} \tag{IV.8}$$

where: n is the number of charges added by a mole of molecules to the top surface, $c_{molecule}$ is the concentration of the molecule used in the solution, V is the volume of the solution and S the active surface of the sensor.

The formula indicates that, in order to have the same density of added charges, a smaller surface of the device needs a lower concentration of the molecule for the same effect. In our case, a 4mm in diameter drop of DNA solution (obtained by visual estimation) deposited at the top surface covers a surface of 50mm², whereas a 10µm long nanowire with a height and a width of 50nm has a sensing area of $1.5 \cdot 10^{-6}$ mm² (considering the three exposed sides of the device). As the quantity of DNA solution added was similar to the one used in the literature (several µL), the difference of surface would mean an equivalent limit of detection of 30 fM for our method if the active surfaces were equal. In this respect,

the reduction of the surface of the device would be necessary in order to ameliorate the sensitivity and nanowire dimensions should be approached.

As determined by the calibration curves, the maximum sensitivity is obtained for 1µM of concentration and it is estimated at approximately 0.5V/decade of concentration of target DNA. In this regard, a broader study should be carried out for a much wider range of concentrations of target DNA and for a higher number of devices.

The results show that the body-potential method is able to perfectly match the results obtained from the traditional current measurements in the Ψ-MOSFET configuration. The main advantage of this method is that it can exploit the subthreshold regime of a device whilst measuring a potential instead of a very low current. With a careful choice of device characteristics, the measuring can be realized at gate voltages close to 0V, which is very advantageous because (1) the molecule layer is disturbed less by the weak electric field and (2) it emphasizes the charge effect of the molecule as opposed to its dielectric effect as described in [25].

A summary of the conclusions drawn after every functionalization step is presented in Table IV.8.

Table IV.8: Summary of the goals and conclusions for every measurement session

Measurements campaign 1: APTES and gold nanoparticles (88nm/145nm)

Goals	*Conclusions*
• Proof of concept for charge detection by body potential measurements	• Ψ-MOSFET detects both positive and negative charges in current and body-potential measurements

Measurements campaign 2: DNA attachment using APTES (70nm/145nm)

Goals	*Conclusions*
• Proof of concept for DNA detection	• Very consistent results with low variability and good detection of DNA both in immobilization and hybridization

Measurements campaign 3: DNA attachment using APTES 2 (70nm/145nm)

Goals	*Conclusions*
• Implementation of body potential measurements • Study of the electrical response of the blocking step	• Body potential detected DNA in hybridization by discriminating the influence of the blocking buffer • the blocking buffer is a limiting factor and needs to be removed

Measurements campaign 4: DNA attachment using GOPS (liquid)

Goals	*Conclusions*
• Implementation of the GOPS attachment process in liquid phase • Characterization realized after every functionalization step • DNA without fluorescent dye for hybridization • Use of both thin film (30/15) and thick (70/145) film SOI	• Robustness problems of the devices • Better consistency of the results on thick film SOI compared to thin film as previously observed • For immobilization and hybridization shift in opposite direction compared to APTES

Measurements campaign 5: DNA attachment using GOPS (vapour)

Goals	*Conclusions*
• GOPS attached in vapor phase • For hybridization DNA in different concentrations (buffer (0), 0.01µM, 0.1µM, 1µM)	• Confirmation of the previous results in terms of shift • Different shifts for different concentrations of DNA which proved the influence of DNA hybridization only

Bibliography

[1] S. M. Sze and K. N. Kwok, *Physics of Semiconductor Devices*, 3rd ed. Hoboken, New Jersey: John Wiley & Sons, 2007.

[2] S. Cristoloveanu, D. Munteanu, and M. S. Liu, 'A review of the pseudo-MOS transistor in SOI wafers: operation, parameter extraction, and applications', *IEEE Trans. Electron Devices*, vol. 47, no. 5, pp. 1018–1027, 2000.

[3] G. Hamaide, F. Allibert, H. Hovel, and S. Cristoloveanu, 'Impact of free-surface passivation on silicon on insulator buried interface properties by pseudotransistor characterization', *J. Appl. Phys.*, vol. 101, no. 11, p. 114513, Jun. 2007.

[4] F. Balestra, S. Cristoloveanu, M. Benachir, J. Brini, and T. Elewa, 'Double-gate silicon-on-insulator transistor with volume inversion: A new device with greatly enhanced performance', *IEEE Electron Device Lett.*, vol. 8, no. 9, pp. 410–412, Sep. 1987.

[5] N. Rodriguez, S. Cristoloveanu, and F. Gamiz, 'Revisited Pseudo-MOSFET Models for the Characterization of Ultrathin SOI Wafers', *IEEE Trans. Electron Devices*, vol. 56, no. 7, pp. 1507–1515, Jul. 2009.

[6] N. Rodriguez, S. Cristoloveanu, T. Nguyen, and F. Gamiz, 'Impact of the top surface density of states on the characteristics of ultrathin SOI pseudo-MOSFETs', presented at the EUROSOI Workshop, Cork, Ireland, 2008.

[7] I. Ionica, A. E. H. Diab, and S. Cristoloveanu, 'Gold nanoparticles detection using intrinsic SOI-based sensor', in *Nanotechnology (IEEE-NANO), 2011 11th IEEE Conference on*, 2011, pp. 38–43.

[8] C. Fernandez, N. Rodriguez, C. Marquez, and F. Gamiz, 'Determination of ad hoc deposited charge on bare SOI wafers', in *Ultimate Integration on Silicon (EUROSOI-ULIS), 2015 Joint International EUROSOI Workshop and International Conference on*, 2015, pp. 289–292.

[9] T. He *et al.*, 'Controlled Modulation of Conductance in Silicon Devices by Molecular Monolayers', *J. Am. Chem. Soc.*, vol. 128, no. 45, pp. 14537–14541, Nov. 2006.

[10] S.-H. Jung, J.-M. Kim, L.-M. Jung, Y.-H. Lee, S. Cristoloveanu, and Y. H. Bae, 'Pseudo-Mosfet Analysis of Proton Irradiated and Annealed SOI Wafer', in *ECS Transactions*, San Francisco, CA, 2009, pp. 329–334.

[11] E. Souteyrand *et al.*, 'Direct Detection of the Hybridization of Synthetic Homo-Oligomer DNA Sequences by Field Effect', *J. Phys. Chem. B*, vol. 101, no. 15, pp. 2980–2985, Apr. 1997.

[12] '(3-Aminopropyl)triethoxysilane Datasheet'. Sigma-Aldrich.

[13] D. A. Giljohann, D. S. Seferos, W. L. Daniel, M. D. Massich, P. C. Patel, and C. A. Mirkin, 'Gold Nanoparticles for Biology and Medicine', *Angew. Chem. Int. Ed.*, vol. 49, no. 19, pp. 3280–3294, Apr. 2010.

[14] N. Majoul, S. Aouida, and B. Bessaïs, 'Progress of porous silicon APTES-functionalization by FTIR investigations', *Appl. Surf. Sci.*, vol. 331, pp. 388–391, Mar. 2015.

[15] G. Ghibaudo, 'New method for the extraction of MOSFET parameters', *Electron. Lett.*, vol. 24, no. 9, p. 543, 1988.

[16] A. K. Y. Wong and U. J. Krull, 'Surface characterization of 3-glycidoxypropyltrimethoxysilane films on silicon-based substrates', *Anal. Bioanal. Chem.*, vol. 383, no. 2, pp. 187–200, Sep. 2005.

[17] R. O. Beauchamp, 'A Critical Review of the Toxicology of Glutaraldehyde', *Crit. Rev. Toxicol.*, vol. 22, no. 3–4, p. 32, 1992.

[18] S. D. Chandradoss, A. C. Haagsma, Y. K. Lee, J.-H. Hwang, J.-M. Nam, and C. Joo, 'Surface Passivation for Single-molecule Protein Studies', *J. Vis. Exp.*, no. 86, Apr. 2014.

[19] Y. Han, D. Mayer, A. Offenhäusser, and S. Ingebrandt, 'Surface activation of thin silicon oxides by wet cleaning and silanization', *Thin Solid Films*, vol. 510, no. 1–2, pp. 175–180, Jul. 2006.

[20] E. Pavlovic, A. P. Quist, U. Gelius, and S. Oscarsson, 'Surface Functionalization of Silicon Oxide at Room Temperature and Atmospheric Pressure', *J. Colloid Interface Sci.*, vol. 254, no. 1, pp. 200–203, Oct. 2002.

[21] T. Denhardt, 'A membrane-filter technique for the detection of complementary DNA', *Biochem. Biophys. Res. Commun.*, vol. 23, no. 5, p. 6, 1966.

[22] 'http://www.biomers.net/'. .

[23] E. T. Vandenberg *et al.*, 'Structure of 3-aminopropyl triethoxy silane on silicon oxide', *J. Colloid Interface Sci.*, vol. 147, no. 1, pp. 103–118, 1991.

[24] R. N. Barnett, 'Charge Migration in DNA: Ion-Gated Transport', *Science*, vol. 294, no. 5542, pp. 567–571, Oct. 2001.

[25] J.-H. Ahn *et al.*, 'Charge and dielectric effects of biomolecules on electrical characteristics of nanowire FET biosensors', *Appl. Phys. Lett.*, vol. 111, no. 11, p. 113701, Sep. 2017.

[26] S. J. Stropoli and M. J. Elrod, 'Assessing the Potential for the Reactions of Epoxides with Amines on Secondary Organic Aerosol Particles', *J. Phys. Chem. A*, vol. 119, no. 40, pp. 10181–10189, Oct. 2015.

[27] S. Williams, P. Davies, J. Bowen, and C. Allender, 'Controlling the Nanoscale Patterning of AuNPs on Silicon Surfaces', *Nanomaterials*, vol. 3, no. 1, pp. 192–203, Mar. 2013.

[28] Y.-W. Wang and G.-C. Yang, 'Modulation and control of DNA charge inversion', *Chin. Phys. B*, vol. 26, no. 12, p. 128706, Dec. 2017.

[29] B. G. Moreira, Y. You, and R. Owczarzy, 'Cy3 and Cy5 dyes attached to oligonucleotide terminus stabilize DNA duplexes: Predictive thermodynamic model', *Biophys. Chem.*, vol. 198, pp. 36–44, Mar. 2015.

[30] J. S. Ploem, 'Future" Review, Biotechnology, vol. 3 (Apr. 1985).', p. 21, 1993.

[31] Y. Wang, R. Wang, B. Cao, Z. Guo, and G. Yang, 'Single Molecular Demonstration of Modulating Charge Inversion of DNA', *Sci. Rep.*, vol. 6, no. 1, Dec. 2016.

[32] J. L. F. Abascal, M. Domercq, and J. C. Gil Montoro, 'Computer Simulation of the Ionic Atmosphere around Z-DNA', *J. Phys. Chem. B*, vol. 110, no. 49, pp. 25080–25090, Dec. 2006.

[33] B. Luan and A. Aksimentiev, 'Electric and electrophoretic inversion of the DNA charge in multivalent electrolytes', *Soft Matter*, vol. 6, no. 2, pp. 243–246, 2010.

[34] A. A. Kornyshev, 'Physics of DNA: unravelling hidden abilities encoded in the structure of "the most important molecule"', *Phys. Chem. Chem. Phys.*, vol. 12, no. 39, p. 12352, 2010.

[35] Y. Cheng, 'Similarities and differences in interaction of K+ and Na+ with condensed ordered DNA. A molecular dynamics computer simulation study', *Nucleic Acids Res.*, vol. 34, no. 2, pp. 686–696, Jan. 2006.

[36] J. Hahm and C. M. Lieber, 'Direct Ultrasensitive Electrical Detection of DNA and DNA Sequence Variations Using Nanowire Nanosensors', *Nano Lett.*, vol. 4, no. 1, pp. 51–54, Jan. 2004.

[37] E. Stern, A. Vacic, and M. A. Reed, 'Semiconducting Nanowire Field-Effect Transistor Biomolecular Sensors', *IEEE Trans. Electron Devices*, vol. 55, no. 11, pp. 3119–3130, Nov. 2008.

[38] G.-J. Zhang *et al.*, 'Highly sensitive measurements of PNA-DNA hybridization using oxide-etched silicon nanowire biosensors', *Biosens. Bioelectron.*, vol. 23, no. 11, pp. 1701–1707, Jun. 2008.

[39] C.-J. Chu *et al.*, 'Improving Nanowire Sensing Capability by Electrical Field Alignment of Surface Probing Molecules', *Nano Lett.*, vol. 13, no. 6, pp. 2564–2569, Jun. 2013.

[40] A. Gao *et al.*, 'Signal-to-Noise Ratio Enhancement of Silicon Nanowires Biosensor with Rolling Circle Amplification', *Nano Lett.*, vol. 13, no. 9, pp. 4123–4130, Sep. 2013.

[41] G. Wenga, E. Jacques, A.-C. Salaün, R. Rogel, L. Pichon, and F. Geneste, 'Step-gate polysilicon nanowires field effect transistor compatible with CMOS technology for label-free DNA biosensor', *Biosens. Bioelectron.*, vol. 40, no. 1, pp. 141–146, Feb. 2013.

Chapter 5 GENERAL CONCLUSIONS AND PROSPECTS

Table of Contents

5.1. General conclusions

In this thesis, we focused on field-effect biosensors based on a silicon on insulator platform. One of the advantages of SOI is that it allows a double gate configuration that provides an increased sensitivity due to the coupling effect between the top and the bottom gate [1], [2]. However, no study took advantage of the floating body effects which are also sensitive to the charge state of the top-gate oxide and which have already been used for DRAM memories [3], [4].

Our study proposes a new reading paradigm based on the out-of-equilibrium body potential of SOI, which is measured instead of the classical conduction/current usually employed. This body potential appears due to the difficulty of injecting carriers in the silicon film when sweeping between the accumulation and inversion regimes. It is a consequence of the electrical isolation of the SOI structure with respect to the bulk and the fact that carriers in the channel can only be provided through the source and drain contacts. Our study uses the Ψ-MOSFET configuration because it offers a simple and large SOI platform suitable for proof-of-concept of the detection. Its structure is composed of a 5x5mm² silicon film where two metallic probes placed on the top silicon film play the role of source and drain and the buried oxide is used as a gate dielectric. This enables a direct contact between the deposited molecules and the structure, allowing a straightforward influence of the deposited surface charges on the conduction channel.

In order to achieve our goal, the thesis was structured into three successive steps, each one providing essential information for the following.

- First, as the out-of-equilibrium body potential is directly related with charge injection through the source and drain contacts, we began by investigating the contacts formed by the metallic probes and the silicon film;
- Subsequently, we implemented the body potential measurements in the Ψ-MOSFET configuration, studied the relationship between the measured parameters and proposed a simplified structure for the biochemical sensing. At the end of this stage, simulations of the body potential confirmed that this method is able to detect charges deposited at the top surface;
- Based on those elements, we showed that the body potential can be used for DNA detection.

Ψ-MOSFET contacts through a nanoindentation perspective

The metallic probes on silicon should theoretically have a Schottky behaviour, but manifest an ohmic one [5]. Craters left after probe positioning, which are a consequence of the extruded material, lead us to investigate an explanation based on nanoindentation. In fact, it is well documented that silicon under a compressive stress higher than approximatively 12 GPa transforms into its metastable allotropic form (Si-II) which has metallic properties [6]. We investigated the possibility that the ohmic behaviour of the contacts in the Ψ-MOSFET configuration might be a consequence of this allotropic transformation.

Two different thicknesses were used for this analysis: 88nm and 12nm, the buried oxide being 145nm thick for both cases. For the thicker silicon film, the drain current versus the pressure characteristics in both the accumulation and in the inversion regimes showed a great resemblance with the ones found in the literature for bulk silicon substrates [7], which hinted that the hypothesis of the metallic phase formation might be correct to explain the ohmic behaviour. For all the pressures available in the range of the probe station, the contacts were ohmic all along. This was not the case for the thin film, where the probes reached the BOX interface from a low pressure (confirmed by the AFM image

and literature [8]). Therefore, there is no physical space under the probes to form the metallic phase of silicon. The critical pressure needs to be reached laterally by the propagation of the compressive stress in the silicon film, in order to lead to the metallic phase formation. The drain current measurements show that at a threshold of approximately 70g is necessary in the accumulation regime so that the contact transforms from Schottky to ohmic.

Moreover, drain current measurements in load-unload cycles showed no hysteresis, proving that contact characteristics are only dependant on pressure. This fact disproves the hypothesis that defects are responsible for the ohmic behaviour of the Ψ-MOSFET contacts, as they would already be created during the first loading phase and should not disappear upon unloading. Also, the lower pressure necessary in the case of a thicker film contradicts the idea that the pressure needs to be high enough to reach the conduction channel.

All the electrical measurements conducted in our investigation are in agreement with the hypothesis that the ohmic contacts in the Ψ-MOSFET configuration are the result of the silicon allotropic transformation, which is an original explanation.

Out-of-equilibrium body potential characteristics in Ψ-MOSFET

The measurement of the body potential (V_B) in the Ψ-MOSFET configuration implied the use of a third probe which took the role of the body contact of a FD-SOI transistor. We observed that the out-of-equilibrium body potential appeared in the depletion region, where the injection of charges the accumulation/inversion channel through the source and drain probes is blocked which indices an out-of-equilibrium state in the silicon film, in which V_B follows V_G. The gate current peak, which appears in the same region, is a displacement current which indicated the charging of the BOX capacitance. V_B derivative with respect to V_G was directly linked to the I_G.

This method proved to be advantageous firstly due to the fact that V_B was measured in a range with a very low current, which means that it is not strongly affected by the access resistance. Indeed, the body potential is not dependant on the pressure applied on the probes nor on the position of those. Moreover, the experiments could be realized without the drain probe, which only provides information about the conduction in the inversion/accumulation channel, but is not mandatory for the V_B measurement. This allows a great degree of freedom in the design of a biosensor.

The out-of-equilibrium regime was simulated using a structure in which the contained both N^+ and P^+ regions in order to have a conduction in both the accumulation and the inversion regimes and the V_B response appeared as in the experiments. The addition of charged molecules at the top surface of the device induced a shift in the electrical characteristics, including in V_B, which proved the concept of such a sensing method. This allowed us to pursue in the last chapter to the experimental part of biochemical detection using well known functionalization methods.

Out-of-equilibrium body potential method towards DNA detection

The Ψ-MOSFET is a simple, but effective technique which has already been used as a sensor for many applications such as APTES ((3-Aminopropyl)triethoxysilane), gold nanoparticles [9], [10] and molecules with electron-donating capabilities [11] detection as well as radiations [12].

We began from the APTES and gold nanoparticle detection realized on the Ψ-MOSFET [9] using the traditional drain current measured shift. This result was compared with the proposed body potential method, which showed that the obtained shifts in electrical characteristics are similar [13].

We subsequently used a more sophisticated functionalization method based on APTES for DNA detection. The procedure was validated using drain current measurements [14] and then compared to the body potential measurements which were consistent with the I_D-V_G response. This step served as a

first experimental proof of concept that V_B is related to the charges added on the top surface by functionalization.

The next step in the evolution of our work was realized by using a simplified functionalization process based on GOPS ((3-Glycidyloxypropyl)trimethoxysilane). This method was also validated using a comparison between drain current and body potential measurements. Our study was concluded by using different concentrations for the target DNA, which revealed an electrical response proportional to the DNA concentration and a limit of detection of 1μM. Considering that in the case of a nanowire, the density of charges on the active surface is the same, the structure is capable of replicating the fM limit achieved in the literature is an equivalent surface reduction is achieved.

All elements considered, the out-of-equilibrium body potential method is beneficial due to the following advantages: (1) it measures an important voltage instead of a weak current in the subthreshold region, (2) it permits fast transient measurements, (3) due to the low V_G voltage needed, the molecule layer is disturbed less by the electric field.

5.2. Prospects

This thesis aimed at assessing the feasibility of the out-of-equilibrium body potential method for sensing applications. The study was conducted in a large spectrum of subjects which may all be further developed.

First, the nanoindentation based theory describing the ohmic contact behaviour in the Ψ-MOSFET may be also tested using specific crystallographic apparatus which allows the precise measurement of the applied charge on the probes. The contact problem might also be avoided by using deposited contacts, although their behaviour might not be ohmic.

The body potential measurements may also be rendered more practical for sensing purposes by implementing fast sweeping speeds imposed by AC signals. In this sense, simulations might also be improved in order to perfectly match the experimental data.

From a sensor perspective, further development should target the large surface area of the device which does not allow a good control of the position, the drying conditions and the uniformity of the deposited analyte concentration. For this, a reduction in the size of the device and/or a microfluidic channel must be considered in order to have a performance level of interest (e.g; lower detection limit). This can be further scaled in order to be used as a mean of detecting unique events such as the signal of neurons. Moreover, larger measurement campaigns are also necessary in order to clearly determine sensor characteristics (sensitivity, limit of detection, linear regime, etc.).

All these preliminary results demonstrate the large potential of the body potential measurements for sensing applications, consisting a great opportunity for future research.

Bibliography

[1] H.-J. Jang and W.-J. Cho, 'Performance Enhancement of Capacitive-Coupling Dual-gate Ion-Sensitive Field-Effect Transistor in Ultra-Thin-Body', *Sci. Rep.*, vol. 4, Jun. 2014.

[2] Y.-J. Huang *et al.*, 'High performance dual-gate ISFET with non-ideal effect reduction schemes in a SOI-CMOS bioelectrical SoC', in *2015 IEEE International Electron Devices Meeting (IEDM)*, Washington, DC, USA, 2015, pp. 29.2.1-29.2.4.

[3] M. Bawedin, S. Cristoloveanu, and D. Flandre, 'A Capacitorless 1T-DRAM on SOI Based on Dynamic Coupling and Double-Gate Operation', *IEEE Electron Device Lett.*, vol. 29, no. 7, pp. 795–798, Jul. 2008.

[4] J. Lacord *et al.*, 'MSDRAM, A2RAM and Z ^{2} -FET performance benchmark for 1T-DRAM applications', in *2018 International Conference on Simulation of Semiconductor Processes and Devices (SISPAD)*, Austin, TX, 2018, pp. 198–201.

[5] S. Williams, S. Cristoloveanu, and G. Campisi, 'Point contact pseudo-metal/oxide/semiconductor transistor in as-grown silicon on insulator wafers', *Mater. Sci. Eng. B*, vol. 12, no. 1–2, pp. 191–194, 1992.

[6] J. Z. Hu, L. D. Merkle, C. S. Menoni, and I. L. Spain, 'Crystal data for high-pressure phases of silicon', *Phys. Rev. B*, vol. 34, no. 7, p. 4679, 1986.

[7] J. E. Bradby, J. S. Williams, and M. V. Swain, '*In situ* electrical characterization of phase transformations in Si during indentation', *Phys. Rev. B*, vol. 67, no. 8, Feb. 2003.

[8] W. Van Den Daele, C. Malaquin, N. Baumel, O. Kononchuk, and S. Cristoloveanu, 'Adaptation of the pseudo-metal–oxide–semiconductor field effect transistor technique to ultrathin silicon–on-insulator wafers characterization: Improved set-up, measurement procedure, parameter extraction, and modeling', *J. Appl. Phys.*, vol. 114, no. 16, p. 164502, Oct. 2013.

[9] I. Ionica, A. E. H. Diab, and S. Cristoloveanu, 'Gold nanoparticles detection using intrinsic SOI-based sensor', in *Nanotechnology (IEEE-NANO), 2011 11th IEEE Conference*, 2011, pp. 38–43.

[10] C. Fernandez, N. Rodriguez, C. Marquez, and F. Gamiz, 'Determination of ad hoc deposited charge on bare SOI wafers', in *Ultimate Integration on Silicon (EUROSOI-ULIS), 2015 Joint International EUROSOI Workshop and International Conference*, 2015, pp. 289–292.

[11] T. He *et al.*, 'Controlled Modulation of Conductance in Silicon Devices by Molecular Monolayers', *J. Am. Chem. Soc.*, vol. 128, no. 45, pp. 14537–14541, Nov. 2006.

[12] S.-H. Jung, J.-M. Kim, L.-M. Jung, Y.-H. Lee, S. Cristoloveanu, and Y. H. Bae, 'Pseudo-Mosfet Analysis of Proton Irradiated and Annealed SOI Wafer', in *ECS Transactions*, San Francisco, CA, 2009, pp. 329–334.

[13] L. Benea, M. Bawedin, C. Delacour, and I. Ionica, 'Out-of-equilibrium body potential measurements in pseudo-MOSFET for sensing applications', *Solid-State Electron.*, vol. 143, pp. 69–76, May 2018.

[14] L. Benea *et al.*, 'Ψ-MOSFET Configuration for DNA Detection', Proceeding of CAS 2018, Romania, 2018.

APPENDIXES

Appendix 1

The model for passivated films ($D_{it2} = 2 \times 10^{11}$ cm^{-2}eV^{-1}) considers the concentration and thus the influence of the interface traps negligible and ignores the film doping concentration compared to the inversion charge of mobile carriers. By integrating the local mobile charge and by using the drain current relationship in the linear region the following formulation is obtained for the threshold voltage which accounts for the interface traps at the silicon – BOX interface and shows thickness dependence:

$$V_T = 2\Phi_{FB} + \frac{2kT}{q}\left(1 + \frac{C_{it1}}{C_{BOX}}\right) ln\left[\frac{1}{t_{Si}}\sqrt{\frac{2kT\varepsilon_{Si}}{q^2 n_i}}\right] \tag{A.1}$$

The model for non-passivated surfaces is obtained using different hypothesis. As the interface trap concentration is high ($D_{it2} = 2 \times 10^{13}$ cm^{-2}eV^{-1}), the surface potential tends to pin to 0 and the electric field cannot be considered as equal to 0. Numeric simulations show that the electric field tends to be constant across the film [1]. The equation for the threshold voltage is in this case the following:

$$V_T = V_{FB} + 2\Phi_F\left(1 + \frac{C_{it1}}{C_{BOX}} + \frac{C_{Si}C_{it2}}{C_{BOX}(C_{Si} + C_{it2})}\right) \tag{A.2}$$

The previous models diverge for silicon films thinner than 50nm, the superposition of the two can be written under the following form:

$$V_T = V_{FB} + \frac{2kT}{q}\left(1 + \frac{C_{it1}}{C_{BOX}}\right) ln\left[\frac{1}{t_{Si}}\sqrt{\frac{2kT\varepsilon_{Si}}{q^2 n_i}}\right] + 2\Phi_F\left(1 + \frac{C_{it1}}{C_{BOX}} + \frac{C_{Si}C_{it2}}{C_{BOX}(C_{Si} + C_{it2})}\right) \tag{A.3}$$

For passivated films, however, in order to ensure a good fit, equation (A.4) can be empirically modified to fit the experimental data:

$$V_T = 2V_{FB} + \frac{2kT}{q}\left(1 + \frac{\Upsilon}{t_{Si}}\frac{C_{it1}}{C_{BOX}}\right) ln\left[\frac{1}{t_{Si}}\sqrt{\frac{2kT\varepsilon_{Si}}{q^2 n_i}}\right] \tag{A.4}$$

where γ is a fitting parameter which artificially increases the interface trap density in ultrathin films.
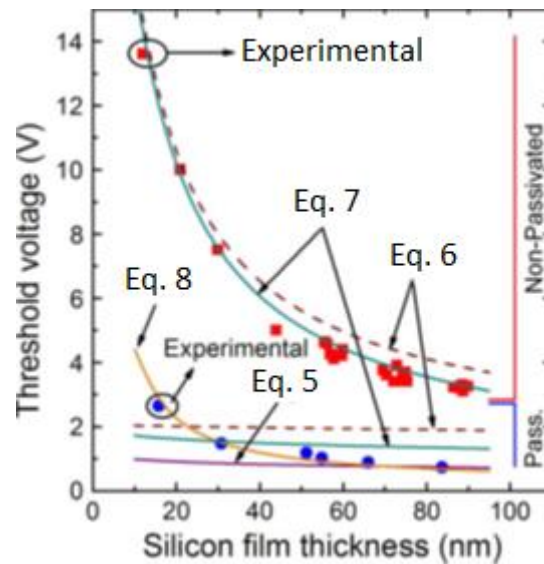
Figure A.1: Threshold voltage vs. film thickness. Comparison between various models, numerical simulations and experimental data [2].

Bibliography

[1]   N. Rodriguez, S. Cristoloveanu, and F. Gamiz, 'Revisited Pseudo-MOSFET Models for the Characterization of Ultrathin SOI Wafers', *IEEE Trans. Electron Devices*, vol. 56, no. 7, pp. 1507–1515, Jul. 2009.

[2]   N. Rodriguez, S. Cristoloveanu, T. Nguyen, and F. Gamiz, 'Impact of the top surface density of states on the characteristics of ultrathin SOI pseudo-MOSFETs', presented at the EUROSOI Workshop, Cork, Ireland, 2008.

Appendix 2

To address the variability of the Ψ-MOSFET device, multiple experiments were considered. The samples used were fabricated from a SOI wafer having t_{Si}=88nm and t_{BOX}=145nm. First, by repeating the measurements with the probes placed in the same position, then, with the probes placed slightly on different positions on the same island (but remaining close to the middle to have a stable geometrical factor fg) and finally for different devices. In all circumstances, the maximum variation between the curves was examined. The results are summarized in the table below. It is important to notice, in the case of the measurements realized with the probes placed on the same position for example, that the variability of the curves is much lower in the subthreshold regime, while for gate voltages higher than the threshold voltage or lower than the flat band voltage, the drain current is very different due to the differences in the series resistance induced by the probes. This is reflected in the body potential characteristics, where the curves follow very similar paths.

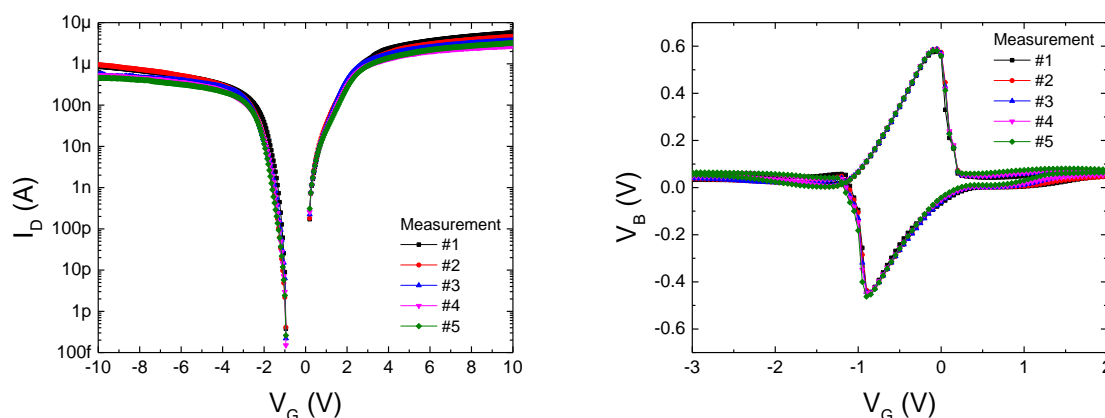|	Maximum voltage shift in accumulation	Maximum voltage shift in inversion
	Same position	
I_D - V_G curve	100mV	50mV
V_B - V_G curve	50mV	50mV
	Different position	
I_D - V_G curve	150mV	50mV
V_B - V_G curve	150mV	150mV
	Different devices	
I_D - V_G curve	300mV	300mV
V_B - V_G curve	300mV	300mV

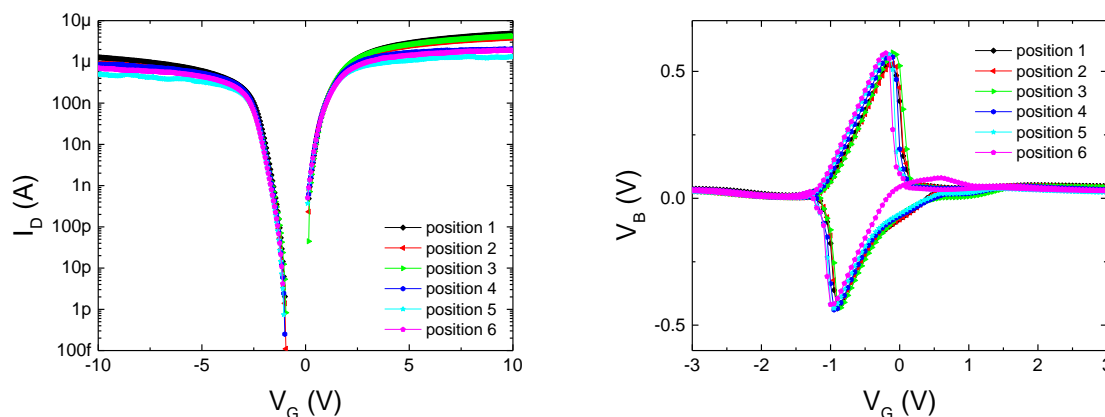*Figure A.2: I_D-V_G and V_B-V_G measurements for the same dye and position. t_{Si}=88nm and t_{BOX}=145nm.*

Figure A.3: I_D-V_G and V_B-V_G measurements for the same dye on different position. t_{Si}=88nm and t_{BOX}=145nm.

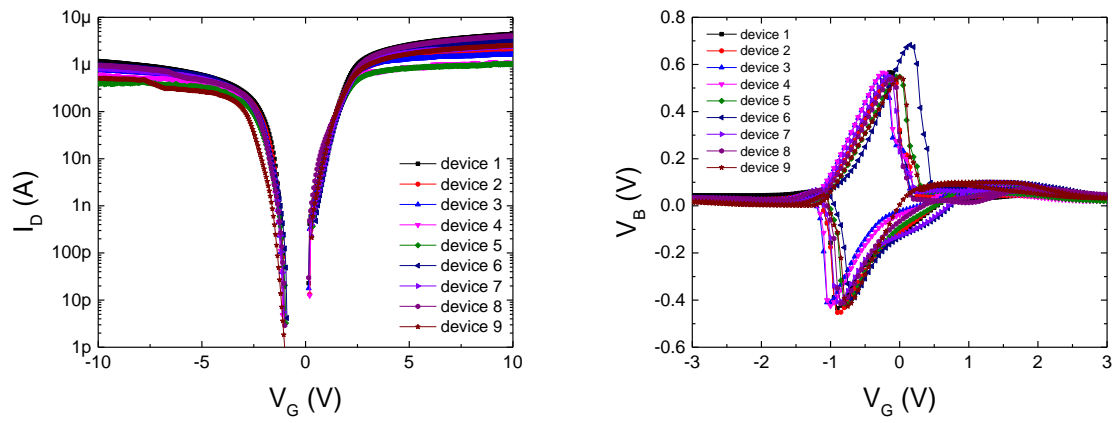*Figure A.4: I_D-V_G and V_B-V_G measurements for different devices of the same type. t_{Si}=88nm and t_{BOX}=145nm.*

List of publications

Journal articles

Benea, L., Bawedin, M., Delacour, C. and Ionica, I., 2018. Out-of-equilibrium body potential measurements in pseudo-MOSFET for sensing applications. Solid-State Electronics, 143, pp.69-76.

Sato, S., Ghibaudo, G., **Benea, L**., Ionica, I., Omura, Y. and Cristoloveanu, S., 2019. Impact of contact and channel resistance on the frequency-dependent capacitance and conductance of pseudo-MOSFET. Solid-State Electronics, 159, pp.197-203.

Alepidis, M., **Benea, L**., Bucci, D., Mescot, X., Bawedin, M. and Ionica, I., 2019. Experimental and simulation investigation of the out-of-equilibrium phenomena on the Pseudo-MOSFET configuration under transient linear voltage ramps. Solid-State Electronics, p.107721.

Conferences and workshops

Benea, L., Cerba, T., Bawedin, M., Delacour, C., Cristoloveanu, S. and Ionica, I., 2018, March. Nanoindentation effects on the electrical caracterizaron in Ψ-MOSFET configuration. In 2018 Joint International EUROSOI Workshop and International Conference on Ultimate Integration on Silicon (EUROSOI-ULIS) (pp. 1-4). **Poster.**

Benea, L., Bawedin, M., Cristoloveanu, S., Ionica, I., Banu, M., Simion, M., Kusko, M. and Delacour, C., 2018, October. Ψ-MOSFET Configuration for DNA Detection. In 2018 International Semiconductor Conference (CAS) (pp. 143-146). **Presentation.**

Sato, S., Omura, Y., Ghibaudo, G., **Benea, L.** and Cristoloveanu, S., 2018, March. Detailed analysis of frequency-dependent impedance in pseudo-MOSFET on thin SOI film. In 2018 Joint International EUROSOI Workshop and International Conference on Ultimate Integration on Silicon (EUROSOI-ULIS) (pp. 1-4). **Poster.**

Benea, L., Bawedin, M., Delacour, C., Cristoloveanu, S. and Ionica, I., 2017, April. Out-of-equilibrium body potential measurements in pseudo-MOSFET for biosensing. In 2017 Joint International EUROSOI Workshop and International Conference on Ultimate Integration on Silicon (EUROSOI-ULIS) (pp. 19-22). **Presentation.**

Benea, L., Banu, M., Bawedin, M., Delacour, C., Simion, M., Kusko, M., Cristoloveanu, S., Ionica, I., 2018, November. DNA detection using the Ψ-MOSFET configuration. In Semi-conducting Nanomaterials for Health, Environment and Security Applications, Grenoble, France. **Presentation.**

Vindret, M., **Benea, L.**, Ionica, I., Delacour, C., Xavier, P., Martins, J., Rauly, D., Chamberod, E., 2018, November. Electrical detection of bacteria on SOI film using the pseudo-MOSFET configuration. In Semi-conducting Nanomaterials for Health, Environment and Security Applications, Grenoble, France. **Presentation.**

Seminars

Benea, L., Bawedin, M., Delacour, C., Cristoloveanu, S. and Ionica, I., 2016, Capteurs innovants en technologie FD-SOI basés sur la détection d'un potentiel hors équilibre, Journées Scientifiques de l'IMEP-LAHC, Bernin, France.

Benea, L., Bawedin, M., Delacour, C., Cristoloveanu, S. and Ionica, I., 2016, Ψ-MOSFET for Biosensing, National Institute for Research and Development in Microtechnologies seminar, Bucharest, Romania.

Mesures de potentiel hors-équilibre sur substrats SOI : implémentation et applications pour la détection biochimique

- résumé en français -

I. Introduction et contexte

Dans cette thèse, nous proposons un nouveau paradigme pour la détection biochimique basé sur les effets de corps flottant (« floating body » en anglais) dans des substrats de silicium sur isolant (SOI), utilisés dans la configuration Ψ-MOSFET. L'originalité de notre approche réside dans le fait qu'au lieu de mesurer le décalage induit par les charges des molécules sur les caractéristiques statiques courant-tension, nous avons développé une nouvelle méthode basée sur le potentiel hors équilibre qui sera décrite dans les parties suivantes.

Le premier chapitre fournit le contexte et les motivations de cette thèse. Dans cette partie, après étude approfondie sur l'état de l'art, une attention particulière est accordée aux capteurs à effet de champ.

Le principe de fonctionnement des biocapteurs à effet de champ est basé sur le fait que la charge ou le potentiel électrochimique induit par les molécules biologiques à la surface de l'oxyde de grille (Figure 1a) décale les caractéristiques électriques du dispositif et, par conséquent, la détection est réalisée (Figure 1b). Ce décalage peut être mesuré par une variation de courant (ΔI) ou de tension (ΔV).

(a)   (b)
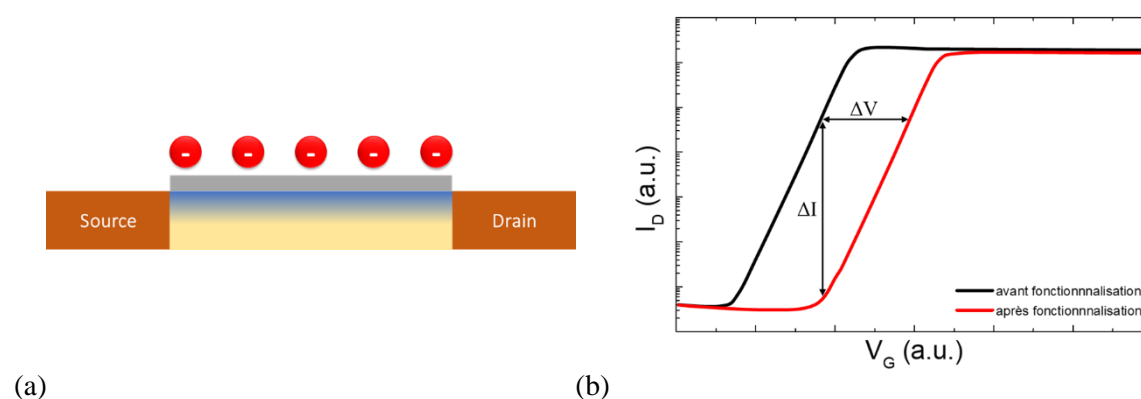
Figure 1: Dispositif avec des molécules chargées (a) et décalage des caractéristiques électriques suite à la déposition des molécules (b).

Depuis la découverte du transistor ISFET (Ion-Sensitive Field Effect Transistor) de Piet Bergveld en 1970 [1] destiné aux mesures neurophysiologiques, le transistor à effet de champ a été développé sous de nombreuses formes afin de produire des détecteurs rapides et fiables de virus [2], des détecteurs [3] ou séquenceurs [4] d'ADN ou détecteurs de l'activité neuronale [5]. L'avantage des transistors à effet de champ est que les dimensions du dispositif peuvent être réduites, tout en augmentant sa sensibilité et donc la résolution des capteurs pour la détection d'un événement/d'une molécule unique. Jusqu'à présent, de nombreuses structures de capteurs ont été proposées à cet effet : nanofils de silicium [6], nanotubes de carbone [7], transistors à base de graphène [8] ou transistors MOSFET classiques [9]. Les capteurs basés sur les nanofils de silicium sont la solution la plus populaire qui ont permis de détecter des concentrations d'ADN allant jusqu'au niveau de fM [10]–[16].

Notre recherche est basé sur l'utilisation de la technologie silicium sur isolant car elle offre un large spectre de phénomènes spécifiques provenant de la configuration à double grille : les phénomènes de couplage ou les effets de « floating body » [17]. Ces phénomènes particuliers peuvent être exploités pour des applications de détection.

Le premier élément à prendre en compte dans les transistors SOI est leur structure à double grille. En effet, en plus de la grille avant du FET, le substrat peut servir de grille arrière, l'oxyde enterré (burried oxide, BOX) servant de diélectrique de grille (Figure 2). Les caractéristiques de la conduction à travers le film de silicium sont donc le résultat d'une combinaison des deux actions de grille. Généralement, la capacité de la grille arrière est plus basse que celle de la grille avant, ainsi une variation de potentiel à la grille avant équivaut à une modification plus importante à la grille arrière, en raison du rapport entre les deux capacités. Un exemple de cet effet a été montré par Ayele et al. [18]. Des transistors FD-SOI en technologie 28nm appliqués à la mesure de pH avec une lecture en grille arrière ont montré une sensitivité de 730mV/pH, soit 12 fois la limite Nerstienne de 59mV/pH. Cette amplification est essentiellement due aux effets de couplage.
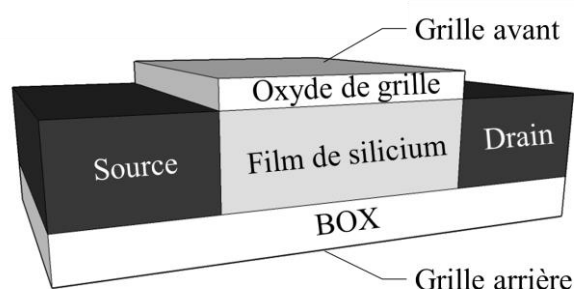

Figure 2: Structure d'un transistor réalisé en technologie SOI.

Alors que la configuration à double grille était utilisée pour la détection dans les SOI et autres nanodispositifs, aucune étude précédente n'a pas utilisé les effets de « floating body » pour réaliser la détection. Le potentiel hors-équilibre apparaît dans la région à faible conduction du transistor (le régime de déplétion) et est fortement influencée par les charges environnantes (de la même manière que la tension de seuil du transistor). Par conséquent, nous pourrions imaginer un capteur basé sur ces observations, ce qui était l'objectif de cette thèse.

Cette méthode a été implémentée dans une configuration 2D, nommée Ψ-MOSFET (pseudo-MOSFET). Elle offre une plate-forme SOI simple et de grande taille, adaptée à la validation du principe de la détection. Sa structure est composée d'un film de silicium de 5x5mm² sur lequel deux pointes métalliques sont placées et qui jouent le rôle de la source et du drain et où l'oxyde enterré est utilisé comme diélectrique de grille. Ceci permet un contact direct entre les molécules déposées et la structure, permettant une influence directe des charges superficielles déposées sur le canal de conduction.

Notre étude comporte trois éléments clés qui sont abordés dans les différents chapitres :

- les contacts dans le Ψ-MOSFET (chapitre 2), leur nature et leur capacité à empêcher/faciliter l'arrivée de porteurs pour la formation du canal, sachant que la manque des porteurs est un élément essentiel du potentiel hors-équilibre;
- la configuration électrique des mesures du potentiel hors-équilibre dans la configuration Ψ-MOSFET (chapitre 3);
- la détection utilisant le potentiel hors-équilibre en configuration Ψ-MOSFET (chapitre 4).

II. Etude des contacts métal - semiconducteur dans la configuration Ψ-MOSFET

La configuration Ψ-MOSFET a été utilisée avec succès pour la caractérisation électrique du substrat SOI depuis 1992 [19]. Cette approche utilise la structure de transistor inversé innée d'un substrat SOI, où le substrat de mécanique de silicium est utilisé en tant que grille et l'oxyde enterré (BOX) comme diélectrique de grille. Le courant de drain (I_D) est mesuré entre deux pointes métalliques placées sur la plaque SOI à pression contrôlée, jouant le rôle de source et de drain (Figure 3a). La conduction est réalisée par des électrons ou des trous en fonction de la polarité du potentiel appliqué sur la grille. Outre sa simplicité d'utilisation, la physique des contacts n'est toujours pas bien comprise. Même si les pointes métalliques (en carbure de tungstène) posées sur un film de silicium faiblement dopé (10^{15} cm^{-3}) devraient en principe se comporter comme un contact de type Schottky, les courbes I_D-V_D révèlent des contacts ohmiques (Figure 3b).
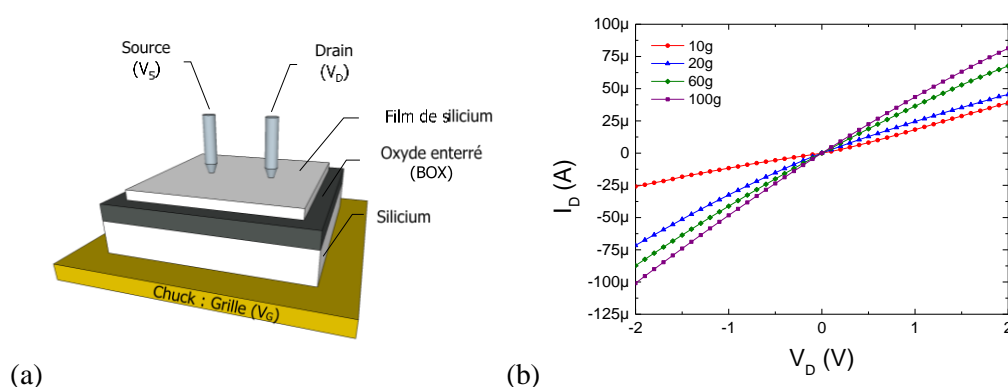

Figure 3: (a) Configuration expérimentale du Ψ-MOSFET. (b) Courant de drain en fonction de la tension du drain pour différentes pressions de pointe en régime d'inversion ($V_G = 7V$, $V_D = 0.1V$). Film (88nm) et BOX (145nm) épais.

Les effets de la pression sur les pointes dans la configuration Ψ-MOSFET ont déjà été documentés [20]. On observe une diminution de la résistance des contacts avec l'augmentation de la pression appliquée. Egalement, du point de vue cristallographique, la phase Si I (utilisée en microélectronique) qui a une structure cubique à faces centrées, subit une transformation allotropique pour des chargements supérieurs à 11 GPa [21]. La nouvelle phase trouvée à des hautes pressions, Si-II, a une structure tétragonale de type β-Sn et un comportement métallique [22]. Un déchargement rapide privilégie la formation du silicium amorphe, alors qu'un déchargement lent favorise la formation de deux autres formes cristallographiques du silicium : Si-III et Si-XII.

Dans le cadre de notre étude, nous avons utilisé des substrats de deux épaisseurs différentes : 88nm et 12nm. Pour le film épais (88 nm), la forme de la courbe courant de drain en fonction de la pression appliquée sur les pointes est similaire à celle trouvée dans la littérature pour le silicium « bulk » [23] . En régime d'inversion (Figure 4a), le courant de drain suit le même chemin pendant deux cycles consécutifs de chargement/déchargement.

Dans le régime d'accumulation (Figure 4b), la forme de la courbe I_D en fonction de la pression est légèrement différente de celle en régime d'inversion. La distinction est faite pendant le déchargement, où pour des pressions inférieures à 20g, le courant de drain est négligeable. Cette dissymétrie entre les phases de charge et décharge pour différentes conditions de polarisation a également été présentée dans [23]. Ceci suggère que la phase Si-II (silicium métallique) a un effet important sur la conduction par des trous.
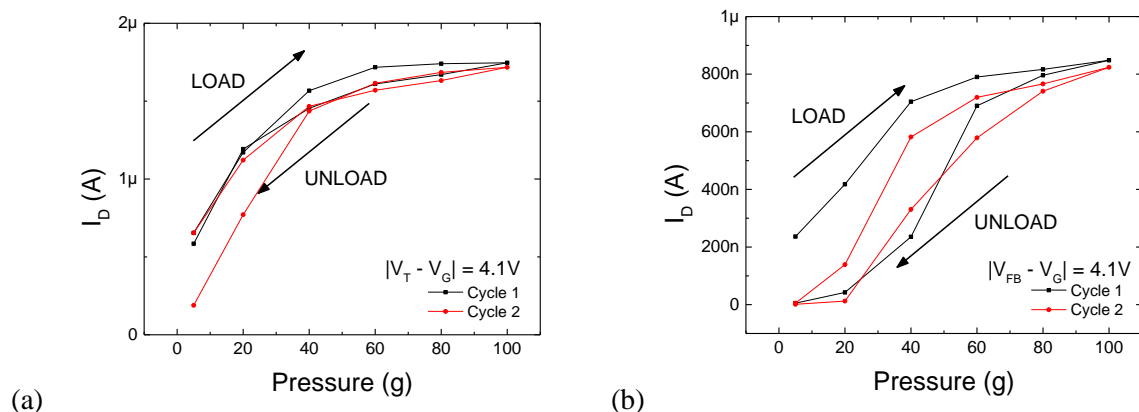
Figure 4: Courant de drain en fonction de la pression des pointes. Film (88 nm) et BOX (145 nm) épais. Mesures effectuées en régime d'inversion (a) (V_G = 6V, V_D = 0.1V, V_T = 2.1V) et en régime d'accumulation (b) (V_G = -5V, V_D = 0.1V, V_{FB} = -1.1V).

Le comportement élastique observé dans les mesures électriques peut être corroboré par l'image FIB-TEM qui révèle un cratère laissé par le matériau extrudé et une microstructure du film de silicium dans la zone qui se trouve au voisinage de la zone d'impact (Figure 5).
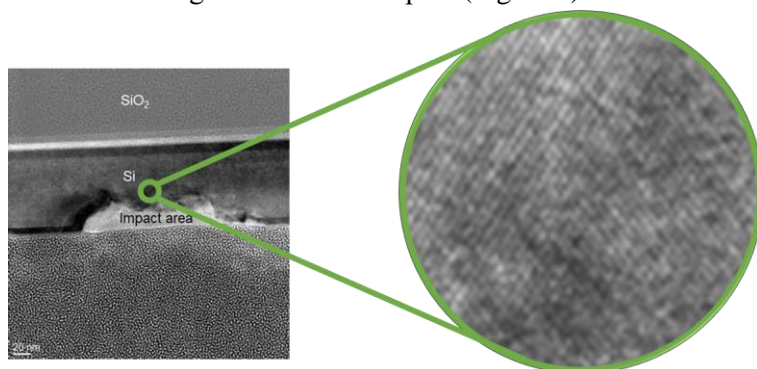

Figure 5: Image FIB-TEM de la puce SOI et du cratère laissé après le chargement de la pointe à 90 g (à gauche) et zoom sur la zone d'impact (à droite). Film de silicium (88 nm) et BOX (145 nm) épais. [24]

Dans le cas d'un film mince (12 nm), les mesures électriques montrent une augmentation du courant de drain qui ne commence qu'à partir d'une pression seuil d'environ 50 g pour les électrons et de 70 g pour les trous (Figure 6). Ceci suggère que la formation de phase Si-II apparaît pour des pressions plus élevées pour cette épaisseur de film. Le mécanisme peut être lié à la proximité de l'interface Si-SiO$_2$. Comme étudié dans [25] pour un film de silicium de 12 nm d'épaisseur et une BOX de 25 nm, la dégradation de l'oxyde due à la pénétration de la pointe se produit même à partir de 15 g. Cela signifie que pour cette épaisseur, la formation de Si-II sous la pointe n'est pas possible. Par conséquent, nous pouvons supposer que la phase de haute pression du silicium apparaît latéralement comme une conséquence de l'étalement latéral de la contrainte de compression, mais cela peut nécessiter des pressions plus importantes.
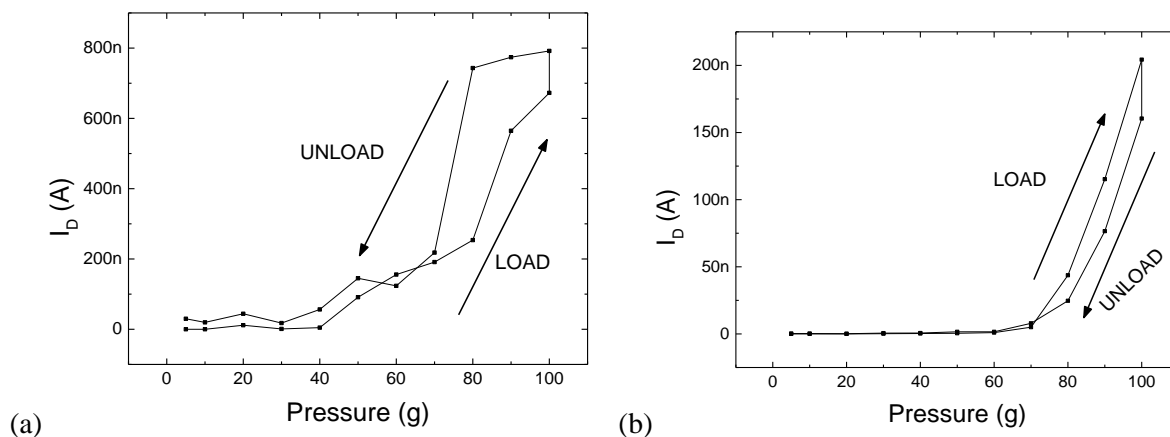
Figure 6: Courant de drain en fonction de la pression des pointes. Film mince (12 nm) et BOX épais (145 nm). Mesures effectuées en régime d'inversion (a) (V_G = 16V, V_D = 0.1V, V_T = 11.2V) et en régime d'accumulation (b) (V_G = -12V, V_D = 0.1V, V_{FB} = -7.1V).

La modification du type de contact à partir d'une pression seuil est également soulignée par les caractéristiques I_D-V_D tracées dans le régime d'accumulation (Figure 7). Entre 60g et 80g, la forme du courant de drain se modifie complètement, évoluant vers une caractéristique ohmique. Cette transformation ne se produit pas dans le cas d'un film épais (figure 10), où la formation de la phase Si-II a lieu sous la pointe.
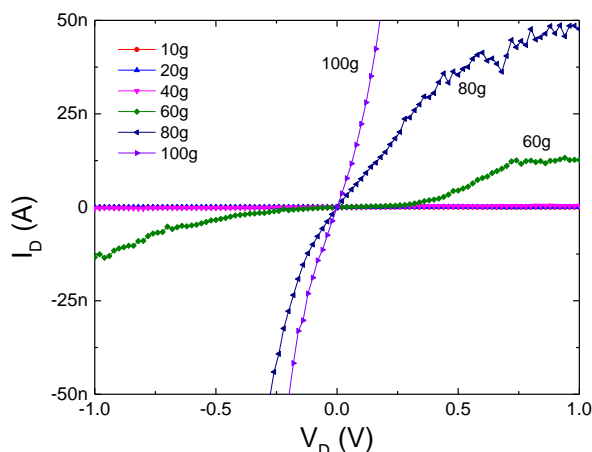

Figure 7: Courant de drain en fonction de la tension de drain pour différentes pressions de pointe dans des conditions d'accumulation pour film mince de 12nm (V_G = -12V, V_D = 0.1V).

De plus, l'image AFM d'un cratère montrant la marque de la pointe chargée à une pression de 100 g (la valeur maximale pouvant être appliquée pendant les mesures électriques) indique une profondeur maximale de 15 nm (Figure 8), ce qui signifie que la pointe de la pointe atteint le BOX. Comme la formation de la phase Si-II a lieu dans la région sous la pointe pour le silicium « bulk » d'après les simulations atomistiques [22], on peut confirmer alors que la transformation de la phase Si-II a lieu latéralement dans le cas du film mince.

En conclusion, nous avons proposé dans ce chapitre une explication originale du comportement ohmique des contacts en Ψ-MOSFET, en se basant sur l'apparition d'une phase métallique sous l'effet de la pression appliquée sur les pointes.
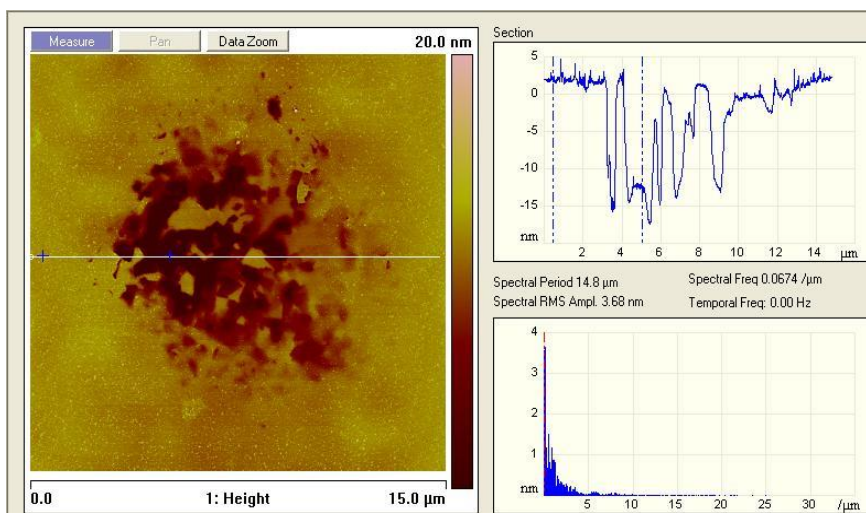
Figure 8: Image AFM (à gauche) et profondeur du cratère laissée par la pointe chargée à 100g en coupe (à droite). Film de silicium mince (12 nm) et BOX épais (145 nm).

III. Mesures de potentiel hors-équilibre sur le Ψ-MOSFET

Dans les transistors FD-SOI, le potenteil hors-équilibre est mesuré grâce à des contacts supplémentaires de body [26]. Dans le cas du Ψ-MOSFET, une troisième pointe a été rajoutée entre la source et le drain pour mesurer V_B (Figure 9).
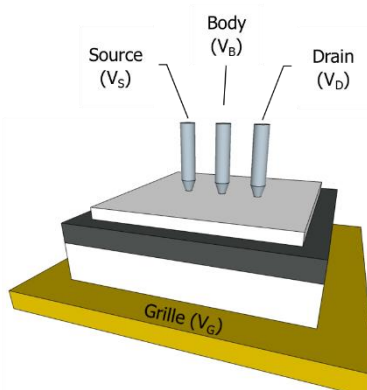

Figure 9: Configuration pour les mesures de potentiel hors-équilibre dans le Ψ-MOSFET.

III.1. Mesure du potentiel hors-équilibre dans la configuration Ψ -MOSFET

La première partie du travail a été consacrée à la recherche de la configuration correcte de mesure et à l'étude de la relation entre les principaux paramètres de ce type de mesure, à savoir le courant de drain (I_D), le potentiel hors-équilibre (V_B) et le courant de grille (I_G) en fonction de la tension de la grille (V_G). La Figure 10 présente les trois paramètres principaux de la méthode du potentiel hors-équilibre (I_D, V_B et I_G) pour différentes directions de balayage de la polarisation de la grille - de l'accumulation à l'inversion (Forward) et de l'inversion à l'accumulation (Reverse).

La variation du potentiel hors-équilibre a lieu dans la région de déplétion, où le courant de drain est négligeable et où le passage d'un canal de trous à un canal d'électrons (ou l'inverse) est imposé par la variation de V_G. Lorsque la grille est balayée de l'accumulation vers l'inversion (Figure 10a), V_B augmente avec un comportement quasi-linéaire, en suivant V_G, puis diminue brusquement lorsque le canal d'inversion commence à se former. Une réponse équivalente peut être observée lorsque la grille

est balayée de l'inversion à l'accumulation (Figure 10b). Cependant, étant donné que les porteurs impliqués ont des polarités opposées, le potentiel a dans ce cas des valeurs négatives.

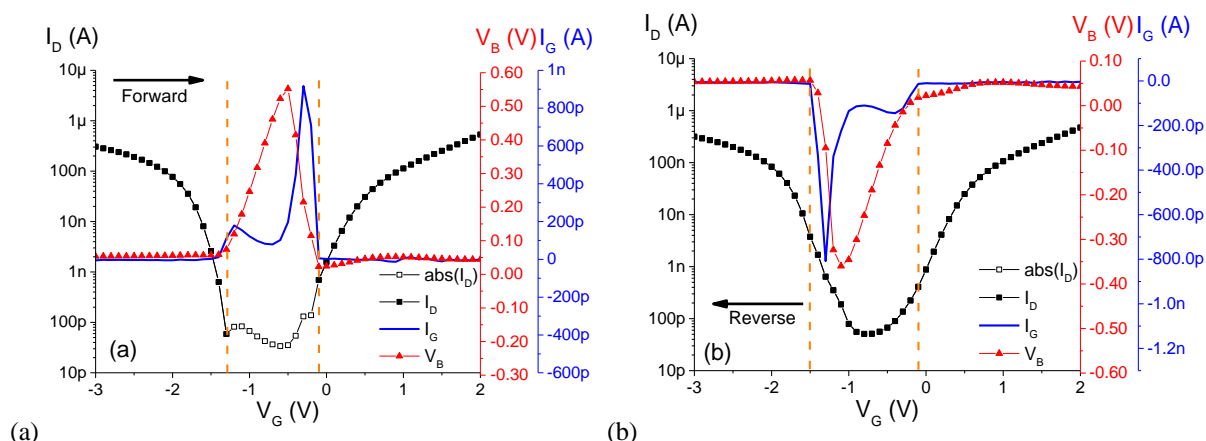(a)   (b)

Figure 10: Courant de drain, potentiel hors-équilibre et courant de grille en fonction du potentiel de la grille. Balayage de l'accumulation à l'inversion (a) et de l'inversion à l'accumulation (b).

Dans le but de simplifier la configuration expérimentale, nous avons investigué l'utilité de la pointe du drain. Le potentiel hors-équilibre et le courant de la grille sont tracés en fonction de la tension de la grille pour trois configurations différentes: avec trois pointes et V_D égaux à 0,1 V et 0 V ou avec deux pointes uniquement (sans la pointe du drain). On peut remarquer que l'absence de pointe du drain n'entraîne qu'une légère augmentation du V_B (ainsi que du pic de courant de grille) (Figure 11). En effet, la pointe du drain, lorsqu'elle est connectée et polarisée, facilite l'évacuation / l'injection de porteurs dans le film (pendant le régime d'accumulation ou d'inversion). Autres expériences ont montré également que le potentiel hors-équilibre est invariable par rapport à : (1) la position des pointes, (2) la distance entre les pointes et (3) la pression appliquée sur les pointes [27].

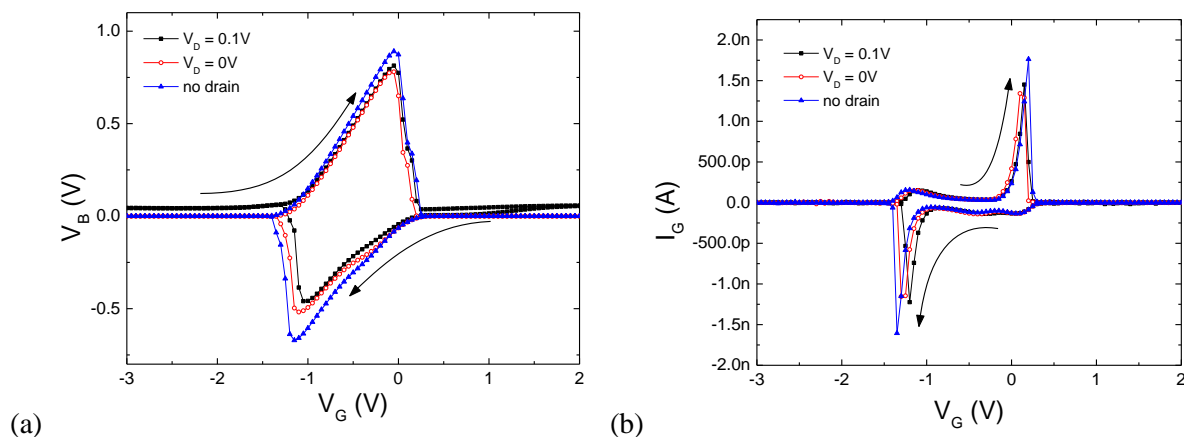(a)   (b)

Figure 11: Potentiel hors-équilibre (a) et courant de grille (b) en fonction de la tension de grille pour différentes configurations de la pointe du drain. Pas de mesure 50mV, P=100g. $t_{Si} = 88nm$, $t_{BOX} = 145nm$.

III.2. Simulation du potentiel hors-équilibre dans la configuration Ψ -MOSFET

Le grand défi pour simuler en TCAD le comportement du Ψ -MOSFET réside dans la manière d'implémenter des contacts métal-film de silicium. Nous avons utilisé la configuration simplifiée à deux contacts construits de deux régions dopés fortement N$^+$ et P$^+$ ($N_D = N_A = 10^{20}$ cm^{-3}) qui permettent de mesurer une conduction réalisée par des électrons et des trous (correspondant aux régimes d'inversion et d'accumulation). Un contact a donc été relié à la masse et utilisé comme source et pour l'autre, nous avons soit imposé une condition de courant nul pour la mesure de potentiel hors-équilibre, soit une tension de drain de 0.1V pour la mesure de l'I$_D$ (Figure 12).

Figure 12: Structure utilisée pour la simulation du potentiel hors-équilibre.

Le courant de drain et le potentiel hors-équilibre ont été simulés dans les mêmes conditions que pour les mesures expérimentales. La tension de la grille a été balayée entre -8V et + 8V, reproduisant exactement les conditions expérimentales. En raison de la structure des contacts qui récupèrent les électrons et les trous à différents endroits dans le film de silicium, les courbes de courant de drain ne sont pas identiques à celles expérimentales (Figure 13a). Pour la même raison, les courbes de potentiel hors-équilibre sont également similaires, mais ont des amplitudes différentes selon la direction de balayage (Figure 13b).

(a) (b)
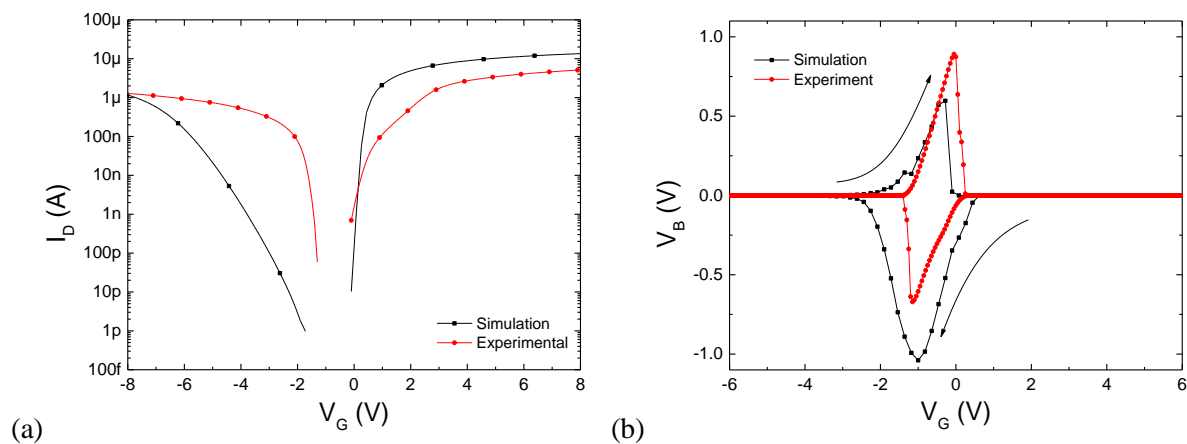
Figure 13: Courbes correspondant au courant de drain (a) et au potentiel hors-équilibre (b) en fonction de la tension de grille.

En utilisant cette structure, nous avons essayé d'anticiper la réponse de la structure fonctionnalisée avec des molécules chargées de différentes polarités et concentrations. Dans ce sens, la structure présentée dans la Figure 12 a été modifiée en ajoutant une couche de dioxyde de silicium de 3 nm d'épaisseur afin de reproduire l'oxyde natif / de passivation sur le film de silicium et une couche de charges imposée directement par un contact (figure 14).
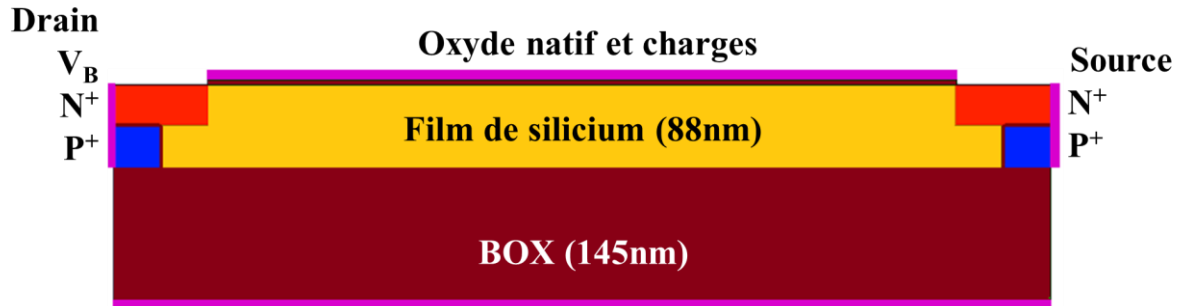
Figure 14: Structure modifiée avec une couche d'oxyde de 3nm (équivalente à l'oxyde natif/ de passivation) sur laquelle des charges étaient rajoutées

Nous avons tracé le courant de drain et le potentiel hors-équilibre simulés par rapport à la tension de la grille (figure 15a). La première montre un décalage négatif lorsque la charge ajoutée varie du négative vers positive, comme prévu par les modèles MOSFET classiques. Le décalage est nettement plus faible dans l'accumulation que dans l'inversion en raison de la structure des contacts qui récupèrent le courant de trous à partir de l'interface film de silicium – oxyde enterré et des électrons plus proches de la partie supérieure du film de silicium où l'influence des charges est plus importante.

Dans le cas des mesures de potentiel (Figure 15b), on peut observer un décalage négatif pour les charges positives et un décalage positif pour les charges ajoutées négatives. Le pic de potentiel est d'autant plus bas que la charge devient plus positive. La sensibilité obtenue est d'environ 400 mV / 10^{16} C, déterminée en mesurant la distance entre les valeurs maximales de V_B. Cela nous permet de conclure que la mesure du potentiel hors-équilibre est une méthode de détection fiable qui peut être utilisée pour détecter des molécules chargées ajoutées à la surface du dispositif.


Figure 15: Simulations du courant de drain (a) et du potentiel hors-équilibre (b) en fonction de la tension de grille pour différentes concentrations de charges ajoutées à la surface.

IV. Le Ψ-MOSFET utilisé comme biocapteur

IV.1. Etude préliminaire avec APTES et nanoparticules d'or

La preuve de concept des mesures de potentiel hors-équilibre pour les applications de détection a tout d'abord été faite sur des échantillons de SOI en utilisant des traitements chimiques connus pour modifier la charge à la surface supérieure du film de silicium pour le Ψ-MOSEFT [28], [29]. Les mesures ont été réalisées après un dépôt d'APTES ((3-aminopropyl)triéthoxysilane) chargé positivement et l'attachement de nanoparticules d'or (Au-np) chargées négativement.

Les courbes I_D-V_G (Figure 16a) ainsi que V_B-V_G (Figure 16b) sont décalées vers la gauche après APTES et vers la droite après le dépôt des nanoparticules d'or comme prévu pour les charges ajoutées. Les déplacements de V_T, V_{FB} et V_B sont présentés dans le Tableau 1. Tous les déplacements sont cohérents, ce qui signifie que le potentiel V_B peut être utilisé pour évaluer l'état de charge en surface. De plus, pour la courbe V_B-V_G, la réponse maximale est obtenue pour une tension de grille plutôt basse, alors que le décalage en I_D doit être observé à une V_G supérieure. Ceci est avantageux pour les applications de détection.

(a)   (b)

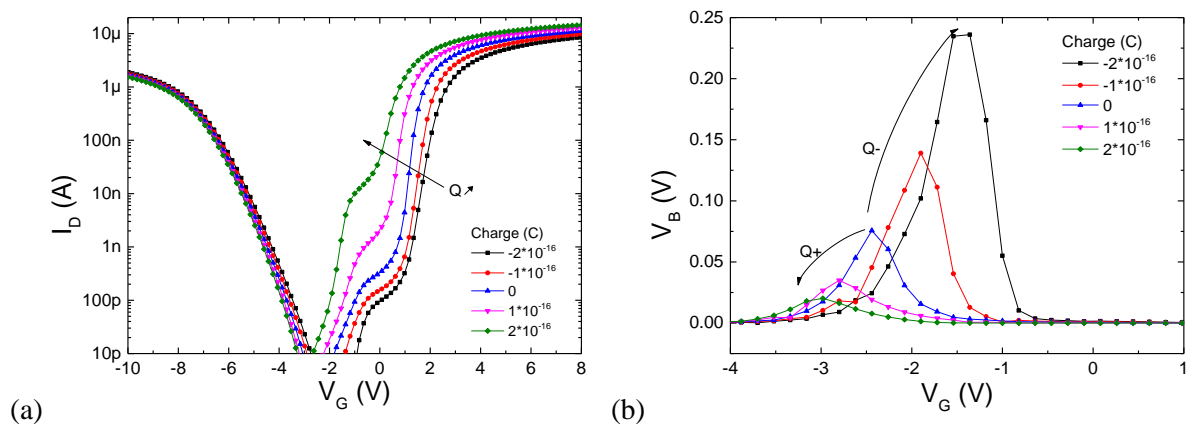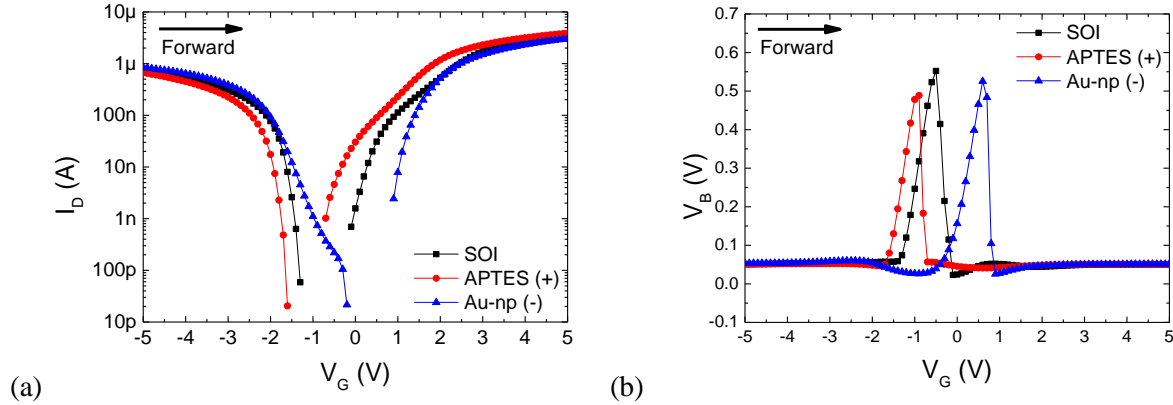*Figure 16: Courant de drain (a), potentiel hors-équilibre (b) en fonction de la tension de grille pour différents traitements chimiques. t_{Si} = 88nm, t_{BOX} = 145nm.*

Tableau 1: Caractéristiques électriques obtenues avant et après la fonctionnalisation avec APTES et Au-np. $\Delta V_G@V_B$ mesuré au point où V_B chute à 0V. t_{Si} = 88nm, t_{BOX} = 145nm.

Fonctionnalisation	V_T (V)	ΔV_T (V)	V_{FB} (V)	ΔV_{FB} (V)	$\Delta V_G@V_B$ (V)
SOI	0.5		-1.1		
APTES	0.1	-0.4	-1.6	-0.6	-0.6
Au-np	0.9	0.8	-0.5	1.1	1.0

IV.2. Détection de l'ADN

Afin de réaliser un capteur, l'ADN sonde doit être attachée à la surface du dispositif. La détection est réalisée lorsque l'hybridation entre l'ADN sonde et l'ADN cible ajoute des charges négatives qui sont détectées par le transducteur [30].

Deux processus différents ont été utilisés pour greffer l'ADN sonde à la surface du Ψ-MOSFET. Ils utilisent deux molécules différentes qui se fixent à la surface supérieure du film de silicium: APTES ((3-aminopropyl) triéthoxysilane) et GOPS ((3-glycidyloxypropyl) triméthoxysilane). Ce dernier présente parmi ses avantages la possibilité de fixer directement l'ADN à la surface du dispositif sans aucun lien supplémentaire, car le groupe époxy du GOPS peut réagir avec le groupe amine présent à l'extrémité de l'ADN sonde. De plus, le processus APTES utilise un composant très toxique : la glutaraldehyde et nécessite une étape en plus à cause du greffage de cette molécule. Les deux ont été développés et testés en collaboration avec l'Institut de Micronanotechnologies de Bucarest, dans le cadre d'un projet bilatérale Campus France pendant la thèse.

IV.2.1. Fonctionnalisation avec APTES

Pour chaque étape de fonctionnalisation, des échantillons contenant six dispositifs ont été utilisés afin de mesurer l'influence du traitement chimique sur les caractéristiques électriques de chaque dispositif. Les échantillons ont été caractérisés avant d'être envoyés pour la fonctionnalisation. Chaque

échantillon a subi un certain nombre d'étapes. Par exemple, l'échantillon dénommé ssADN, l'APTES, la glutaraldéhyde et l'ADN sonde ont été greffés à la surface du dispositif, tandis que l'échantillon de contrôle n'a subi que l'étape de nettoyage. On remarque également que, alors qu'on disposait initialement de six dispositifs pour chaque étape de fonctionnalisation, pour certaines d'entre elles, la couche d'oxyde enterré présentait des fuites après un traitement spécifique, les données correspondantes ne sont donc pas représentées. Les nombre suivant de dispositifs étaient toujours fonctionnels : contrôle (3/6), APTES (2/6), GAD (5/6), ssADN (6/6), dsADN (2/6).

V_T et V_{FB} ont ensuite été extraits après chaque étape de fonctionnalisation à l'aide de la fonction Y [31]. Les décalages de caractéristiques ΔV_T et ΔV_{FB} ont été calculés comme la différence entre la valeur après l'étape respective de fonctionnalisation et la valeur initiale du même dispositif sans aucune étape de fonctionnalisation. La variation de la tension de seuil (Figure 17a) montre que les étapes d'immobilisation et d'hybridation induisent des décalages positifs uniformes de +0,31V et +0,3V, respectivement. Ceci correspond à la charge négative du squelette phosphate-sucre de l'ADN. La même observation peut être faite dans le cas de la tension de bandes plates (Figure 17b). Le décalage induit par la détection de l'ADN est cependant plus faible : + 0,04 V pour l'étape d'immobilisation et + 0,11 V pour l'hybridation. Les valeurs des décalages sont plus fiables en régime d'inversion, car le décalage de V_{FB} est ici du même ordre de grandeur que la variabilité entre les dispositifs.
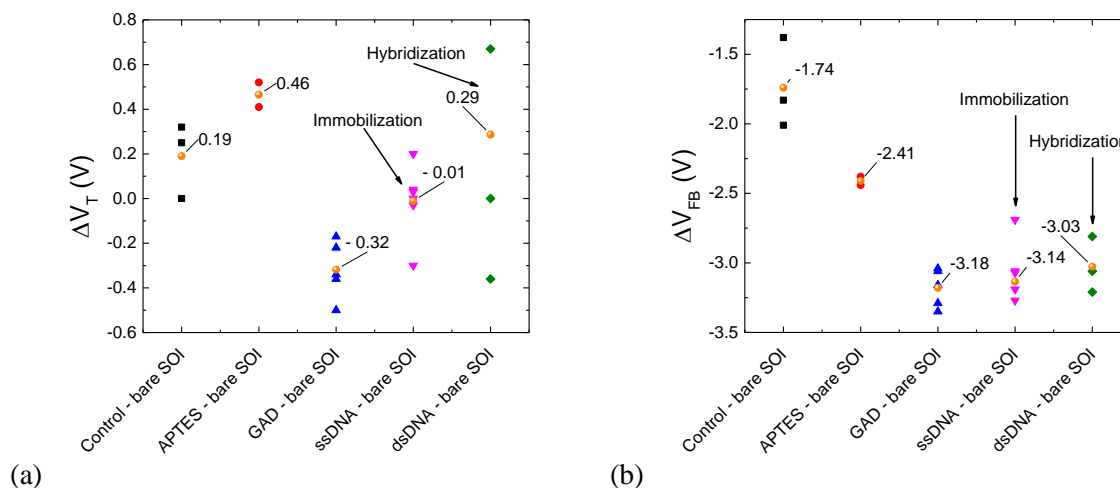

Figure 17: Variation de la tension de seuil (a) et de la tension de bandes-plates (b) pour différentes étapes de fonctionnalisation. Les valeurs moyennes sont représentées par des points orange. L'ADN chargé négativement induit un décalage positif comme prévu.

IV.2.2. Fonctionnalisation avec GOPS

Pour ce processus, la caractérisation électrique des dispositifs a été réalisée après chaque étape de fonctionnalisation. Cela garantissait un meilleur suivi de l'influence de chaque étape sur les caractéristiques électriques.

Les variations de la tension de seuil et de bandes-plates (Figure 18a et b respectivement) montrent des résultats cohérents pour les deux premières étapes: GOPS décale les courbes vers les tensions de grille positives, alors que l'immobilisation fait le contraire. Pour l'hybridation, les mesures montrent un décalage négatif pour la tension de seuil et pour de la tension de bande plates, qui augmentent tous deux avec la concentration de l'ADN cible.
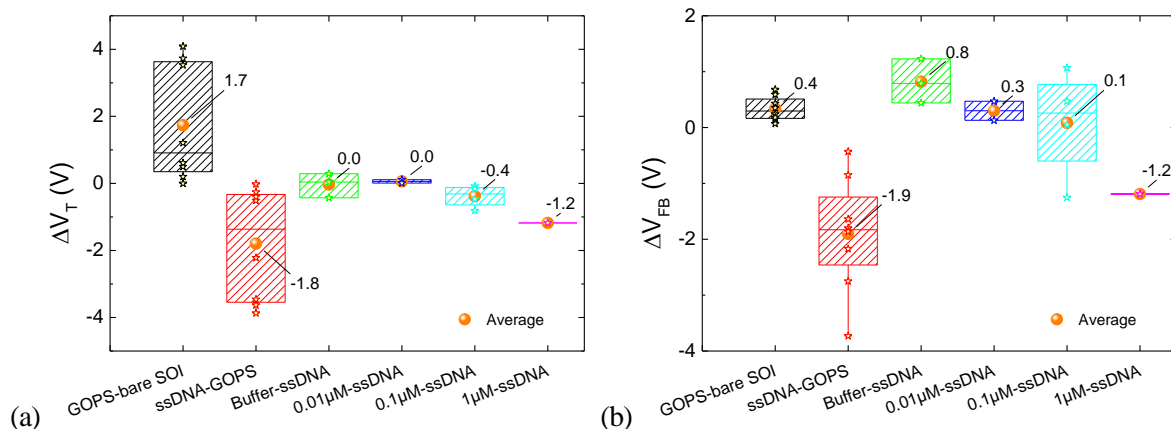
Figure 18: Variation de la tension de seuil (a) et de la tension de bandes-plates (b) pour différentes étapes de fonctionnalisation. Les valeurs moyennes sont représentées par des points orange.

Les mesures relatives de V_B pour chaque dispositif étaient représentées à la Figure 19 pour un sens de balayage Forward (tension de grille de négatif à positif). Les décalages sont cohérents avec les mesures de courant (Figure 18), le décalage $\Delta V_G @ V_{B0}$ (V_{B0} correspondant au point où le potentiel commence à croître) induit par le dépôt de GOPS étant positif, alors que pour l'immobilisation, il est négatif. Pour l'hybridation, les mesures montrent une nette tendance négative, qui augmente avec la concentration en ADN cible, ce qui prouve une fois encore que ce type de mesures est exclusivement sensible à la molécule d'ADN, et pas à la solution tampon.
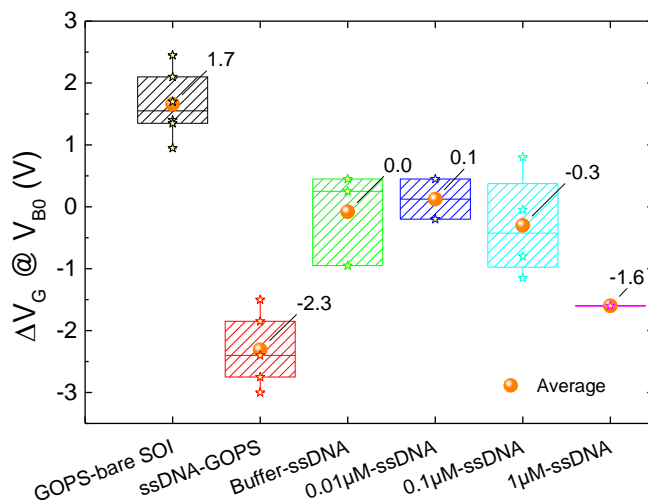

Figure 19: Variation correspondant au potentiel hors-équilibre pour différentes étapes de fonctionnalisation. Les valeurs moyennes sont représentées par des points orange.

V. Conclusions et perspectives

L'objectif principal de la thèse a été l'étude des mesures de potentiel hors-équilibre dans la configuration Ψ-MOSFET et l'application de cette méthode pour la détection des espèces biochimiques. Pour cela, une étude des contacts entre la pointe métallique et le film de silicium a été d'abord menée pour comprendre leur comportement ohmique qui est bien connu, mais pas clairement expliqué. En raison des cratères observés dans le film de silicium, nous avons proposé une nouvelle hypothèse basée sur le changement de phase du silicium induit par la nanoindentation. Les recherches réalisées jusqu'à présent dans la littérature ont montré que sous haute pression, une forme allotropique métastable du

silicium modifiait le comportement électrique du contact métal-semiconducteur de Schottky à ohmique. Nos résultats expérimentaux ont prouvé qu'il existait bien une charge seuil à partir de laquelle un changement de courant important pouvait être observé. Les hypothèses ont été vérifiées par plusieurs types de mesures expérimentales : caractérisation électrique, imagerie FIB-TEM et AFM.

Les mesures de potentiel hors-équilibre ont été analysées de façon détaillée du point de vue expérimental, mais aussi simulées de manière qualitative en utilisant TCAD Sentaurus. Les avantages de cette méthode ont également été présentés :

- la simplicité de la fabrication ;
- l'utilisation avec succès des wafers SOI avec film de silicium et oxyde enterré épaisses ;
- la mesure d'un potentiel à la place d'un faible courant ;
- l'invariance par rapport à la position des pointes et la pression appliquée ;
- la sensibilité élevée grâce :
  - aux distances très courtes (de l'ordre des dizaine des nanomètres correspondant à l'épaisseur du film) entre la charge amenée par les espèces chimiques en surface et le canal d'inversion/d'accumulation ;
  - au rapport des capacités entre l'oxyde enterré et la couche d'oxyde natif de la surface supérieure du film de silicium ;
- la stabilité provenant de la grande surface de détection qui permet d'obtenir des résultats provenant d'un très grand nombre de molécules.

Enfin, la détection des espèces biochimiques a donné des résultats très satisfaisants pour les nanobilles d'or et pour la détection de l'ADN en utilisant le procédé basé sur l'APTES. Le procédé GOPS a été utilisé pour différentes concentrations d'ADN cible. Cela a permis de déterminer que le décalage induit varie en fonction de la concentration et qu'il est dû exclusivement aux molécules d'ADN et pas de la solution tampon. Les résultats électriques obtenus montrent malheureusement un effet d'inversion de charge de l'ADN pour lequel la cause reste à déterminer. La limite de détection de notre configuration est d'approximativement 1 µM d'ADN cible. Même si elle est très élevée par rapport aux fM trouvés dans la littérature pour les nanofils de silicium, en la normalisant par rapport aux surfaces actives, on obtient une efficacité d'attachement de l'ADN comparable.

L'étude a été menée sur un large spectre de sujets, pouvant tous être développés. Premièrement, l'explication basée sur la nanoindentation décrivant le comportement de contact ohmique dans le Ψ-MOSFET devrait être consolidée à l'aide d'un appareil spécifique à la cristallographie qui permet la mesure précise de la charge appliquée sur les indentateurs.

Les mesures de potentiel hors-équilibre peuvent également être rendues plus pratiques pour la détection en mettant en œuvre des vitesses de balayage rapides imposées par des signaux alternatifs. En outre, les simulations pourraient également être améliorées afin de mieux correspondre aux données expérimentales.

Du point de vue des capteurs, les développements ultérieurs doivent cibler la grande surface du dispositif, qui ne permet pas un bon contrôle de la position, des conditions de séchage et de l'uniformité de la concentration en analyte déposée. Pour cela, une réduction de la taille du dispositif et / ou l'ajout d'un canal microfluidique doivent être envisagés afin d'atteindre un niveau de performance intéressant (une limite de détection plus favorable). De plus, des campagnes de mesure plus importantes sont également nécessaires pour déterminer clairement les caractéristiques du capteur (sensibilité, limite de détection, régime linéaire, etc.).

Tous ces résultats préliminaires démontrent le potentiel important des mesures de potentiel pour les applications de détection, ce qui représente une grande opportunité pour les futurs travaux de recherche.

Bibliographie

[1]   Piet Bergveld, 'Development of an Ion-Sensitive Solid-State Device for Neurophysiological Measurements', *IEEE Trans. Biomed. Eng.*, Jan. 1970.

[2]   F. Patolsky, G. Zheng, O. Hayden, M. Lakadamyali, X. Zhuang, and C. M. Lieber, 'Electrical detection of single viruses', *Proc. Natl. Acad. Sci. U. S. A.*, vol. 101, no. 39, pp. 14017–14022, 2004.

[3]   P. Xie, Q. Xiong, Y. Fang, Q. Qing, and C. M. Lieber, 'Local electrical potential detection of DNA by nanowire–nanopore sensors', *Nat. Nanotechnol.*, vol. 7, no. 2, pp. 119–125, Dec. 2011.

[4]   A. Manickam, R. Singh, N. Wood, B. Li, A. Ellington, and A. Hassibi, 'A fully-electronic charge-based DNA sequencing CMOS biochip', in *VLSI Circuits (VLSIC), 2012 Symposium on*, 2012, pp. 126–127.

[5]   Fernando Patolsky, Gengfeng Zheng, and Charles M. Lieber, 'Nanowire-based Biosensors', *Am. Chem. Soc. - Anal. Chem.*, pp. 4261–4269, Jul. 2006.

[6]   Yi Cui, Qingqiao Wei, Hongkun Park, and Charles M. Lieber, 'Nanowire Nanosensors for Highly Sensitive and Selective Detection of Biological and Chemical Species', *Sci. Rep.*, vol. 293, no. 5533, pp. 1289–1292, Aug. 2001.

[7]   Y. Wang and J. T. W. Yeow, 'A Review of Carbon Nanotubes-Based Gas Sensors', *J. Sens.*, vol. 2009, pp. 1–24, 2009.

[8]   F. Veliev, Z. Han, D. Kalita, A. Briançon-Marjollet, V. Bouchiat, and C. Delacour, 'Recording Spikes Activity in Cultured Hippocampal Neurons Using Flexible or Transparent Graphene Transistors', *Front. Neurosci.*, vol. 11, Aug. 2017.

[9]   J. M. Rothberg *et al.*, 'An integrated semiconductor device enabling non-optical genome sequencing', *Nature*, vol. 475, no. 7356, pp. 348–352, Jul. 2011.

[10] J. Hahm and C. M. Lieber, 'Direct Ultrasensitive Electrical Detection of DNA and DNA Sequence Variations Using Nanowire Nanosensors', *Nano Lett.*, vol. 4, no. 1, pp. 51–54, Jan. 2004.

[11] G.-J. Zhang *et al.*, 'Highly sensitive measurements of PNA-DNA hybridization using oxide-etched silicon nanowire biosensors', *Biosens. Bioelectron.*, vol. 23, no. 11, pp. 1701–1707, Jun. 2008.

[12] A. Gao *et al.*, 'Silicon-Nanowire-Based CMOS-Compatible Field-Effect Transistor Nanosensors for Ultrasensitive Electrical Detection of Nucleic Acids', *Nano Lett.*, vol. 11, no. 9, pp. 3974–3978, Sep. 2011.

[13] A. Gao *et al.*, 'Enhanced Sensing of Nucleic Acids with Silicon Nanowire Field Effect Transistor Biosensors', *Nano Lett.*, vol. 12, no. 10, pp. 5262–5268, Oct. 2012.

[14] C.-J. Chu *et al.*, 'Improving Nanowire Sensing Capability by Electrical Field Alignment of Surface Probing Molecules', *Nano Lett.*, vol. 13, no. 6, pp. 2564–2569, Jun. 2013.

[15] G. Wenga, E. Jacques, A.-C. Salaün, R. Rogel, L. Pichon, and F. Geneste, 'Step-gate polysilicon nanowires field effect transistor compatible with CMOS technology for label-free DNA biosensor', *Biosens. Bioelectron.*, vol. 40, no. 1, pp. 141–146, Feb. 2013.

[16] M. N. Nuzaihan *et al.*, 'Top-Down Nanofabrication and Characterization of 20 nm Silicon Nanowires for Biosensing Applications', *PLOS ONE*, vol. 11, no. 3, p. e0152318, Mar. 2016.

[17] S. Cristoloveanu, M. Bawedin, and I. Ionica, 'A review of electrical characterization techniques for ultrathin FDSOI materials and devices', *Solid-State Electron.*, vol. 117, pp. 10–36, Mar. 2016.

[18] G. T. Ayele *et al.*, 'Ultrahigh-Sensitive and CMOS Compatible ISFET Developed in BEOL of Industrial UTBB FDSOI', *Symp. VLSI Technol. Dig. Tech. Pap.*, p. 2, 2018.

[19] S. Williams, S. Cristoloveanu, and G. Campisi, 'Point contact pseudo-metal/oxide/semiconductor transistor in as-grown silicon on insulator wafers', *Mater. Sci. Eng. B*, vol. 12, no. 1–2, pp. 191–194, 1992.

[20] I. Ionica, I. Savin, W. Van Den Daele, T. Nguyen, X. Mescot, and S. Cristoloveanu, 'Characterization of silicon-on-insulator films with pseudo-metal-oxide-semiconductor field-effect transistor: Correlation between contact pressure, crater morphology, and series resistance', *Appl. Phys. Lett.*, vol. 94, no. 1, p. 012111, Jan. 2009.

[21] J. Z. Hu, L. D. Merkle, C. S. Menoni, and I. L. Spain, 'Crystal data for high-pressure phases of silicon', *Phys. Rev. B*, vol. 34, no. 7, p. 4679, 1986.

[22] D. E. Kim and S. I. Oh, 'Atomistic simulation of structural phase transformations in monocrystalline silicon induced by nanoindentation', *Nanotechnology*, vol. 17, no. 9, pp. 2259–2265, May 2006.

[23] S. Ruffell, J. E. Bradby, J. S. Williams, and O. L. Warren, 'An in situ electrical measurement technique via a conducting diamond tip for nanoindentation in silicon', *J. Mater. Res.*, vol. 22, no. 03, pp. 578–586, Mar. 2007.

[24] L. Benea, T. Cerba, M. Bawedin, C. Delacour, S. Cristoloveanu, and I. Ionica, 'Nanoindentation effects on the electrical caracterizaron in Ψ-MOSFET configuration', in *Ultimate Integration on Silicon (EUROSOI-ULIS), 2018 Joint International EUROSOI Workshop and International Conference on*, 2018, pp. 1–4.

[25] W. Van Den Daele, C. Malaquin, N. Baumel, O. Kononchuk, and S. Cristoloveanu, 'Adaptation of the pseudo-metal–oxide–semiconductor field effect transistor technique to ultrathin silicon–on-insulator wafers characterization: Improved set-up, measurement procedure, parameter extraction, and modeling', *J. Appl. Phys.*, vol. 114, no. 16, p. 164502, Oct. 2013.

[26] J.-P. Colinge, *Silicon-on-insulator technology: materials to VLSI*. New York: Springer Science, 2004.

[27] L. Benea, M. Bawedin, C. Delacour, and I. Ionica, 'Out-of-equilibrium body potential measurements in pseudo-MOSFET for sensing applications', *Solid-State Electron.*, vol. 143, pp. 69–76, May 2018.

[28] C. Fernandez, N. Rodriguez, C. Marquez, and F. Gamiz, 'Determination of ad hoc deposited charge on bare SOI wafers', in *Ultimate Integration on Silicon (EUROSOI-ULIS), 2015 Joint International EUROSOI Workshop and International Conference on*, 2015, pp. 289–292.

[29] I. Ionica, A. E. H. Diab, and S. Cristoloveanu, 'Gold nanoparticles detection using intrinsic SOI-based sensor', in *Nanotechnology (IEEE-NANO), 2011 11th IEEE Conference on*, 2011, pp. 38–43.

[30] E. Souteyrand *et al.*, 'Direct Detection of the Hybridization of Synthetic Homo-Oligomer DNA Sequences by Field Effect', *J. Phys. Chem. B*, vol. 101, no. 15, pp. 2980–2985, Apr. 1997.

[31] G. Ghibaudo, 'New method for the extraction of MOSFET parameters', *Electron. Lett.*, vol. 24, no. 9, p. 543, 1988.